

Diagnostics for plasma-based electron accelerators

Downer, M. C.; Zgadzaj, R.; Debus, A.; Schramm, U.; Kaluza, M. C.;

Originally published:

August 2018

Reviews of Modern Physics 90(2018), 035002

DOI: <https://doi.org/10.1103/RevModPhys.90.035002>

Perma-Link to Publication Repository of HZDR:

<https://www.hzdr.de/publications/Publ-27870>

Release of the secondary publication
on the basis of the German Copyright Law § 38 Section 4.

Diagnostics for plasma-based electron accelerators

M. C. Downer* and R. Zgadzaj

*Department of Physics,
University of Texas at Austin,
Austin, TX 78712,
USA*

A. Debus and U. Schramm

*Helmholtz-Zentrum Dresden-Rossendorf,
Institute for Radiation Physics, 01328 Dresden,
Germany*

M. C. Kaluza

*Institute of Optics and Quantum Electronics,
Friedrich-Schiller-University, 07743 Jena,
Germany
Helmholtz Institute Jena, 07743 Jena,
Germany*

(Dated: May 3, 2018)

Plasma-based accelerators that impart energy gain as high as several GeV to electrons or positrons within a few centimeters have engendered a new class of diagnostic techniques very different from those used in connection with conventional radio-frequency (RF) accelerators. The need for new diagnostics stems from the micrometer scale and transient, dynamic structure of plasma accelerators, which contrasts with the meter scale and static structure of conventional accelerators. Because of this micrometer source size, plasma-accelerated electron bunches can emerge with smaller normalized transverse emittance ($\epsilon_n < 0.1$ mm mrad) and shorter duration ($\tau_b \sim 1$ fs) than bunches from RF linacs. We review single-shot diagnostics that determine such small ϵ_n and τ_b non-invasively and with high resolution from wide-bandwidth spectral measurement of electromagnetic radiation the electrons emit: ϵ_n from x-rays emitted as electrons interact with transverse internal fields of the plasma accelerator or with external optical fields or undulators; τ_b from THz to optical coherent transition radiation emitted upon traversing interfaces. The duration of ~ 1 fs bunches can also be measured by sampling individual cycles of a co-propagating optical pulse or by measuring the associated magnetic field using a transverse probe pulse. Because of their luminal velocity and micrometer size, the evolving structure of plasma accelerators, the key determinant of accelerator performance, is exceptionally challenging to visualize in the laboratory. Here we review a new generation of laboratory diagnostics that yield snapshots, or even movies, of laser- and particle-beam-generated plasma accelerator structures based on their phase modulation or deflection of femtosecond electromagnetic or electron probe pulses. We discuss spatiotemporal resolution limits of these imaging techniques, along with insights into plasma-based acceleration physics that have emerged from analyzing the images, and comparing them to simulated plasma structures.

CONTENTS

I	Introduction	1	1	Standard LWFA and PWFA.	7
II	Properties of plasma accelerator structures and beams	3	2	Self-modulated LWFA and PWFA.	8
A	General properties of plasma electron accelerators	3	3	Multi-Pulse LWFA and PWFA.	8
1	Ponderomotive and Coulomb forces	3	C	Electron beams from strongly nonlinear LWFAs	8
2	Wake structures	3	1	Charge and energy spread	9
3	Accelerating and focusing fields	5	2	Transverse emittance.	11
4	Plasma density range	6	3	Bunch duration.	12
5	De-phasing, pump depletion and transformer ratio	6	III	Diagnostics of Plasma-Accelerated Electron Bunches	12
6	Atomic composition of the plasma	7	A	Radiation from plasma-accelerated electrons	13
B	Plasma accelerator configurations.	7	1	Synchrotron radiation	13
			2	Undulator and Thomson backscatter radiation	13
			3	Betatron radiation	15
			4	Transition radiation	16
			B	Bunch charge and energy measurement	20
			1	Total and spatially-resolved charge measurement	20
			2	MeV and GeV magnetic spectrometers	22
			3	Spectroscopy of on-axis undulator radiation	23

* downer@physics.utexas.edu

4	Slice energy spread	24
C	Transverse emittance measurement	25
1	Conventional mask and focus-scan methods	25
2	Betatron x-ray spectroscopy	26
3	Undulator and transition radiation diagnostics	27
D	Bunch length measurement	28
1	Time-domain methods	29
2	Frequency-domain methods	31
I	Diagnostics of Plasma Accelerator Structures	33
A	Light emission and scattering from plasma waves	33
1	Plasma self-emission	33
2	Light scattering	34
B	Multi-shot sub- λ_p probes	36
1	Electron witness bunches	36
2	Laser probe pulses	38
C	“Snapshots” of wake structures	40
1	Frequency-domain holography	41
2	Longitudinal optical shadowgraphy	45
3	Transverse optical probing	46
4	Electron radiography	48
D	“Movies” of wake evolution	49
1	Multi-shot transverse probes	49
2	Single-shot frequency-domain streak camera	50
3	Single-shot imaging of meter-long wakes	52
E	Scaling of wake probes with plasma density	54
V	Conclusion	55
	References	58

I. INTRODUCTION

Energetic electron and positron beams from accelerators probe the fundamental structure of sub-atomic matter, irradiate cancerous tumors, and produce bright x-rays that sterilize food and medical equipment and reveal the structure of molecules essential to life. For decades, radio-frequency (RF) technology has underlain all such accelerators, but is inherently limited to accelerating fields of ~ 1 MV/cm by the electrical breakdown threshold of metallic structures. Consequently, with RF technology, the next electron-positron collider at the energy frontier (electron energy $E_e \sim$ TeV) will cost over \$10 B, and require construction of tunnels tens of kilometers long (Behnke, 2015). Even GeV-class electron accelerators that underlie the current generation of x-ray lasers and Compton gamma-ray sources at the frontiers of experimental biomedical, materials and nuclear science typically cost hundreds of millions of dollars and occupy several square kilometers of real estate. These prohibitive costs are forcing a widespread re-alignment of accelerator research and development toward alternative accelerator technologies that can provide high electron beam quality, energy and current at dramatically lower cost and size (Ritz, 2014).

Accelerators based on plasmas of sub-atmospheric electron density ($10^{17} < n_e < 10^{19}$ cm $^{-3}$) perturbed by ultrashort laser pulses or relativistic charged particle bunches have emerged as a promising pathway toward compact, low-cost electron and positron accelera-

tion. In such accelerators, the electro-magnetic (-static) force of the drive laser pulse (particle bunch) expels plasma electrons from within the driver’s envelope, creating a positively-charged, light-speed accelerating cavity, or “wake”, with dimensions of a plasma wavelength $\lambda_p[\mu\text{m}] = (3.3 \times 10^{10})/\sqrt{n_e [\text{cm}^{-3}]}$, which is tens of microns for the n_e range cited above. Electrostatic fields within these cavities are of order $E_z[\text{V/cm}] \approx \sqrt{n_e [\text{cm}^{-3}]}$, and thus reach $\sim 10^9$ V/cm for the cited n_e range, thousands of times larger than fields that conventional accelerators can sustain, yet without breakdown concern. This plasma cavity can capture electrons or positrons that are injected into it with mildly relativistic speed along its propagation direction. In some cases, a small independent conventional RF pre-accelerator injects the initial particle bunch. A common alternative, unique to electron accelerators, is that the initial driver-plasma interaction creates a mildly relativistic high-energy tail of ambient plasma electrons that self-injects into the cavity. Section II.B discusses a variety of injection strategies, and their consequences for beam quality. In all cases, the transient plasma cavity accelerates the captured particles further with GV/cm field strength until either they dephase from it or the drive pulse (bunch) depletes.

Since Tajima and Dawson first proposed the concept of plasma-based, laser-driven electron acceleration in 1979 (Tajima and Dawson, 1979), wakefield acceleration has grown into an international research and development effort encompassing laboratory demonstrations, theoretical modeling and computer simulations of rapidly increasing sophistication and scope (Esarey *et al.*, 2009). Within the last few years, two laboratories demonstrated single-stage laser-driven wakefield accelerators (LWFAs) that captured ambient plasma electrons and accelerated them to 2 to 4 GeV energy with few percent energy spread and up to 0.1 nC charge within an acceleration distance of only a few centimeters (Leemans *et al.*, 2014; Wang *et al.*, 2013). Many laboratories have converted LPAs into femtosecond x-ray sources based on betatron radiation from electrons accelerating within the plasma structure, synchrotron radiation in external undulators, or Thomson backscatter of laser light from accelerated electrons outside the LWFA (Corde *et al.*, 2013), while the pursuit of tabletop x-ray free electron lasers based on LWFA beams is a forefront research challenge (Gruener *et al.*, 2007; Nakajima, 2008). Dual-stage LWFAs using one (Kim *et al.*, 2013a) or two independent (Steinke *et al.*, 2016) laser drive pulses, a critical step toward multi-stage LWFAs required for colliders at the energy frontier (Leemans and Esarey, 2009), were also recently demonstrated.

Meanwhile, single-stage plasma accelerators driven by relativistic electron or positron bunches (Chen *et al.*, 1985) — usually called simply plasma wakefield accelerators (PWFAs) — have imparted energy gain of several GeV within an acceleration distance of approxi-

mately a meter to independent, externally injected, co-propagating electron (Litos *et al.*, 2014) and positron (Corde *et al.*, 2015) witness bunches of 0.1 nC charge while maintaining high beam quality. The possibility of accelerating trailing electrons to twice the energy of the drive electron bunch in a single stage has been demonstrated in principle (Blumenfeld *et al.*, 2007), opening the prospect of compact, plasma-based, energy-doubling afterburners for conventional electron accelerators (Harris, 2016; Lee *et al.*, 2002). Computer simulations have shown that PWFAs driven by bunches of relativistic *protons* can in principle accelerate electrons or positrons to the energy frontier in one sub-kilometer stage (Caldwell *et al.*, 2009; Lotov, 2010), a possibility that the AWAKE project at CERN is now beginning to explore in the laboratory (Caldwell *et al.*, 2016; Geschwendtner *et al.*, 2016).

Despite rapid recent progress with LWFA and PWFAs, concern remains about whether plasma wakefield techniques can be incorporated into practical accelerators useful for high-energy physics or other areas of discovery science, in view of stringent requirements for narrow energy spread, emittance, beam stability and control, and brightness preservation (HEPAP, 2015). This concern brings the subject of this review — diagnostics for plasma-based electron accelerators — to center stage. Diagnostics link the micron-scale structure and femtosecond-scale dynamics of plasma wakes to the key beam properties — bunch duration, transverse emittance, charge and energy spread — that govern the performance of a collider or light source. They also link observable accelerator properties to theory and computer simulation output. However, diagnostics in widespread use with conventional RF accelerators have, by and large, proven insufficient for characterizing plasma-based electron accelerators.

There are two reasons for this. First, because of the micrometer scale of plasma accelerator structures, plasma-accelerated electron bunches can emerge with shorter duration ($\sigma_s/c \sim 1$ fs), and smaller transverse beam size ($0.1\mu\text{m} \lesssim \sigma_r \lesssim 0.1\mu\text{m}$) than bunches from meter-scale RF accelerator structures. Thus, beams from plasma-based accelerators can have smaller normalized transverse emittance ($\epsilon_n < 0.1$ mmrad) than beams from conventional accelerators. Here ϵ_n is the product of a beam’s geometric emittance (roughly $\sigma_r\sigma_r'$ at a beam waist, where σ_r' is its angular divergence) and its Lorentz factor γ_e that is conserved in an ideal beam transport system. Small ϵ_n is potentially a key advantage over conventional accelerators, because it enables high luminosity in collider interactions and wide tuning range in free electron lasers (FELs). Together with short bunch length σ_z , it is also essential for achieving high peak brightness from Thomson backscatter and FEL light sources. Section II reviews these unique properties of plasma-accelerated electron bunches, and the laser-plasma conditions that optimize them, while Section III reviews new

methods now emerging to measure them with the resolution required to operate practical plasma-based accelerators. Second, plasma accelerator structures, in contrast to fixed, stationary conventional accelerator structures, are evolving and transient as they propagate at luminal velocity, and must be re-created with high fidelity for each bunch. Accelerator performance depends sensitively on details of the plasma structure and dynamics. For example, “bubble”-like electron density cavities created via highly nonlinear interaction of drive pulses/bunches with a plasma yield more mono-energetic beams than sinusoidal wakes created via linear interactions (Pukhov and Meyer-ter-Vehn, 2002). Moreover, evolution of the bubble structure during propagation governs self-injection of plasma electrons (Kalmykov *et al.*, 2009). Accurate single-shot visualization of these plasma structures and their dynamics in the laboratory is essential not only for operating practical plasma accelerators, but for validating individual stages of holistic computer simulation output, and for understanding LWFA physics in detail. Section IV reviews the many innovative diagnostic methods that have been, and continue to be, invented for capturing images of these plasma structures in the act of accelerating electrons and positrons to relativistic energy. This aspect of diagnostics has no counterpart in conventional RF acceleration, and is likely to be a continuing source of innovation and discovery. Sec.V presents our conclusions, and our assessment of important future directions in plasma acceleration diagnostics.

II. PROPERTIES OF PLASMA ACCELERATOR STRUCTURES AND BEAMS

A. General properties of plasma electron accelerators

We refer the reader to (Esarey *et al.*, 2009; Hooker, 2013; Leemans and Esarey, 2009; Malka, 2012; Malka *et al.*, 2008; Norreys, 2009) for reviews of the physics and applications of *laser*-driven plasma-based electron accelerators, and to (Caldwell *et al.*, 2016; Hogan *et al.*, 2010; Muggli, 2016; Muggli and Hogan, 2009) for reviews of *particle-beam*-driven plasma wakefield acceleration. Here we summarize basic features of LWFA and PWFA structures and beams that are needed for the subsequent discussion of diagnostics.

1. Ponderomotive and Coulomb forces

The simplest LWFA consists of a single intense laser pulse focused into a confined gas or pre-ionized underdense plasma. For gas targets, the leading edge of the pulse ionizes the gas, creating plasma. The intense portion of the pulse then creates a light-speed accelerating structure by expelling plasma electrons longitudinally and radially from within its envelope via “pon-

deromotive” pressure, which is equivalent to the gradient $\vec{\nabla}(\epsilon_0 E_L^2/2)$ of the pulse’s cycle-averaged electromagnetic energy density. Here, E_L is the local amplitude of the laser electric field in V/m. When each electron’s quiver motion in the field E_L is non-relativistic, the ponderomotive force \vec{F}_p on each electron (mass m_e) is (Esarey *et al.*, 2009; Kruer, 1988)

$$\vec{F}_p = -m_e c^2 \vec{\nabla}(a^2/2), \quad (1)$$

where $a = eE_L/m_e \omega c$ is the local dimensionless normalized vector potential, equal to the ratio of momentum eE_L/ω that the laser field of frequency ω imparts to an electron in an optical cycle to $m_e c$ as a function of position within the pulse profile. Thus $a \approx 1$ is a soft boundary between non-relativistic electron undulation and linear laser-plasma interaction at $a < 1$, and relativistic electron motion and nonlinear laser-plasma interaction at $a > 1$. We can relate a to local intensity $I = E_L^2/2Z_0$ of a pulse of wavelength λ by $I(\text{W/m}^2) = (\pi c/2)(4\pi\epsilon_0)(m_e c^2 a/e\lambda)^2$, where $Z_0 = \sqrt{\mu_0/\epsilon_0}$ is the impedance of free space. Thus, from Eq. (1), \vec{F}_p is proportional to the intensity gradient $\vec{\nabla}I$. Identical expressions relate intensity I_0 , field amplitude E_{L0} and laser strength parameter a_0 at the *peak* of a pulse. Using units W/cm^2 for I_0 and μm for λ , the relationship becomes:

$$a_0 = 0.85 \sqrt{\lambda^2 (\mu\text{m}) I_0 (10^{18} \text{W/cm}^2)}. \quad (2)$$

For highly relativistic ($a_0 \gg 1$) pulses, the ponderomotive force can be written $\vec{F}_p = -m_e c^2 \vec{\nabla}\gamma_e$, where $\gamma_e \equiv [1 + (p_e/m_e c)^2]^{1/2} \approx (1 + a^2)^{1/2}$ is the Lorentz factor associated with the electron’s quiver motion and p_e is the oscillating electron’s momentum. Ions also experience \vec{F}_p , but respond much more slowly than electrons. Consequently charge separates, creating longitudinal (accelerating) and transverse (focusing) fields, or wakefields, that can trap and accelerate leptons.

In the PWFA, the Coulomb force of a bunch of density n_b replaces the ponderomotive force (1) as plasma wake driver. For relativistic bunches, the Lorentz-contracted Coulomb electric field is essentially transverse ($\vec{E} \approx E_r \hat{e}_r$), and the bunch’s internal space-charge force $en_b E_r$ is reduced by a factor γ_e^{-2} compared to non-relativistic bunches (Muggli, 2016). Consequently, transverse bunch dynamics over meter-scale path lengths is dominated by emittance and external focusing forces, rather than space-charge (Hogan *et al.*, 2003; Muggli *et al.*, 2008b). The boundary between linear (Chen *et al.*, 1985) and nonlinear (Rosenzweig *et al.*, 1991) wake excitation occurs at $n_b \sim n_e$ for PWFA, analogous to $a_0 \sim 1$ for LWFA. Unlike laser drivers, particle bunch drivers can either “blow out” or “suck in” plasma electrons, depending on whether they are negatively or positively charged. Indeed, PWFA experiments have been (and are being) performed with electron (Blumenfeld *et al.*, 2007; Litos

et al., 2014), positron (Blue *et al.*, 2003; Corde *et al.*, 2015), and proton (Caldwell *et al.*, 2016; Geschwendtner *et al.*, 2016) drive bunches.

2. Wake structures

The shape and dynamics of a wake’s electron density profile $n_e(r, z, t)$ depend on the duration, focus and energy (and for PWFAs, charge; for LWFAs, λ) of the drive pulse, and on the density, composition and pre-formed structure of the plasma target. As a simple example, a 1D laser pulse of longitudinal duration τ_L (FWHM) less than a plasma period $\tau_p \equiv f_p^{-1} \equiv 2\pi/\omega_p$ and amplitude $a_0 \ll 1$ propagating at group velocity $v_g \approx c$ in a uniform, underdense plasma of unperturbed electron density \bar{n}_e linearly excites a sinusoidal 1D electron density wake (Tajima and Dawson, 1979)

$$\delta n_e(z, t) = \delta n_{e,0} \sin k_p \zeta. \quad (3a)$$

Here, $\delta n_e(z, t) \equiv n_e - \bar{n}_e$ is the local density perturbation of amplitude $\delta n_{e,0}$, $k_p = \omega_p/v_g$ is the plasma wavenumber, $\omega_p = (\bar{n}_e e^2/\epsilon_0 m_e)^{1/2}$ is the plasma frequency for collective electron density oscillations, $v_{ph,p} = \omega_p/k_p = v_g$ is the plasma wave phase velocity set by v_g , and $\zeta \equiv z - v_g t$. As τ_L varies, $\delta n_{e,0}$ exhibits a broad resonant peak at $\tau_L \sim \tau_p/2$.

In 3D with cylindrical symmetry, a sub-relativistic ($a_0 \ll 1$) pulse of duration $\tau_L \lesssim \tau_p/2$, focused to Gaussian transverse profile $a_0 \exp(-r^2/w_0^2)$ of width $w_0 \lesssim \lambda_p$, linearly excites a wake of the form

$$\begin{aligned} \delta n_e(r, z, t) &= \delta n_z(r, z, t) + \delta n_r(r, z, t) \\ &= A e^{-r^2/w_0^2} [1 + f(r)] \sin k_p \zeta \end{aligned} \quad (3b)$$

that can be calculated analytically from cold fluid equations (Esarey *et al.*, 1989; Gorbunov and Kirsanov, 1987). Here, A depends on the pump’s peak power and its Rayleigh length $z_R = \pi w_0^2/\lambda$, and $f(r) \equiv (\lambda_p^2/\pi \lambda z_R)(1 - r^2/w_0^2)$. The first (second) term in square brackets corresponds to the contribution δn_z (δn_r) arising from the longitudinal (radial) ponderomotive force. Such 2D linear laser wakes were the first to be observed directly in the laboratory with sub- λ_p resolution, using ultrashort laser probe pulses (see Sec. IV.B.2). Researchers took advantage of tight focusing to create $\delta n_r \sim \bar{n}_e$ over $\lesssim 0.1$ mm path with sub-terawatt (sub-TW) lasers (Marquès *et al.*, 1996; Siders *et al.*, 1996b), before multi-TW lasers (Backus *et al.*, 1998) became widely available.

With advances in laser technology, excitation of wakes with short ($\tau_L \lesssim \tau_p/2$), mildly relativistic ($a_0 \sim 1$) pulses over multi-mm paths became possible. In this regime, numerical calculations are required to describe wake excitation in 3D, although analytic 1D solutions that exhibit the main physical effects are possible with simplifying assumptions such as a non-evolving driver and a quasi-static plasma structure (Sprangle *et al.*, 1990a,b). The

wake develops non-sinusoidal features attributable to the relativistic mass increase of the strongly-driven plasma electrons. In 1D, the main new features are steepened wavefronts and lengthened wake period (Berezhiani and Murusidze, 1990; Bulanov *et al.*, 1989; Sprangle *et al.*, 1990a,b). In 3D, these effects depend on r . A mildly relativistic drive laser pulse that is peaked on axis creates a period-lengthened, steepened wake on axis, but a linear wake off axis. As a result, wave fronts curve, with curvature increasing with distance behind the driver (Andreev *et al.*, 1997b; Bulanov *et al.*, 1995; Decker and Mori, 1994; Sprangle *et al.*, 1992). Reduction of \bar{n}_e on axis (*e.g.* by ponderomotive channeling) can further lengthen the on-axis period, and accentuate the curvature. Fig. 1a shows a computer simulation of a wake excited in this regime. Ultimately transverse wave-breaking can occur (Bulanov *et al.*, 1997b). Sec. IV.C describes single-shot diagnostic experiments in which these features of mildly relativistic plasma wakes were first observed in the laboratory (Dong *et al.*, 2010a; Matlis *et al.*, 2006).

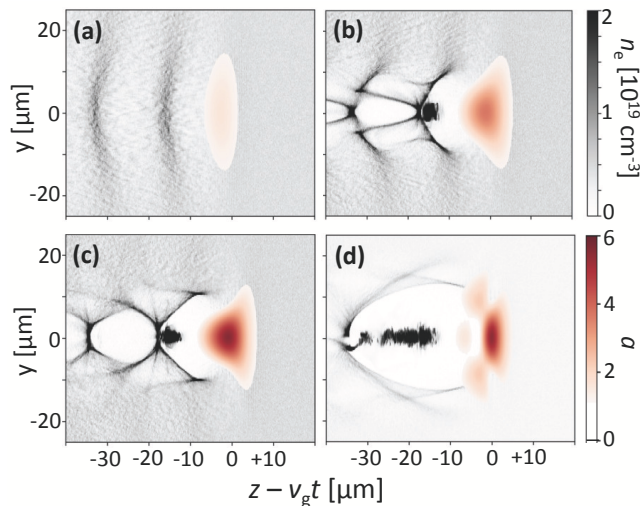


FIG. 1 Color online. Particle-in-cell simulation of evolving laser-driven plasma bubble. Grey scale: local electron density n_e ; color scale: local strength a of drive laser profile centered at $y = z - v_g t = 0$. Gas jet: He with 1% N, with linear entrance ramp ($0 < z < 0.55$ mm), plateau ($0.55 < z < 2.55$ mm) at $\bar{n}_e = 4.4 \times 10^{18} \text{ cm}^{-3}$ after ionization, exit ramp ($2.55 < z < 3.1$ mm). Laser pulse: $\lambda = 800$ nm, $\tau_L = 30$ fs, beam waist $w_0 = 19 \mu\text{m}$ at $z = 4.1$ mm. (a) $z = 1.72$ mm, $a_0 \approx 1$, mildly nonlinear wake; (b) $z = 2.15$ mm, $a_0 \approx 3$, bubble has formed, ionized inner-shell electrons from N-dopant injected and trapped; (c) $z = 2.37$ mm, $a_0 \approx 6$, bubble evolves, trapped electrons advance; (d) $z = 2.8$ mm, $a_0 \approx 6$, bubble lengthens in downramp. Courtesy R. Pausch.

As the drive pulse intensifies further to $a_0 \gtrsim 3$, it can evacuate electrons completely from its immediate wake (Fig. 1b). This strongly nonlinear LWFA regime, first discovered in computer simulations (Pukhov and Meyerter-Vehn, 2002), leaves behind a nearly spherical bare ion cavity bounded by a thin, dense electron “wall”. Fig. 1b-

d show simulations of the self-consistent evolution of the drive laser pulse (red) and trailing ion cavity excited in this strongly nonlinear regime, which researchers began calling the “bubble” regime (Kostyukov *et al.*, 2004). Using 3D simulations, (Lu *et al.*, 2007) comprehensively documented properties of bubble-regime LWFAs over a wide range of laser-plasma parameters. Because of their special importance for plasma accelerator science in general, and diagnostic development in particular, we review properties of bubble-regime LWFAs separately in Sec. II.C. Sec. III reviews a new generation of single-shot electron bunch diagnostics developed primarily to meet the challenge of measuring the unusually narrow ($\sigma_r \ll 1 \mu\text{m}$), short ($\sigma_s \sim 1 \mu\text{m}$), “quasi-monoenergetic” electron bunches that bubble-regime LWFAs are uniquely capable of producing, often injected from within the plasma (Fig. 1b). Secs. IV.C, IV.D review diagnostic experiments that observed the unique structure and strongly nonlinear propagation dynamics of bubble-regime wakes in the laboratory, using ultrashort laser probe pulses.

Electron drive bunches of duration $\tau_b \lesssim \omega_p^{-1}$, width $\sigma_r \lesssim \lambda_p$, because they expel plasma electrons from their envelope, create a hierarchy of plasma wake structures that closely resemble those described above for LWFAs. (Chen *et al.*, 1985) developed the linear theory of the standard PWFA. Predictions of steepened wavefronts and period lengthening in 1D nonlinear theory of PWFA (Rosenzweig, 1987), and of wavefront curvature in 2D (Rosenzweig *et al.*, 1991), preceded, but closely parallel, corresponding predictions for LWFA. Sec. IV.B.1 describes diagnostic experiments in which linear and mildly nonlinear PWFAs were first observed in the laboratory. (Rosenzweig *et al.*, 1991) also developed the theory of the *strongly* nonlinear ($n_b > \bar{n}_e$) PWFA regime, usually called the “blowout” regime in the context of PWFA, which produces wake structures similar to those shown in Fig. 1b-d. The uniform ion column that an electron driver creates in this regime guides drive and trailing accelerating bunches over many initial beam “beta-function” lengths, analogous to Rayleigh lengths of a laser driver. However, electron (Blumenfeld *et al.*, 2007; Litos *et al.*, 2014) and positron (Corde *et al.*, 2015) drivers produce different wake structures, a distinction that does not arise with LWFAs. Direct observation of these differences, using probing techniques developed for LWFAs (see Secs. IV.C, IV.D) is an important opportunity for future diagnostics research.

3. Accelerating and focusing fields

The wake’s electron density change $\delta n_e(r, z, t)$ is the source of its enormous internal accelerating $[\hat{e}_z E_z(r, z, t)]$ and focusing $[\hat{e}_r E_r(r, z, t)]$ fields. In 1D, Poisson’s equation $\partial E_z / \partial z = -e \delta n_e(z, t) / \epsilon_0$ yields 1D solutions for the accelerating field $E_z(z, t) = E_0 \cos k_p \zeta$ corresponding to

Eq. (3a). Since the maximum density perturbation is of order $\delta n_e^{(max)} \approx \bar{n}_e$, the maximum accelerating field is

$$E_0 = m_e \omega_p c / e \quad (4a)$$

$$\approx 0.96 \sqrt{\bar{n}_e (\text{cm}^{-3})} \text{ V/cm}. \quad (4b)$$

Eq. (4a) is the so-called cold nonrelativistic wave breaking field (Dawson, 1959). In the form Eq. (4b), it provides a simple estimate of the maximum accelerating field achievable in a plasma of density \bar{n}_e . Drive fields of amplitude $a_0 \gtrsim 1$ are required to reach E_0 . For $a_0 \gtrsim 2$, the wake becomes strongly nonlinear (see Fig. 1b-d). 3D computer simulations show that the maximum accelerating field is then (Lu *et al.*, 2007):

$$E_z^{(max)} \approx E_0 \sqrt{a_0}. \quad (4c)$$

Eqs. (4) can be compared with accelerating fields in conventional RF accelerators, which are currently limited to $\sim 10^6$ V/cm. The plasma accelerator in Fig. 1c ($\bar{n}_e = 4.4 \times 10^{18} \text{ cm}^{-3}$, $a_0 \approx 6$), in contrast, has maximum accelerating field $E_0 \sqrt{a_0} \approx 5 \times 10^9$ V/cm.

In 3D, both accelerating and focusing fields pervade the plasma wake. Fig. 2 shows (a) accelerating and (b) focusing fields inside the wake in Fig. 1c. In the back half of the positively-charged bubble, E_z accelerates electrons forward from their internal injection point near the back wall (see Fig. 1b) toward the bubble's center. Simultaneously E_r focuses these electrons toward the propagation axis, maintaining low emittance. The strong E_r of bubbles in longitudinally shaped plasmas can potentially provide emittance-preserving beam transport between LWFA stages, or between an LWFA and conventional accelerator or FEL undulator (Xu *et al.*, 2016).

Field structures in blowout-regime electron-beam-driven PWFAs resemble those in Fig. 2, and those of conventional RF linacs (Rosenzweig *et al.*, 1998). With PWFAs, unlike LWFAs, acceleration of *positrons*, an essential element for a collider, has been investigated extensively through theory (Lee *et al.*, 2001), simulation and experiments (Blue *et al.*, 2003; Corde *et al.*, 2015; Hogan *et al.*, 2003) because of the availability of a relativistic positron bunch injector at SLAC's Facility for Advanced Accelerator Experimental Tests (FACET) (Hogan *et al.*, 2010) and its predecessors. E_z accelerates positrons forward from an external injection point just in front of the bubble's center, toward the front of the bubble. Unfortunately, E_r defocuses these positrons away from the propagation axis, causing emittance growth. A possible solution for preserving the emittance is to excite the PWFA in a hollow channel surrounded by an annular plasma (Chiou and Katsouleas, 1998; Gessner *et al.*, 2016; Kimura *et al.*, 2011; Schroeder *et al.*, 1999b). Alternatively, (Corde *et al.*, 2015) demonstrated that a positron driver can draw a quasi-static reservoir of plasma electrons to the bubble's axis that compensates

the defocusing fields. Similar issues will arise when LWFAs accelerate positrons. They highlight the importance of developing laboratory diagnostics of internal fields of plasma lepton accelerators.

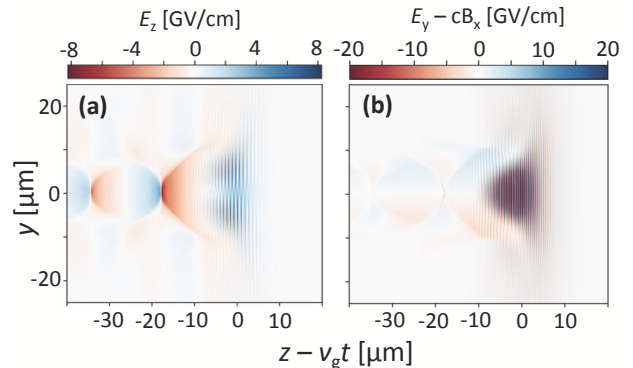


FIG. 2 Color online. Internal fields of laser-driven plasma bubble shown in Fig. 1c and its driving laser pulse. (a) Accelerating field $E_z(y, \zeta)$; (b) Focusing field. Courtesy R. Pausch.

Whereas ultrashort optical pulses mostly probe electron-density structure of plasma wakes, *electron* bunches directly probe their internal *fields*. The above-cited experiments of (Rosenzweig *et al.*, 1988, 1989), detailed in Sec. IV.B.1, used sub- λ_p electron “witness” bunches to probe $E_z(r, z, t)$ and $E_r(r, z, t)$, rather than $\delta n_e(r, z, t)$, of linear and non-linear PWFAs. Sec. IV.C.4 details more recent experiments in which few-fs electron witness bunches — derived, ironically, from a diagnostic bubble-regime LWFA — probed the internal electric fields of a subject bubble-regime LWFA (Zhang *et al.*, 2017). An important exception to the role of optical probes is ultrafast Faraday rotation probes of a plasma wake’s internal *magnetic* fields, created by the current of the accelerating electron bunch and/or by the displacement current of the wake’s dynamic electric fields (Buck *et al.*, 2011; Kaluza *et al.*, 2010). Secs. III.D.1.c and IV.C.3.a detail these diagnostic experiments.

4. Plasma density range

A reasonable criterion for plasma accelerators to provide significant advantage over conventional RF accelerators is that E_0 be at least $100\times$ their breakdown field $\sim 10^6$ V/cm. Eq. (4b) then dictates a lower limit $\bar{n}_e > 10^{16} \text{ cm}^{-3}$ on plasma density. In fact, this is about the lowest density at which *laser*-driven electron acceleration has been reported in the laboratory (Amiranoff *et al.*, 1998; Clayton *et al.*, 1993). Self-injection of plasma electrons into a LWFA becomes inefficient as \bar{n}_e decreases (Froula *et al.*, 2009), and guiding of the drive pulse, either via its own relativistic Kerr effect (Sprangle *et al.*, 1987) or via self- (Sprangle *et al.*, 1992) or pre-formed (Durfee III *et al.*, 1995) plasma waveguides, becomes in-

creasingly difficult at low \bar{n}_e . Thus the above-cited experiments, and others up to $\bar{n}_e \approx 10^{17} \text{ cm}^{-3}$ (Amiranoff *et al.*, 1995; Kitagawa *et al.*, 2004), required either external injection or a capillary waveguide. For these reasons most LWFA experiments have used $\bar{n}_e > 3 \times 10^{17} \text{ cm}^{-3}$.

PWFAs have used density as low as $\bar{n}_e \approx 10^{13} \text{ cm}^{-3}$ (Rosenzweig *et al.*, 1988, 1989), but then E_0 approaches that of conventional accelerators. Recent PWFAs, however, have used \bar{n}_e from $5 \times 10^{16} \text{ cm}^{-3}$ (Litos *et al.*, 2014) to $8 \times 10^{16} \text{ cm}^{-3}$ (Corde *et al.*, 2015).

An *upper* limit on \bar{n}_e for LWFAs comes from the requirement that the plasma be underdense — *i.e.* $\omega_p < \omega$. When it is *not*, a laser pulse penetrates only a skin depth ($c/\omega_p \lesssim 10^{-2} \text{ cm}$) into the plasma, and reflects. When it *is*, the laser pulse can propagate over distances $0.1 \text{ cm} < z < 10 \text{ cm}$ required for its wake to accelerate electrons to $0.1 \text{ GeV} < E_e < 10 \text{ GeV}$ with gradient $E_0 \sim 10^9 \text{ V/cm}$. Stated equivalently, \bar{n}_e must be less than the critical plasma density

$$n_{cr} = \frac{\epsilon_0 m_e \omega^2}{e^2} = \frac{1.1 \times 10^{21}}{[\lambda(\mu\text{m})]^2} \text{ cm}^{-3}. \quad (5)$$

Thus LWFAs driven by near-infrared ($0.8 < \lambda < 1 \mu\text{m}$) solid-state lasers, the dominant technology for reaching $a_0 \geq 1$ since the 1990s, are limited to $\bar{n}_e < 10^{21} \text{ cm}^{-3}$. CO₂ lasers ($\lambda \approx 10 \mu\text{m}$), which drove the earliest LWFAs at $a_0 \ll 1$ in the early 1990s (Clayton *et al.*, 1992), and which, with recent advances in chirped pulse amplification (Polyanskiy *et al.*, 2015), promise to drive future LWFAs at $a_0 \geq 1$ (Pogorelsky and Ben-Zvi, 2014), are limited to driving LWFAs at $\bar{n}_e < 10^{19} \text{ cm}^{-3}$.

For particle-bunch drivers there is no counterpart to the critical frequency (5). Nevertheless, for both LWFAs and PWFAs, the pulse (bunch) duration τ_L (τ_b) available at power (bunch density) needed to drive a high-amplitude wake, together with the resonant criterion $\tau_{L,b} \lesssim \omega_p^{-1}$, set a practical upper limit on \bar{n}_e . Multi-TW laser pulses at $\lambda \approx 0.8 \mu\text{m}$ are currently limited to $\tau_L \gtrsim 10 \text{ fs}$, limiting resonant LWFA to $\bar{n}_e \lesssim 3 \times 10^{19} \text{ cm}^{-3} \approx 0.02 n_{cr}$. Chicane compressors can provide nC bunches with $\tau_b \gtrsim 100 \text{ fs}$, limiting resonant PWFA to $\bar{n}_e \lesssim 3 \times 10^{17} \text{ cm}^{-3}$. Future multi-TW CO₂ laser pulses ($\lambda \approx 10 \mu\text{m}$) are likely to be limited to $\tau_L \gtrsim 500 \text{ fs}$ (Pogorelsky and Ben-Zvi, 2014), limiting resonant LWFA at this λ to $\bar{n}_e \lesssim 10^{16} \text{ cm}^{-3} \approx 0.03 n_{cr}$. So-called “self-modulated” LWFAs and PWFAs, discussed in Sec. II.B, use non-resonant excitation ($\tau_{L,b} \gg \omega_p^{-1}$). Then \bar{n}_e can be higher than the limits stated above.

Diagnostics should be versatile enough to probe wake structure over a wide \bar{n}_e range. While many optical probe methods discussed in Secs. IV.C and IV.D were developed to visualize wakes in $\bar{n}_e \sim 10^{19} \text{ cm}^{-3}$ plasma, diagnostic electron bunches have probed wakes at $\bar{n}_e \sim 10^{17} \text{ cm}^{-3}$ (Sec. IV.C.4) or lower (Sec. IV.B.1) density. Sec. IV.E discusses density scaling of wake diagnostics.

5. De-phasing, pump depletion and transformer ratio

Within the practical LWFA density range $3 \times 10^{17} \text{ cm}^{-3} \lesssim \bar{n}_e \lesssim 3 \times 10^{19} \text{ cm}^{-3}$ for a $\lambda \sim 0.8 \mu\text{m}$ drive pulse, useful acceleration length and achievable single-stage energy gain ΔW_e vary widely. There are two main reasons for this. First, the group velocity $v_g = c(1 - \bar{n}_e/n_{cr})^{1/2}$ of the drive pulse (and thus the phase velocity of the plasma accelerating structure) decreases with increasing \bar{n}_e , dropping by a fraction $(c - v_g)/c \approx 0.015$ below c at the upper limit $\bar{n}_e/n_{cr} \approx 0.03$ of the LWFA density range. Consequently, a relativistic electron propagating at $\sim c$ in the laboratory frame drifts at velocity $c - v_g$ through the wake’s accelerating cavity, which has length of order $\sim \lambda_p/2$. Dephasing between electron and driver limits acceleration time to $\sim \lambda/[2(c - v_g)]$ and acceleration distance in the lab frame to dephasing length $L_d \approx c\lambda_p/[2(c - v_g)]$, or in common laboratory units

$$L_d(\text{cm}) \approx \lambda_p^3/\lambda^2 \approx \frac{3.7}{[\bar{n}_e(10^{18} \text{ cm}^{-3})^3/2[\lambda(\mu\text{m})]^2]}. \quad (6)$$

Thus for $\lambda = 1 \mu\text{m}$ and uniform $\bar{n}_e = 0.03 n_{cr} = 3 \times 10^{19} \text{ cm}^{-3}$, $L_d \approx 0.02 \text{ cm}$, limiting electron energy gain to $\Delta W_e = eE_0 L_d \approx 100 \text{ MeV}$. $\Delta W_e \propto (\bar{n}_e)^{-1}$ at other densities. Introduction of a gradual density up-ramp ($d\bar{n}_e/dz > 0$) along the drive pulse propagation path can, in principle, compensate dephasing, since the accelerating cavity then shrinks in proportion to $\lambda_p \propto (\bar{n}_e)^{-1/2}$ as it propagates, keeping the accelerating electron bunch at its rear (Bulanov *et al.*, 1997b; Katsouleas, 1986; Sprangle *et al.*, 2001). However, laser-driven tapered plasmas in the laboratory (Abuazoum *et al.*, 2012; Kaganovich *et al.*, 1999; Kim *et al.*, 2013b; Rittershofer *et al.*, 2010) have not yet accelerated electrons significantly beyond the limit given by Eq. (6).

In contrast, for PWFA, a drive bunch with Lorentz factor γ_b propagates at velocity $v_b = (1 - \gamma_b^{-2})^{1/2} c$ independent of \bar{n}_e . Thus a highly relativistic driver and its wake propagate vanishingly close to c — *e.g.* $(c - v_b)/c \approx 10^{-11}$ for 20 GeV ($\gamma_b = 4 \times 10^5$) drive bunches used in (Corde *et al.*, 2015; Litos *et al.*, 2014) — effectively eliminating dephasing, an advantage of PWFA over LWFA.

Secondly, depletion of the drive laser pulse energy increases with increasing \bar{n}_e . Various laser-plasma instabilities can contribute to depletion, depending on the intensity and duration of the drive pulse. In the strongly nonlinear ($a_0 > 1$), short pulse ($\omega_p \tau_L < 1$) regime of greatest interest for electron acceleration, erosion of the leading edge of the drive pulse due to diffraction, scattering and photon deceleration by the density spike at the leading edge of the plasma wake dominates pump depletion (Decker *et al.*, 1996). 3D simulations in this regime show that pump depletion limits effective acceleration length in the lab frame to $L_{pd} \approx (n_{cr}/\bar{n}_e) c \tau_L$ (Lu

et al., 2007), or in common laboratory units

$$L_{pd}(cm) \approx \frac{0.03 \tau(\text{fs})}{\bar{n}_e(10^{18}\text{cm}^{-3})[\lambda(\mu\text{m})]^2}. \quad (7)$$

Thus a $\tau_L = 30$ fs, $\lambda = 1\mu\text{m}$ pulse driving a strongly nonlinear wake in plasma of density $\bar{n}_e = 3 \times 10^{19} \text{ cm}^{-3}$ depletes within $L_{pd} \approx 0.03$ cm, similar to the dephasing limit for a uniform plasma. Pump depletion fundamentally limits LWFA. No methods exist to compensate it. Pump depletion and dephasing together limit practical laser-plasma electron accelerators to $\bar{n}_e < 0.03n_{cr}$.

PWFA is subject to beam-plasma instabilities (Deng *et al.*, 2006; Dodd *et al.*, 2002; Huang *et al.*, 2007). Moreover, maximum energy gain per stage is limited to the product of the drive bunch kinetic energy and a transformer ratio (Ruth *et al.*, 1984), which is equivalent to the pump depletion limit of LWFA. Thus, for example, a PWFA driven by an electron bunch of energy E_{drive} is limited to accelerating trailing electrons to $\sim 2E_{drive}$. Special shaping of the drive bunch can extend this limit (Chen *et al.*, 1986).

6. Atomic composition of the plasma

In addition to density, atomic composition of the plasma must be chosen carefully. Nearly all LWFA experiments use targets comprised mostly of H_2 or He. This is because field strengths in the range $0.01 < a_0 < 0.1$, realized in the leading edge of relativistic ($a_0 \gtrsim 1$) drive pulses or in separate pre-ionizing pulses, can field-ionize these low- Z atoms *completely* over a wide footprint. This avoids complicating the wake-forming laser-plasma interaction at $a_0 \sim 1$ with delayed ionization of inner-shell electrons, which occurs at $a_0 \gtrsim 1$ in higher- Z atoms. On the other hand, few-percent admixtures of high- Z gases (*e.g.* N_2 , Ar) into H_2 or He targets can facilitate injection of electrons into a laser-driven wake (McGuffey *et al.*, 2010; Pak *et al.*, 2010), as discussed in Sec. II.C.1.

For PWFA, lithium is a common choice of target gas (Muggli *et al.*, 1999) because the drive bunch, or a synchronized laser pulse, can ionize it over a multi-meter path. Self-ionization can degrade accelerator performance (Deng *et al.*, 2003; O’Connell *et al.*, 2006) so pre-ionization is preferred (Green *et al.*, 2014). As with LWFAs, high- Z admixtures can stimulate injection from within the plasma, known as “Trojan horse” injection (Hidding *et al.*, 2012) in the context of PWFA.

B. Plasma accelerator configurations.

LWFAs (PWFAs) can be excited with one, two, or multiple drive pulses (bunches). (Esarey *et al.*, 2009) reviews the various configurations for LWFAs and (Caldwell *et al.*, 2016; Muggli, 2016; Muggli and Hogan, 2009)

for PWFAs. Here we summarize configurations important for the ensuing discussion of diagnostics.

1. Standard LWFA and PWFA.

Sec. II.A described general properties of simple “standard” LWFAs and PWFAs, driven, respectively, by one laser pulse (see Figs. 1, 2) or one particle bunch of duration $\tau \lesssim \omega_p^{-1}$. Wake excitation in linear ($a_0 \ll 1$, $n_b \ll \bar{n}_e$), weakly nonlinear ($a_0 \sim 1$, $n_b \sim \bar{n}_e$) or strongly nonlinear ($a_0 \gg 1$, $n_b \gg \bar{n}_e$) regimes results in very different lepton bunch properties.

Most standard LWFA experiments in linear and weakly nonlinear regimes produced no self-injected electrons [an exception was (Kitagawa *et al.*, 2004)]. Some experiments in this regime accelerated electrons injected from a linac (Amiranoff *et al.*, 1998; Bernard *et al.*, 1999; Dewa *et al.*, 1998).

Standard strongly nonlinear LWFAs can capture, trap and accelerate electrons from surrounding plasma (see Fig. 1b) through various mechanisms. They can produce bunches of a few pC to few hundred pC charge, few-% energy spread, and kA peak current without external injection. Because of their special importance in motivating beam diagnostic development reviewed in Sec. III, we discuss them separately in Sec. II.C.

Standard PWFAs producing high-quality bunches have so far required externally-injected witness bunches whether in linear (Rosenzweig *et al.*, 1988), weakly nonlinear (Rosenzweig *et al.*, 1989), or blowout (Corde *et al.*, 2015; Litos *et al.*, 2014) regimes, although internal injection is an active field of research (Hidding *et al.*, 2012; Wittig *et al.*, 2015). For example, (Litos *et al.*, 2014) matched the injected electron bunch sufficiently well that 74 pC of injected charge extracted wake energy with up to 30% efficiency while gaining $\Delta E_e > 1$ GeV and maintaining energy spread as low as 0.7%. Emittance, duration, energy spread of the accelerated bunches were determined by the external conventional injector rather than the plasma physics of the bubble, and were measurable by standard beam diagnostics. Standard PWFAs, and linear and mildly nonlinear standard LWFAs have provided the context for many innovations in wake structure diagnostics (see Sec. IV).

2. Self-modulated LWFA and PWFA.

Starting in 1995, LWFA experiments using “long” ($\tau_L \sim 1\text{ps} \gg \omega_p^{-1}$) energetic (~ 1 J) laser pulses to drive $\bar{n}_e \sim 10^{19} \text{ cm}^{-3}$ plasma yielded copious, self-injected, tens-of-MeV electrons with thermal energy distribution (Coverdale *et al.*, 1995; Modena *et al.*, 1995; Nakajima *et al.*, 1995). Strong wake generation and energetic electron production occurred when the peak power P of the

drive pulse exceeded the critical power (Andreev, 1992; Antonsen and Mora, 1992; Sprangle *et al.*, 1992)

$$P_c[GW] = 17(n_{cr}/\bar{n}_e), \quad (8)$$

for relativistic self-focusing (RSF). RSF, favored at high \bar{n}_e , enabled the drive pulse to focus to, and self-guide at (Wagner *et al.*, 1997), higher a_0 inside the plasma than it reached at the plasma entrance. This enabled it to drive self-modulation and forward Raman instabilities efficiently over \sim mm paths (Andreev, 1992; Antonsen and Mora, 1992; Sprangle *et al.*, 1992). These instabilities broke up the incident pulse into a train of sub-pulses of length $c\tau \lesssim \lambda_p$ spaced by λ_p . Simultaneously a wake grew, and Stokes and anti-Stokes sidebands at $\pm n\omega_p$ ($n = 1, 2, 3, \dots$) appeared on the transmitted drive pulse spectrum, sometimes out to multiple orders, signifying a high-amplitude wake ($E_z \rightarrow E_0 \sim$ GV/cm). An extensive literature, summarized by (Esarey *et al.*, 2009), developed around such “self-modulated” (SM) wakes. Sec. IV.A describes time-resolved light-scattering experiments that diagnosed SM-LWFAs under conditions of high (Gordon *et al.*, 1998; Le Blanc *et al.*, 1996) and moderate (Ting *et al.*, 1996) accelerated charge.

SM-LWFA experiments yielded energetic electron beams more simply than standard LWFA experiments, requiring no external injector or waveguide, and generated much higher charge [*e.g.* $Q \approx 0.5$ nC at $E_e > 1$ MeV (Wagner *et al.*, 1997)]. As a result, SM-LWFA dominated LWFA science in the decade following 1995. Breaking of the high-amplitude SM-wave injected plasma electrons indiscriminately throughout the wake, yielding wide energy and angular [*e.g.* $\sim 8^\circ$ (Wagner *et al.*, 1997)] spread. High \bar{n}_e restricted L_d to ~ 0.1 cm (see Eq. (6)), and thus energy gain to $eE_0L_d \lesssim 100$ MeV. These electron bunch properties posed no special challenges for, and stimulated no significant advances in, beam diagnostics.

The self-modulation *beam-plasma* instability (Bret *et al.*, 2010) has emerged as a key first step in re-shaping $\tau_b \sim 300$ ps, TeV *proton* bunches from the CERN Super Proton Synchrotron (SPS) or Large Hadron Collider (LHC) into λ_p -spaced multi-bunch trains that can excite high-gradient ($E_0 \gtrsim 10^8$ V/cm, $\bar{n}_e \gtrsim 10^{16}$ cm $^{-3}$) plasma wakes efficiently (Caldwell and Lotov, 2011). Compressing CERN proton bunches to single $\tau_b \sim 300$ fs bunches needed to drive high-gradient wakes resonantly would be prohibitively expensive using conventional techniques. Effective seeding of the instability is needed to create a stable bunch train, and to avoid parasitic instabilities. Initial experiments in the AWAKE project (Caldwell *et al.*, 2016; Geschwendtner *et al.*, 2016) are using an ionization front created by a short laser pulse that co-propagates in the front part of the proton drive bunch. Single-shot wake diagnostics (Sec. IV.C,D) scaled to the appropriate \bar{n}_e (Sec. IV.E) can potentially play a key role in evaluating these seeding strategies.

3. Multi-Pulse LWFA and PWFA.

LWFAs can be driven by two or more laser pulses. In the plasma beat-wave accelerator (PBWA), two long pulses of frequencies ω_1 and ω_2 resonantly excite a plasma wave when $\Delta\omega \equiv \omega_1 - \omega_2 \approx \omega_p$. The first laser-driven plasma electron accelerators (Amiranoff *et al.*, 1995; Clayton *et al.*, 1993; Kitagawa *et al.*, 1992) utilized PBWA, and provided the context for extensive plasma wave diagnostic development based on collective Thomson scattering (Clayton *et al.*, 1985). Sec. IV.A discusses later applications of these techniques to SM-LWFA. See (Clayton, 2009; Esarey *et al.*, 2009) for reviews of PBWA.

Related to PBWA and SM-LWFA is excitation of LWFA with optimized trains of short ($\tau < \omega_p^{-1}$) pulses, *i.e.* multiple-pulse (MP) LWFA (Hooker *et al.*, 2014; Umstadter *et al.*, 1994, 1995). (Esarey *et al.*, 2009) and (Hooker *et al.*, 2014) cite earlier theoretical work. In a simple MP-LWFA, m identical pulses of energy \mathcal{E} , field strength $a_0 \ll 1$ separated by λ_p each adds coherently to the wake, ultimately generating a wake equivalent to that generated by a single identically-shaped pulse of energy $m\mathcal{E}$. Nevertheless, the weaker pulses can potentially be generated by lasers capable of higher wall-plug efficiency and repetition rate than lasers that generate single joule-class pulses. The flexibility to tailor inter-pulse spacing, or shape and amplitude of individual pulses, offers additional potential advantages. In the nonlinear regime ($a_0 \gtrsim 1$), an optimized pulse train can excite a stronger wake than the equivalent-energy single pulse (Umstadter *et al.*, 1994, 1995). In addition, an appropriately timed trailing pulse can remove the wake behind the primary accelerating bucket, recover its energy by blue-shifting, and avoid unnecessary plasma heating (Hooker *et al.*, 2014). Recently (Cowley *et al.*, 2017) reported the first MP-LWFA experiments, using diagnostic techniques described in Sec. IV.C.

PWFAs can benefit similarly from excitation via optimized particle-bunch trains. Sec. IV.B.1 reviews diagnostic experiments on the multi-bunch PWFA (Kallos *et al.*, 2008; Muggli *et al.*, 2008a).

C. Electron beams from strongly nonlinear LWFAs

Three reports of “bubble” regime LWFAs that produced relativistic electron bunches with $\Delta E_e/E_e$ ranging from ~ 0.02 (Geddes *et al.*, 2004; Mangles *et al.*, 2004) to 0.24 (Faure *et al.*, 2004) transformed laser-plasma accelerator science in 2004. Reported charge within the “quasi-monoenergetic” peak ranged from 22 pC (Mangles *et al.*, 2004) to > 100 pC (Faure *et al.*, 2004; Geddes *et al.*, 2004). The transformation was so complete that today most LWFAs operate in the “bubble” regime.

The peaked electron energy distributions highlighted in these reports originated from a unique process that, al-

TABLE I Properties of electron bunches from strongly nonlinear LWFAs, determined by diagnostic methods reviewed in Sec. III. Best reported values (boldface type) are *not* achieved simultaneously. Q = charge within $\Delta E_e/E_e$; E_e = electron energy gain; $\Delta E_e/E_e$ = fractional energy spread; ϵ_n = normalized transverse emittance; τ_b = bunch duration.

Bunch property	Typical range	See Sections...
Q (nC)	0.01 – 0.5^a	II.C.1, III.B.1
E_e (GeV)	0.01 – 4^b	III.B.2
$\Delta E_e/E_e$ (FWHM)	0.01^c – 1	II.C.1, III.B.2-4
ϵ_n (mm mrad)	~0.1^d – 1	II.C.2, III.C
τ_b (fs)	~1.6^e – 10	II.C.3, III.D

^a $E_e \approx 0.3$ GeV, $\Delta E_e/E_e \approx 0.15$ (Couperus *et al.*, 2017)

^b $Q \approx 0.006$ nC, $\Delta E_e/E_e \approx 0.06$ (Leemans *et al.*, 2014)

^c $Q \approx 0.01$ nC, $E_e \approx 0.2$ GeV (Rechatin *et al.*, 2009); $Q \sim 0.02$ nC, $E_e \approx 0.06$ GeV (Gallacher *et al.*, 2009); $0.01 < Q < 0.08$ nC, $0.2 < E_e < 0.6$ GeV (Wang *et al.*, 2016)

^d $Q \sim 0.001$ nC, $E_e \approx 0.4$ GeV (Plateau *et al.*, 2012)

^e $Q \approx 0.015$ nC, $E_e \approx 0.085$ GeV (Lundh *et al.*, 2011)

though highly nonlinear, injected electrons precisely into a small fraction of the bubble’s $\sim \lambda_p^3$ volume. Simulations (Pukhov and Meyer-ter-Vehn, 2002) showed that, as a bubble formed, an electron density spike built up at its rear (see Fig. 1b) and eventually broke, injecting electrons. Since these electrons were localized in space and time (see black dot at back of bubble in Fig. 1b), they experienced nearly the same field, and thus accelerated with small energy spread.

This injection mechanism had two corollaries beyond the question of energy spread. First, the small injection volume could lead to unusually small normalized transverse emittance ϵ_n , as discussed in Sec. II.C.2. Second, the small injection volume could also lead to unusually short bunch duration τ_b , as discussed in Sec. II.C.3. In 2004, researchers could only speculate about the values of ϵ_n and τ_b . Simulations provided only rough guidance, and methods for measuring them did not exist. Sec. III reviews new diagnostic methods that emerged in the past decade specifically to address the challenge that bubble-regime LWFAs first posed in 2004. Table II summarizes reported bunch properties that these methods determined, with forward references to appropriate subsections of Sec. III. The properties of beams accelerated in PWFAs, on the other hand, are, to a large extent, governed by the conventional accelerator that injected them. Thus PWFA beam diagnostics are closer to those used widely at conventional accelerators. We refer the reader to (Green *et al.*, 2017; Li and Hogan, 2011) for an overview of beam diagnostics at the FACET project.

1. Charge and energy spread

The 2004 results were based on measurements with standard magnet spectrometers and charged particle sen-

sors, instruments that had not previously been used to measure few-MeV-wide spectral peaks from LWFAs, nor to evaluate charge within these peaks. Unlike conventional accelerators, LWFAs produced copious poorly-characterized low-energy electrons and background radiation. Moreover, their beams fluctuated in pointing from shot to shot, and diverged in a few-mrad angle cone. Questions about the accuracy of absolute values of Q and $\Delta E_e/E_e$ reported under these conditions in early bubble-regime LWFA papers emerged [*e.g.* (Glinec *et al.*, 2006)]. Sec. III.B details how researchers met the diagnostic challenges that bubble-regime LWFAs posed for absolute charge and energy measurements.

Efforts to *improve* upon the tens-to-hundreds pC charge, “quasi”-monoenergetic energy spread, and shot-to-shot fluctuations of self-injected LWFA beams by micro-controlling the injection process are a highlight of post-2004 research. FELs and colliders demand bunches with $< 1\%$ energy spread, nC charge, and high reproducibility. (Faure, 2017) has reviewed several “controlled injection” schemes applied to bubble-regime LWFAs. The right-hand column of Fig. 3 depicts them schematically, while the main panels summarize results of 21 studies. For consistency, $\Delta E_e^{(\text{FWHM})}$ values in Fig. 3 represent raw electron spectrometer output, without corrections for instrument resolution. Thus, in some cases, a plotted value exceeds the value reported in the corresponding publication, after such corrections were applied. With this uniform criterion we can compare the relative effectiveness of different injection methods for producing high Q and/or small $\Delta E_e/E_e$ objectively.

Experiments that relied on self-injection (gold data points in Fig. 3a,b) yielded the most widely-varying (a) $\Delta E_e/E_e$ and (b) Q results. The former include some of the widest (50 – 100 MeV) and one of the narrowest (3 MeV) reported $\Delta E_e^{(\text{FWHM})}$ values. After deconvolving instrument broadening, (Gallacher *et al.*, 2009) reported $\Delta E_e^{(\text{FWHM})}/E_e \approx 0.01$ for the last result (plotted at $E_e = 65$ MeV in Fig. 3a), a milestone in LWFA research. The wide variation of $\Delta E_e^{(\text{FWHM})}$ shows the sensitivity of self-injection to different experimental conditions, and the difficulty of controlling it. Reported Q varied from a few pC to ~ 50 pC (Fig. 3b).

(Faure *et al.*, 2006), based on theory by (Esarey *et al.*, 1997), controlled injection with a second pulse (amplitude $0.1a_0 \lesssim a_1 \lesssim 0.4a_0$) that collided with the LWFA drive pulse (a_0) of similar wavelength λ (see Fig. 3, right column, second schematic). The resulting interference introduced a ponderomotive force wave of period λ , amplitude proportional to $2a_0a_1/\lambda_0$, and near-zero phase velocity. When positioned near the back of the bubble, this wave could induce injection with spatial precision $\sim \lambda$ into a LWFA operating below its self-injection threshold (Faure *et al.*, 2006), or control phase space volume for trapping within a self-injected bubble, thus controlling

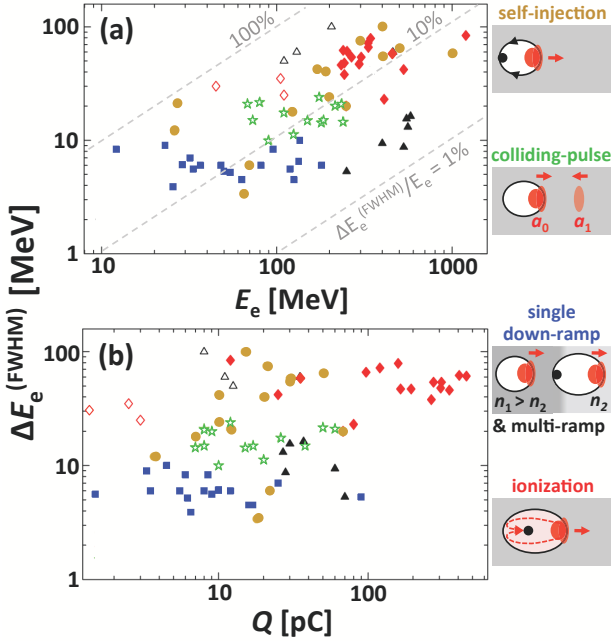


FIG. 3 Color online. Measured energy spread $\Delta E_e^{(\text{FWHM})}$ of quasi-monoenergetic peak of electrons from bubble-regime LWFA versus (a) peak energy E_e , and (b) charge Q within the peak, from 21 experiments using electron injection methods depicted schematically in right-hand column: self-injection, filled gold circles (Faure *et al.*, 2004; Gallacher *et al.*, 2009; Kim *et al.*, 2013a; Kneip *et al.*, 2009; Leemans *et al.*, 2006; Li *et al.*, 2017; Mangles *et al.*, 2004; Osterhoff *et al.*, 2008; Wang *et al.*, 2013); colliding pulses, green stars (Faure *et al.*, 2006; Rechatin *et al.*, 2009); single shock-induced density ramp, filled blue squares (Buck *et al.*, 2013; Khrennikov *et al.*, 2015a; Schmid *et al.*, 2010; Swanson *et al.*, 2017); tailored multi-ramp, open black (Gonsalves *et al.*, 2011) and filled black (Wang *et al.*, 2016) triangles; ionization-induced, open red (McGuffey *et al.*, 2010; Pak *et al.*, 2010) and filled red (Couperus *et al.*, 2017; Mirzaie *et al.*, 2015; Pollock *et al.*, 2011) diamonds. Plotted $\Delta E_e^{(\text{FWHM})}$ are not corrected for instrumental broadening.

accelerated charge and its energy spread (Rechatin *et al.*, 2009). Adjusting delay between the pulses controlled the collision point location within the jet, and thus acceleration length. Adjustment of a_1 fine-tuned Q and ΔE_e . Experiments using colliding-pulse injection (green data points, Fig. 3) have consistently yielded $\Delta E_e^{(\text{FWHM})}$ between 10 and 25 MeV, showing improved control compared to self-injection. E_e and Q tuning ranges 60-200 MeV and 6-60 pC, respectively, have been achieved. After deconvolving instrument response, (Rechatin *et al.*, 2009) reported $\Delta E_e^{(\text{FWHM})}/E_e \approx 0.01$, also a milestone. Use of two or more injection pulses may yield further improvements (Esarey *et al.*, 1997).

Another group of experiments (blue and black data points, Fig. 3) controlled injection by sculpting the plasma’s longitudinal density profile $\bar{n}_e(z)$. A density

downramp $\partial \bar{n}_e / \partial z < 0$ along a wake’s propagation direction decreases its phase velocity, encouraging injection (Bulanov *et al.*, 1998; Suk *et al.*, 2001). Downramp injection can occur below the self-injection threshold, enabling better control. (Geddes *et al.*, 2008) demonstrated longitudinal momentum spread as small as 0.17 MeV/c for < 1 MeV electrons emerging from a LWFA generated in a downramp of length $> \lambda_p$. Later (Buck *et al.*, 2013; Schmid *et al.*, 2010) introduced a more abrupt downramp of scale length $< \lambda_p$ (Fig. 3, right column, third schematic) by inserting a knife edge into a supersonic gas flow to create a local shock front. This simple approach has proven robust, enabling consistent output of bunches with $\Delta E_e^{(\text{FWHM})} < 10$ MeV as E_e tuned up to ~ 200 MeV (blue points, Fig. 3a). Most results yielded $Q < 30$ pC (blue points, Fig. 3b), although $Q \approx 90$ pC was achieved with more laser energy.

The success and simplicity of downramps prompted researchers to tailor more sophisticated density distributions to improve flexibility (Guillaume *et al.*, 2015). Using one laser pulse, (Gonsalves *et al.*, 2011; Wang *et al.*, 2016) drove tandem, differently-sloped ramps, each performing a separate function: injection, rephasing, beam focusing. Recent work with this approach yielded more energetic (250 – 500 MeV) and higher Q (30 – 70 pC) bunches than single down-ramps, while maintaining $\Delta E_e^{(\text{FWHM})} \sim 10$ MeV (solid black triangles, Fig. 3). After deconvolving instrument resolution, (Wang *et al.*, 2016) reported $\Delta E_e^{(\text{FWHM})}/E_e < 0.01$, the smallest yet reported for LWFA.

For controlled injection of $Q > 100$ pC bunches, researchers have driven bubble-regime LWFA in H_2 or He carrier gas doped with higher- Z gas (*e.g.* N_2). The leading edge of the drive pulse fully ionizes the carrier [*e.g.* He I, II form at $a_0 \approx 0.03, 0.1$, respectively (Augst *et al.*, 1991)] and outer shell electrons of the dopant. From these electrons, the main part of the drive pulse ($a_0 > 1$) forms the bubble, and ionizes K -shell electrons of the dopant *inside* the bubble. The bubble’s internal fields can then trap and accelerate these electrons (see Fig. 3, right column, fourth schematic), even below the self-injection threshold. Early “ionization-injected” LWFA yielded 45-250 MeV electrons (open red diamonds, Fig. 3a) with < 10 pC charge (open red diamonds, Fig. 3b), and energy spread from ~ 30 MeV (McGuffey *et al.*, 2010; Pak *et al.*, 2010) to ~ 300 MeV (Clayton *et al.*, 2010). Subsequently, (Liu *et al.*, 2011; Pollock *et al.*, 2011) reduced energy spread by confining dopant gas to a short initial stage, followed by a longer acceleration stage without dopant. (Mirzaie *et al.*, 2015) achieved a similar goal by focusing 100 TW pulses into uniformly-doped gas in an unmatched geometry. Subsequent co-evolution of laser pulse and bubble self-truncated ionization injection, yielding accelerated bunches with $Q \sim 10$ (50) pC, $E_e > 1$ GeV (< 1 GeV), $\Delta E_e^{(\text{FWHM})} < 100$ MeV.

(Couperus *et al.*, 2017) accelerated $Q \sim 0.5$ nC bunches to $E_e \sim 300$ MeV, $\Delta E_e \sim 45$ MeV, exploiting beam-loading to improve beam quality. Solid red diamonds in Fig. 3 show a selection of these later results.

Two broad conclusions emerge from this brief overview of controlled LWFA injection. First, controlled injection has improved consistency of LWFA output, compared to self-injection. Each method generates bunches within a narrower ΔE_e range than self-injection, although methods differ from each other: *e.g.* colliding-pulse and down-ramp methods yield $\Delta E_e < 10$ MeV over wide E_e and Q ranges, while ionization injection yields $\Delta E_e \sim 50$ MeV with higher charge. Secondly, a few milestone results (Gallacher *et al.*, 2009; Rechatin *et al.*, 2009; Wang *et al.*, 2016) notwithstanding, the goal of producing $\Delta E_e/E_e \ll 0.01$ has proven difficult to realize consistently with single stage LWFAs. Although research continues, and although $\Delta E_e/E_e$ may improve in multi-stage LWFAs, emphasis in FEL design (Huang *et al.*, 2012) and diagnostics (Lin *et al.*, 2012) has shifted from *overall* ΔE_e to *correlated* energy spread of longitudinal slices within a bunch profile, which can be smaller than ΔE_e . Secs. III.B.4 and III.D.1.a discuss how the plasma accelerator community has met the diagnostic challenge of measuring slice energy spread of LWFA electron bunches.

2. Transverse emittance.

Electron bunches that emerge from bubble-regime plasma accelerators have potentially outstanding properties for compact light sources and colliders: ultra-small transverse ($\sigma_r \sim 0.3 \mu\text{m}$) and longitudinal ($\sigma_s \sim 1 \mu\text{m}$) size, which when combined with moderate charge ($Q \sim 0.3$ nC), could yield “condensed matter” charge density ($Q/e\sigma_r^2\sigma_s \sim 2 \times 10^{22} \text{ cm}^{-3}$) and 100 kA peak currents. Here $r(s)$ denote transverse (longitudinal) beam coordinates. To be useful, however, LWFA bunches must be transported to the usage point without losing these outstanding properties. Conventional particle transport lines consisting of magnetic solenoids and quadrupoles were designed for beams with not only larger source size ($\sigma_r \sim 1$ mm, dictated by cathode size), but smaller divergence $\sigma'_r \ll 1$ mrad and energy spread $\Delta E_e/E_e = \Delta\gamma_e/\gamma_e < 10^{-3}$ than LWFA bunches, for which $\sigma'_r \gtrsim 1$ mrad and $\Delta\gamma_e/\gamma_e \gtrsim 10^{-2}$ are typical. The different σ'_r and $\Delta\gamma_e/\gamma_e$ originate from contrasting conditions under which LWFA and conventional bunches are “born” (Antici *et al.*, 2012). LWFA bunches form within focusing and accelerating fields of magnitude E_0 (see Eq.(4a)), which impart initial momenta $p_r(0) \sim p_s(0) \sim eE_0/\omega_p \sim m_e c \sim \text{MeV}/c$ and uncorrelated energy spread $\sim \text{MeV}$ to the bunch electrons. Subsequent acceleration of a bunch to $\sim \text{GeV}$ energy over distance L yields $\sigma'_r \sim p_r(0)/p_s(L) \sim 10^{-3}$ rad at the accelerator exit, as observed. Correlated energy spread also

grows, due to the non-uniform accelerating field. In contrast, electrons emerge from conventional cathodes with momenta $p_r \sim p_s \sim eV/c$. In ideal uniform extraction fields, subsequent acceleration of a collimated bunch to MeV/c would yield $\sigma'_r \sim 10^{-3}$ mrad and $\Delta\gamma_e/\gamma_e \sim 10^{-6}$. Because of their larger σ'_r , $\Delta\gamma_e/\gamma_e$ and initial energy, LWFA beams are poorly matched to conventional particle transport systems (Antici *et al.*, 2012). Innovative capture and transport methods are therefore needed to realize LWFA applications (Dornmair *et al.*, 2015; Steinke *et al.*, 2016; van Tilborg *et al.*, 2015; Xu *et al.*, 2016).

Here we focus on diagnostic challenges of *measuring* LWFA beam transport properties. Large σ'_r and $\Delta\gamma_e/\gamma_e$ render many conventional diagnostics unsuitable for LWFA beams (Cianchi *et al.*, 2013). Secs. III.C.2 and III.C.3 describe new diagnostics researchers have developed in response to this challenge. Emittance ε is the area of transverse phase space (units: mm mrad) occupied by a beam of particles, each with spatial and angular coordinates x and $x' = dx/ds = p_x/p_s = p_x/(\beta\gamma_e m_e c)$. Some authors express ε as the area of an ellipse in phase space, using units π mm mrad. Here we omit the factor π . Under conditions of the Liouville Theorem, ε is motion invariant, like the wavelength of a laser beam in an optical transport system. Geometric rms emittance of a relativistic ($\beta \approx 1$) beam is defined by

$$\varepsilon^2 = \langle x^2 \rangle \langle x'^2 \rangle - \langle xx' \rangle^2 \quad (9)$$

where $\langle \rangle$ is an average over the particle ensemble. For a beam of given ε , local spread in particle position and trajectory slope is described by Twiss or Courant-Snyder beam envelope parameters (Lee, 2004)

$$\beta_T = \frac{\langle x^2 \rangle}{\varepsilon}, \quad \gamma_T = \frac{\langle x'^2 \rangle}{\varepsilon}, \quad \alpha_T = -\frac{\langle xx' \rangle}{\varepsilon}. \quad (10)$$

Beta-function $\beta_T(s)$ describes the rate at which local beam size $\sigma_x(s) = \sqrt{\langle x^2(s) \rangle} = \sqrt{\beta_T(s)\varepsilon}$ changes along s in free space, analogous to the Rayleigh range of a laser beam. γ_T describes local divergence. α_T is the correlation between x and x' ; $\alpha_T = 0$ at a beam waist.

Analysis of a collimated ($\alpha_T = 0$) electron bunch — which *e.g.* “matched” propagation in a fully blown out plasma channel can produce — illustrates use of Eqs. (10), and estimates $\sigma_x(L)$ of a bunch emerging from a strongly nonlinear LWFA. Transverse forces within the bubble confine the matched (subscript m) bunch to constant radius $\sigma_{x,m} = \sqrt{\beta_{T,m}\varepsilon}$, leading to beta-function (Krall and Joyce, 1995; Reiser, 2008)

$$\beta_{T,m} = \frac{1}{k_\beta} = \frac{\sqrt{2\gamma_e}}{k_p} \quad (11a)$$

$$\approx 7 \times 10^6 \sqrt{\gamma_e/n_e} [\text{cm}^{-3}] \text{ mm}, \quad (11b)$$

where k_β (k_p) denote betatron (plasma) wavenumbers. From (11b), $\beta_{T,m} < 1$ mm for LWFAs, in contrast to

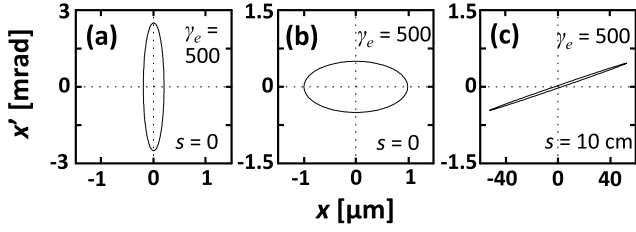


FIG. 4 Emittance evolution of LWFA beams for conditions similar to those of (Weingartner *et al.*, 2012). Calculated phase space ellipses (a) at LWFA exit ($s = 0$) after matched propagation in LWFA, acceleration to $\gamma_e = 500$, and passage through steep plasma boundary that preserved phase-space ellipse; (b) same, except after adiabatic emittance-preserving ($\varepsilon_n = 0.25 \text{ mm mrad}$) transition at plasma edge; (c) bunch from (b) after 10 cm of ideal propagation ($\sigma_{\gamma_e} = 0$).

$> 1\text{m}$ for confined conventional beams. Fig. 4a shows matched $\sigma_{x,m} \sim 0.2\mu\text{m}$ and $\sigma'_{x,m} = \sigma_{x,m}/\beta_{T,m}$ for $\gamma_e = 500$ under conditions similar to those in which (Weingartner *et al.*, 2012) measured $\varepsilon = 0.5 \cdot 10^{-9} \text{ mrad}$.

Normalized emittance ε_n facilitates description of beams with relative energy spread $\sigma_{\gamma_e}^2 = (\langle \gamma_e^2 \rangle - \langle \gamma_e \rangle^2) / \langle \gamma_e \rangle^2$, as well as meaningful comparison of beams with different γ_e . Assuming $\beta = 1$, negligible space charge (Gruener *et al.*, 2007), and negligible correlation between transverse coordinates and energy, ε_n is

$$\varepsilon_n^2 = \langle x^2 \rangle \langle \gamma_e^2 x'^2 \rangle - \langle x \gamma_e x' \rangle^2. \quad (12a)$$

(Antici *et al.*, 2012) pointed out that for LWFA beams with large σ'_r and $\Delta\gamma_e/\gamma_e$, it is more meaningful to express Eq. (12a) in terms of $\sigma_{\gamma_e}^2$. It then becomes

$$\varepsilon_n^2 = \langle \gamma_e \rangle^2 (\sigma_{\gamma_e}^2 \sigma_x^2 \sigma_x'^2 + \varepsilon^2) \quad (12b)$$

$$\approx \langle \gamma_e \rangle^2 (\sigma_{\gamma_e}^2 \sigma_x'^4 s^2 + \varepsilon^2), \quad (12c)$$

where Eq. (12c) holds far from the accelerator (large s), where $\sigma_x(s) \approx \sigma'_x s$. In Eq. (12b), the second term in parentheses is just (9). For beams with small σ_{γ_e} and σ'_x , the first term is negligible, leaving the simple relationship $\varepsilon_n = \langle \gamma_e \rangle \varepsilon$ between ε_n and ε . For LWFA beams, on the other hand, the first term in Eq. (12b) dominates. This contribution is *not* motion-invariant, but grows as the bunch propagates (see Eq. (12c)). Thus in contrast to mono-energetic beams, for which ε_n is conserved, $\varepsilon_n(s)$ grows for LWFA beams (Cianchi *et al.*, 2013). In principle one could refocus the bunch — *i.e.* decrease s again in Eq. (12c) — and reverse ε_n growth. However, conventional optics cannot refocus to the small $\beta_T(s \approx 0)$ typical of bunches exiting a LWFA. If energy spread is strongly *correlated*, “slice” emittance at longitudinal position ζ within a bunch will grow via Eq. (12c) at a slower rate determined by local slice energy spread (Sec. III.B.4). These issues complicate measurement and interpretation of ε_n downstream of a LWFA.

An electron bunch’s out-coupling from a LWFA influences its downstream propagation. Fig. 4a shows the phase-space profile of a beam that exited the LWFA non-adiabatically through a steep density gradient, preserving its shape. In contrast, the profile in Fig. 4b results from exiting the LWFA adiabatically, with focusing strength changing slowly within a betatron wavelength. This conserves ε_n and rotates the ellipse to favor smaller σ'_x (Floettmann, 2014; Sears *et al.*, 2010a; Weingartner *et al.*, 2012). Consequently this beam diverges more slowly. Fig. 4c shows this beam’s ellipse after 10 cm ideal ($\sigma_{\gamma_e} = 0$) free-space propagation, illustrating rapid conversion of angular spread into correlated divergence, necessitating careful matching of downstream acceleration stages (Dornmair *et al.*, 2015; Xu *et al.*, 2016). Non-zero σ_{γ_e} accelerates beam divergence in both cases.

3. Bunch duration.

Bunch duration τ_b determines peak current, a critical parameter for LWFA-based FELs and colliders. No single prediction of the duration of bunches emerging from strongly nonlinear LWFAs exists. Different laser-plasma conditions can yield different τ_b , τ_b can change with propagation, and numerical instabilities can arise when simulating electron dynamics that vary strongly over ultra-small space and time scales (Lehe *et al.*, 2013). Nevertheless, a few simulation studies have addressed the question of bunch duration near the exit of a nonlinear LWFA. Continuous injection into a continuously evolving bubble can lead to τ_b as long as half a plasma period (Kalmykov *et al.*, 2012). At the opposite extreme, (Li *et al.*, 2013a) predict that a broad ($w_0 \sim 20\lambda$), intense ($a_0 \sim 6$) laser pulse passing from a density up-ramp to a density plateau can inject an electron sheet as short as tens of attoseconds into a subsequent wake. In between these extremes, simulations of colliding-pulse (Fubiani *et al.*, 2004; Schroeder *et al.*, 1999a), down-ramp (Fubiani *et al.*, 2006) and ionization-induced (Li *et al.*, 2016) injection have predicted τ_b to be a small fraction of a plasma period, generally $1 \text{ fs} \lesssim \tau_b \lesssim 5 \text{ fs}$ for the specified conditions. Sec. III.D reviews new diagnostic methods that researchers have developed over the past decade to measure τ_b in this range.

III. DIAGNOSTICS OF PLASMA-ACCELERATED ELECTRON BUNCHES

Unconventional methods have become necessary to diagnose the few-fs duration, initially sub- μm radius, kA-peak-current, mrad-divergence, few-percent energy spread LWFA electron bunches described in Sec. II.C, both within the accelerator, and in the downstream world of applications. As an added challenge, when rapid feed-

back is needed, repetition rate is low, or shot-to-shot fluctuations are significant, single-shot diagnosis is essential.

This section reviews new beam diagnostics that have emerged to meet these challenges. Electromagnetic radiation from THz to γ -rays that electron bunches emit both within the accelerator and at downstream instruments is central to many of these diagnostics. Thus, as a prelude, Sec. III.A reviews the theory of radiation from plasma-accelerated electrons. Therein we summarize short-wavelength Thomson, undulator (Sec. III.A.2) and betatron (Sec. III.A.3) radiation briefly for completeness, but refer the reader to (Corde *et al.*, 2013) for a more in-depth summary. On the other hand, we describe the theory of longer-wavelength transition radiation (TR) at greater length (Sec. III.A.4), because TR diffraction and spectroscopy are emerging as primary beam diagnostics for plasma accelerators. Moreover, other reviews of TR in this context are lacking. Subsequent sub-sections review experimental procedure and results for diagnosing bunch charge and energy distribution (Sec. III.B), transverse emittance (Sec. III.C) and bunch length (Sec. III.D).

(Clayton, 2009) reviewed the state of beam diagnostics for plasma-based accelerators approximately a decade ago. Here we emphasize developments since then. (Green *et al.*, 2017; Li and Hogan, 2011) reviewed the comprehensive suite of *e-beam* diagnostics used in PWEA experiments at FACET. Thus we do not review them here. We review *plasma structure* diagnostics at FACET in Sec. IV.D.3.

A. Radiation from plasma-accelerated electrons

Relativistic electrons that oscillate transversely emit forward Doppler-upshifted radiation into a relativistically contracted solid angle cone (width $\sim 1/\gamma_e$) in the laboratory frame (Corde *et al.*, 2013; Esarey *et al.*, 1993; Ride *et al.*, 1995). Insertion devices with alternating magnetic dipoles (undulators or wigglers), counter-propagating electromagnetic radiation (Thomson-backscatter), or focusing plasma wake fields (betatron radiation) provide the fields needed to stimulate such radiation.

1. Synchrotron radiation

The description of radiation from plasma-accelerated electrons begins naturally with synchrotron radiation (SR), which provides a foundation for describing all other classical radiation effects based on electron trajectories. Classical radiation is emitted when charges accelerate. The total power P that one relativistic electron of normalized velocity $\vec{\beta}$ [Lorentz factor $\gamma_e = (1 - \beta^2)^{-1/2}$] ra-

diates is given by the Lorentz-invariant Larmor formula

$$P = \frac{e^2 c}{6\pi\epsilon_0} \left[\left(\frac{d(\gamma_e \vec{\beta})}{d\tau} \right)^2 - \frac{1}{c^2} \left(\frac{d\gamma_e}{d\tau} \right)^2 \right], \quad (13)$$

where τ denotes Lorentz-invariant proper time. For a charge moving with constant β in a circle of radius ρ , as in a synchrotron, Eq. (13) becomes

$$P = \frac{e^2 c \gamma_e^2}{6\pi\epsilon_0} \left(\frac{d(\gamma_e \vec{\beta})}{dt} \right)^2 = \frac{e^2 c \gamma_e^4}{6\pi\epsilon_0 \rho^2}. \quad (14)$$

Eq. (14) displays the strong γ_e^4 electron energy scaling of SR explicitly. Any centripetal force yields an effective instantaneous radius ρ . For example $\rho = m_e c \beta \gamma_e / eB$ in a constant magnetic field of magnitude B .

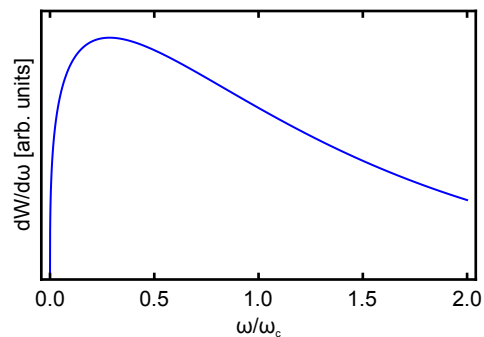


FIG. 5 Color online. Spectral power of synchrotron radiation (SR), given by Eq. (16) of text.

The far-field spectral intensity that one electron with acceleration $\vec{\ddot{\beta}}$ radiates into solid angle $d\Omega$ in direction \vec{n} is (Jackson, 1999)

$$\frac{d^2 I}{d\omega d\Omega} = \frac{e^2}{16\pi^3 \epsilon_0 c} \left\| \int_{-\infty}^{+\infty} f(\vec{n}, \vec{\beta}) e^{i\omega(t - \vec{n} \cdot \vec{r}(t)/c)} dt \right\|^2, \quad (15)$$

where $f(\vec{n}, \vec{\beta}) \equiv \vec{n} \times [(\vec{n} - \vec{\beta}) \times \vec{\ddot{\beta}}] / (1 - \vec{\beta} \cdot \vec{n})^2$. The far-field approximation is valid for interaction volumes with dimensions much smaller than the distance to the observer. Integrating (15) over all angles and one revolution yields spectral power

$$\frac{dW_{\text{SR}}}{d\omega} = \sqrt{3} \frac{e^2}{4\pi\epsilon_0 c} \gamma_e \frac{\omega}{\omega_c} \int_{\omega/\omega_c}^{+\infty} d\xi K_{5/3}(\xi), \quad (16)$$

plotted in Fig. 5. K_ν is a modified Bessel function of the second kind, and

$$\omega_c = 3c\gamma_e^3/2\rho \quad (17)$$

is the *critical frequency*. Intuitively, ω_c is related to the reciprocal of the duration $\Delta t = 2/\omega_c$ of a single ultra-short “lighthouse” burst of radiation, with corresponding broadband spectrum (Fig. 5), that a fixed distant

observer in the orbital plane sees from the circulating electron. Formally, ω_c is the median frequency of SR spectral intensity that this observer sees — *i.e.* half the total energy is emitted above, half below ω_c (Clarke, 2004; Jackson, 1999; Onuki and Elleaume, 2002). The angular energy distribution observed at angle θ from the particle’s orbital plane is

$$\frac{dW_{\text{SR}}}{d\Omega} = \frac{7e^2}{96\pi\epsilon_0 c} \frac{\omega_c \gamma_e^2}{(1 + \gamma_e^2 \theta^2)^{5/2}} \left(1 + \frac{5}{7} \frac{\gamma_e^2 \theta^2}{1 + \gamma_e^2 \theta^2} \right). \quad (18)$$

Each electron emits light in a directional $1/\gamma_e$ angle cone centered on its instantaneous velocity, polarized predominantly in the plane of its orbit (power ratio $P_{\parallel}/P_{\perp} = 7$). Relativistic electrons generally emit x-rays. Since the $0.1 - 1\mu\text{m}$ dimension of plasma-accelerated electron *bunches* exceeds an x-ray wavelength, x-ray SR from such bunches is spatially and temporally incoherent.

2. Undulator and Thomson backscatter radiation

From Eq. (15), $f(\vec{n}, \vec{\beta})$ (and thus $d^2I/d\omega d\Omega$) is maximized when the denominator $(1 - \vec{\beta} \cdot \vec{n})^2$ is minimized — *i.e.* when $\beta \approx 1$ and $\vec{\beta} \parallel \vec{n}$ — and when the numerator $(\vec{n} - \vec{\beta}) \times \vec{\beta}$ is maximized — *i.e.* when $\vec{\beta} \perp \vec{n}$. These two conditions are realized for an observer along the axis of a wiggler or undulator, in which periodic external fields perturb relativistic ($\beta \approx 1$) electrons propagating toward the observer ($\beta \parallel \vec{n}$) transversely ($\vec{\beta} \perp \vec{n}$). (Clarke, 2004; Onuki and Elleaume, 2002) have reviewed the principles behind, and characteristics of, wiggler and undulator radiation. Here we summarize the main points required for subsequent discussion.

When electrons pass through N_u periods of alternating magnetic fields (strength B_0 , period λ_u), they bend into a sinusoidal trajectory with maximum deflection angle $\phi_e = K/\gamma_e$, where

$$K = e\lambda_u B_0 / (2\pi m_e c) \approx 0.93 \lambda_u [\text{cm}] B_0 [\text{T}], \quad (19)$$

is the *normalized undulator parameter*. K is the ratio of the deflection angle ϕ_e to the emission cone angle γ_e^{-1} , and distinguishes wiggler ($K > 1$) from undulator ($K < 1$) modes. Here we focus on the latter, for which emission cones of consecutive oscillations of one electron overlap, and thus superpose coherently.

Locally, a portion of this electron’s trajectory within one undulator period can be approximated by a portion of a circle of radius ρ . Eqs. (14)-(18) and Fig. 5 then describe the properties of this single radiation burst approximately. Repetition over N_u periods sends to a distant observer a train of Doppler-shifted bursts separated by time $\Delta t_u(\lambda_u, \theta, \beta)$ determined by the Lorentz-contracted λ_u , the observer’s angle θ from the electron beam axis, and β . These bursts interfere in the frequency domain,

modulating the broadband SR spectrum (Fig. 5) at spectral period $\omega_u = 2\pi/\Delta t_u$, provided $\omega_u < \omega_c$. When the latter condition is realized (generally for $K \rightarrow 1$), the observer sees radiation at a fundamental frequency $\omega_u(\lambda_u, \theta, \beta)$ and its harmonics $n\omega_u$ ($n = 1, 2, 3, \dots$), each with bandwidth $\Delta\omega_u/\omega_u = 1/N_u$, as in Fig. 6c. This is analogous to the train of high-order harmonics observed from atoms excited near the ionization threshold by a multi-cycle laser pulse (Protopapas *et al.*, 1997). When $\omega_u > \omega_c$ (generally for $K \ll 1$), the observer sees only a single spectral peak at $\omega_u(\lambda_u, \theta, \beta)$, as in Fig. 6a. The detected frequencies are (Clarke, 2004; Corde *et al.*, 2013; Onuki and Elleaume, 2002)

$$\omega_{sc} = \frac{2\gamma_e^2}{1 + K^2/2 + \gamma_e^2 \theta^2} n\omega_u, \quad (20)$$

where the term $K^2/2$ takes into account the reduction of longitudinal electron velocity caused by transverse quiver motion. The frequency up-shift (20) is the combined result of Lorentz contraction of λ_u seen by the electron and Doppler shift of the electron’s oscillation frequency viewed in the lab frame. Emission from an electron bunch of dimensions greater than a radiated wavelength is incoherent, although pinhole spatial filtering, when possible, can recover spatial coherence (Attwood *et al.*, 1999).

In the past decade, researchers have studied undulator radiation from LWFA electrons at visible (Gallacher *et al.*, 2009; Schlenvoigt *et al.*, 2008), UV (Lambert *et al.*, 2012), and XUV (Anania *et al.*, 2014; Fuchs *et al.*, 2009; Shaw *et al.*, 2012) wavelengths. Compact, short-period undulators custom-designed for LWFAs have emerged (Eichner *et al.*, 2007). This radiation underlies single-shot, non-intercepting diagnostics of LWFA bunch energy and energy spread (Sec. III.B.3) and transverse emittance (Sec. III.C.3). Moreover, these results are widely viewed as first steps toward a LWFA-driven XFEL (Gruener *et al.*, 2007; Nakajima, 2008). Achieving gain, however, will require beams with ϵ_n and slice energy spread that challenge current LWFA capabilities (Maier *et al.*, 2012; Seggebrock *et al.*, 2013). This highlights the need for improved diagnostics and control of these quantities.

The oscillating electric field of a linearly-polarized laser field (frequency ω_0 , field strength a_0) that “collides” with electrons can serve as an optical undulator of period $\lambda_u \sim 1\mu\text{m}$. Undulator radiation from one electron — now known as Thomson backscatter — is emitted at frequencies (Bardsley *et al.*, 1989; Brown and Kibble, 1964; Esarey *et al.*, 1993)

$$\omega_{sc} = \frac{2\gamma_e^2(1 - \cos \varphi_{\text{coll}})}{1 + a_0^2/2 + \gamma_e^2 \theta^2} n\omega_0, \quad (21)$$

equivalent to Eq. (20), with a_0 playing the role of K , and ω_0 the role of ω_u . Here, φ_{coll} is the collision angle. For head-on collisions ($\varphi_{\text{coll}} = 180^\circ$), exact back-scatter ($\theta = 0$), and $a_0 \ll 1$, Eq. (21) reduces to $\omega_{sc} \approx 4\gamma_e^2 \omega_0$.

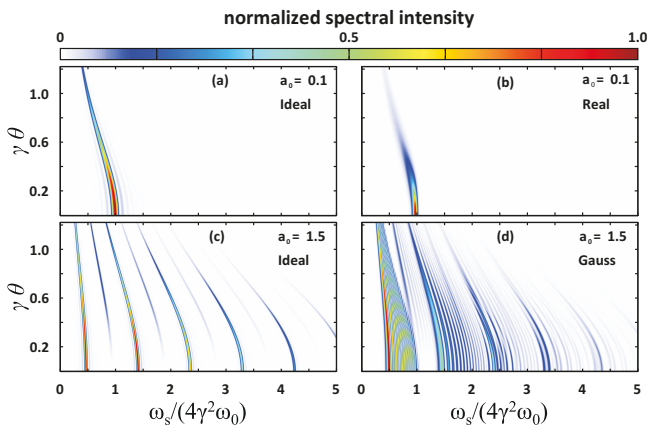


FIG. 6 Color online. Calculated Thomson-scatter spectra for head-on electron-photon collision vs. observation angle $\gamma\theta$ in the bending plane. Top row: plane wave excitation at $a_0 = 0.1$ for (a) mono-energetic and (b) realistic electron energy distribution, showing emission of $n = 1$ peak. Bottom row: excitation of mono-energetic electrons at $a_0 = 1.5$ for (c) plane wave and (d) temporally Gaussian pulse, showing emission of several harmonics. Color scale is normalized to maximum value for each plot. Adapted from (Debus *et al.*, 2009).

Thus Thomson back-scatter of near-infrared ($\hbar\omega_0 \approx 1$ eV) light from $\gamma_e \gtrsim 500$ electrons – a range available from LWFA – provides tunable, directional MeV photons. For $\varphi_{\text{coll}} = 180^\circ$, Eq. (21) differs from (20) by a factor of 2, since two Doppler shifts are involved instead of one. Fig. 6 shows calculated θ -dependent Thomson spectra for $\varphi_{\text{coll}} = 180^\circ$ that illustrate Eq. (21) for various cases. Fig. 6a,c show spectra for idealized plane-wave scatter from mono-energetic electrons at (a) $a_0 \ll 1$ or (c) $a_0 \sim 1$. The plane wave is analogous to a long magnetic undulator with (a) $K \ll 1$ or (c) $K \sim 1$ with many identical units that enforce constant oscillation amplitude, yielding narrow (a) single or (c) multiple harmonics. Fig. 6b shows the slightly broadened spectra for plane-wave Thomson scatter (at $a_0 < 1$) from poly-energetic electrons. Fig. 6d shows drastic red-shift and smearing of the multi-harmonic spectrum for a few-cycle spatially and temporally Gaussian pulse ($a_0 \sim 1$) scattering from monoenergetic electrons (Debus *et al.*, 2009).

The upper limit of total photon yield from linear ($a_0 \ll 1$, thus $n = 1$) Thomson scatter is (Esarey *et al.*, 1993)

$$N_{sc} = 2\pi\alpha_f N_u N_e a_0^2 (\Delta\omega_{sc}/\omega_{sc}) \quad (22)$$

where $\alpha_f = 1/137$ is the fine-structure constant, N_u the number of laser oscillations, and N_e the number of electrons in the overlap region. Actual yield can be much smaller for non-ideal beams and laser pulses (Debus *et al.*, 2009; Rykovanov *et al.*, 2014). (Hartemann *et al.*, 2005) calculated that peak brightness of Thomson backscatter of a laser pulse ($N_{h\nu}$ overlapping photons) colliding head-on with an electron bunch of normalized emittance ε_n , duration τ_b scales as $\gamma_e^2 N_e N_{h\nu} / \varepsilon_n^2 \tau_b$. The small ε_n ,

τ_b bunches available from LWFA are thus advantageous for high Thomson backscatter yield. Explicit calculations (Hartemann *et al.*, 2007) for backscatter of a laser pulse (21 fs, $\hbar\omega_0 = 1.5$ eV, $a_0 \approx 0.3$) from a LWFA electron bunch ($N_e \approx 3 \times 10^9$, $\gamma_e = 340$, $\varepsilon_n \approx 4$ mm mrad) predicted $\sim 10^7$ Thomson photons at $\hbar\omega_{sc} = 0.7$ MeV, comparable to the limit (22) for these conditions. (Debus *et al.*, 2010b) have suggested that Thomson yields $N_{sc} \sim 10^{10}$ are achievable with a similar LWFA using a laser pulse with tilted front in a side-scatter geometry, which enables a longer laser-electron interaction length (*i.e.* higher N_u) than a head-on, backscatter geometry.

In the past decade, starting with (Schwoerer *et al.*, 2006), researchers have developed many LWFA-based Thomson x-ray sources, most using the near-head-on, backscatter geometry. (Umstadter, 2015) has reviewed developments through 2015. Developments since 2015 include linear ($a_0 < 1$) backscatter from GeV electrons, resulting in γ -ray photons up to $\hbar\omega_{sc} \approx 85$ MeV (Shaw *et al.*, 2017), and nonlinear ($a_0 > 1$) backscatter from sub-GeV electrons, resulting in high energy tails up to ~ 20 MeV (Yan *et al.*, 2017). Like undulator radiation, Thomson backscatter underlies diagnostics of LWFA bunch energy and energy spread (Sec. III.B.3) and transverse emittance (Sec. III.C.3).

3. Betatron radiation

(Esarey *et al.*, 2002; Kostyukov *et al.*, 2003; Wang *et al.*, 2002) predicted that electrons accelerating in plasma wakes would emit betatron radiation when they undulate transversely in response to the wake’s radial field E_r (see Fig. 7a). The ion cavity can act as either an undulator or wiggler, depending on how far from the axis electrons are injected. Soon thereafter, (Rousse *et al.*, 2004) observed betatron radiation in the laboratory. Since then betatron radiation has become a versatile ultrashort broadband x-ray source (Albert *et al.*, 2013, 2008; Kneip *et al.*, 2010, 2008; Phuoc *et al.*, 2006; Schnell *et al.*, 2013) as well as an important electron diagnostic (see Sec. III.C.2). (Corde *et al.*, 2013) has reviewed betatron (and other x-ray) radiation from plasma accelerators comprehensively, and introduced its basic physics based on original work by (Esarey *et al.*, 2002; Kostyukov *et al.*, 2003; Thomas, 2010). Here we focus on properties of betatron radiation required for diagnostics.

As for wigglers, one can assign betatron oscillations a period $\lambda_\beta = 2\pi/k_\beta \simeq 2\pi\sqrt{2\gamma_e}/k_p = \lambda_p\sqrt{2\gamma_e}$, where γ_e is averaged over an oscillation and k_p (λ_p) is plasma wavenumber (wavelength). Thus, for example, in an accelerator producing $\gamma_e = 200$ electrons in $\bar{n}_e = 10^{19}$ cm $^{-3}$ plasma ($\lambda_p = 10\mu\text{m}$), we get $\lambda_\beta \approx 200\mu\text{m}$. We can also assign oscillation amplitude r_β , which injection dynamics determine. The product of γ_e , k_β and r_β defines dimen-

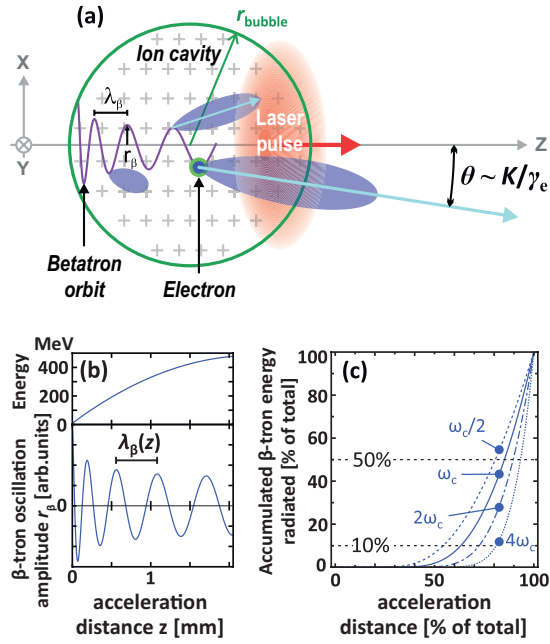


FIG. 7 Color online. Properties of betatron motion and radiation. (a) Schematic of betatron radiation from relativistic electrons oscillating in the electron-depleted LWFA-cavity with uniform ion-background. (b) Electron acceleration (top) and typical electron trajectory (bottom) within an LWFA cavity. As electron accelerates, betatron wavelength λ_β increases, betatron oscillation amplitude r_β decreases. (c) Percentage of accumulated spectral energy radiated for selected frequencies with respect to the acceleration length, assuming linear acceleration and uniformly distributed turning points.

sionless plasma wiggler parameter

$$K = \gamma_e k_\beta r_\beta = 1.33 \times 10^{-10} \sqrt{\gamma_e n_e [\text{cm}^{-3}]} r_\beta [\mu\text{m}]. \quad (23)$$

For the $\gamma_e = 200$, $\lambda_p = 10 \mu\text{m}$ accelerator with $r_\beta = 1 \mu\text{m}$, we get $K = 2\pi$. Oscillations with $K \gg 1$ and constant γ_e radiate a quasi-continuous broadband spectrum (Esarey *et al.*, 2002)

$$\frac{dW_\beta}{d\omega} \simeq 2N_\beta \frac{dW_{\text{SR}}}{d\omega} \quad (24)$$

$$\frac{dW_\beta}{d\Omega} \simeq 2N_\beta \frac{dW_{\text{SR}}}{d\Omega} \quad (25)$$

as for SR [see Eqs. (16), (18)], where N_β is the number of oscillation periods. For betatron radiation, θ in Eq. (18) is the angle between the mean electron direction and \vec{n} . Half the energy is radiated below (or above) the critical frequency, which can now be expressed in terms of K :

$$\omega_c = 3K\gamma_e^2(2\pi c/\lambda_\beta) \quad (26)$$

For the above example, $\hbar\omega_c \approx 4.7$ keV. From Eq. (25) and Fig. 7, betatron radiation is emitted within a cone of half-angle $\theta_{1/2} = K/\gamma_e$ ($= \pi/100$ for above example).

Electron energy loss per unit distance is

$$W_\beta^{(\text{loss})} = \frac{e^2}{48\pi\epsilon_0} \gamma_e^2 k_p^4 r_\beta^2 \simeq 1.5 \times 10^{-45} (\gamma_e n_e [\text{cm}^{-3}] r_\beta [\mu\text{m}])^2 \frac{\text{MeV}}{\text{cm}} \quad (27)$$

$W_\beta^{(\text{loss})} \approx 0.006$ MeV/cm for the above example. Thus one electron emits on average

$$\langle N_{\omega_c} \rangle = \frac{2\pi}{9} \frac{e^2}{\hbar c (4\pi\epsilon_0)} N_\beta K \simeq 5.6 \times 10^{-3} N_\beta K \quad (28)$$

photons of mean energy $\hbar\omega_c$ over N_β oscillation periods. For our example, each electron emits $\langle N_{\omega_c} \rangle / N_\beta \approx 10^{-3}$ photons per oscillation. Thus a 100 pC bunch emits $\sim 10^7$ photons per oscillation.

Betatron radiation *differs* from wiggler radiation in that radiating electrons simultaneously *accelerate* longitudinally. Thus γ_e increases along the acceleration path, which implies $\lambda_\beta \propto \gamma_e^{1/2}$ (see Fig. 7b). Moreover, it can be shown (Corde *et al.*, 2013) that $r_\beta \propto \gamma_e^{-1/4}$ (see again Fig. 7b), implying $K \propto \gamma_e^{1/4}$ [via Eq. (23)], and $\omega_c \propto \gamma_e^{7/4}$ [via Eq. (26)]. Because of these scalings, the conceptually simple spectrum consisting of a fundamental frequency ω_c and discrete harmonics of order $N_c \simeq 3K^2/4$ (Corde *et al.*, 2013) smears into a broad continuum. In addition, betatron power increases nonlinearly with γ_e [see Eqs. (25),(18)]. Thus most radiation, especially frequencies beyond ω_c , is emitted at the highest γ_e , near the end of the accelerator (see Fig. 7c). The source can be further localized longitudinally for electron bunches undergoing collective, high K oscillation, for which radiation is generated mostly at extrema of the electron trajectory (see Fig. 7a). If N_β is small, most betatron radiation can be generated at the final extremum, within the time scale of an electron bunch duration.

Variations in K , γ_e during acceleration also render betatron radiation of even a single electron temporally incoherent. Betatron radiation from electron *bunches* is *both* temporally *and* spatially incoherent. This is because a typical critical energy $\hbar\omega_c \approx 10$ keV corresponds to $\lambda \approx 1.24$ angstrom, much smaller than the spatial extent of a μm -scale LWFA electron bunch. Nevertheless, (Kneip *et al.*, 2010; Shah *et al.*, 2007) observed interference fringes in the shadow of an atomically sharp knife edge inserted into a bright betatron beam at distance l from the source. The knife-edge selected radiation from a small angle range $\theta \ll K/\gamma_e$. The limiting condition $L_{\text{trans}} \Delta k = 1$ then yielded transverse coherence length $L_{\text{trans}} \approx \lambda l / 4\pi\sigma_r$. Such transverse coherence properties provide one diagnostic of σ_r via betatron radiation. The betatron spectrum provides another (see Sec. III.C.2). A simpler measurement of the penumbra of a mask (Schnell *et al.*, 2013) can set an upper limit on σ_r . (Litos and Corde, 2012) proposed that observations of the profile and spectrum of betatron radiation emitted

by a PWFA drive bunch could diagnose its proximity to matched beam propagation.

4. Transition radiation

Transition radiation (TR) is emitted when a relativistic electron passes suddenly from one medium into another with a different refractive index (Frank, 1966; Ginzburg, 1979; Ginzburg and Frank, 1946; Ter-Mikaelian, 1972). Within a material, the transiting electron repels surrounding electrons, exciting time-varying radial currents (in metals, Fig. 8a) or polarization waves (in dielectrics) that radiate. However, in the bulk, as long as the phase velocity of the radiation differs from the velocity of the relativistic electron — *i.e.* there is no Čerenkov radiation — various contributions to the radiation field interfere destructively on volume average. For every plane wave excited at one position there is another with opposite phase. Bulk absorption can also suppress residual radiation when cancellation is incomplete. However, an interface or free surface breaks volume symmetry, enabling net radiation. Moreover, net radiation into vacuum is not absorbed. In contrast to synchrotron, Compton and betatron radiation, here the *medium*, rather than the relativistic electron, radiates.

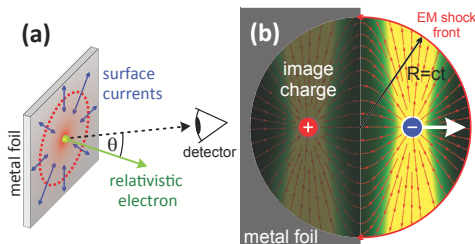


FIG. 8 Color online. Transition radiation (TR). (a) Relativistic electron bunch passing through metal foil induces transient surface currents that radiate radially polarized light. (b) Electric field lines (thin red arrows) emanating from relativistic electron (blue circle enclosing “-” sign) emerging from conductor, and converging upon its image charge (red circle enclosing “+” sign) inside conductor. The electron’s previously shielded field expands at c as it emerges from conductor. The electromagnetic shock front (solid red arc) that terminates this expanding field, and bends field lines back to the surface, is the source of TR.

Several authors have derived rigorous expressions for TR from Maxwell’s macroscopic equations (Pafomov, 1971; Schroeder *et al.*, 2004; Sütterlin *et al.*, 2007; Ter-Mikaelian, 1972). Here one applies Maxwell’s interface conditions $\vec{n}_{12} \times (\vec{E}_2 - \vec{E}_1) = 0$ and $(\vec{D}_2 - \vec{D}_1) \cdot \vec{n}_{12} = \rho_s$ to the Coulomb field of a relativistic electron passing through an interface of given geometry, then identifies the radiating part of the field. Alternatively, the image charge (or “annihilation radiation”) picture (see Fig. 8b) describes TR microscopically and intuitively (Bolotovskii

and Serov, 2009; Carron, 2000; Ter-Mikaelian, 1972). As a relativistic electron propagating inside a conductor reaches the surface at time $t = 0$, its previously shielded Coulomb field expands into vacuum at the speed of light, and combines with the field of its image charge receding into the metal. At time t , this field vanishes beyond an expanding sphere of radius ct centered where the electron emerges from the metal. Since electric field lines terminate only at charges, field lines at this electro-magnetic shock front bend back to the conductor surface. This shock front, which for an ideal conductor with an infinite planar surface is infinitesimally thin, is the source of broadband TR.

a. TR from one electron. The angular (Ω) distribution of TR spectral power $dW_e/d\omega$ from a *single* electron (e) transiting the step-like surface of an ideal, semi-infinite conductor at normal incidence provides a foundation for describing many basic observable characteristics of TR. It is given by the Ginzburg-Frank formula (Schroeder *et al.*, 2004; Ter-Mikaelian, 1972)

$$\frac{d^2W_e}{d\omega d\Omega} = \frac{r_e m_e c}{\pi^2} \frac{\beta^2 \sin^2 \theta}{(1 - \beta^2 \cos^2 \theta)^2}, \quad (29)$$

where $r_e = e^2/(4\pi\epsilon_0 m_e c^2)$ is the classical electron radius and θ the angle between the observation direction and the electron propagation direction (see Fig. 8a). The spectral power distribution (29) vanishes on axis ($\theta = 0$), and for highly relativistic ($\gamma_e \gg 1$) electrons, peaks at $\theta \simeq 1/\gamma_e$, and falls off rapidly at larger θ (see Fig. 9a). The angular width of this cone is thus a signature of electron energy. The power distribution is axially symmetric, and the TR field is linearly polarized within a plane defined by the electron trajectory and the observation direction. Thus the entire TR beam can be described as radially polarized, consistent with it vanishing on-axis. A lens centered on the electron propagation axis focuses the TR cone to a radially polarized, “donut”-shaped intensity profile (see Fig. 9b) with FWHM $\simeq \sqrt{2}\lambda$ (Artru *et al.*, 1998b; Castellano and Verzilov, 1998). Integrating Eq. (29) over Ω for $\gamma_e \gg 1$ yields single-electron TR spectral power

$$\frac{dW_e}{d\omega} = (2r_e m_e c / \pi) \ln(\gamma_e), \quad (30)$$

which depends only weakly on γ_e . A relativistic electron generates backward (reflected) and forward (transmitted) TR cones, respectively, upon entering and exiting a foil (see Fig. 9c).

Eqs. (29) and (30) are frequency-independent, a consequence of the assumption of a semi-infinite, perfectly conducting planar foil. In reality, radiator size and conductivity $\sigma(\omega)$ are finite, and $\sigma(\omega)$ and foil relative permittivity $\epsilon(\omega)$ depend on frequency. These factors lead to frequency-dependent TR power spectrum, including low-

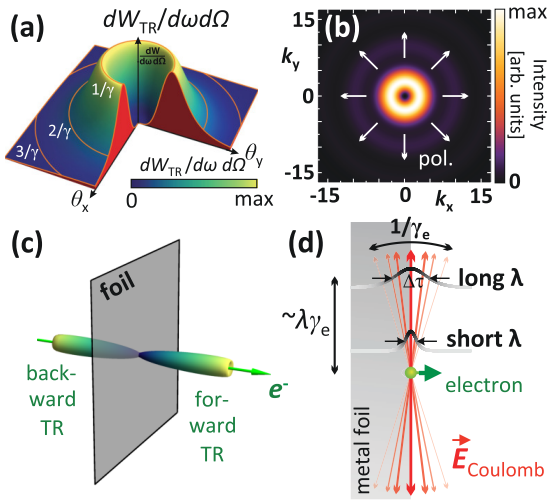


FIG. 9 Color online. Properties of TR for relativistic electron incident normally on foil. Angular distribution of power: (a) far from the source; (b) imaged to focus, for arbitrary wavelength λ , $k_{x,y}$ in units of λ^{-1} , white arrows show radial polarization; (c) backward (left) and forward (right) TR emission. (d) Envelope of Lorentz-contracted Coulomb field (fan of near-vertical red arrows) expands laterally at angle $\sim 1/\gamma$, creating electromagnetic disturbance of longitudinal extent λ at transverse distance $\sim \lambda\gamma$. Thus shorter TR wavelengths are emitted closer to electron.

and high-frequency cutoffs. The effect of finite radiator size stems from the expansion of the electron’s relativistic Coulomb field envelope at angle $\sim 1/\gamma_e$ in the plane perpendicular to its propagation direction (see Fig. 9d). As a result, the passing electron perturbs metal electrons at distance ρ from its path over longitudinally extent $\sim \rho/\gamma_e$, which in turn determines the TR wavelength. Thus TR of wavelength λ originates at characteristic distance $\sim \lambda\gamma_e$ from the electron’s path. A small radiator thus emits less energy at long wavelengths, and diffracts these wavelengths more. Both effects combine to create a low-frequency cutoff of the TR spectrum. Conversely, the critical cut-off frequency $\omega_{\text{crit}} = \gamma_e\omega_p$ of the foil sets a *high*-frequency limit on TR. Above ω_{crit} , both metals and dielectrics become transparent. Consequently the discontinuity in index of refraction that underlies TR disappears, and spectral power $dW_{\text{TR}}/d\omega$ drops as rapidly as ω^{-4} (Dolgoshein, 1993). For Al, $\hbar\omega_p = 32.8\text{eV}$. Generally, ω_{crit} lies in the EUV to soft X-ray range for solid foils. (Schroeder *et al.*, 2004), however, observed much lower ω_{crit} for low-energy electrons passing through an underdense plasma-vacuum interface.

Practical e-beam diagnostics often use foils that are tilted, thin or rough, introducing additional TR characteristics beyond Eqs. (29) and (30). A foil with surface normal oriented *obliquely* to the electron’s path generates a backward TR cone centered on the specular “back-reflected” direction (see Fig. 10a). The forward “transmitted” TR cone is still centered around

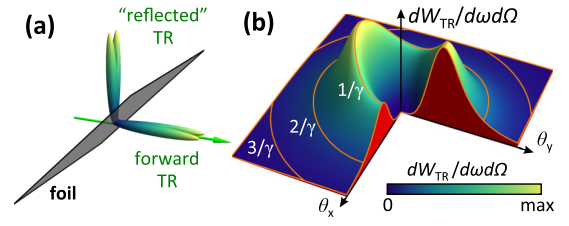


FIG. 10 Color online. Angular distribution of TR power for relativistic electrons incident at 45° on foil: (a) “reflected” and forward TR cones; (b) far-field distribution of one cone, showing break in azimuthal symmetry.

the electron propagation direction. Rotational symmetry of both cones is broken (see Fig. 10b). In addition, a TR radiator must be thicker than the *formation length* $L_f = \beta c/(\omega|1 - \beta\sqrt{\epsilon}\cos\theta|)$ (Carron, 2000; Dolgoshein, 1993; Ter-Mikaelian, 1972) over which TR (observed at angle θ from the electron’s trajectory) accumulates. Physically, this is the distance over which the Coulomb field of the relativistic electron and the emitted TR drift by one wavelength from one another. TR is greatly diminished for media thinner than L_f . In a transparent medium, such as underdense plasma, L_f can be $\sim 100\mu\text{m}$. In metals, $\epsilon \simeq i\sigma/\epsilon_0\omega$ is imaginary, and L_f reduces to $\simeq \delta/\sqrt{2}\cos\theta$, where skin depth $\delta = \sqrt{2/\omega\mu_0\sigma}$ is typically in the nm range. Thus silver-coated Kapton foils can be a good flat TR source.

A related quantity is *vacuum formation length* $L_{f,0}$, which defines a coherence length over which TR fields from two or more spatially separated sources interfere. For example, when forward TR from one foil reflects from a second tilted foil, separated by distance $L_{\text{sep}} < L_{f,0}$, in which the same e-bunch generates back-reflected TR, the two TR *fields* (not intensities) add coherently. Diagnostics based on the Wartski interferometer (Fiorito and Rule, 1994; Fiorito *et al.*, 2006; Wartski *et al.*, 1975) and TR radiators using multiple interfaces (Artru *et al.*, 1975; Dolgoshein, 1993) exploit this effect experimentally. It can also impact the resolution of imaged TR (Artru *et al.*, 1998a,b). In the frequency-domain this can lead to intensity-modulations, whose frequency-width $\Delta\omega = (\omega_2 - \omega_1)$ is defined by L_{sep} . For some natural number l , $L_{\text{sep}} = l \cdot L_{f,0}(\omega_1)$ for the lower frequency and $(l + 1) \cdot L_{f,0}(\omega_2)$ for the higher frequency. As a numerical example, $L_{f,0} = \gamma_e^2 c/\omega$ for $\epsilon = 1$ and $\theta = 0$ and equals $\sim 1\text{ cm}$ for TR of wavelength $\lambda \approx 1\mu\text{m}$ generated by 100 MeV electrons. Generally $L_{f,0}$ greatly exceeds the RMS *height* (σ_{RMS}) of surface roughness features. Nevertheless roughness can impact TR significantly if surface variations exceed λ within a characteristic disc of radius $\gamma_e\lambda$. In this case, various, sometimes conflicting, effects of roughness on TR have been reported: increased flux due to increased surface area; decreased flux due to transverse shielding, which can also lead to depolarization and disappearance of the central intensity

minimum; and a speckled intensity pattern (Arutyunyan *et al.*, 1979; Baghiyan, 2001, 2004; Reiche and Rosenzweig, 2001). Roughness affects forward and backward TR in the same way.

b. TR from electron bunches. TR is a useful diagnostic to the extent that it can reveal internal structure of relativistic electron *bunches* containing N_e electrons. To describe TR from a bunch, one must superpose the TR fields of the individual electrons. At wavelengths λ much longer than longitudinal (σ_z) and transverse (σ_r) bunch dimensions, these fields differ negligibly in phase, and add coherently. The spectral energy

$$\frac{d^2 W_{\text{CTR}}}{d\omega d\Omega} = N_e^2 \cdot \frac{d^2 W_e}{d\omega d\Omega} \quad (31a)$$

of such *coherent* transition radiation (CTR) scales with N_e^2 . On the other side, at wavelengths much smaller than the bunch dimensions, the TR fields of different electrons differ by $\geq 2\pi$ in phase, and thus add incoherently. The spectral energy

$$\frac{d^2 W_{\text{ITR}}}{d\omega d\Omega} = N_e \cdot \frac{d^2 W_e}{d\omega d\Omega} \quad (31b)$$

of such *incoherent* transition radiation (ITR) scales linearly with N_e . Longitudinal and transverse coherence influence TR in different ways. For $\lambda \gg \sigma_z$, forward TR is fully coherent, and thus $\sim N_e \times$ stronger than for $\lambda \ll \sigma_z$. The result is a high-frequency cut-off in the bunch TR spectrum that has no counterpart in single-electron TR theory. Similarly, bunch radius σ_r governs transverse coherence. Transverse coherence is maintained for $\sigma_r \ll \gamma_e \lambda$ for a collimated bunch, or $\sigma_r \ll \lambda / \Delta\psi$ for a bunch with divergence $\Delta\psi \ll 1$. For this reason CTR foils often are placed close to LWFAs, before their beams diverge to larger radii.

Micro-bunching or complex longitudinal bunch profiles complicate the CTR spectrum. A train of two or more bunches separated by delay $\Delta t > \sigma_z / c$ create a corresponding train of TR bursts. The power spectrum of the train is intensity-modulated with period $2\pi / c \Delta t$ in the frequency domain. The spectrum of a complex micro-bunched format with multiple Δt contains multiple modulation periods, and is not easily distinguished from a single bunch with complex internal structure.

The total energy loss W_{tot} of an electron bunch to CTR can be estimated by integrating Eq. (30) over all frequencies and multiplying by N_e^2 . For an electron incident normally on a TR foil, and for W_{tot} much less than total bunch kinetic energy $N_e(\gamma - 1)m_e c^2$, the result is (Schroeder *et al.*, 2004)

$$W_{\text{tot}} \simeq (4r_e m_e c^2) N_e^2 \ln(\gamma_e) / \lambda_{\text{min}} \quad (32a)$$

$$\simeq 3.6 \times 10^{-2} (Q[\text{nC}])^2 \ln(\gamma_e) / \lambda_{\text{min}} [\mu\text{m}], \quad (32b)$$

where Q denotes bunch charge. This energy loss criterion determines limits on maximum Q , radiated bandwidth and time-resolution for diagnostics based on CTR.

Weak ITR at short λ is useful for calibrating degree of coherence at longer λ , and for testing detector dynamic range. Collimated ITR from small sources can reveal spatial bunch characteristics through statistical analysis of intensity noise in its spectrum (Sannibale *et al.*, 2009).

The ideal conductor approximation usually suffices for modeling TR from realistic electron bunches quantitatively (Casalbuoni *et al.*, 2008, 2005a,b; Schroeder *et al.*, 2004; van Tilborg *et al.*, 2004). The most general expression for TR from a bunch of N_e electrons transiting an infinitely wide ideal conductor surface is an integral over individual electron contributions:

$$\frac{d^2 W_{\text{OTR}}}{d\omega d\Omega} = \frac{e^2 N_e}{(4\pi\epsilon_0)\pi^2 c} \left\{ \left[\int d^3 \vec{p} g(\mathcal{E}_{\parallel}^2 + \mathcal{E}_{\perp}^2) \right]_{\text{ITR}} + N_e' \left[\left| \int d^3 \vec{p} g \mathcal{E}_{\parallel} F \right|^2 + \left| \int d^3 \vec{p} g \mathcal{E}_{\perp} F \right|^2 \right]_{\text{CTR}} \right\}, \quad (33a)$$

where $g \equiv g(\vec{p})$ is electron momentum distribution, $N_e' \equiv N_e - 1$, normalized TR field amplitudes are

$$\mathcal{E}_{\parallel} = \left(\frac{u \cos \psi [u \sin \psi \cos \phi - (1 + u^2)^{1/2} \sin \theta]}{\mathcal{N}(\theta, u, \psi, \phi)} \right) \quad (33b)$$

$$\mathcal{E}_{\perp} = \left(\frac{u^2 \cos \psi \sin \psi \sin \phi \cos \theta}{\mathcal{N}(\theta, u, \psi, \phi)} \right) \quad (33c)$$

with denominator

$$\mathcal{N}(\theta, u, \psi, \phi) = [(1 + u^2)^{1/2} - u \sin \psi \cos \phi \sin \theta]^2 - u^2 \cos^2 \psi \cos^2 \theta, \quad (33d)$$

where $u = p/mc = \gamma_e \beta$ is normalized momentum, and the form factor is

$$F = \frac{1}{g(\vec{p})} \int d^2 \vec{r}_{\perp} e^{-i\vec{k}_{\perp} \cdot \vec{r}_{\perp}} \times \int dz e^{-iz(\omega - \vec{k}_{\perp} \cdot \vec{v}_{\perp})/v_z} h(\vec{r}, \vec{p}), \quad (33e)$$

where v_z is electron velocity projected along z . Quantities with subscript “ \parallel ” are oriented along the normal \vec{z} to the foil surface; “ \perp ” quantities lie in this surface (xy -plane). Polar angle ψ and azimuthal angle ϕ denote electron directions with respect to \vec{z} . Without loss of generality, the observation angle θ with respect to \vec{z} lies in the x, z -plane. The 6D frequency distribution $h(\vec{r}, \vec{p})$, with corresponding $g(\vec{p})$, describes electron phase-space. Both h and g are normalized to yield unity when integrated over all of their respective coordinates.

From the general Eqs. (33), one can generate simpler, approximate expressions useful for analyzing many experiments. As one example, when transverse electron momentum is negligible ($\psi \ll 1$), electrons are highly

relativistic ($\gamma_e \gg 1$), and electron position \vec{r} and momentum \vec{p} are uncorrelated, one can write $h(\vec{r}, \vec{p}) = \rho(\vec{r})g(\vec{p})$. The form factor (33e) then simplifies to

$$F(\omega, \theta) = \int d\vec{r} \rho(\vec{r}) e^{-i\vec{k} \cdot \vec{r}}, \quad (34)$$

i.e. the Fourier transform of the normalized 3D bunch charge distribution $\rho(\vec{r})$. This is the quantity of interest in most beam characterization experiments. If additionally the bunch is cylindrically symmetric (ϕ -independent) and incident normally ($\langle \psi \rangle = 0$) on a TR foil, Eqs. (33) simplify to (Schroeder *et al.*, 2004)

$$\frac{d^2 W_{\text{TR}}}{d\omega d\Omega} = \left\langle \frac{d^2 W_e}{d\omega d\Omega} \right\rangle [N_e + N_e^2 |F(\omega, \theta)|^2], \quad (35)$$

where $\langle d^2 W_e / d\omega d\Omega \rangle$ is the weighted average of (29) over the bunch's separately measured electron energy distribution, and equals (29) for a mono-energetic bunch. For fully coherent (incoherent) TR, $F = 1$ ($F = 0$) and (35) reduces to Eq. (31a) (Eq. (31b)). If additionally the transverse and longitudinal bunch charge distributions are uncorrelated, we can write $\rho = \rho_{\perp}(\vec{r}_{\perp})\rho_{\parallel}(z)$ and $F = F_{\perp}(\vec{k}_{\perp})F_{\parallel}(k_z)$ (Schroeder *et al.*, 2004; van Tilborg *et al.*, 2004). For a Gaussian bunch with $h(\vec{r}, \vec{p}) = g(\vec{p})[(2\pi)^{3/2}\sigma_r^2\sigma_z]^{-1} \exp(-r_{\perp}^2/2\sigma_r^2) \exp(-z^2/2\sigma_z^2)$,

$$F_{\perp} = e^{-(1/2)(\omega/c)^2\sigma_r^2 \sin^2 \theta} \quad (36a)$$

$$F_{\parallel} \simeq e^{-(1/2)(\omega\sigma_z/v)^2}. \quad (36b)$$

If F_{\perp} is characterized independently, then CTR spectral intensity measured over a wide bandwidth directly yields $|F_{\parallel}(\omega, \theta)|^2$ via Eq. (35). This is the basis of frequency-domain measurements of ultrashort bunch length (Heigoldt *et al.*, 2015). However, the longitudinal bunch profile ρ_{\parallel} does not follow directly from $|F_{\parallel}(\omega, \theta)|$ via Eq. (34) because phase information is lacking. Additional information and assumptions are needed to extract ρ_{\parallel} (Bajlekov *et al.*, 2013; Bakkali Taheri *et al.*, 2016).

As a second example, Eqs. (33) can be adapted to evaluate TR from a radiator with lateral structure, or finite lateral extent, instead of an infinite foil. This example underlies several important diagnostic applications. These include evaluation of TR in the *far field*, which is defined by observation distances that are large with respect to *finite* source size. A far-field description is essential, in turn, for modeling focused TR (see Fig. 9b) from electron bunches (Artru *et al.*, 1998b; Castellano and Verzilov, 1998), which diagnoses the bunch's lateral density profile, and for modeling time-domain TR, which diagnoses bunch duration (van Tilborg *et al.*, 2004). This example is also relevant for TR from an electron bunch passing through a hole of characteristic size $\sim \gamma_e \lambda$ in a foil, a configuration that avoids electron scattering within the foil, while sensitively diagnosing variations in electron bunch pointing and transverse structure (Fiorito, 2001),

and for modeling TR generated as electrons exit a μm -scale plasma channel or wakefield structure (van Tilborg *et al.*, 2004). When the radiator is transversely confined or structured, *diffraction* of TR comes into play. When diffraction is significant, (C)TR is then often called (*Coherent*) *Diffraction Radiation*, or (C)DR (Bolotovskii and Voskresenski, 1966; Karlovets and Potylitsyn, 2008; Pafomov, 1971; Ter-Mikaelian, 1972). A circular disc radiator of radius ρ_0 is an important special case, for which Eq. (33a) becomes (Schroeder *et al.*, 2004)

$$\frac{d^2 W_{\text{CDR}}}{d\omega d\Omega} = \frac{e^2}{\pi^2 c (4\pi\epsilon_0)} N_e (N_e - 1) \sin^2 \theta \times \left| \int du g_{\parallel}(u) F(\theta, u) \frac{u(1+u^2)^{1/2}}{1+u^2 \sin^2 \theta} D(\rho_0, u, \theta) \right|^2, \quad (37a)$$

where we suppressed the dependence of F and D on $k = \omega/c$ for brevity, and $D(\rho_0, u, \theta)$ is a *diffraction factor*

$$\begin{aligned} D(\rho, u, \theta) &= D(b, u \sin \theta) \\ &= 1 - J_0(bu \sin \theta) \left[bK_1(b) + \frac{b^2}{2} K_0(b) \right] \\ &\quad - \frac{b^2}{2} K_0(b) J_2(bu \sin \theta), \end{aligned} \quad (37b)$$

where $b \equiv k\rho_0/u$, and J_{ν} (K_{ν}) are ordinary (modified) Bessel functions. Diffraction is important for long-wavelength TR, specifically when $\gamma_e \lambda \gtrsim \rho_0$ (or equivalently $b \lesssim 2\pi/\beta$). In the opposite limit, $D(\rho_0, u, \theta)$ is close to unity for all θ within the TR radiation cone. $d^2 W_{\text{CDR}}/d\omega d\Omega$ for an electron bunch passing through a circular *hole* of radius ρ_0 can be derived from (37) using Babinet's principle (Jackson, 1999). Other important analytic CDR results for different D include the donut-shaped intensity distribution

$$I(k, \rho) = \frac{e^2 k^2 c}{8\pi^2 \epsilon_0 v^2} \left| \int_0^1 d\zeta \frac{\zeta^2}{\zeta^2 + (\beta\gamma)^{-2}} J_1(k\rho\zeta) \right|^2 \quad (38)$$

of CTR/CDR imaged from a foil surface to a detector (Fig. 9b), and the CTR field observed at distance R from a foil of dimensions $\ll R$ (van Tilborg *et al.*, 2004)

$$\begin{aligned} \vec{E}(\vec{x}, t) &= -\frac{eN}{\pi R (4\pi\epsilon_0)} \vec{e}_{\perp} \int dk \langle \mathcal{E}(\theta, u) D(\omega, u, \theta, \rho) \\ &\quad \times F(\omega, u, \theta) \rangle_u e^{-ik(ct-R)}, \end{aligned} \quad (39)$$

which is the basis of time-domain measurements of the electron bunch duration. For more complex CTR/CDR sources, the general integral (33) can often be solved numerically (Shkvarunets and Fiorito, 2008).

B. Bunch charge and energy measurement

Single-shot measurement of total charge $Q = N_e e$ of each N_e -electron bunch, and of the distribution

$dQ/dE_e = e dN_e/dE_e$ of charge with electron energy E_e , are among the most important, beam diagnostics required for any accelerator. Event rate at a collider interaction point or brightness of undulator radiation depend directly on Q , while narrow energy spread is essential for exciting meaningful particle collisions or for driving an FEL. Plasma electron acceleration science has adopted some standard charge and energy spectrum diagnostics from conventional accelerators. Yet unique properties of plasma-accelerated bunches have necessitated re-design or re-calibration of these standard instruments. Sec. III.B.1 reviews re-designed integrating current transformers (ICTs) that measure absolute Q non-invasively in a noisy environment, and cross-calibrated scintillating screens and imaging plates that measure spatially-resolved electron charge at the sub-pC/mm² level in one shot. Sec. III.B.2 reviews magnet spectrometer designs that accommodate unique electron energy distributions and pointing fluctuations typical of plasma-accelerated beams. Remaining sections review emerging diagnostics with origins inside the plasma accelerator community: non-intercepting E_e and dN_e/dE_e diagnostics based on undulator radiation spectroscopy (Sec. III.B.3), and diagnostics of correlated “slice” energy spread based on CTR imaging and optical or plasma-wave micro-deflectors (Sec. III.B.4).

Fig. 11 schematically overviews a LWFA beam diagnostic system. Non-invasive ICTs are placed early in the diagnostic chain. Absorbing spatially-resolved charge detectors at the magnetic spectrometer’s focal plane comprise the end of the beam-line. Beam dumping and radiation protection are also needed. Charge detectors are shown in the context of betatron x-ray, TR and undulator radiation diagnostics.

1. Total and spatially-resolved charge measurement

Faraday cups are a classic method to measure total Q , but intercept the beam, and can become unacceptably bulky when they must capture GeV electrons with large stopping distances. Nevertheless, they have been tested for low-MeV LWFA (Hidding *et al.*, 2007). Nuclear activation provided invasive, cumulative total Q measurements in early LWFA experiments (Leemans *et al.*, 2001; Reed *et al.*, 2007). However, integrating current transformers (ICTs), which measure integrated current $\int I(t) dt$ that a bunch induces in a coil upon passing through it, have become the instrument of choice for measuring total Q from plasma-based accelerators, because they are compact, *non-invasive*, single-shot and energy-independent over a wide range (Bergoz *et al.*, 1991; Unser, 1989). The constant of proportionality between Q and $\int I(t) dt$ depends on the ICT’s geometry and electrical characteristics, and must be calibrated. ICTs were used to report Q in many early “bubble”-regime

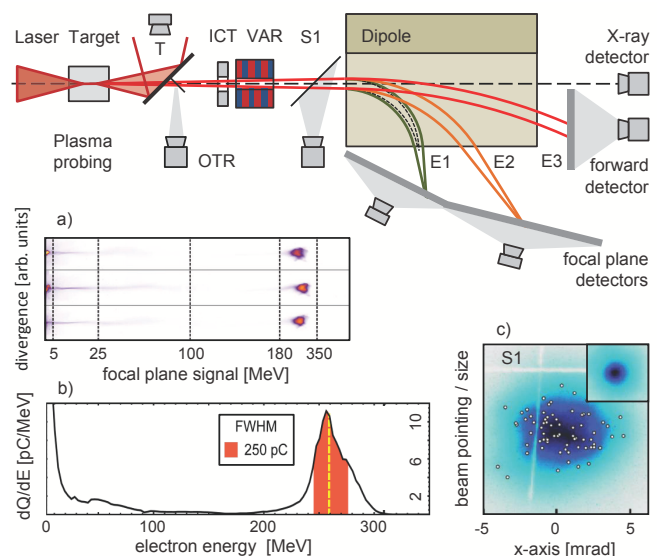


FIG. 11 Color online. Schematic LWFA beam diagnostic setup [top, adapted from (Schramm *et al.*, 2017)] and sample results [bottom, adapted from (a) (Schramm *et al.*, 2017), (b) (Couperus *et al.*, 2017), (c) (Osterhoff *et al.*, 2008)]. After decoupling from co-propagating laser light, wakefield accelerated electron bunches pass through radiating (OTR) or scintillating foils to monitor beam profile and pointing (S1), integrating current transformer (ICT) for charge analysis, optional undulator (VAR) and focusing magnets, and a dispersive dipole magnet for energy analysis, before terminating at spectrometer focal plane detectors. X-rays emitted by the electron bunch are measured behind the magnet, which bends electrons away from x-ray detector. Bottom: electron spectrometer data including (a) raw data for three consecutive pulses from focal plane detectors, and (b) energy spectrum, from Draco 150TW laser at HZDR; (c) beam pointing and profile (inset) data recorded with Lanex screen, from ATLAS at MPQ.

LWFA experiments (see Sec. II.C.1).

The major problem that LWFA posed for ICTs was strong background radiation that unavoidably accompanied LWFA electron bunches, and contaminated ICT signals. The charge of interest from LWFA is usually contained within a primary quasi-monoenergetic peak (see *e.g.* ~ 270 MeV peak in Fig. 11a,b). Often, however, lower-energy electrons (see $\lesssim 5$ MeV feature in Fig. 11a,b), and uncharacterized additional electrons below the spectrometer’s detection edge, outnumber electrons in the main high-energy group. Unless shielded, ICTs are sensitive to all of these electrons, and thus can overestimate Q of the energetic peak. LWFA are also prolific sources of electromagnetic pulses (EMP) *e.g.* from electronic devices that drive high-power lasers, supersonic gas jets or high-voltage capillary discharges, or from the laser-plasma interaction itself. An ICT, or its connecting cables, can pick up prompt EMP from these sources that obscures the electron signal. Interaction of the drive laser or accelerated bunch with gas

cell, alignment apertures, or the ICT itself can create prompt secondary particles or x-rays that also distort the signal. The first calibrations of ICTs against EMP-insensitive detectors [scintillating screens (Glinec *et al.*, 2006); imaging plates (Hidding *et al.*, 2007)] that were independently calibrated at RF accelerators, showed that in noisy LWFA environments, ICTs overestimated Q by factors ranging from $3 - 4\times$ (Hidding *et al.*, 2007) to $> 10\times$ (Glinec *et al.*, 2006). This called into question Q values reported in previous LWFA experiments.

(Nakamura *et al.*, 2011) investigated the reasons for these discrepancies by cross-calibrating an ICT with a scintillating screen (Kodak Lanex) and a nuclear activation measurement (Leemans *et al.*, 2001). ICT and Lanex were first cross-calibrated using electrons of energy up to 1.5 GeV from an RF accelerator. Then all three detectors were cross-calibrated at a LWFA outputting electrons over the same energy range. In the LWFA environment, special care was taken to shield the ICT from EMP, secondary radiation, and < 1 MeV electrons. All three diagnostics agreed within $\pm 8\%$ for $Q \gtrsim 5$ pC bunches, showing that ICTs could measure Q from LWFAs accurately with proper shielding. Further research showed that residual EMP within a narrow frequency bandwidth was the primary limit on ICT sensitivity for $Q < 5$ pC. Frequency filtering of the ICT's signal processing electronics improved sensitivity to the sub-pC level, while improving noise immunity and retaining excellent cross-calibration with other detectors (Nakamura *et al.*, 2016). The filtered ICT has been marketed, an example of commercial product development spurred by plasma accelerator diagnostics research.

Spatially-resolved absolute charge measurement underlies beam profile monitors and magnetic spectrometers. Plasma accelerator researchers have used a variety of detectors to resolve accelerated electrons spatially, including cloud chambers and surface barrier detectors (Clayton *et al.*, 1994), scintillators with photomultipliers (Umstadter *et al.*, 1996), scintillating fibers (Gahn *et al.*, 2000), radiochromic film (Galimberti *et al.*, 2005; Giulietti *et al.*, 2002), imaging plates (IPs) (Mangles *et al.*, 2004; Wang *et al.*, 2013), and scintillating screens with cameras. Scintillating screens and IPs have become the most popular choices because they combine wide area detection, high spatial resolution, insensitivity to EMP, wide dynamic range, re-usability and low cost with sensitivity good enough to detect spatially-dispersed few-pC electron bunches in one shot. Nevertheless, the sensitivity of these detectors to X-ray radiation has to be considered in designing detector assemblies.

The working principle and read-out concept of scintillating screens and image plates (IPs) differ considerably from each other. Scintillating screens are based on prompt cathodoluminescence, *i.e.* rapid conversion of deposited electron (or x-ray) energy into light. Transparent rare-earth oxysulfide host crystals (*e.g.* $\text{Gd}_2\text{O}_2\text{S}$) doped

with luminescing rare-earth ions (*e.g.* Tb^{3+}) were developed as medical x-ray phosphors in the 1970s (Wickersheim *et al.*, 1970). As a powder embedded in urethane binder, they comprise the active layer of Kodak “Lanex” screens, used widely at conventional and plasma-based electron accelerators (Buck *et al.*, 2010). The high density (7.44 g/cm^3) and high average Z of $\text{Gd}_2\text{O}_2\text{S}$ favor strong electron energy deposition [~ 0.1 MeV per incident $1 \text{ MeV} \lesssim E_e \lesssim 1 \text{ GeV}$ electron (Glinec *et al.*, 2006)] via impact excitation. This, combined with high [$\sim 16\%$ (Glinec *et al.*, 2006)] intrinsic conversion efficiency of deposited electron energy to excited states of Tb^{3+} , and thence to light emission (typically green), results in high electron detection sensitivity. For example, (Buck *et al.*, 2010) reported a lower detection limit of ~ 0.5 pC in a spot with 11 mm FWHM (*i.e.* $\sim 10 \text{ fC/mm}^2$) for $E_e = 40$ MeV, $\tau_b = 2$ ps electron bunches incident on KODAK Biomax MS screens. However, this limit depends on the type of scintillator and the optical detection system, and may depend also on E_e and τ_b . The efficiency of imaging system and camera can be calibrated absolutely using reference light sources in the plane of the screen (Buck *et al.*, 2010; Kurz *et al.*, 2018; Nakamura *et al.*, 2011). Light emission increases linearly with charge density over 3 to 4 orders of magnitude, with saturation setting in typically at $10 - 100 \text{ pC/mm}^2$ (Buck *et al.*, 2010). Saturation corrections, however, extend their usable range to many 100 pC/mm^2 . The short (~ 1 ms) luminescence lifetime is well-suited to high-repetition-rate electron sources. Recently, the consortium responsible for the scintillating screen calibration of (Buck *et al.*, 2010) updated the work under improved conditions, and will soon report revised calibrations (Kurz *et al.*, 2018). They also identified signs of permanent aging at accumulated charge densities of only few 10 nC/mm^2 , which may necessitate frequent replacement or scrolling of screens that monitor ~ 100 pC bunches at high repetition rate.

IPs, also developed for medical radiography (Amemiya and Miyahara, 1988; Miyahara *et al.*, 1986), are based on photo-stimulated luminescence (PSL) (Iwabuchi *et al.*, 1994). Incoming electrons, positrons, x-rays or ions deposit energy in fine Eu^{2+} -doped phosphor crystals (*e.g.* BaFBr), embedded in flexible plastic, by converting Eu^{2+} ions to Eu^{3+} . Color centers in the host crystal trap the freed electrons, storing the deposited energy and “exposing” the plate. Sequential visible (typically $\lambda = 0.632 \mu\text{m}$) irradiation of $50 - 200 \mu\text{m}$ “pixels” (defined by the focused light, not by material boundaries) in a calibrated off-line scanner (manufactured by Fuji-film) releases the trapped electrons. These recombine with Eu^{3+} ions to form excited Eu^{2+} ions, which luminesce (typically $\lambda_{PSL} = 0.39 \mu\text{m}$) with intensity proportional to the deposited energy. A photomultiplier tube detects the PSL. Exposed IPs fade over several hours (Tanaka *et al.*, 2005; Zeil *et al.*, 2010), are erasable by exposure to intense light, and re-usable almost indefi-

nately. IP sensitivity to relativistic electrons is high, and nearly energy-independent. For example, (Tanaka *et al.*, 2005) reported detection of 10^3 electrons with $E_e > 80$ MeV within a $\sim 100\mu\text{m}$ pixel — *i.e.* $\sim 10^{-2}$ pC/mm². However, detection limits vary depending on the noise floor from co-exposure to x-rays, cosmic rays and other background radiation. IPs provide large dynamic range ($>10^5$) — (Zeil *et al.*, 2010) report no observable saturation effects — but multiple, time-consuming, scans are required to read highly exposed plates. IPs are insensitive to EMP (Tanaka *et al.*, 2005; Zeil *et al.*, 2010). The measured signal in a well-tested (Hidding *et al.*, 2007; Tanaka *et al.*, 2005; Zeil *et al.*, 2010) range is absolute and universal. Since exposed IPs must be scanned off-line, they are best suited for low-repetition-rate systems or for cross-calibration of scintillating screens.

A decade ago, measurements of total Q from LW-FAs were plagued with order-of-magnitude uncertainties (Glinec *et al.*, 2006), while convenient spatially-resolved charge detectors, despite decades of use as slowly integrating medical x-ray detectors, remained uncalibrated as single-shot detectors of intense, sub-ps, relativistic electron bunches. The plasma accelerator community has now transformed this situation. Shielded, filtered ICTs that measure sub-pC, absolute Q accurately in noisy LWFA environments are now commercially available. Scintillating screens and IPs are now extensively cross-calibrated at conventional ($\tau_b \sim \text{few ps}$) and LWF ($\tau_b \sim \text{few fs}$) electron accelerators for matching bunch structure and energy. Ongoing research is examining response of these detectors to high *average* charge flux (Kurz *et al.*, 2018), and the dependence of sensitivity, saturation, and linearity on τ_b in the sub-ps range.

2. MeV and GeV magnetic spectrometers

The dipole magnet spectrometer (Brown, 1975) is the workhorse for single-shot measurement of electron energy spectra both in conventional (Brown, 1975) and plasma-based (Glinec *et al.*, 2006; Nakamura *et al.*, 2008; Sears *et al.*, 2010b) accelerators. Plasma-based electron accelerators, however, pose two special challenges. First, their electrons usually span a wide energy range (as much as low-MeV to multi-GeV). Even in “quasi-monoenergetic” plasma accelerators, low-energy electrons usually accompany the main high-energy peak (see Fig. 11a,b). Accurate, simultaneous measurement of both is essential to diagnosing accelerator performance. In contrast, conventional accelerator beams usually need to be characterized accurately only over a narrow energy band. Secondly, plasma accelerators usually launch electrons over a few-mrad range of angles into the magnetic spectrometer, due to betatron oscillations or to pointing fluctuations of the driver. While a well-designed spectrometer can bring angularly-dispersed low-MeV electrons of a given E_e to

a common focus at the detector, this is often not feasible with GeV electrons. Special measures are therefore needed to characterize GeV electron trajectories through a spectrometer to avoid errors in evaluating dN_e/dE_e . In contrast, electron beams in conventional accelerators usually enter the spectrometer highly collimated.

Magnetic spectrometers for plasma accelerators can cover MeV to multi-GeV energies in one setup, albeit with varying resolution. The bending radius ρ of a relativistic electron in homogeneous magnetic field B

$$\rho = \frac{m_e c \beta \gamma_e}{eB} \approx 1.7 \times 10^{-3} \frac{\gamma_e}{B[\text{T}]} \text{ m} \quad (40)$$

defines the scale of the spectrometer — *e.g.* $\rho \approx 1$ m for $\gamma_e = 600$ with a practical upper limit $B \sim 1$ T.

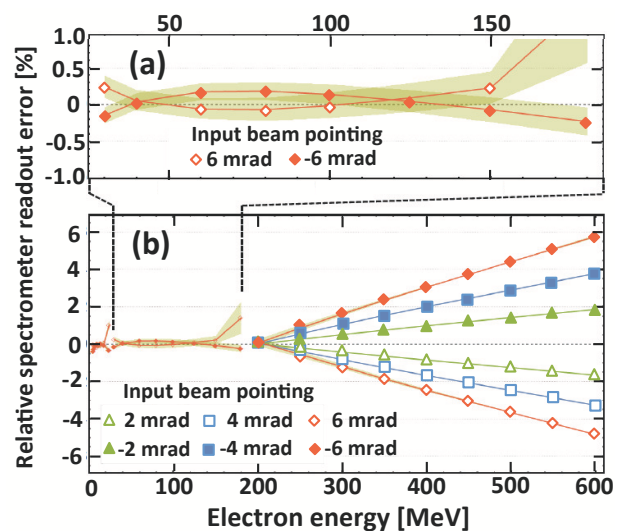


FIG. 12 Energy read-out error of dipole magnetic spectrometer for various electron entrance angles (-6 to 6 mrad) and energies ($0 < E_e < 600$ MeV): (a) low electron energy, detector in focal plane of magnet (corresponding to $E_{1,2}$ in Fig. 11), and (b) high electron energy, detector in forward direction before focal plane (corresponding to E_3 in Fig. 11). Adapted from (Schramm *et al.*, 2017).

Fig. 11 illustrates schematically the trajectories of electrons at three representative energies $E_1 < E_2 < E_3$ through a uniformly magnetized rectangular area, which is usually limited by available space and by magnet weight and cost. At energy E_1 , circular trajectories bounding the envelope of an incoming beam cross just outside the magnetic field, at deflection angle $\theta_{\text{def}} \approx 90^\circ$. Shifts in the object plane towards the magnet entrance (equivalent to a divergent incoming beam) simply shift the image plane. Resolution is thus limited only by the (negligible) source size in the object plane or by aberrations in the focusing field (Nakamura *et al.*, 2008; Sears *et al.*, 2010b). Electrons of somewhat higher energy E_2 exit the magnetic field at an oblique angle. The image plane shifts significantly, often necessitating a separate

detector as shown in Fig. 11. In addition, the influence of fringe fields becomes energy-dependent. Nevertheless, relative energy resolution $\Delta E_e/E_e$ on the percent level is usually possible without additional magnet design modifications (Savran *et al.*, 2010), as shown in Fig. 12a. Mapping of the field distribution (including fringe fields) and numerical analysis of beam trajectories is needed to define image plane and resolution precisely.

For energy E_3 , reached when ρ equals roughly twice the magnet length, focal plane detection must be abandoned in the near forward direction. This regime includes the critical quasi-monoenergetic peak of many plasma-based electron accelerators. Declining spectrometer dispersion $d\theta_{\text{def}}/dE_e$ at high E_e by itself tends to decrease energy resolution in this regime. With loss of focal plane detection, uncompensated beam divergence further compromises resolution. The detection point of an electron becomes sensitive to beam pointing jitter, as shown in Fig. 12b, impairing energy *calibration*. Special measures are then needed to ensure accurate energy measurement. If space is available, additional beam optics can recover focal plane detection (Litos *et al.*, 2014; Weingartner *et al.*, 2011). Alternatively, hard apertures can collimate the beam at the expense of charge. Reference grids, transmission beam pointing monitors (Cha *et al.*, 2012) or feedback from secondary radiation (Shaw *et al.*, 2017) can monitor beam pointing, allowing shot-to-shot correction for jitter. (Clayton *et al.*, 2010; Pollock *et al.*, 2009) introduced a correction scheme with two tandem scintillating screens. By correlating common electron spectral features on each screen, they deduced the complete electron trajectory through the spectrometer, including launch angle. For greater precision, (Wang *et al.*, 2013) employed two tandem grids of $125\mu\text{m}$ tungsten wires to cast sharply defined shadows on dispersed electron signals recorded on one IP. Analysis enabled measurement of E_e up to 2 GeV, and associated launch angles, with only $\pm 5\%$ uncertainty at the 2σ level using a 1.1 T magnetic field within a 4×4 cm central plateau. This is a low-cost solution for accurately calibrating dN_e/dE_e up to low-GeV energy. Alternatively, much larger magnets can be used — *e.g.* a circular 1.25 T field of 40 cm diameter was used to characterize 4 GeV LWFA electrons (Leemans *et al.*, 2014; Nakamura *et al.*, 2008).

Dipole magnet spectrometers have accurately characterized plasma-accelerated electrons from low-MeV to multi-GeV energies (Blumenfeld *et al.*, 2007; Leemans *et al.*, 2014; Litos *et al.*, 2014), resolving peaks as narrow as $\Delta E_e/E_e \approx 0.01$ (Rechatin *et al.*, 2009). With the highest-performing plasma accelerators currently producing bunches with few-% energy spread, the field has not yet challenged magnetic spectrometer technology to achieve higher energy resolution. With scintillating screens, read-out sensitivities of 0.1 pC/MeV can be achieved. Scintillating fibers (Sears *et al.*, 2010b) enable higher sensitivity, at greater cost and with digitized en-

ergy resolution. Since beam propagation remains undisturbed in the non-bending plane, the spectrometer's detector simultaneously measures beam divergence.

3. Spectroscopy of on-axis undulator radiation

A non-intercepting alternative to magnet spectrometers is spectroscopy of forward-directed light that relativistic electron bunches emit on passing through an undulator or Thomson backscatter light field (see Sec. III.A.2). For diagnostics, low values of undulator parameter K (Eq. 19) or field strength a_0 (Eq. 2) are preferred to avoid perturbing the electron bunch or complicating the spectrum of emitted radiation (see Fig. 6). Such a noninvasive approach will be essential for monitoring E_e , ΔE_e , angular divergence and other beam characteristics in early stages of a multi-stage plasma accelerator (Steinke *et al.*, 2016). It will be especially valuable for characterizing few-GeV electrons, a range in which dipole electron spectrometers have difficulty providing image plane diagnostics (see Sec. III.B.2) and require large expensive magnets.

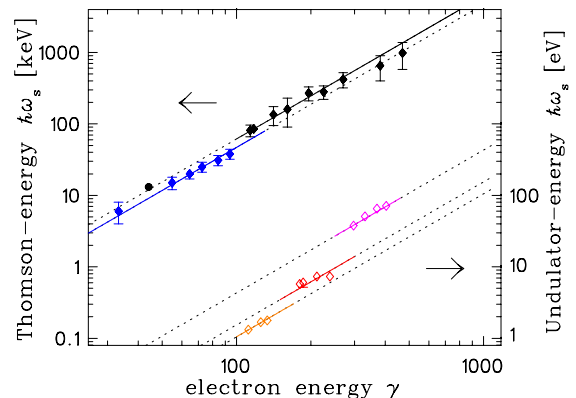


FIG. 13 Photon energies of undulator and Thomson backscatter radiation from LWFA electrons. Lower right, from low to high $\hbar\omega_s$: radiation (open diamonds) from undulators of period $\lambda_u = 20$ mm (orange, $1 < \hbar\omega_s < 2$ eV) (Schlenvoigt *et al.*, 2008); 15 mm (red, $5 < \hbar\omega_s < 8$ eV) (Anania *et al.*, 2014); 5 mm (magenta, $40 < \hbar\omega_s < 70$ eV) (Fuchs *et al.*, 2009). Upper left: Thomson back-scatter radiation (filled diamonds) generated by ultrashort $\lambda_0 = 0.8\mu\text{m}$ laser pulses of fields strength $a_0 \sim 0.8$ (blue, $6 < \hbar\omega_s < 40$ keV) (Khrennikov *et al.*, 2015b); 0.3 (black, $80 < \hbar\omega_s < 1000$ keV) (Powers *et al.*, 2014). Note red-shift of higher a_0 data. Black circle: data from Fig. 16 for comparison.

Measurement of maximum frequency $\omega_{sc}^{(max)} \propto [\gamma_e^{(max)}]^2$ of light emitted on-axis directly determines the maximum electron Lorentz factor $\gamma_e^{(max)}$, which in quasi-monoenergetic plasma accelerators corresponds to the primary spectral peak of interest. The lower right portion of Fig. 13 summarizes results of correlated measurements of Lorentz factors of single-stage LWFA electrons in the

range $100 < \gamma_e^{(max)} < 400$ (made with magnetic spectrometers) and of the photon energy of undulator radiation from visible (1.8 eV) (Gallacher *et al.*, 2009; Schlenvoigt *et al.*, 2008) to EUV (83 eV) (Anania *et al.*, 2014; Fuchs *et al.*, 2009) that the electrons generated in undulators of periods $0.5 \text{ cm} < \lambda_u \leq 2.0 \text{ cm}$. The measurements agreed well with the relation $\hbar\omega_{sc} = 2\gamma_e^2\hbar\omega_u$ (solid orange, red, magenta lines), from Eq. (20) for $K < 1$, $\theta \rightarrow 0$. In this photon energy range, and probably up to $\hbar\omega_{sc} \sim \text{few keV}$ (corresponding to $E_e \sim \text{few GeV}$), optical to soft x-ray spectrometers can measure $\hbar\omega_{sc}$ at least as accurately as magnetic spectrometers can measure γ_e . The emergence of miniature, short-period undulators designed specifically for LWFA (Eichner *et al.*, 2007) will help to make such non-invasive $\gamma_e^{(max)}$ measurement compact and cost-effective.

The upper left portion of Fig. 13 summarizes corresponding results for Thomson backscatter of $\lambda = 0.8\mu\text{m}$ light from LWFA photons of similar $\gamma_e^{(max)}$ range. Since $\omega_0 \gg \omega_u$, photon energies now range from 60 keV to 1 MeV (Golovin *et al.*, 2016; Khrennikov *et al.*, 2015b; Powers *et al.*, 2014; Tsai *et al.*, 2015), and agree well with the relation $\hbar\omega_{sc} = 4\gamma_e^2\hbar\omega_0$ (solid blue, black lines), from Eq. (21) for $a_0 < 1$, $\theta \rightarrow 0$, $\varphi_{\text{coll}} = 180^\circ$. Experiments with 1-2 GeV ($2000 < \gamma_e < 4000$) electrons (not shown) extended the range to $\hbar\omega_{sc} \sim 80 \text{ MeV}$ (Shaw *et al.*, 2017). In this photon energy range, the challenge shifts to accurate spectroscopy of such hard x-rays (Gahn *et al.*, 1998; Golovin *et al.*, 2016; Günther *et al.*, 2011; Horst *et al.*, 2015; Sarri *et al.*, 2014). If adequate resolution can be achieved, the possibility of realizing Thomson backscatter from low-MeV (Ta Phuoc *et al.*, 2012) to multi-GeV (Shaw *et al.*, 2017) electrons simply by inserting a plasma mirror (foil) after the plasma to back-reflect the spent drive laser pulse (see Sec. III.A.2) offers an exceptionally low-cost electron energy diagnostic.

In addition to $\gamma_e^{(max)}$, spectroscopy of undulator/Thomson radiation can also diagnose *spread* $\Delta\gamma_e$ of a peaked electron energy distribution if additional beam parameters are known (Brown and Hartemann, 2004; Chouffani *et al.*, 2006; Golovin *et al.*, 2016; Jochmann *et al.*, 2013; Krämer *et al.*, 2018; Schlenvoigt *et al.*, 2008) (see Sec. III.C). Relative on-axis photon energy spread (for $K \ll 1$, $a_0 \ll 1$) is determined not only by relative electron energy spread $\Delta\gamma_e/\gamma_e$, but by electron angular spread σ'_r , laser bandwidth $\Delta\omega_0$ (for Thomson backscatter only), number of periods N_u , and solid angle Ω_{det} covered by the on-axis detector:

$$\left(\frac{\Delta\omega_{sc}}{\omega_{sc}}\right)^2 = \left(\frac{2\Delta\gamma_e}{\gamma_e}\right)^2 + \left(\gamma_e^2\sigma_r'^2\right)^2 + \left(\frac{2\Delta\omega_0}{\omega_0}\right)^2 + \left(\frac{1}{N_u}\right)^2 + \left(\gamma_e^2\Delta\Omega_{det}^2\right)^2. \quad (41)$$

Electron beam optics can reduce divergence (Anania *et al.*, 2014; Becker *et al.*, 2009; Fuchs *et al.*, 2009), but

then chromatic selectivity distorts the spectrum.

Absolute E_e and $\Delta E_e/E_e$ of LWFA beams of energies ($60 \text{ MeV} < E_e < 120 \text{ MeV}$) and divergences ($1 \text{ mrad} < \sigma'_r < 3.5 \text{ mrad}$) have been resolved with undulator radiation ($N_u \sim 50$) ranging from near-IR (Gallacher *et al.*, 2009) to vacuum ultraviolet (Anania *et al.*, 2014). After deconvolving the σ'_r contribution, (Gallacher *et al.*, 2009) obtained $\Delta\gamma_e/\gamma_e$ as small as ~ 0.01 , in agreement with independent magnet spectrometer measurements, equivalent to the smallest LWFA energy spread observed with magnetic spectrometer alone (Rechatin *et al.*, 2009). When magnetic quadrupoles pre-collimated the LWFA beam, $\Delta\gamma_e$ of the selected main peak became the dominant contribution to $\Delta\omega_{sc}$. However, discrepancies between $\Delta\gamma_e$ determined from undulator and magnetic spectrometer were observed (Anania *et al.*, 2014). Extension of such measurements to GeV electrons will be a priority for future research.

4. Slice energy spread

More than a decade after first demonstrations of “quasi-monoenergetic” plasma accelerators, electron bunches with overall energy spread $\Delta E_e/E_e$ below 0.01 have not been observed. Yet $\Delta E_e/E_e \sim 10^{-3}$ and kA peak current are vital for short-wavelength conventional (Behrens *et al.*, 2014; Röhrs *et al.*, 2009) and LWFA-driven (Gruener *et al.*, 2007) free electron lasers (FELs). $\Delta E_e/E_e$ of high quality plasma-accelerated bunches can, however, be dominated by *correlated* spread. This means that $\Delta E_e/E_e$ is the sum of spreads of longitudinal slices of the bunch, each of which is individually much lower than $\Delta E_e/E_e$. Relative slice energy spread 10^{-3} could enable FEL gain with plasma accelerators (Huang and Kim, 2007). Bunch decompression reduces energy spread over the slice at the expense of decreasing the peak current (Seggebrock *et al.*, 2013). Dispersively matched transverse gradient undulators could then operate with different energy slices (Huang *et al.*, 2012) simultaneously. Diagnosis of slice energy spread is thus a key component of current plasma accelerator research.

(Lin *et al.*, 2012) deduced slice properties of LWFA bunches *indirectly* by imaging visible CTR several meters downstream from an LWFA. If $\Delta E_e/E_e \sim 0.05$ were present throughout the bunch’s longitudinal profile, sub- μm density and momentum modulations, a prerequisite for non-zero form factor F [Eq. (34)] and thus for generating *coherent* TR at visible wavelengths [Eq. (35)], would disappear within a few centimeters of propagation (Glinec *et al.*, 2007; Lundh *et al.*, 2011). (Lin *et al.*, 2012) created such modulations by generating wakes in sufficiently dense ($\bar{n}_e > 10^{19} \text{ cm}^{-3}$) plasma that the trailing edge of the drive laser pulse modulated the accelerating bunch. Yet several meters downstream of the LWFA, they observed two clear signatures of CTR: (1) intensity

up to $10^3 \times$ stronger than calculated from Eq. (35) with $F = 0$; (2) imaged TR spatial profiles containing “hot spots” much smaller than the overall beam profile. Persistence of coherent features over such long propagation lengths required $\Delta E_e/E_e|_{\text{slice}} \lesssim 0.005$, well below the total energy spread.

A method for measuring $\Delta E/E|_{\text{slice}}$ *directly* in the time domain was developed for FEL drivers and FACET (Dolgashev *et al.*, 2014): an X-band (typically 11.4 or 12 GHz) RF transverse deflection cavity streaks the bunch. Energy-resolved monitoring of the streaked transverse profile recovers longitudinally-distributed dN_e/dE_e . A slice resolution of 70 fs was demonstrated at SLAC for the 20 GeV FACET beam ($\epsilon_n \sim 40 \mu\text{m}$) where for LCLS operating conditions (energy < 14 GeV and $\epsilon_n \sim 0.5 \mu\text{m}$) values of < 4 fs can be reached, illustrating the influence of transverse beam parameters on the resolution. However, RF cavities cannot resolve $\Delta E/E|_{\text{slice}}$ of few-fs LWFA bunches. New approaches employing light fields (Zhang *et al.*, 2016a) or plasma wakefields (Dornmair *et al.*, 2016) as transverse deflectors are now emerging. Since these methods are closely connected with bunch duration measurement, we discuss them in Sec. III.D.1.a.

C. Transverse emittance measurement

Early measurements of transverse emittance of LWFA electron bunches adopted mask and focus-scan techniques developed for conventional accelerator beams (Sec. III.C.1). But resolution and E_e range limits motivated development of new methods based on betatron x-ray spectroscopy (Sec. III.C.2), and undulator and transition radiation (Sec. III.C.3).

1. Conventional mask and focus-scan methods

a. Masks. Techniques using beam-intercepting masks (subscript m) with 1D (2D) arrays of slits (pinholes) — *i.e.* “pepper-pots” — were designed to characterize emittance of low-MeV, space-charge-dominated electron beams (Lejeune and Aubert, 1980; Mostacci *et al.*, 2008), although (Delerue, 2011; Thomas *et al.*, 2013) recently extended their use to RF-accelerated GeV electrons. Fig. 14a shows a schematic 1D geometry. A beam impinges at centroid position \bar{x} with average x -momentum x' on an array of slits, each of width d , centered at $x_{i,m}$. The i^{th} slit transmits a beamlet of well-defined origin and low enough charge en_i that it becomes “emittance-dominated” — *i.e.* positions x_j and transverse momenta x'_j of electrons passing through the slit ($j = 1, 2, \dots, n_i$), rather than Coulomb repulsion, dominate beamlet propagation. A screen (subscript s) at distance l , often thin Ce:YAG to avoid grain-size resolution limits of Lanex,

records the centroid position $x_{i,s}$ (yielding average x -momentum $x'_i = (x_{i,s} - x_{i,m})/l$), spatial profile (diameter $d_{i,s}$), and (if linear in response) relative electron number n_i of each expanded beamlet. As long as each beamlet’s angular spread $\Delta x'_i$ is not too large, the averages $\langle x^2 \rangle_i$, $\langle x'^2 \rangle_i$ and $\langle xx' \rangle_i$ that contribute to its x -emittance ϵ_i [see Eq. (9)] are related straightforwardly to observed beamlet ($n_i, x_{i,m}, x'_i, d_{i,s}$) and whole beam (\bar{x}, x') quantities. A sum of ϵ_i over slits then yields emittance ϵ of the subset of incident electrons that passed through the slits, assuming negligible space-charge. (Zhang, 1996) derives complete expressions for ϵ_i and ϵ . Generalization to 2D (Fig. 14b) is straightforward. With sufficient charge, the pepper-pot technique can measure ϵ in one shot. Analogous pin-hole or lenslet arrays characterize transverse phase structure of optical beams (Platt and Shack, 2001).

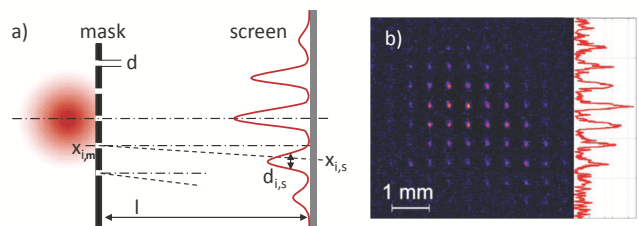


FIG. 14 Color online. Pepper-pot measurement of beam emittance. (a) Opaque mask with slits or holes transmits diverging beamlets across beam profile. Thin downstream Ce:YAG screen at distance l detects expanded beamlet profiles (width $d_{i,s}$, location $x_{i,s}$) with typically $\lesssim 10 \mu\text{m}$ resolution. (b) Screen image of 125 MeV LWFA beam 30 cm downstream of source, yielding $\epsilon_n \sim 2.2 \pm 0.7$ mm mrad (resolution ~ 1.2 mm mrad), divergence ~ 3 mrad. Panel b) from (Brunetti *et al.*, 2010).

(Cianchi *et al.*, 2013) pointed out limits of the pepper-pot method for resolving ϵ of LWFA beams, which is dominated by divergence rather than space-charge. While for typical injector beams, the ratio of divergence to initial beam size is ~ 1 mrad/mm, for LWFA beams it is $\sim 10^3$ mrad/mm (*e.g.* $\sigma_r(0) \approx 1 \mu\text{m}$, $\sigma'_r \approx 1$ mrad). Because of their relatively strong divergence, the phase-space profile of LWFA beams flattens after a few cm of free-space propagation, with x' strongly correlated with x (see Fig. 4c). Consequently, a slit at $x = x_i$ sees a very small uncorrelated spread $\Delta x'_i = (d_{s,i} - d \cdot x_{s,i}/x_i)/l$ of x' values, and has difficulty resolving it above the uninformative geometric slit projection $d(x_{i,s}/x_i)/l$. Narrowing slit width d to compensate scatters the beam. Thus pepper-pots tend to under-sample transverse phase space of LWFA beams.

Nevertheless, pepper-pot measurements placed first-generation upper limits on LWFA beam emittance before other measurements existed. Experiments for quasi-monoenergetic, $\sigma'_r \sim$ few-mrad LWFA beams in the energy range 15 to 200 MeV with scanning pin-hole (Fritzier *et al.*, 2004), scanning slit (Sears *et al.*, 2010a),

and pepper-pot masks (Brunetti *et al.*, 2010; Manahan *et al.*, 2014) yielded upper-limit ε_n estimates between 1-3 mm mrad with $\sim 30\%$ relative errors. These results were based on estimated upper limit initial beam size $\sigma_r(0) \sim \lambda_p \sim 10 \mu\text{m}$. However, (Cianchi *et al.*, 2013) later showed that for $\sigma_r(0) \sim 1 \mu\text{m}$ (see *e.g.* Fig. 4a,b), the phase space ellipse of a $\sigma'_r \sim \text{few-mrad}$ beam flattens so quickly that pepper-pots with realistic pin-hole diameters (tens of μm) cannot resolve their emittance. Indeed betatron x-ray spectroscopy shows $\sigma_r < 1 \mu\text{m}$ (see Sec. III.C.2). On the other hand, mask techniques remain useful for characterizing LWFA beams transmitted through emittance-increasing optics (Manahan *et al.*, 2014), or for evaluating transport conditions between acceleration stages (Dornmair *et al.*, 2015; Xu *et al.*, 2016).

b. Focus Scans. Conventionally, ε of *non-space-charge-dominated* beams is often characterized by measuring their transverse profile after focusing optics, *e.g.* at a fixed location while changing focusing strength (quadrupole scan), or at multiple locations with fixed optics (multi-screen measurements) (Minty and Zimmermann, 2013; Rees and Rivkin, 1984). To recover three Twiss parameters [Eq. (10)], at least three measurements, usually over multiple shots, are needed. (Mostacci *et al.*, 2012) succinctly reviewed this technique, and analyzed new measurement uncertainties that come into play for LWFA and other beams with $\gtrsim \text{few-}\%$ energy spread (see Fig. 3a), compared to $\sim 0.1\%$ for conventional focus-scan measurements, and with large σ_r (due to strong divergence) at the first quadrupole in a sequence. The resulting chromatic effects can not only introduce systematic errors into measurement of ε , but can degrade ε of the beam under test. The severity of these effects depends on the specific quadrupole configuration and on incident beam properties. For example, to characterize a beam with $E_e \sim 150 \text{ MeV}$, $\Delta E_e/E_e \sim 0.01$ and $\varepsilon_n \sim 1 \text{ mm mrad}$ using a single quadrupole requires sub-mm spot size to avoid strong emittance dilution (Cianchi *et al.*, 2013).

(Weingartner *et al.*, 2012) turned energy spread into a diagnostic advantage by inserting an energy-dispersing magnetic dipole between a fixed high-gradient quadrupole doublet (Becker *et al.*, 2009) and a Ce:YAG screen located 10 cm and $\sim 2 \text{ m}$, respectively, after a $\sim 250 \text{ MeV}$ LWFA. Screen luminescence displayed *energy-resolved* beam size as quadrupole position scanned over multiple shots, avoiding chromatic errors in determining ε . Alternatively, this configuration enabled a rare *single-shot* focus-scan measurement by exploiting the quadrupole focal length's dependence on E_e . Thus the beam's natural energy spread mapped onto an equivalent focus-scan at the detector without the need for moving or adjusting the field strength of the quadrupole. Both multi- and single-shot measurements yielded $\varepsilon_n =$

0.2 mm mrad with 5-10% uncertainty, well below the upper limits set by pepper-pot measurements. Active lensing in plasma discharge cavities provides a complementary means for performing focus scans close to the plasma accelerator, ensuring small spot size (van Tilborg *et al.*, 2015). Recently (Barber *et al.*, 2017) applied an energy-resolved focus-scan to determine the influence of injection scheme on beam emittance. Results showed that shock-induced down-ramp injection yielded a factor of two lower normalized emittance ($\varepsilon_n \sim 1 \text{ mm mrad}$) than ionization injection at equal charge densities ($dQ/dE \sim 2 \text{ pC/MeV}$).

2. Betatron x-ray spectroscopy

In contrast to conventional beam-intercepting emittance diagnostics outside the accelerator, betatron spectroscopy (see Sec. III.A.3) emerged as a non-invasive, albeit indirect, alternative for diagnosing ε_n *within*, and near the end of, the accelerator, where most betatron radiation is emitted (see Fig. 7c). Measured quantities are electron spectrum dQ/dE_e (Fig. 11b), betatron x-ray spectrum $dW_\beta^{(meas)}/d\omega$ (Fig. 15) and \bar{n}_e . A simple analysis fits $dW_\beta^{(meas)}/d\omega$ to a calculated single-electron betatron power spectrum $dW_\beta/d\omega$ [Eqs. (16), (24); see green curve, Fig. 15], and extracts the critical frequency ω_c [Eq. (26)], typically $\sim 10 \text{ keV}$ for LWFAs producing few-hundred-MeV electrons. Then via the relation $\omega_c \propto \gamma_e^3 k_\beta^2 r_\beta \propto \gamma_e^2 \omega_p^2 r_\beta$ [from Eqs. (23), (26)], one obtains the betatron oscillation amplitude r_β of a single electron, using γ_e and ω_p from the quasi-monoenergetic peak of dQ/dE_e and the \bar{n}_e measurement, respectively. The extracted r_β can be interpreted as an ensemble average amplitude \bar{r}_β , then equated with (Plateau *et al.*, 2012), or related with help from auxiliary measurements to (Schnell *et al.*, 2012), intra-LWFA bunch radius σ_r . Combining σ_r with measured beam divergence $\sigma'_r{}^{(meas)}$ *outside* the accelerator – *e.g.* from the width of the electron spectrometer signal orthogonal to the dispersion plane – yields the estimate

$$\varepsilon_n \approx \gamma_e \sigma_r \sigma'_r{}^{(meas)} \quad (42)$$

for the uncorrelated component of normalized emittance [*i.e.* first term on right-hand side of Eq. (12a)]. However, Eq. (42) neglects correlations between x and x' [second term on right-hand side of Eq. (12a)]. Moreover, $\sigma'_r{}^{(meas)}$ can misrepresent $\langle \gamma_e^2 x'^2 \rangle$ inside the LWFA if the plasma-vacuum boundary re-shapes the beam's phase-space ellipse (see Fig. 4a,b), thereby altering its downstream divergence (Sears *et al.*, 2010a; Weingartner *et al.*, 2012).

(Köhler *et al.*, 2016; Plateau *et al.*, 2012; Schnell *et al.*, 2012) used this simple analysis method to estimate ε_n from quasi-monoenergetic LWFAs under a variety of conditions. They measured $dW_\beta^{(meas)}/d\omega$ in a single shot

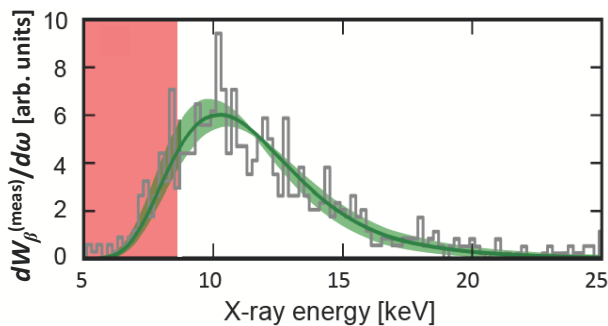


FIG. 15 Color online. Measured betatron radiation spectrum $dW_{\beta}^{(meas)}/d\omega$ (solid black histogram) used to determine beam radius σ_r inside LWFA that produced a peaked electron energy spectrum similar to the one shown in Fig.11b. Solid green curve: calculated spectrum $dW_{\beta}/d\omega$, assuming $\sigma_r \lesssim r_{\beta} = 0.8 \mu\text{m}$. Shaded green area: variation in $dW_{\beta}/d\omega$ for 25% variation in σ_r . Red-shaded area (5 – 8 keV): low-energy regime with reduced detection efficiency and measurement quality. Experimental conditions matched those of (Couperus *et al.*, 2017; Köhler *et al.*, 2016).

using a shielded, back-illuminated x-ray CCD camera operating in photon-counting mode — *i.e.* each pixel absorbed on average less than one x-ray photon. The charge deposited in an illuminated pixel determined the photon’s energy. The x-ray spectrum consisted of a histogram of all illuminated pixels (Fig. 15). (Plateau *et al.*, 2012) found r_{β} as low as $0.1 \mu\text{m}$ for a 0.4 pC , $\gamma_e = 920$ bunch, in agreement with the matched beam radius $\sigma_r = \sqrt{2\gamma_e}\sigma_r'/k_p$ inferred from down-stream divergence measurements and plasma conditions. Use of Eq. (42) yielded $\varepsilon_n \sim 0.1 \text{ mm mrad}$. (Schnell *et al.*, 2012) observed monotonically decreasing r_{β} (4 to $0.4 \mu\text{m}$) as γ_e increased (50 to 250), a consequence of the relativistic electron mass increase. (Köhler *et al.*, 2016) integrated the evolving x-ray spectrum of the accelerating electron bunch in fitting $dW_{\beta}^{(meas)}/d\omega$, thereby determining r_{β} with unprecedented resolution (Fig. 15). These researchers cross-checked extracted r_{β} values, typically with lower resolution, by independently analyzing x-ray shadows of sharp edges or wires. For a $\gamma_e = 160$ bunch for which betatron spectroscopy yielded $r_{\beta} = 0.9 \pm 0.3 \mu\text{m}$, (Schnell *et al.*, 2012) found x-ray source size $\sigma_x = 1.8 \pm 0.3 \mu\text{m}$ from x-ray shadowgraphy, and inferred $\sigma_r = 1.6 \pm 0.3 \mu\text{m}$ by modeling radiation from a Gaussian bunch. (Kneip *et al.*, 2012) used x-ray shadowgraphy alone to estimate σ_r , but observed no γ_e -dependence.

(Curcio *et al.*, 2017) used the same single-shot experimental method to obtain $dW_{\beta}^{(meas)}/d\omega$, but introduced a more sophisticated analysis that included ensemble averages $\langle x^2 \rangle$, $\langle \gamma_e^2 x'^2 \rangle$ and $\langle x\gamma_e x' \rangle^2$ from the outset in calculating $dW_{\beta}/d\omega$, instead of single-electron theory. They assumed bunches were radially symmetric and did not interact with the tail of the drive pulse. Accordingly, they confined analysis to shots that produced ra-

dially symmetric betatron x-ray profiles, and to conditions for which bubble radius significantly exceeded drive pulse length. With these simplifications, they solved the inverse problem to recover a complete intra-LWFA radial beam profile $P(r)$, instead of just an average σ_r , and a complete distribution $\Theta(\theta_d)$ of transverse angles $\theta_d = dr/dz$, including correlations $r(\theta_d)$. This enabled determination of $\varepsilon_n = 0.6 \pm 0.1 \text{ mm mrad}$ for a $\gamma_e = 640 \pm 6$ beam, including correlations $\langle x\gamma_e x' \rangle^2$, solely from $dW_{\beta}^{(meas)}/d\omega$ and dQ/dE_e measurements, without invoking $\sigma_r'^{(meas)}$. Nevertheless, calculated σ_r' agreed with $\sigma_r'^{(meas)}$ for the conditions investigated. On the other hand, estimating emittance of the same beam from Eq. (42), using $\sigma_r'^{(meas)}$, yielded $\varepsilon_n = 1.5 \pm 0.3 \text{ mm mrad}$, demonstrating that correlations contribute significantly to ε_n inside a plasma bubble.

Accelerating electrons with non-planar trajectories — *i.e.* angular momentum — can generate radially *asymmetric* betatron x-ray intensity profiles (Phuoc *et al.*, 2006). Although a linearly-polarized drive laser pulse imparts no net angular momentum to its wake, if it has a radially asymmetric spatial profile, it creates a plasma bubble with asymmetric focusing forces $F_x \neq F_y$. Accelerating electrons and their heavier plasma cavity can then acquire equal and opposite, cyclically-evolving angular momenta, while total angular momentum remains constant. (Thaury *et al.*, 2013) observed such periodic cycling of betatron x-ray asymmetry by controlling acceleration length with colliding-pulse injection (see Sec. II.C.1). Since angular momentum, over and above emittance, influences downstream beam propagation, its accurate single-shot diagnosis is essential. Additionally, observation of a non-uniformly *polarized* betatron x-ray profile signifies a preferred oscillation direction, which can arise from bunch interaction with the rear of the drive laser pulse (Cipiccia *et al.*, 2011; Curcio *et al.*, 2015; Mangles *et al.*, 2006; Németh *et al.*, 2008).

3. Undulator and transition radiation diagnostics

Radiation that electron beams emit *outside* an accelerator — *e.g.* undulator/Thomson-scatter (Sec. III.A.2) or TR (Sec. III.A.4) — can also characterize their emittance indirectly. (Leemans *et al.*, 1996) and (Chouffani *et al.*, 2006; Jochmann *et al.*, 2013; Krämer *et al.*, 2018) developed basic principles for diagnosing beam divergence $\sigma'_{x,y}$ using 90° and 180° Thomson scattering, respectively. These studies used tens-of-MeV electron bunches of negligible energy spread ($\Delta\gamma_e/\gamma_e \lesssim 0.003$) from conventional linacs. In the 90° geometry, a $\sim 100 \text{ fs}$ laser pulse scattered from a longitudinal slice of a 10-15 ps bunch, selected by changing bunch-laser delay. The energy-integrated transverse Thomson x-ray intensity profile was measured on a phosphor screen, then fit to a single-

electron angular power distribution $dW_{sc}/d\Omega$ integrated over a Gaussian distribution of electron propagation angles to extract $\sigma'_{x,y}$. The 180° geometry integrated over bunch length, but θ -dependent Thomson-scatter *spectra* — given by Eq. (21) with $\varphi_{coll} = 180^\circ$ for *one* electron — were measured with high spectral/angular resolution using either Si(Li) and PIN detectors (Choufani *et al.*, 2006) or a pixelated x-ray CCD (Jochmann *et al.*, 2013) similar to those used in betatron x-ray spectroscopy (see Sec. III.C.2). Fig. 16 shows typical results from (Jochmann *et al.*, 2013). The *peak* of the x-ray photon energy distribution $dN(\theta)/dE$ (red swath) closely tracked Eq. (21) (black dotted curve), except for a $\sim 5\%$ red-shift near $\theta = 0$, attributable to the fraction of the diverging electron ensemble that deviated from $\varphi_{coll} = 180^\circ$. The width and asymmetry of $dN(\theta)/dE$ (black solid curves) changed dramatically with increasing observation angle θ . Numerical fits to these distinctive features enabled extraction of electron angular distribution with unprecedented accuracy.

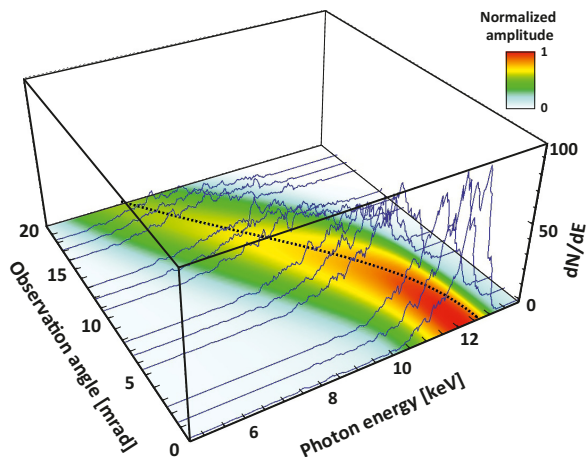


FIG. 16 Color online. Thomson-backscattering spectra dN/dE vs. observation angle θ . Electron beam: $E_e = 22.5$ MeV, $\Delta E_e/E_e \approx 0.0025$, $\tau_b \approx 4$ ps, $Q = 77$ pC linac bunches; laser: $\lambda = 800$ nm, $\Delta\lambda \approx 20$ nm, $a_0 \approx 0.05$. Black solid curves: experimental data; dotted curve: Eq. 21; linear color scale: numerical model of $dN(\theta)/dE$ with blue minimum, red maximum. From (Jochmann *et al.*, 2013).

The accuracy of the above measurements relied on small relative energy spread $\Delta\gamma_e/\gamma_e$, just as undulator-based measurements of $\Delta\gamma_e/\gamma_e$ relied conversely on small angular spread (see Sec. III.B.3). Small detector angle (Ω_{det}) and small laser ($\Delta\omega_0$)/undulator (N_u^{-1}) bandwidth were also essential. Eq. (41) summarized the trade-offs (Krämer *et al.*, 2018). The principal new challenge that LWFA beams presented for undulator/Thomson-based emittance characterization was their comparatively large $\Delta\gamma_e/\gamma_e$ (see Sec. II.C.1, Fig. 3). (Fuchs *et al.*, 2009) chromatically focused an LWFA beam into an undulator, thereby selecting a narrow energy band.

However, the measurement is then destructive. As a non-invasive alternative, (Golovin *et al.*, 2016) obtained single-shot, θ -resolved spectra equivalent to Fig. 16 by Thomson-scattering a 40 fs ($\Delta\omega_0/\omega_0 \sim 0.03$) laser pulse at $\varphi_{coll} = 170^\circ$ from a ~ 60 MeV LWFA beam with $\Delta\gamma_e/\gamma_e \sim 0.1$. Under these conditions $\Delta\gamma_e$, σ'_r and $\Delta\omega_0$ all contributed to the observed spectral width. They then simulated Thomson scatter using a beam of variable γ_e , $\Delta\gamma_e$ and σ'_r to achieve the best global fit to the θ -dependent spectrum. The fit correctly recovered independently-measured γ_e and $\Delta\gamma_e$, and output the beam's local σ'_r at the collision point. The latter was observed approximately to double as the beam propagated from the LWFA exit to a point 40 cm downstream, a signature of emittance growth due to space charge.

In addition to σ'_r , a measurement of σ_r is needed to estimate ε_n via Eq. (42). (Golovin *et al.*, 2016), like (Kneip *et al.*, 2012; Köhler *et al.*, 2016; Schnell *et al.*, 2012) earlier (see Sec. III.C.2), used x-ray knife-edge shadowing, which has difficulty resolving $\sigma_r \lesssim 1\mu\text{m}$ beams expected near a LWFA exit. A potential minimally invasive alternative is TR imaged from a thin foil surface to a detector. For $\sigma_r \gg 1\mu\text{m}$ beams, this image is simply a replica of the transverse beam profile. For $\sigma_r \lesssim 1\mu\text{m}$ beams, TR images formed from visible light no longer directly resolve this profile. On the other hand, the imaged profile transforms to the annular point spread function of a single electron [Fig. 9b, Eq. (38)]. Properties of the central minimum, which has been observed from extremely low ε_n conventional beams (Karataev *et al.*, 2011), can potentially diagnose σ_r in this range. (Bourgeois *et al.*, 2012) recovered transverse LWFA beam profiles from CTR images using an iterative algorithm. Near an LWFA exit, a second upstream foil is needed to deflect the intense drive laser pulse.

D. Bunch length measurement

Conventional radio-frequency electron accelerators based on photocathodes illuminated with short laser pulses generally produce electron bunches as short as a few picoseconds, limited by energy spread, and peak currents up to ~ 100 A. The advent of compact XUV and x-ray free-electron lasers drove development of magnetic chicane compressors capable of reducing these durations to ~ 100 fs, while increasing peak current to >1 kA (Dohlus *et al.*, 2005). Such sources have provided drive and injected bunches for recent electron-beam-driven PWFAs experiments (Corde *et al.*, 2015; Litos *et al.*, 2014). Time-domain diagnostic methods such as transverse deflection structures (TDSs) (Behrens *et al.*, 2012) and electro-optic (EO) methods (Berden *et al.*, 2007) are well-suited, and widely used, for characterizing bunch durations in this range. LWFAs operating in the “bubble” regime, on the other hand, are capable of

producing electron bunches of only a *few femtoseconds* duration. Measurement of such short bunch durations, and their internal profiles, is one of the greatest new, ongoing diagnostic challenges that plasma electron accelerators have posed. Some researchers have addressed this challenge with creative extensions of time-domain TDS (Zhang *et al.*, 2016a) and EO (Debus *et al.*, 2010a; van Tilborg *et al.*, 2006) methods. (Buck *et al.*, 2011) introduced a time-domain *magneto-optic* (MO) method to resolve LWFA bunch durations in the few-fs range (Secs. III.D.1.c and IV.C.3). Most recently, frequency-domain, wide-bandwidth OTR methods have successfully characterized few-fs bunch profiles (Heigoldt *et al.*, 2015; Lundh *et al.*, 2013). Preliminary CDR (Castellano *et al.*, 2001; Fiorito, 2001) and Smith-Purcell radiation (Andrews *et al.*, 2014a) results also appear promising.

1. Time-domain methods

Purely electronic time-domain bunch characterization methods, such as integrating current transformers (Nakamura *et al.*, 2016), resolve bunch duration at best down to the nanosecond level. TDS and EO methods, on the other hand, provide sub-ps characterization.

a. Transverse deflecting structures. A TDS, analogous to a streak camera, imparts a rapidly time-varying transverse momentum kick to an electron bunch that deflects electrons at different longitudinal positions within a bunch to different transverse locations on a downstream detector. Microwave transverse deflecting cavities have resolved longitudinal features of bunches from conventional rf accelerators down to the hundreds of fs scale (Behrens *et al.*, 2012; Ding *et al.*, 2011; Röhrs *et al.*, 2009; Xiang *et al.*, 2011). However, microwave TDS's have not yet been applied to LWFA beams.

The problem of characterizing few-fs LWFA bunches has spurred the proposal (Bettoni *et al.*, 2016; Dornmair *et al.*, 2016; Xiang and Huang, 2007) and laboratory demonstration (Bettoni *et al.*, 2016; Zhang *et al.*, 2016a) of new TDS configurations that use near-IR light fields (Xiang and Huang, 2007; Zhang *et al.*, 2016a) or wake fields (Bettoni *et al.*, 2016; Dornmair *et al.*, 2016) with few-fs periods to deflect electrons, instead of microwaves with ns periods. (Bettoni *et al.*, 2016) proposed and demonstrated a *passive* deflector based on the self-transverse wakefield interaction of the bunch passing off-axis through a dielectric-lined or corrugated waveguide. (Dornmair *et al.*, 2016) proposed to propagate the subject electron bunch obliquely through the zero-crossing between focusing and defocusing fields in a linear LWFA, where fields vary rapidly enough to deflect different longitudinal slices of a few-fs bunch in substantially different directions. (Xiang and Huang, 2007) proposed to prop-

agate the subject bunch through a small aperture in a CTR foil oriented at 45° to its propagation direction. Radiation recoil from back-reflected near-IR CTR (see Fig. 10a) deflects electrons in proportion to the product of bunch charge and form factor (33e), from which bunch length can be estimated.

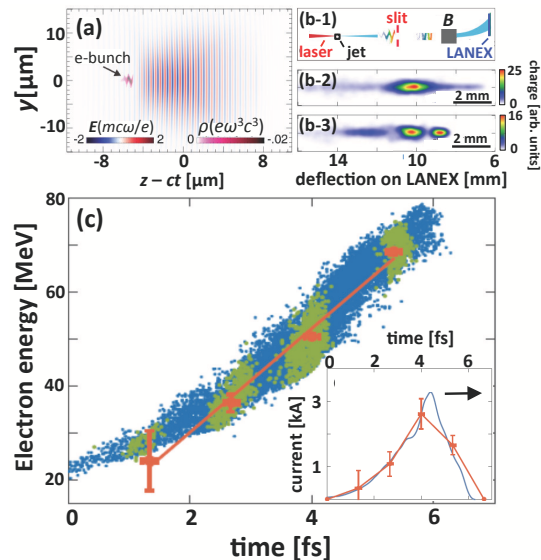


FIG. 17 Color online. Time-domain longitudinal profiling of few-fs LWFA electron bunch. (a) Simulation snapshot showing chirped, accelerating LWFA e-bunch (charge density ρ) with periodic transverse deflections driven by trailing edge of right-propagating $\lambda = 0.8\mu\text{m}$ drive pulse (field strength E). (b) Measurement of transverse deflections: (b-1) slit after laser-driven jet blocks most deflected parts of bunch, imprinting periodic energy modulation (b-3) on electron spectra recorded at detector (LANEX screen) of magnetic spectrometer; (b-2) unmodulated reference electron spectrum with slit removed. (c) Reconstructed energy-time phase profile of bunch. Inset: energy-integrated longitudinal bunch profile. Arrow indicates propagation direction. Adapted from (Zhang *et al.*, 2016a).

The experiment of (Zhang *et al.*, 2016a) used electric fields in the trailing edge of a near-IR LWFA drive pulse to transversely deflect electrons in an energy-chirped bunch accelerating *inside* a LWFA, thereby locally enhancing their betatron motion in opposite directions every half-cycle (see Fig. 17a). The technique could equally well be implemented with a separate probe pulse overlapping and co-propagating with the accelerating bunch. (Zhang *et al.*, 2016a) relied on *energy chirp* within the accelerating bunch to map longitudinal position within the bunch onto energy. Thus when the modulated bunch exited the accelerator, and passed through a slit that blocked its most deflected parts (Fig. 17b-1), a periodic series of minima appeared in the energy distribution observed at the detection plane of a magnetic spectrometer (Fig. 17b-3). Simply counting these minima yielded the bunch duration in units of optical half-cycles. By ana-

lyzing energy-dependent modulation amplitudes, (Zhang *et al.*, 2016a) reconstructed the longitudinal *shape* of the ~ 4 fs bunch (Fig. 17c). Although invasive and reliant on energy chirp in its current form, the method of (Zhang *et al.*, 2016a) is an important first demonstration of the promise of advanced TDS methods for characterizing few-fs bunches.

b. Electro-optic methods. EO methods convert either the Lorentz-contracted Coulomb field of the electron bunch itself (Casalbuoni *et al.*, 2005a) or a sub-cycle, THz-frequency CTR pulse that the bunch generated (Berden *et al.*, 2007, 2004; Jamison *et al.*, 2003; Schmidt, 2006; Steffen *et al.*, 2009; Wilke *et al.*, 2002) into an optical signal of similar duration. The temporal envelope $|\vec{\mathcal{E}}(t)|$ of the bunch or CTR field approximates the bunch's longitudinal profile. The quasi-static $|\vec{\mathcal{E}}(t)|$ overlaps a time-synchronized, co-propagating optical probe pulse in a transparent EO crystal (*e.g.* ZnTe, GaP), and modulates the probe's polarization via the Pockels effect. A polarization analyzer filters out this modulated portion of the probe (see Fig. 18a), which carries information about the duration $\tau_{\mathcal{E}}$ and profile of the $|\vec{\mathcal{E}}(t)|$ impulse. Direct EO detection of the fields of LWFA bunches near the LWFA exit (where they are shortest) is challenging because of strong background signals from the drive laser and irradiated plasma. The CTR approach avoids this background by propagating a CTR THz pulse generated near the accelerator to remote detectors, and has been used for most EO measurements of LWFA bunch length.

Time resolution of EO measurements has been discussed extensively in the literature. A conceptually simple EO measurement of $|\vec{\mathcal{E}}(t)|$ would use a transform-limited probe pulse with duration $\tau_{pr}^{(0)} \lesssim \tau_{\mathcal{E}}$, then record intensity of the EO-modulated probe vs. probe-CTR delay Δt . This procedure maps $|\vec{\mathcal{E}}(t)|$ with resolution $\tau_{pr}^{(0)}$, but requires multiple shots. For single-shot EO measurements, (Sun *et al.*, 1998) *chirped* the probe to duration $\tau_{pr}(ch) > \tau_{\mathcal{E}}$, so that it overlapped the entire $|\vec{\mathcal{E}}(t)|$ profile. The THz field then encoded its waveform onto the probe spectrum (see Fig. 18a). Measurement of the modulated probe spectrum then decoded this waveform, but degraded resolution to $[\tau_{pr}^{(0)} \tau_{pr}(ch)]^{1/2}$, because the THz pulse modulated only a portion of the probe spectrum (Sun *et al.*, 1998). However, (Berden *et al.*, 2004) showed that by instead reconstructing the time-domain *field* of the EO-modulated probe using standard single-shot cross-correlation (Salin *et al.*, 1987), one could recover resolution $\sim \tau_{pr}^{(0)}$ in single-shot bunch profile measurements. They thereby recovered the profiles of ~ 275 fs RMS (650 fs FWHM), 50 MeV bunches from a radio-frequency accelerator with ~ 50 fs resolution. EO measurements of shorter LWFA bunches, however, encounter further limits from THz transverse optical phonon reso-

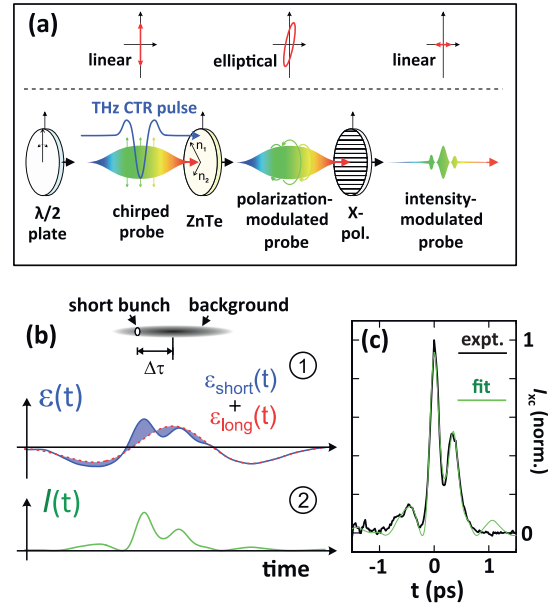


FIG. 18 Color online. Electro-optic (EO) bunch length measurement. (a) Schematic procedure. Below dashed line: THz CTR pulse $\vec{\mathcal{E}}(t)$ (solid curve) generated by, and approximating longitudinal profile of, subject electron bunch, co-propagates with time-synchronized, linearly-polarized, chirped optical probe pulse ($\lambda/2 =$ half-wave plate). Via Pockels effect, $\vec{\mathcal{E}}(t)$ modulates probe polarization in zinc telluride (ZnTe) crystal. Crossed polarization analyzer (X-pol) selects modulated component, which a photodetector, spectrometer, or cross-correlator then characterizes. Above dashed line: probe polarization at each stage of measurement. (b) Schematic depiction of (1) total CTR field profile $\mathcal{E}(t)$, and (2) corresponding intensity $I(t)$, from time-domain interference of CTR fields $\mathcal{E}_{short}(t)$, $\mathcal{E}_{long}(t)$ generated, respectively, by short 40 MeV bunch and trailing background electrons from LWFA, depicted left-propagating at top. (c) Experimental (thick black solid curve) and fitted (thin solid green curve) $I(t)$ profiles, measured by cross-correlator (xc). Panels b) and c) adapted from (Debus *et al.*, 2010a).

nances of common EO crystals (*e.g.* 5.3 THz for ZnTe, 11 THz for GaP), which absorb THz light and cause group-velocity walk-off of the THz signal from the optical probe. These effects can severely distort fs-duration profiles (Casalbuoni *et al.*, 2005a; Gallot *et al.*, 1999). By using thin (100-300 μm) ZnTe crystals, (van Tilborg *et al.*, 2006) minimized these distortions, and obtained an upper limit of ~ 50 fs RMS (120 fs FWHM) on LWFA bunch duration from a multi-shot EO measurement.

(Debus *et al.*, 2010a) reduced this upper limit further to 13 fs RMS (32 fs FWHM) in a *single-shot* EO measurement that took advantage of the CTR signal from a relatively long (0.71 ps) low-energy background electron bunch with thermal energy distribution ($kT_e = 6$ MeV) that emerged from a LWFA (45 fs, 0.5 J drive pulse, $\bar{n}_e = 1.5 \times 10^{19} \text{ cm}^{-3}$ plasma) along with the main quasi-monoenergetic $[40 \pm 7$ (RMS) MeV, ~ 30 pC] bunch.

At a CTR foil 5 mm downstream of the accelerator, the centroid of the background bunch trailed the main bunch by 0.36 ps, with its leading edge overlapping (see Fig. 18b, top). Consequently the two contributions to the CTR signal formed a time-domain interference pattern (Fig. 18b, bottom) that encoded the duration and phase of the ultrashort portion of the signal, and that a cross-correlator measured. (Debus *et al.*, 2010a) exploited the strong THz dispersion of the ZnTe crystal to re-shape the ultrashort CTR component in a way that enhanced visibility of the interference fringes. A theoretical fit (Fig. 18c, green curve) of the measured time-domain interference pattern (Fig. 18c, bold black curve) yielded the bunch duration cited above. This milestone notwithstanding, EO measurements remain limited by probe pulse bandwidth and by the accuracy with which EO crystal dispersion can be modeled. Thus they have provided only an upper limit on LWFA bunch duration.

c. Magneto-optic methods. MO methods convert the Lorentz-contracted *magnetic* field of a relativistic bunch into an optical signal via Faraday rotation. They differ from EO techniques in two key ways. First, since \vec{B} of a bunch is azimuthal (rather than radial), it is probed most effectively with a *transverse* (rather than co-propagating) probe. This is because Faraday rotation occurs when $\vec{k}_{pr} \parallel \vec{B}$ (Kaluza *et al.*, 2010). The transverse geometry, however, places stringent limits on probe pulse duration τ_{pr} , which must be $\lesssim \tau_b$ to avoid transit time broadening. Thus (Buck *et al.*, 2011) required ~ 6 fs probe pulses to resolve ~ 6 fs LWFA bunches. Secondly, Faraday rotation, unlike the Pockels effect, does not require a non-centrosymmetric crystal such as ZnTe. Faraday rotation can be observed in *any* transparent magnetized medium, including the plasma in which the wake propagates. Thus phonon resonances do not limit the time resolution of MO methods. Moreover, τ_b can be measured *inside* the plasma accelerator (Buck *et al.*, 2011). There, since polarization rotation angle $\Delta\phi_{rot} \propto Bn_e$, the largest rotation occurs in the bubble wall, the densest structure in the plasma, and, because of its proximity to the accelerating bunch, the most strongly magnetized. Changes in τ_b during acceleration can be tracked by changing probe delay over multiple shots (Buck *et al.*, 2011). In principle, MO methods could continue to track τ_b outside an LWFA, or to characterize the evolving structure of the bubble wall inside an LWFA. Since MO methods also serve as diagnostics of plasma accelerator *structures*, we discuss them in detail in Sec. IV.C.3 in conjunction with other transverse probes of such structures.

2. Frequency-domain methods

Spectral bunch length measurements are based on analyzing TR over a bandwidth that can extend from far infrared ($\lambda \sim 30\mu\text{m}$) to ultraviolet ($\lambda \sim 0.3\mu\text{m}$), including both coherent and incoherent emission (see Fig. 19). In principle, spectral methods can measure bunch length practically anywhere along an electron beam line with sub-fs resolution in a single shot, while disturbing the beam minimally. The principal challenges lie in calibrating TR spectral intensity accurately and with high spectral resolution over a wide wavelength and dynamic range, and in solving the difficult inverse problem of retrieving a (sometimes complicated) bunch profile uniquely from spectral intensity measurements. Bunches whose shortest features are of duration $\tau_b \gtrsim 100$ fs generate TR predominantly at far-IR wavelengths ($\lambda \gtrsim c\tau_b \sim 30\mu\text{m}$), a range where sensitive detectors with high spectral resolution are lacking. Time-domain EO methods are thus superior in this τ_b range (see Fig. 19). On the other hand, bunches with $\tau_b \lesssim 10$ fs – *i.e.* those from strongly nonlinear LWFAs – can be accurately characterized via their mid-IR to UV TR, a range that is amenable to broad-band, high-resolution spectral detection.

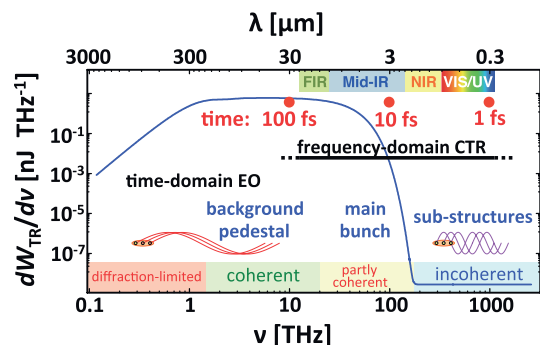


FIG. 19 Color online. Overview of time and spectral scales for *single-shot* profiling of longitudinal LWFA bunch profile, including (right to left) sub-structures, main bunch profile, and background pedestal. Solid blue curve: TR spectrum of 200 MeV, 20 pC (Gaussian) bunch with $\tau_b = 10$ fs (FWHM). Horizontal black lines: ranges best suited for time-domain EO (left) and frequency-domain CTR (right) techniques.

(Leemans *et al.*, 2003) first observed terahertz CTR from LWFA bunches. (Ohkubo *et al.*, 2007) first attempted to deduce the *duration* of these bunches from CTR spectra. Bolometer measurements at 5 discrete far-IR wavelengths on separate shots indicated a cutoff corresponding to $\tau_b \sim 130$ fs. However, the CTR foil was 180 mm downstream of the LWFA, far enough that the bunch not only elongated, but diverged sufficiently during transport to degrade transverse TR coherence. Hence the result may not have accurately reflected τ_b near the LWFA exit. Subsequent experiments have placed the CTR foil closer, often employing movable tape to remove

foil damaged by the LWFA drive pulse after each shot.

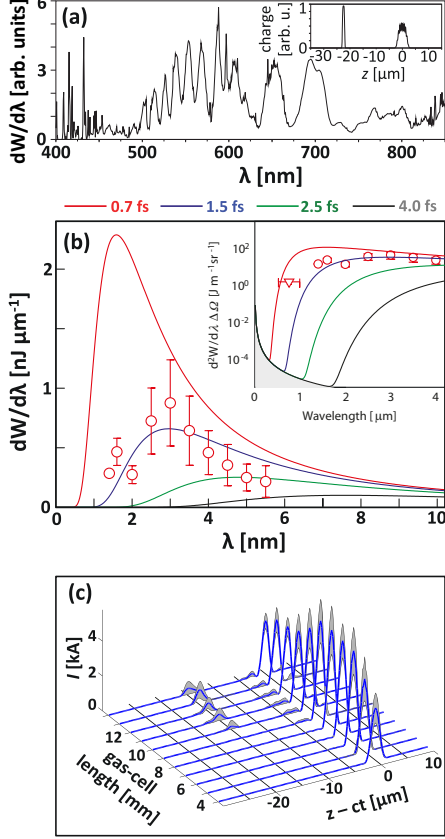


FIG. 20 Color online. CTR spectra of electron bunches from strongly nonlinear LWFA, and longitudinal bunch profile reconstruction. (a) Single-octave CTR power spectrum with periodic modulations, originating from electron bunches separated longitudinally by $\sim \lambda_p$, as shown in inset. Adapted from (Glinec *et al.*, 2007). (b) Three-octave CTR spectrum of electron bunches injected into strongly nonlinear LWFA by colliding laser pulses, recorded by IR-monochromator (circles) and visible spectrometer (triangle). Solid curves: calculated CTR spectra for indicated bunch durations, assuming Gaussian profiles. Inset: Data divided by solid angle of solid collection angle of detection instrument. Grey area: ITR intensity. Adapted from (Lundh *et al.*, 2011). (c) Longitudinal profiles (solid blue curves) of bunches from LWFA driven in gas cell of adjustable length (3 – 14mm), reconstructed from four-octave single-shot CTR spectra. Grey band around each curve indicates variance over 30-shot data set. Panel c) adapted from (Heigoldt *et al.*, 2015).

(Glinec *et al.*, 2007), used a foil placed only 1.5 mm beyond a quasi-monoenergetic LWFA, and spectrally analyzed CTR in a single shot over a range $400 < \lambda < 850$ nm (see Fig. 20a). This ~ 1 -octave bandwidth was too narrow to resolve τ_b , or internal bunch structure. However, (Glinec *et al.*, 2007) observed strong frequency-domain interference fringes (discussed further in Sec. IV.B.2) with period $\Delta\omega = (\Delta t)^{-1}$, consistent with CTR from two sources separated longitudinally by $\Delta t = 74$ fs. A model of the CTR spectra suggested that

these sources were a ~ 10 fs bunch in the first wakefield bucket, followed by a few-fs bunch – or one with substructure on this scale – in the second (see Fig. 20a, inset). Later (Lundh *et al.*, 2013) used similar spectral interference fringes to diagnose bunch distribution among multiple buckets.

(Lundh *et al.*, 2011) analyzed CTR and ITR spectra from a foil 15 mm downstream of a quasi-monoenergetic (85 MeV) LWFA over a 3.3-octave range extending from mid-IR ($\lambda = 5.5 \mu\text{m}$) to visible ($\lambda = 0.55 \mu\text{m}$) wavelengths (see Fig. 20b). They combined an optical spectrometer with an infrared monochromator that could only acquire the IR portion of the spectra over multiple shots. Nevertheless, a fit based on Eq. (39) to the measured TR spectra, which exhibited a coherent threshold at $\lambda \approx 1 \mu\text{m}$, yielded a most probable ensemble duration 1.4 - 1.8 fs (RMS). The researchers could not determine whether this was the duration of the entire bunch or the shortest feature in a longer bunch, nor whether their use of colliding optical pulse injection influenced the bunch duration. Nevertheless, this remains the shortest τ_b reported from a LWFA.

(Bajlekov *et al.*, 2013) and (Heigoldt *et al.*, 2015) demonstrated the first *single-shot* high-resolution spectroscopic bunch length measurements by distributing > 4 octaves of CTR bandwidth amongst visible (0.4 – 1.1 μm), near-IR (1.1 – 1.8 μm) and mid-IR (1.7 – 7.1 μm) spectrometers. In these experiments, a ~ 50 TW laser pulse drove a nonlinear LWFA in $\bar{n}_e = 3.9 \times 10^{19} \text{ cm}^{-3}$ plasma in a cell that tuned in length L from 3 to 14 mm in 1 mm increments. As L increased from 3 mm, (Heigoldt *et al.*, 2015) observed electron energy increased to a maximum ~ 650 MeV at $L = 9$ mm, consistent with the pump depletion length L_{pd} . For $L < 9$ mm, they observed smooth CTR spectral profiles, and correspondingly reconstructed longitudinal charge profiles $\rho_{||}(t)$ consisting of single bunches of duration 5 fs (FWHM) (see Fig. 20c). For $L > 9$ mm, on the other hand, they observed CTR spectra that were modulated at a single dominant frequency (as in Fig. 20a). Correspondingly, the reconstructed $\rho_{||}(t)$ included an additional bunch trailing by $\Delta t \approx 50$ fs (Fig. 20c), slightly less than a plasma period ($2\pi/\omega_p = 56$ fs). As \bar{n}_e changed, Δt tracked, but remained less than, $2\pi/\omega_p$. The authors conjectured that the trailing bunch was injected within the first LWFA cavity in response to a transition from LWFA to beam-driven PWFA starting at $L \approx L_{pd}$. Indeed, such tunable bunch pairs are of interest as drive-witness pairs for tabletop PWFAs, of interest in turn for compact electron acceleration free of dephasing. These results demonstrate the ability of multi-octave-bandwidth CTR to reconstruct $\rho_{||}(t)$ simultaneously on the few-fs scale of a single bunch and the tens-of-fs scale of separated bunches. They also demonstrate quantitative diagnosis of bunch evolution with propagation through a LWFA.

In general, all CTR spectral intensity measurements

described above diagnose electron bunch profiles indirectly. As discussed in Sec. III.A.4, these yield the *magnitude* $|F_{\parallel}(\omega, \theta)|$ of the form factor via Eq. (35), but not its spectral *phase*, which is required to extract $\rho_{\parallel}(z)$ directly via Eq. (34). In principle, the spectral phase of F_{\parallel} could be determined from the spectral phase of the CTR field (via Eq. (39)), measured *e.g.* by CTR interferometry. However, this has so far proven impractical to do with high resolution over a multi-octave bandwidth. Hence the inverse problem of reconstructing $\rho_{\parallel}(z)$ from CTR spectra is ill-posed, analogous to determining the structure of a molecule from a diffraction pattern generated by coherent x-rays. Iterative algorithms — see (Bajlekov *et al.*, 2013; Bakkali Taheri *et al.*, 2016; Heigoldt *et al.*, 2015) and references therein — are used to reconstruct $\rho_{\parallel}(z)$ — subject to physical constraints — from spectral intensity measurements alone. Briefly, most reconstruction algorithms are variants of the following approach: one starts with an initial guess $\rho_{\parallel}^{(0)}(z)$, calculates its complex Fourier transform $|G(k)| \exp[i\psi(k)]$, then replaces the amplitude $|G(k)|$ with the experimental $|F_{\parallel}(k)|$. An inverse Fourier transform then yields a revised estimate $\tilde{\rho}_{\parallel}^{(0)}(z)$. Finally, one forcibly adjusts $\tilde{\rho}_{\parallel}^{(0)}(z)$ to satisfy physical constraints — *e.g.* it must be real, positive-definite, and non-zero only within a realistic temporal range — yielding $\rho_{\parallel}^{(1)}(z)$, to complete the first iteration. One then re-iterates until, hopefully, the solution converges. Challenges include ensuring convergence, demonstrating uniqueness, and quantifying uncertainty of the result based on uncertainties of measured inputs. As with many inverse-problems, simply searching for one “needle” — *i.e.* a best fit to available data — in a figurative haystack of possibilities is not enough. One must exhaust a sizable portion of the haystack to ensure there is only one, or no, needle left (Tarantola, 2006).

Current bunch profile reconstruction algorithms solve a 1D problem of reconstructing $\rho_{\parallel}(z)$ from Ω -integrated CTR power spectra. Expanding retrieval algorithms and CTR spectral data to 2 and 3 dimensions, analogous to x-ray scattering from molecules, will be an important future direction. Adding an angular dimension to spectral data not only enables simultaneous access to $\rho_{\perp}(\vec{r}_{\perp})$, but can reduce ambiguities in reconstructed $\rho_{\parallel}(\vec{r}_{\parallel})$ that are fundamental in the corresponding 1D problem. Diffraction radiation (DR) from bunches passing through non-interceptive slits and apertures adds such a dimension (Karlovetz and Potylitsyn, 2008), and has led to reconstructions of transverse and longitudinal profiles of \sim ps bunches that benchmark successfully with independent diagnostics (Castellano *et al.*, 2001; Fiorito, 2001). Its non-invasiveness is especially attractive for $\sim\mu\text{m}$ -scale LWFA bunches. DR thus appears ripe for extension to few-fs LWFA bunches, but will require small apertures to avoid short-wavelength/short-time-scale cutoffs, and hence good pointing stability. Sim-

ilar remarks apply to Smith-Purcell radiation, emitted when a relativistic beam passes over a grating — *i.e.* a regular array of diffractive radiators placed within a vacuum formation length (Brownell *et al.*, 1998; Karlovets and Potylitsyn, 2006; Kesar, 2010; Smith and Purcell, 1953). The freedom to tailor grating dimension, spacing, blazing angle, groove shape and material to a specific wavelength/time-scale range makes Smith-Purcell radiation a versatile bunch length diagnostic. Indeed, the RF-accelerator community has demonstrated Smith-Purcell bunch length measurement down to sub-ps (Andrews *et al.*, 2014a,b; Blackmore *et al.*, 2009; Korbly *et al.*, 2006), even few-fs (Bartolini *et al.*, 2012) resolution. Extending these methods to plasma-accelerated beams should have high priority in future research.

IV. DIAGNOSTICS OF PLASMA ACCELERATOR STRUCTURES

Diagnostics of electron and positron beams only indirectly characterize the plasma structure that captured and accelerated them. Beam diagnostics alone rarely pinpoint the cause of sub-optimal performance, or provide clear guidance on corrective action. Direct observation of the plasma structure in the laboratory, and comparison of laboratory images with simulations, then become essential. This is challenging for four reasons:

(i) The structures are microscopic. For the \bar{n}_e range of interest for particle acceleration (see Sec. II.A.4) accelerator cavities have overall dimension $100\mu\text{m} \gtrsim \lambda_p \gtrsim 10\mu\text{m}$. Moreover, nonlinear wakes possess sharp micron-scale sub-structures (see Fig. 1). Diagnostic probes must resolve these spatial scales.

(ii) The structures have low optical contrast, for wavelengths $\lambda \ll \lambda_p$ that resolve structural details. For example, for a $\lambda = 1\mu\text{m}$ optical probe, an evacuated “bubble” in $\bar{n}_e = 10^{18} \text{ cm}^{-3}$ plasma differs in refractive index by only $\Delta n \approx n_e/2n_{cr} = .0005$ from surrounding plasma.

(iii) The structures propagate at $\sim c$ over mm to meter distances. To minimize image blurring, a probe should co-propagate with the structure. However, even if temporal slip between probe and wake is negligible, wakes can evolve on a ps time scale in ways that are important to diagnose. A co-propagating probe integrates over this evolution. Thus diagnostics must combine longitudinal and transverse probing.

(iv) The structures are transient, and prone to shot-to-shot variation. Single-shot probes are desirable.

These challenges have no counterpart in conventional RF acceleration, which uses macroscopic, stationary, permanent structures. This section reviews plasma wake diagnostics and results that have emerged uniquely with development of plasma-based electron accelerators. They address the above challenges using wide bandwidth op-

TABLE II Properties of plasma wakes, and methods developed to diagnose them. Key to wake properties: Plasma frequency (ω_p), wave-vector (\vec{k}_p), wavelength (λ_p); $\delta n_e(z, \zeta, r) =$ wake electron density profile as function of driver propagation distance (z), distance behind driver (ζ), and distance r from propagation axis; $\vec{E}(\zeta, r) =$ wake electric field profile. In column 3, the probe is described as optical (o) or electron (e); propagating longitudinally (L), transversely (T), or obliquely (O) to \vec{k}_p ; having duration much less than (\ll), less than ($<$), similar to (\approx), or greater than ($>$) a plasma period τ_p ; and diagnosing the wake in single- (s) or multi- (m) shot.

Wake property	Diagnostic method	Probe properties	See Section...
wave-breaking, sheath dynamics	light emission ^a	n/a	IV.A.1
global $\omega_p, \vec{k}_p, \delta n_e(\zeta)$	CTS ^b	o, L or T, $>$, s or m	IV.A.2
quasi-static sub- λ_p	FDI ^c	o, L, $<$, m	IV.B.2
$\delta n_e(\zeta, r)$ structures	FDH ^d , FDS ^e Faraday rotation ^f transverse shadowgraphy ^g	o, L, $>$, s o, T, \ll , s o, T, \ll , s	IV.C.1,2 IV.C.3.a IV.C.3.b
evolving sub- λ_p structures	shadowgraphic movies ^h FDSC ⁱ , FDT ^j MOPI ^k	o, T, \ll , m o, O, $>$, s o, O, $<$, m	IV.D.1 IV.D.2 IV.D.3
quasi-static sub- λ_p profiles	delayed witness bunch ^l transverse radiography ^m longitudinal radiography ⁿ	e, L, $<$, m e, T, \ll , s e, L, \approx , s	IV.B.1 IV.C.4 IV.C.4

^a (Hamster *et al.*, 1994; Helle *et al.*, 2010; Thomas *et al.*, 2007)

^b Collective Thomson Scattering (Clayton, 2009)

^c Frequency-Domain Interferometry (Marquès *et al.*, 1997; Siders *et al.*, 1996b)

^d Frequency-Domain Holography (Matlis *et al.*, 2006)

^e Frequency-Domain Shadowgraphy (Dong *et al.*, 2010b)

^f (Kaluza *et al.*, 2010)

^g (Buck *et al.*, 2011)

^h (Sävert *et al.*, 2015)

ⁱ Frequency-Domain Streak Camera (Li *et al.*, 2014a)

^j Frequency-Domain Tomography (Li *et al.*, 2014b)

^k Multi-Object-Plane Imaging (Li *et al.*, 2013b)

^l Applied to PWFA (Kallos *et al.*, 2008; Rosenzweig *et al.*, 1989) (Zhang *et al.*, 2017)

ⁿ Applied to PWFA (Clayton *et al.*, 2016)

tical probe pulses or ultrashort electron witness bunches that are temporally synchronized with the wake structure. The earliest diagnostics detected wakes globally, without resolving internal structure (Sec. IV.A). Sub- λ_p resolution initially came at the cost of multi-shot probing, and integrating over wake evolution (Sec. IV.B). Development of holistic, single-shot probes that resolve internal wake structure and dynamics is a more recent, and ongoing, field of research (Secs. IV.C, IV.D). Examples of quantitative comparison of diagnostic measurements with simulation results are described throughout. (Clayton, 2009) previously reviewed several early LWFA structure diagnostics. Here we complement that review, and emphasize new developments since then.

A. Light emission and scattering from plasma waves

1. Plasma self-emission

Just as electromagnetic radiation from plasma-accelerated electrons (Sec. III.A) underlies multifarious beam diagnostics (Secs. III.B.3, III.C.2, III.C.3, III.D), electromagnetic emission from the plasma wave itself helps to diagnose wake structure and dynamics. (Hamster *et al.*, 1994, 1993) first detected laser wakefields by observing far-infrared radiation (FIR) that they emit, using a liquid-helium-cooled bolometer in conjunction with a Fourier transform spectrometer. As \bar{n}_e changed from $\sim 10^{15}$ to $\sim 10^{19}$ cm⁻³, FIR frequency closely tracked ω_p in the few-THz range where it was measurable, while FIR intensity peaked at the resonant condition, which the authors defined as $\omega_p \tau = 2$, corresponding to $\bar{n}_e \approx 7 \times 10^{16}$ cm⁻³ and laser pulse duration $\tau = 120$ fs. This showed that the FIR originated from collective charge density oscillations of a standard LWFA (see Sec. II.B.1). The observed time duration and angular distribution of FIR qualitatively diagnosed the wake's lifetime and 3D structure, respectively.

In strongly nonlinear wakes, light emission is useful for diagnosing ultrafast, small-scale phenomena beyond the resolution of impinging probe pulses. One example is “wave-breaking” radiation (Thomas, 2010; Thomas *et al.*, 2007), a broadband light flash accompanying electron injection into a plasma bubble. Used in conjunction with transverse optical probes, it can pinpoint injection spatially and temporally within the larger wake formation and acceleration process. Fig. 35 and accompanying text (Sec. IV.D.1) will show an example. A second example is radiation emitted at the second-harmonic of the drive pulse frequency from the ultra-thin electron sheath surrounding a plasma bubble (see Fig. 1b-d). Here the source current is contained within a region smaller than the emitted wavelength, while fulfilling a Cherenkov-angle condition for the laser second-harmonic (Gordon *et al.*, 2008). The resulting electro-optic shock is emitted in a characteristic ring pattern (Helle *et al.*, 2010).

The distinctive spectral, angular and temporal features of wake self-emission have potential to become quantitative diagnostics with advances in simulation capabilities. Recent work aims to calculate quantitative features of observed emission, such as angle- and time-resolved spectra, within PIC simulations, taking into account all simulated particles (Pausch *et al.*, 2014a,b).

2. Light scattering

Among the earliest diagnostics of plasma accelerator structures were experiments that scattered probe pulses of duration $\tau_{pr} \gg \omega_p^{-1}$ from laser-driven electron plasma waves (EPWs). The theory (Froula *et al.*, 2011) and ex-

perimental approach (Clayton, 2009; Villeneuve *et al.*, 1991) resemble those for light scattering from ultrasonic waves in transparent media (Born and Wolf, 1980). In these experiments, a probe pulse of frequency $\omega_{pr} \gg \omega_p$ and wave vector of magnitude $|\vec{k}_{pr}| \gg |\vec{k}_p|$ impinged on a plasma wave (frequency ω_p , wave-vector \vec{k}_p) either collinearly ($\vec{k}_{pr} \parallel \vec{k}_p$), transversely ($\vec{k}_{pr} \perp \vec{k}_p$) or obliquely. Uncorrelated individual plasma electrons scatter probe light at frequency ω_{pr} in a dipole pattern, due to their individual light-driven oscillatory motion, a process known as linear Thomson scattering (Jackson, 1999). However, a collective electron density oscillation $\delta n_e(\vec{x}, t)$ driven above the level of thermal fluctuations — *i.e.* $k_p \lambda_D < 1$, where λ_D is the plasma Debye length (Froula *et al.*, 2011) — appears to the probe as a refractive index grating

$$\begin{aligned} \eta(\vec{x}, t) - \eta_0 &= \{1 - [\bar{n}_e + \delta n_e(\vec{x}, t)]/n_{cr}\}^{1/2} - \eta_0 \\ &\approx \delta n_e(\vec{x}, t)/2n_{cr} \end{aligned} \quad (43)$$

moving at phase velocity $\omega_p/|\vec{k}_p|$. Here, $\eta_0 = [1 - \bar{n}_e/n_{cr}]^{1/2}$ is the refractive index of unperturbed plasma, and the second line is valid for $\omega_{pr} \gg \omega_p$. This grating imprints a moving sinusoidal phase-modulation on the probe, resulting in scattered light at frequency $\omega_{pr} \pm \omega_p$ and wave vectors $\vec{k}_{pr} \pm \vec{k}_p$, over and above the linear Thomson scattering background. This is known as linear *collective* Thomson scatter (CTS) (Slusher and Surko, 1980; Villeneuve *et al.*, 1991). For $\tau_{pr} \gg \omega_p^{-1}$, the probe bandwidth can be much less than ω_p . If so, the CTS spectrum consists of discrete Stokes/anti-Stokes sidebands well outside the incident probe bandwidth, making it easily distinguishable in a spectrometer from background Thomson-scattered probe light. Moreover in the same limit, a *collimated* probe has wave-vector spread much smaller than $|\vec{k}_p|$. When such a probe interacts transversely with an EPW, CTS light scatters at discrete angles $\theta \approx |\vec{k}_p|/|\vec{k}_{pr}|$ (typically a few degrees) from \hat{k}_{pr} , well outside the transmitted probe diffraction cone, providing additional spatial discrimination. Thus frequencies $\omega_{pr} \pm \omega_p$ and wave-vectors $\vec{k}_{pr} \pm \vec{k}_p$ of CTS light are the main observables. Analysis yields the frequency ω_p , wave vector \vec{k}_p , and local amplitude δn_e of the EPW. When τ_{pr} is less than the EPW lifetime, the time evolution of δn_e behind the driver can also be measured by varying pump-probe delay Δt (Le Blanc *et al.*, 1996; Ting *et al.*, 1996). Nonlinear EPWs generate harmonics $\pm m\omega_p$ ($\pm m\vec{k}_p$), where $m = 1, 2, 3, \dots$, of the frequency-(wave-vector) shift of scattered light as an additional diagnostic (Everett *et al.*, 1995). When one or more harmonics is (are) present, analysis of harmonic *ratios* (Lal *et al.*, 1997) enables more accurate estimates of absolute δn_e than estimates based on $m = \pm 1$ sidebands alone, which are subject to uncertainties in estimating propagation distance and transverse dimension of the EPW. Light scattering experiments, however, do not resolve internal sub- λ_p structure of the EPW. (Clayton, 2009) has

reviewed light scattering from plasma accelerator structures in detail. Thus here we only discuss two examples.

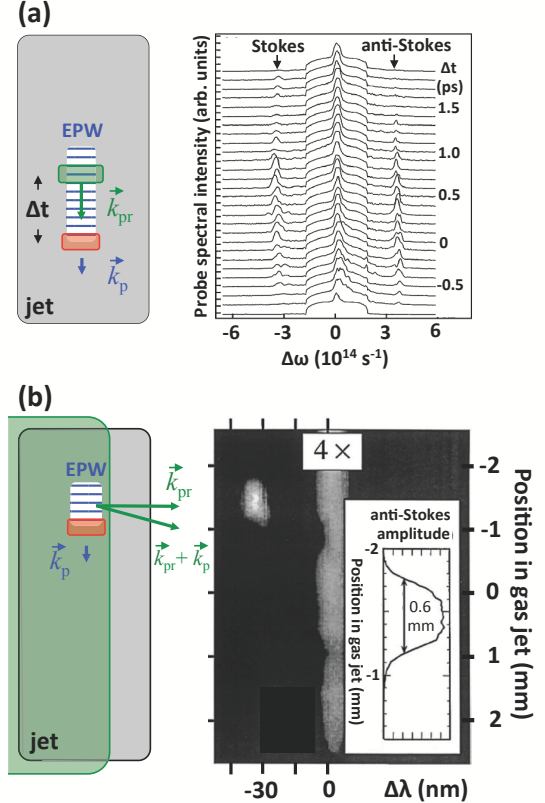


FIG. 21 Color online. Collective Thomson scatter from self-modulated LWFA. (a) Left: schematic of EPW (blue rectangle with horizontal lines denoting wave peaks, wave-vector \vec{k}_p) in He jet (large grey rectangle, ionized to $\bar{n}_e = 3 \times 10^{19} \text{ cm}^{-3}$), with probe pulse (green rectangle, wave-vector \vec{k}_{pr} , $\tau_{pr} = 0.4$ ps) *co-propagating* top to bottom at delay Δt behind drive pulse (red rectangle at front of EPW). Right: probe pulse spectra for $-1 \text{ ps} < \Delta t < 2 \text{ ps}$ showing growth and decay of Stokes and anti-Stokes sidebands at $\Delta\omega = \mp\omega_p$, acquired over multiple shots. Adapted from (Le Blanc *et al.*, 1996). (b) Left: same as (a), but with 20 ps, loosely focused ($w_0 \approx 5$ mm) probe pulse (large green rectangle) illuminating entire length of jet, propagating *transversely* to drive pulse. Right: space-resolved spectrum of anti-Stokes ($\Delta\lambda = -35$ nm) light scattered in direction $\vec{k}_{pr} + \vec{k}_p$ ($3.4^\circ \pm 1.9^\circ$ from \vec{k}_{pr}) from EPW localized at $-2 \text{ mm} < z < -1 \text{ mm}$, acquired in one shot along with background unshifted probe light ($\Delta\lambda = 0$, attenuated 4 \times). Inset: z -lineout of anti-Stokes scattered light, and thus of EPW amplitude. Panel b) adapted from (Gordon *et al.*, 1998).

Figure 21a (left) schematically illustrates experiments by (Le Blanc *et al.*, 1996; Ting *et al.*, 1996) in which a sub-ps probe pulse ($\lambda_{pr} = 0.53 \mu\text{m}$, green rectangle) *co-propagated* at delay Δt behind a drive pulse (peak power $P = 1 - 2$ TW, $\tau = 0.4$ ps, $\lambda_{pu} = 1.053 \mu\text{m}$, red rectangle) in a gas jet (grey) that the drive pulse ionized to density $0.75 \times 10^{18} \text{ cm}^{-3} < \bar{n}_e < 3 \times 10^{18} \text{ cm}^{-3}$ (Le Blanc

et al., 1996) or $\bar{n}_e \approx 10^{19} \text{ cm}^{-3}$ (Ting *et al.*, 1996). When P exceeded the critical power $P_{cr} = 17(\omega^2/\omega_p^2)$ GW for relativistic self-focusing, the drive pulse efficiently drove a self-modulated (SM) LWFA (blue rectangle, see Sec. II.B.2). Under conditions of (Le Blanc *et al.*, 1996), the wake produced a strong collimated ~ 2 MeV electron beam (Umstadter *et al.*, 1996). In both experiments, the probe pulse overlapped 10-20 periods of this wake. A spectrometer, aided by a notch filter, isolated and recorded spectra of the transmitted wake-modulated probe as Δt varied over multiple shots. Results showed Δt -dependent Stokes and anti-Stokes sidebands (Fig. 21a, right), with amplitudes proportional to $\delta n_e(\Delta t)$. Using this data, (Le Blanc *et al.*, 1996) measured EPW *growth* rate: sidebands appeared at $\Delta t \approx -0.5$ ps, then grew to a maximum corresponding to $\delta n_e/\bar{n}_e \sim 0.1$ at $\Delta t \approx 0.3$ ps. This wake, however, started earlier, and grew more slowly, than a 2D theory of forward Raman scattering instability in uniform pre-formed plasma predicted (Decker *et al.*, 1996; Tzeng *et al.*, 1996). (Le Blanc *et al.*, 1996) thus concluded that plasma noise generated at the ionization front ($\Delta t \approx -0.7$ ps) seeded the instability earlier than expected, and that a 3D theory (Andreev *et al.*, 1995; Esarey *et al.*, 1994) was required to explain its growth.

Both (Le Blanc *et al.*, 1996) and (Ting *et al.*, 1996) measured EPW *decay* rate, with different results. (Le Blanc *et al.*, 1996) found that sidebands (and thus δn_e) decayed to undetectable levels within 1.5 ps (Fig. 21a, right). They attributed the rapid decay to efficient conversion of collective EPW energy into electron beam energy. (Ting *et al.*, 1996), on the other hand, working at higher \bar{n}_e with less efficient electron beam production, found that probe sidebands persisted out to $\Delta t \approx 5 - 7$ ps. They explained the slower decay rate via conversion of the EPW into ion acoustic waves (IAWs), a subject of considerable prior theoretical work (Mora *et al.*, 1988; Zakharov, 1972). They confirmed this by observing a sharp increase in scatter of the *central* probe spectral peak at angle $\sim 30^\circ$ from the pump-probe propagation axis over time interval $5 \lesssim \Delta t \lesssim 30$ ps, correlated with decay of Stokes/anti-Stokes sidebands. They attributed this rising signal to CTS from growing EPW-fed, slow IAWs, which they observed to decay subsequently over $30 \text{ ps} \lesssim \Delta t \lesssim 100 \text{ ps}$. The physics of EPW \rightarrow IAW conversion is re-surfacing in recent theoretical (Lotov *et al.*, 2014; Sahai *et al.*, 2016) and experimental (Zgadaj *et al.*, 2016) wake diagnostic work because it is a strong plasma heating mechanism (see Sec. IV.D.3).

(Filip *et al.*, 2004) collinearly probed PBWAs (see Sec. ??) driven by a 2-color CO₂ laser in plasma of density $10^{16} \text{ cm}^{-3} \lesssim \bar{n}_e \lesssim 10^{17} \text{ cm}^{-3}$. At such low \bar{n}_e , special techniques were required to distinguish Stokes, anti-Stokes sidebands from the unshifted probe spectrum (Filip *et al.*, 2003). CTS showed that high δn_e wakes were achievable even when the beat frequency was far from

ω_p . With emergence of TW, ps CO₂ lasers (Polyanskiy *et al.*, 2015), researchers are now also beginning to probe CO₂-laser-driven SM-LWFAs, first studied theoretically by (Andreev *et al.*, 2003), using collinear CTS.

Figure 21b (left) schematically illustrates a complementary “transverse” CTS geometry in which a probe pulse crossed the path of a EPW of transverse width $\lesssim \lambda_p$ at $\sim 90^\circ$ (*i.e.* $\vec{k}_{pr} \perp \vec{k}_p$). This geometry has characterized PBWAs (Clayton *et al.*, 1993) and decay of laser-driven EPWs into a manifold of daughter waves (Everett *et al.*, 1995). Fig. 21b (right) shows an example of transverse CTS data (Gordon *et al.*, 1998) from a SM-LWFA that produced copious collimated electrons up to 94 MeV energy when driven in $\bar{n}_e = 1.4 \times 10^{19} \text{ cm}^{-3}$ plasma by tightly focused drive pulses of similar wavelength and duration ($\lambda = 1.053 \mu\text{m}$, $\tau = 1$ ps), but higher power ($P \approx 20$ TW), than those used in the experiments of (Le Blanc *et al.*, 1996; Ting *et al.*, 1996). The duration ($\tau_{pr} \approx 20$ ps) and radius ($w_0 \approx 0.5$ cm) of the transverse probe pulse ($\lambda_{pr} = 0.53 \mu\text{m}$) were adjusted so that it illuminated the wake during its entire transit through the ~ 0.1 cm long gas jet. (Gordon *et al.*, 1998) used anti-Stokes ($\Delta\lambda \approx -35$ nm) light scattered at $\vec{k}_{pr} + \vec{k}_p$ ($\sim 3.4^\circ$ from \vec{k}_{pr}) to image the EPW propagation path onto the slit of an imaging spectrometer. In Fig. 21b (right), this anti-Stokes image is visible at $\Delta\lambda \approx -35$ nm, from only a ~ 1 mm section ($-2 \text{ mm} < z < -1 \text{ mm}$) of the gas jet, along with background unshifted probe light ($\Delta\lambda = 0$) that scattered from the jet’s entire length. This showed that the wake had significant amplitude only in this 1mm section, because of tight pump focus there. For looser pump foci, on other other hand, wakes persisted for longer distances (up to the entire jet), but yielded lower energy electrons. Transverse CTS provides this information about the wake’s trajectory in a *single shot*, information unavailable from co-propagating CTS because it integrates over the main pulse’s propagation direction. The complementarity of diagnostic information available from co-propagating (Sec. IV.B, C.1,2) vs. transverse (or oblique) probes (Sec. IV.C.3,4, D,E) is a recurring theme throughout the remainder of this section.

B. Multi-shot sub- λ_p probes

Optical diagnosis of sub- λ_p structure of plasma accelerators requires probes of bandwidth $\Delta\omega_{pr} > \omega_p$. This precludes CTS, since Stokes and anti-Stokes shifts would be less than $\Delta\omega_{pr}$. In this sub-section, we describe experiments in which optical *or electron* probes of duration $\tau_{pr} < \omega_p^{-1}$ co-propagate behind the wake driver with controlled time delay Δt . The probe overlaps a sub- λ_p longitudinal slice of the structure, which modifies the probe. Photon frequency or electron energy analysis, or optical interferometry detects these modifications. In addition, the wake’s transverse fields or density gradients deflect

probe electrons or photons sideways. These transverse probe profile modifications are also detected downstream of the accelerator. Thus by varying Δt over multiple shots, these methods can map out both longitudinal and transverse wake structures with sub- λ_p resolution, if the structure is stable from shot to shot. The co-propagating geometry also maximizes the probe's interaction length with the slice of the structure that it overlaps, thus optimizing sensitivity to low-contrast sub-structures.

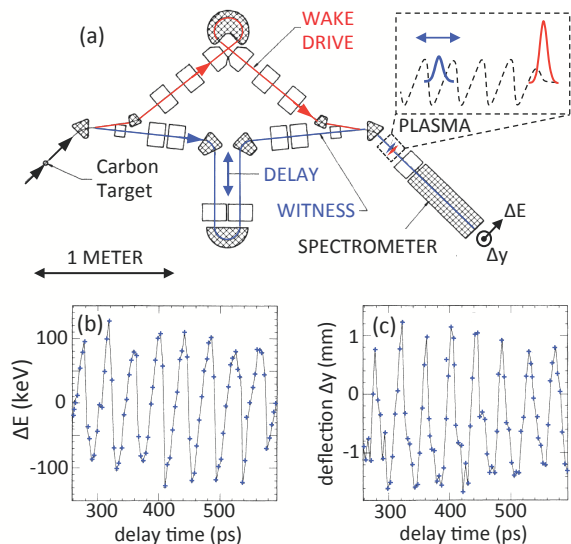


FIG. 22 Color online. Measurements of local electric field $\vec{E}(r, z - ct)$ of e-bunch-generated nonlinear plasma wave in $\bar{n}_e = 0.7 \times 10^{13} \text{ cm}^{-3}$ plasma. (a) Schematic experimental setup. Carbon target decreased energy of part of incoming 21 MeV electron drive bunches (left) to create 15 MeV witness bunch, which dipole magnets (cross-hatched boxes) separated, guided through paths of variable relative length, and recombined collinearly with controlled time delay Δt . Upper right inset: schematic of plasma wave potential (dashed curve) and right-propagating drive (solid red, right) and witness (solid blue, left) bunches. Adapted from (Rosenzweig *et al.*, 1988). (b) Energy change ΔE and (c) transverse deflection Δy perpendicular to energy dispersion plane of witness bunch vs. Δt . Panels b) and c) adapted from (Rosenzweig *et al.*, 1989).

1. Electron witness bunches

Beam-driven PWFAs (Chen *et al.*, 1985) were not only the first plasma-based electron accelerators to be demonstrated in the laboratory, but the first to be spatially and temporally diagnosed. The Advanced Accelerator Test Facility at Argonne National Laboratory (ANL) measured wake fields of an electron drive bunch ($E_e = 21 \text{ MeV}$, $2 \text{ nC} \leq Q \leq 4 \text{ nC}$, $\tau_b = 16 \text{ ps}$) through their effect on a 15 MeV “witness” bunch created by degrading the energy of part of the drive bunches with a carbon target, and splitting them away with a dipole magnet. Separate beam transport lines delivered the two synchro-

nized bunches collinearly to the plasma, the witness leg containing an adjustable “trombone” section that varied witness delay Δt (see Fig. 22a). A dipole magnet spectrometer after the plasma measured witness bunch energy with $\sim .01 \text{ MeV}$ resolution, and transverse witness bunch deflection perpendicular to the spectrometer dispersion plane, as Δt varied. (Rosenzweig *et al.*, 1988, 1989) used this facility to drive and probe wakes in $\sim 30 \text{ cm}$ -long plasma of density $\bar{n}_e \approx 10^{13} \text{ cm}^{-3}$. Available bunch duration $\tau_b \sim 16 \text{ ps}$ (FWHM) dictated this choice of \bar{n}_e , which enabled these bunches to resonantly drive and resolve individual plasma oscillations of period $\omega_p^{-1} \sim 30 \text{ ps}$ (see Fig. 22b,c).

Initial experiments drove the plasma with 2 nC bunches of longitudinal (s) and radial (r) half-widths $\sigma_s \approx \sigma_r \approx 2.1 \text{ mm}$, yielding bunch density $n_b \approx .015\bar{n}_e$ (Rosenzweig *et al.*, 1988). Since $n_b \ll \bar{n}_e$, these excited linear wakes with accelerating field $E_z^{(max)} \ll E_0 \sim 300 \text{ MV/m}$ (see Eq. 4a) and density perturbation $\delta n_e \ll \bar{n}_e$ (Lu *et al.*, 2005). These wakes modulated witness bunch centroid energy E_e sinusoidally as a function of Δt , with amplitude $\Delta E_e^{(max)} \approx \pm .05 \text{ MeV}$. The quotient of $\Delta E_e^{(max)}$ and acceleration length yielded effective gradient $E_z^{(eff)} \sim .05 \text{ MeV}/0.3 \text{ m} \approx 0.16 \text{ MV/m}$. However, fits of the data to a 2D linear theory of plasma wakes (Chen, 1985) showed that fields as high as $E_z^{(max)} \approx 1 \text{ MV/m} \approx .03E_0$ were generated. Radial averaging over wake and witness bunch profiles accounted for the discrepancy.

In follow-up experiments, (Rosenzweig *et al.*, 1989) delivered 5-fold denser bunches (4 nC, $\sigma_r \approx 1.4 \text{ mm}$) to the plasma. These self-pinch, increasing peak current further. They excited nonlinear wakes in which $E_z(z - ct)$ oscillated in a sawtooth waveform (see Fig. 22b). Fourier analysis showed that the waveform contained harmonics of ω_p , as expected for a nonlinear wake. Transverse deflections of the witness bunch also oscillated with Δt in phase with E_z (see Fig. 22c), simultaneously profiling radial fields $E_r(z - ct)$. 2D modeling suggested peak E_z up to 5 MV/m was achieved, with $E_z^{(eff)}$ smaller as before. Two features of these results were surprising. First, wake oscillations, despite their distinct nonlinearity, were observed out to 18 periods behind the driver with little degradation in form or amplitude. Second, the relativistic increase in plasma period $\sqrt{\gamma} \omega_p^{-1}$ expected (Rosenzweig, 1987) for such steepened plasma waves was not observed. Instead a slight decrease in period was observed as wake amplitude increased. Later, (Marquès *et al.*, 1997) re-visited, and partially explained, similar features of nonlinear laser-driven plasma wakes (see Sec. IV.B.2). Still later, (Matlis *et al.*, 2006), in a study of high-amplitude laser-driven wakes (see Sec. IV.C.1), finally observed the expected relativistic increase in ω_p^{-1} .

Continuing experiments (Barov *et al.*, 2000) scaled bunch density into the strongly nonlinear “blowout” regime ($n_b \gg \bar{n}_e$), discussed in Secs II.A.2 and II.A.3.

This work produced drive and witness bunches more compactly by exciting a photocathode with tandem laser pulses. However, they were higher in emittance, longer, and less reproducible than expected. Thus, although this work observed $E_z^{(eff)} \sim 25$ MV/m, and inferred $E_z \sim 60$ MV/m, amongst its major conclusions was the need for improved methods of generating drive and witness bunches. Simulations by (Serafini, 1996) analyzed the challenges of producing high-quality, $\gtrsim 0.1$ nC, 30 – 150 fs bunches suitable for high-density ($\bar{n}_e \sim 10^{18}$ cm $^{-3}$) PWFA experiments both by ultrafast photocathode illumination and by compression of ps-duration bunches.

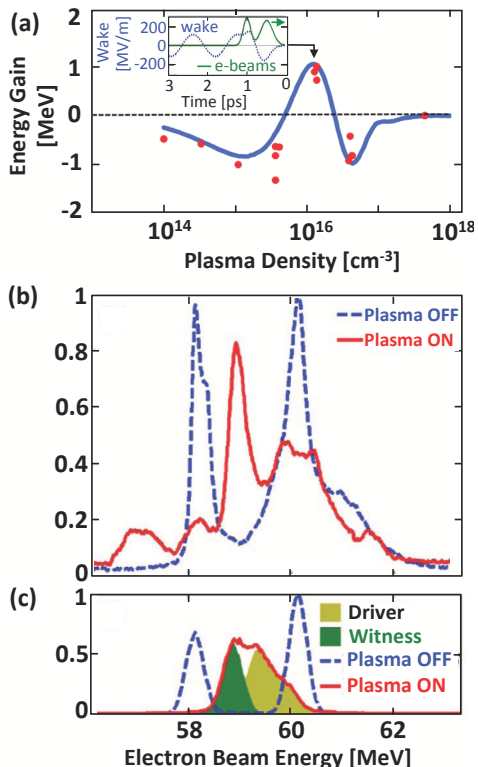


FIG. 23 Color online. Measurements of peak longitudinal electric field E_z of e-bunch-generated linear plasma wave in $\bar{n}_e = 10^{16}$ cm $^{-3}$ plasma. (a) Energy gain of witness bunch at fixed $\Delta t = 500$ fs behind drive bunch as \bar{n}_e changes. Inset: simulated plasma wave potential (dashed blue) and right-propagating drive and witness bunches (solid green). (b) Measured and (c) simulated energy spectra of witness and drive bunches without (dashed blue) and with (solid red) plasma of density $\bar{n}_e = 10^{16}$ cm $^{-3}$. Adapted from (Kallos *et al.*, 2008).

The work of (Kallos *et al.*, 2008; Muggli *et al.*, 2011, 2008a) delivered these improvements. A photocathode rf gun and S-band linac at Brookhaven National Laboratory’s (BNL’s) Accelerator Test Facility (ATF) (Catravas *et al.*, 1999) provided 1.5 ps, 500 pC, 60 MeV bunches. Using a chicane compressor and “dog-leg” magnetic dipole configuration (Kimura, 2006), (Kallos *et al.*, 2008) compressed and split these bunches into drive (witness) bunches of 150 (90) fs duration, 300 (180) pC charge

and 60 (58) MeV energy, with fixed delay $\Delta t = 500$ fs. The resulting drive bunches ($n_b \approx 10^{14}$ cm $^{-3}$) drove standard linear ($n_b < \bar{n}_e$) wakes in a 6 mm-long ablative capillary discharge hydrogen plasma (Kaganovich *et al.*, 1999) with \bar{n}_e ranging from 10^{14} to 4×10^{17} cm $^{-3}$, orders of magnitude denser than plasmas studied at ANL. Restricted to fixed Δt , (Kallos *et al.*, 2008) tuned \bar{n}_e , and observed maximum witness bunch energy gain $\Delta W_e \approx 0.9$ MeV at $\bar{n}_e \approx 10^{16}$ cm $^{-3}$, corresponding to $\Delta t = 1.5\lambda_p/c$. This corresponded to $E_z^{(eff)} = 0.9$ MeV/0.06 m = 150 MV/m, which matched the peak simulated E_z . Thus the witness bunch was sufficiently compressed and focused to observe the maximum E_z directly, without mathematical deconvolution of radial averaging.

(Muggli *et al.*, 2008a) refined the bunch-splitting technique by inserting a mask at a position in the dogleg where the beam’s energy was transversely chirped. The incident bunch could then be split into a train of sub-ps micro-bunches of controllable number, length and spacing by adjusting beam and mask parameters. An analogous technique generates controlled trains of ultrashort optical pulses (Weiner, 2000). This enabled production not only of a witness bunch, but of a train of drive bunches. Strategic adjustment of their spacing, shape and charge can increase transformer ratio (Laziev *et al.*, 1988) and energy extraction efficiency (Maeda *et al.*, 2004) of a PWFA, in theory, by more than an order of magnitude (Farmer *et al.*, 2015; Nakajima, 1989) compared to a single-bunch driver (Lotov, 2013; Ruth *et al.*, 1984). (Muggli *et al.*, 2011) demonstrated acceleration of a witness bunch in a wake driven by *two* mask-generated drive bunches. However, experiments have not yet realized full predicted capabilities of the multi-bunch PWFA. Direct 2D mapping of a multi-bunch PWFA with an electron or optical witness bunch as drive parameters change is a promising future diagnostic experiment.

Recent experiments at SLAC’s Facility for Advanced Accelerator Experimental Tests (FACET) (Hogan *et al.*, 2010) used co-propagating electrons to diagnose internal fields of strongly blown out PWFAs in $\bar{n}_e \sim 2 \times 10^{17}$ cm $^{-3}$ plasma. (Clayton *et al.*, 2016) mapped these fields in *one shot*, using electrons in the trailing portion of a drive bunch itself as witnesses. This is discussed with other single-shot experiments in Sec. IV.C.4. When the charge of a separate witness bunch becomes large enough to perturb the wake in which it is accelerating, it ceases to act purely as a diagnostic “witness” bunch. Such “beam loading” becomes beneficial when the accelerating bunch flattens local gradients in the wake field, helping the bunch to accelerate mono-energetically (Lu *et al.*, 2006; Tzoufras *et al.*, 2008). Recent PWFA experiments realized this beam-loaded regime, and imparted energy gains of several GeV to high-charge electron (Litos *et al.*, 2014) and positron (Corde *et al.*, 2015) bunches. 2D *optical* profiling of beam-loaded PWFAs is a promising future diagnostic experiment (Zgadżaj *et al.*, 2016).

2. Laser probe pulses

Delayed, co-propagating *electromagnetic* probe pulses of duration $\tau_{pr} < \omega_p^{-1}$ have also diagnosed plasma wake structure. For *laser-driven* wakes, inexpensive beam-splitters trivially separate perfectly synchronized probe(s) from the driver while preserving durations $\tau \lesssim 30$ fs. For beam-driven wakes, state-of-the-art electronic techniques can synchronize an e-beam and independent laser probe with < 1 fs jitter (Xin *et al.*, 2017).

The direct optical analog of e-beam diagnostics described in Sec. IV.B.1 is “photon acceleration” (Bulanov *et al.*, 1993; Esarey *et al.*, 1990; Wilks *et al.*, 1989) – *i.e.* blue- or red-shifts $\Delta\omega_{pr}$ of probe pulses that co-propagated with a longitudinal slice of the wake at which n_e locally increases ($dn_e/d\Delta t > 0$) or decreases ($dn_e/d\Delta t < 0$), respectively, with increasing Δt . From Poisson’s equation, maximum $|dn_e/d\Delta t|$ correspond to strongest $|E_z|$. For co-propagation distance L ,

$$\Delta\omega_{pr}(r, \Delta t) = -(\omega_{pr}/c) \int_0^L (d\eta/d\Delta t) dz \quad (44a)$$

$$\approx (\omega_{pr}L/2n_{cr}c) dn_e/d\Delta t. \quad (44b)$$

Here, η denotes local refractive index $\eta(r, \Delta t; z) = (1 - n_e(r, \Delta t; z)/n_{cr})^{1/2}$, and (44b) holds when $dn_e/d\Delta t$ is z -independent and $n_e \ll n_{cr}$. Both expressions assume L is short enough that the probe remains collimated. Thus a longitudinal wake slice that maximally accelerates an electron also maximally blue-shifts a probe pulse. Multi-shot pump-probe blue-shift experiments have diagnosed ionization front structure in atmospheric density gases (Wood *et al.*, 1991). However, despite in-depth theoretical analyses (Dias *et al.*, 1998; Kasim *et al.*, 2015) and initial experiments (Trines *et al.*, 2009), photon acceleration has not yet probed detailed plasma wake structure $n_e(r, \Delta t)$. This can be attributed to the small magnitude of $|dn_e/d\Delta t|$ in linear wakes in sub-atmospheric density gases, and to the wide bandwidth of probe pulses capable of resolving sub- λ_p features, making subtle spectral centroid shifts difficult to observe. Photon deceleration (red-shift) of wakefield *drive* pulses, which characterizes their energy transfer to plasma waves, *has* been observed (Murphy *et al.*, 2006; Shiraishi *et al.*, 2013), but does not measure detailed wake structure.

Researchers have had greater success diagnosing wake structure by analyzing *phase shift* $\Delta\phi_{pr}(r, \Delta t)$ that a wake imprints on a co-propagating probe. Unlike $\Delta\omega_{pr}$, $\Delta\phi_{pr}$ can be measured *interferometrically* with high accuracy even for a wide-bandwidth probe. A collimated probe of duration $\tau_{pr} < \omega_p^{-1}$ experiences phase shift

$$\Delta\phi_{pr}(r, \Delta t) = (\omega_{pr}/c) \int_0^L \eta(r, \Delta t; z) dz \quad (45a)$$

$$\approx (\omega_{pr}L/2n_{cr}c) n_e(r, \Delta t), \quad (45b)$$

uniformly over its longitudinal profile. Here, (45b) holds

in the same limit as (44b). Thus $\Delta\phi_{pr}(r, \Delta t)$ is proportional to the local *density* $n_e(r, \Delta t)$, rather than the local field $E_z(r, \Delta t)$, at which the probe propagates. By varying Δt and imaging the transverse probe profile, $n_e(r, \Delta t)$ can be mapped over multiple shots.

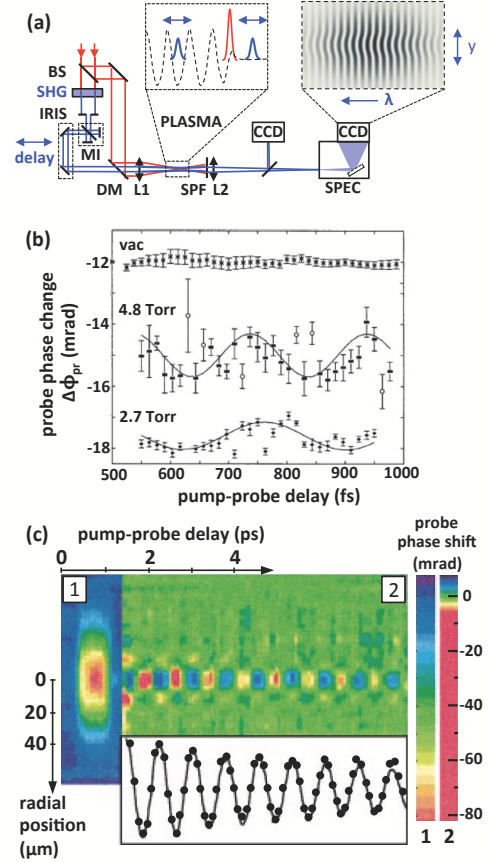


FIG. 24 Color online. Measurements of laser-generated electron density waves $n_e(r, z - ct)$ in $0.25 < \bar{n}_e < 3 \times 10^{17} \text{ cm}^{-3}$ plasma. (a) Schematic frequency-domain interferometry (FDI) setup: BS = beam splitter; SHG = second-harmonic generation; MI = Michelson interferometer; DM = dichroic mirror; L = lens; SPEC = spectrometer; CCD = charge-coupled device. Top-center inset: schematic of plasma wave density (dashed curve) created by right-propagating drive laser pulse (tall, red), with probe (trailing) and reference (leading) diagnostic pulses (short, blue). Top-right inset: schematic FD interferogram. Adapted from (Marquès *et al.*, 1996). (b) Optical probe phase change $\Delta\phi_{pr}(\Delta t)$ vs. pump-probe delay Δt for fully-ionized $\bar{n}_e = 0$ (top), 1.7 (middle) and 3 (bottom) $\times 10^{17} \text{ cm}^{-3}$ He plasmas excited by 100 fs, $0.8 \mu\text{m}$, 10 mJ laser pulses focused with $f/4$. Adapted from (Siders *et al.*, 1996b). 4.8 (2.7) Torr data was acquired with standard (differential) FDI. (c) 2D map $\Delta\phi_{pr}(r, \Delta t)$ of left-propagating nonlinear plasma wave for $\bar{n}_e = 0.25 \times 10^{17} \text{ cm}^{-3}$. Panel c) adapted from (Marquès *et al.*, 1997).

Frequency-domain interferometry (FDI) has mapped $\Delta\phi_{pr}(r, \Delta t)$ in a variety of multi-shot pump-probe experiments (Geindre *et al.*, 1994; Reynaud *et al.*, 1989; Tokunaga *et al.*, 1992). Fig. 24a shows a schematic FDI

setup. A diagnostic pulse is split from the drive pulse, then shifted in frequency, rotated in polarization, or both to help discriminate it from scattered pump light after the interaction. The diagnostic pulse is sub-divided into a reference pulse $E_{ref}^{(0)}(t)$, and a probe pulse $E_{pr}^{(0)}(t - T)$ that trails the reference by time T (e.g. by a Michelson interferometer with unequal arm lengths). These recombine with the pump (e.g. at a dichroic or polarizing mirror), and all three pulses co-propagate through the interaction region without overlap.

Different 3-pulse sequences can be used. In “standard” FDI, $E_{ref}^{(0)}(t)$ leads, and $E_{pr}^{(0)}(t - T)$ trails, the pump with T fixed (see Fig. 24a, center inset). The pump-induced index change $\eta(r, \Delta t)$ then affects only the probe, phase-shifting it to $E_{pr}(t - T) = E_{pr}^{(0)}(t - T)e^{i\Delta\phi_{pr}(r, \Delta t)}$. This configuration has two limits. First, the requirement that the reference lead the pump limits pump-probe delay to $0 < \Delta t < T$. Second, if the pump ionizes neutral gas before generating a wake, both static plasma (density \bar{n}_e) and wake oscillations (amplitude δn_e) contribute to $\eta(r, \Delta t)$. But if $\delta n_e \ll \bar{n}_e$, and $\bar{n}_e L$ fluctuates from shot to shot, the fluctuations can mask the wake. “Differential” FDI, in which reference and probe *both* trail the pump, separated by a half-integer number of plasma periods, can then extend the Δt range and discriminate small wake oscillations more effectively (Marquès *et al.*, 1997, 1996; Siders *et al.*, 1996b). In this configuration, the reference pulse shifts to $E_{ref}(t) = E_{ref}^{(0)}(t)e^{i\Delta\phi_{ref}(r, \Delta t)}$, and the relative phase shift $\Delta\phi \equiv \Delta\phi_{pr} - \Delta\phi_{ref}$ is measured. The static contribution to $\Delta\phi$ cancels, while the oscillatory component doubles in amplitude compared to $\Delta\phi_{pr}$ in the standard configuration. In both configurations, lens L2 (see Fig. 24a) images $E_{ref}(r, t)$ and $E_{pr}(r, t - T)$ to the entrance slit of an imaging spectrometer. The slit selects a slice along a direction hereafter called “ y ”. Spectral dispersion temporally broadens both pulses, causing them to overlap at the spectrometer’s array detector, which records their combined spectral intensity

$$\begin{aligned} I(y, \omega) &= |F[E_{ref}(y, t) + E_{pr}(y, t - T)]|^2 \\ &= |E_{ref}(y, \omega) + E_{pr}(y, \omega)e^{-i\omega T}|^2 \quad (46a) \\ &= S(y, \omega) + E_{ref}(y, \omega)E_{pr}^*(y, \omega)e^{i\omega T} \\ &\quad + E_{ref}^*(y, \omega)E_{pr}(y, \omega)e^{-i\omega T}. \quad (46b) \end{aligned}$$

Here, F denotes Fourier transform, $S(y, \omega) \equiv |E_{ref}(y, \omega)|^2 + |E_{pr}(y, \omega)|^2$, and $E_j(y, \omega) = E_j^{(0)}(y, \omega)e^{i\Delta\phi_j(y, \omega)}$ ($j = ref, pr$) are perturbed FD fields expressed in terms of unperturbed fields $E_j^{(0)}(y, \omega)$. For $E_{ref}^{(0)} = E_{pr}^{(0)} = E$ with no losses, refraction or diffraction in the plasma, Eq. (46) becomes (Tokunaga *et al.*, 1992)

$$I(y, \omega) = 2|E(y, \omega)|^2 \{1 + \cos[\omega T - \Delta\phi(y, \omega)]\}. \quad (46c)$$

Eq. (46c), an oscillating function of frequency with period $2\pi/T$, is the “frequency-domain interferogram” that

encodes probe-reference phase shifts (Reynaud *et al.*, 1989). In the absence of an interaction ($\Delta\phi = 0$), straight (y -independent) fringes appear on the detector. In the presence of a y -dependent interaction, fringes distort in pump-excited y -regions (see Fig. 24a, right inset). Straight fringes in unexcited y -regions then serve as the reference null interferogram, from which the fringe *shift* $\Delta\phi(y, \omega)$ in excited y -regions is extracted for each Δt . If $\tau_{pr} \ll \omega_p^{-1}$, then $n_e(y, \Delta t)$, $\eta(y, \Delta t)$ and $\Delta\phi(y, \Delta t)$ are constant in *time* at each y over the probe *longitudinal* profile. If, in addition, probe bandwidth $\delta\omega_{pr} \ll \omega_{pr}$, then $\eta(y, \Delta t)$ and $\Delta\phi(y, \Delta t)$ are also constant in *frequency* over the probe bandwidth. In this “FDI approximation”, $\Delta\phi(y, \omega) = \Delta\phi(y, \Delta t)$, both quantities being frequency-independent at each y and Δt . All fringes at each y and Δt then shift by the same amount, and the distinction between spectral and temporal phase disappears. Eq. (46c) then becomes

$$I(y, \omega) = 2|E(y, \omega)|^2 \{1 + \cos[\omega T - \Delta\phi(y, \Delta t)]\}. \quad (46d)$$

$\Delta\phi(y, \Delta t)$ can now be extracted directly from the measured fringe shift between “signal” and null interferograms. Accurate extraction requires only that the pixel density of the spectrometer’s 2D array detector be high enough for a given T (typically $\gtrsim 10$ pixels per fringe) to resolve the fringe shift. The FDI approximation remains valid even when the Taylor expansion $\Delta\phi(y, t) \approx \Delta\phi(y, \Delta t) + \partial_t \Delta\phi(y, t)|_{t=\Delta t}(t - \Delta t)$ includes *linear* temporal variations within the probe longitudinal profile, since $\partial_t \Delta\phi(y, t)|_{t=\Delta t}$ is simply an overall probe centroid frequency shift (photon acceleration) (Siders *et al.*, 1996a). Only when quadratic and higher-order temporal variations within the probe become significant is the equivalence of $\Delta\phi(y, \omega)$ and $\Delta\phi(y, \Delta t)$ lost, necessitating more sophisticated Fourier analysis of the interferograms. They then become FD “holograms” (see Sec. IV.C).

The first FDI experiments to characterize plasma wakes (Marquès *et al.*, 1996; Siders *et al.*, 1996b) used first-generation sub-TW Ti:S ($\lambda = 0.8\mu\text{m}$) chirped-pulse amplified (CPA) laser technology (Backus *et al.*, 1998), for which pulse duration was limited to $\tau \sim 100$ fs, pump energy to $10 \text{ mJ} \lesssim \mathcal{E} \lesssim 30 \text{ mJ}$. This τ limited \bar{n}_e to $\leq 3 \times 10^{17} \text{ cm}^{-3}$ (λ_p to $\geq 60\mu\text{m}$), in order to excite wakes resonantly and resolve sub- λ_p features, while this \mathcal{E} necessitated focusing to strongly sub- λ_p spot sizes ($3.5\mu\text{m} < w_0 < 6\mu\text{m}$) to reach field strengths ($0.35 < a_0 < 0.5$) sufficient to excite observable wakes. An advantage of such tight focus was that the drive pulse’s *radial* ponderomotive force dominated wake excitation, producing larger $\delta n_e/\bar{n}_e$ (up to ~ 1) and $\Delta\phi_{pr}$ (up to ~ 30 mrad) than its *longitudinal* ponderomotive force alone would have produced. Eq. (3b) quantifies this advantage. On axis ($r = 0$), the ratio $\delta n_r/\delta n_z = (\lambda_p/\pi w_0)^2$ of radial to longitudinal wake contributions ranged from 30 to 300 in the experiments of (Marquès *et al.*, 1996; Siders *et al.*, 1996b). Moreover, the contribution of the longitudinal

(radial) component of δn_e to $\Delta\phi_{pr}$ is proportional to δn_{zR} (δn_{rZR}). From Eq. (3b), δn_{zR} is independent of pump focus, whereas δn_{rZR} increases in proportion to $1/z_R$ as focus tightens. Thus with available lasers, tight focus was critical to initial FDI wake observation.

A *disadvantage* of tight pump focus was that the probe pulse averaged over radial wake profiles as it transited the interaction region. For example, the data in Fig. 24b correctly shows $\Delta\phi_{pr}(\Delta t)$ oscillating *longitudinally* at ω_p for each of two \bar{n}_e , but does not directly convey *radial* wake structure (Siders *et al.*, 1996b). Instead these researchers inferred radial structure *indirectly* by calculating it via Eq. (3b), computing $\Delta\phi_{pr}(\Delta t)$ induced on a focused (Siders *et al.*, 1996b) or collimated (Marquès *et al.*, 1996) probe, and confirming that the computed $\Delta\phi_{pr}(\Delta t)$ oscillation amplitude agreed with the measured value. The relationship between $\Delta\phi_{pr}(\Delta t)$ and δn_e was thus more complicated than Eq. (45b), which assumed longitudinally invariant wake structure and collimated probe. Limited direct radial information was obtained by imaging the transverse profile of $\Delta\phi_{pr}(y, \Delta t)$ with the probe at a wake peak or valley (Marquès *et al.*, 1996), or by observing increased $\Delta\phi_{pr}(\Delta t)$ as the spectrometer slit narrowed (Siders *et al.*, 1996b).

In a follow-up study, (Marquès *et al.*, 1998, 1997) mapped $\Delta\phi_{pr}(y, \Delta t)$ behind a tightly focused drive pulse in greater detail. Fig. 24c illustrates these expanded results. The left part (“1”) of the image, acquired with standard FDI, shows $\Delta\phi_{pr}(y, \Delta t)$ primarily from plasma formation. Regions of doubly- (red) and singly-ionized (green) He, integrated along the laser axis, can be seen. The right part (“2”) of the image, acquired with differential FDI, shows only wake oscillations, which are localized within the doubly-ionized region. The axial lineout below this image shows damped oscillation of the form $\Delta\phi_{max} \exp(-\gamma\Delta t) \sin(\omega_p\Delta t)$ behind the pump.

Analysis led to two new discoveries. First, ω_p of the first few oscillations was $\sim 5\%$ *higher* than later oscillations, the frequency of which matched ω_p for doubly-ionized helium. This finding resembled the temporary increase in ω_p that (Rosenzweig *et al.*, 1989) reported for a nonlinear PWEA (Sec. IV.B.1). Plasma heating, which increases electron thermal velocity v_{th} and thus plasma frequency via $[\omega_p(k)]^2 = \omega_p^2 + 3k_p^2 v_{th}^2$, could account for $< 1\%$ increase in ω_p , and would not relax within a few oscillation periods. Relativistic electron mass increase in high-amplitude electron oscillations, if present, would *decrease*, rather than increase, ω_p (Rosenbluth and Liu, 1972). Instead a simple electrostatic mechanism unique to high-amplitude radial wakes appeared to dominate: the radial displacement δr of an electron away from its initial position r_0 produced greater charge density at the center of symmetry, and thus a stronger restoring force, than in a planar wake, resulting in fractional increase $\Delta\omega_p/\omega_p \approx (\delta r/r_0)^2/12$ in ω_p (Dawson, 1959). Computer simulations reproduced the observed increase, as

well as its temporal relaxation. Second, damping rate γ was faster than expected from mechanisms expected in a uniform plasma – *e.g.* fine-scale mixing of orbits of electrons with amplitude-dependent oscillation frequencies (Dawson, 1959), or thermal convection. Instead radial electron excursions that cross the $\text{He}^{2+}/\text{He}^+$ boundary and de-phase from the wake provided the best quantitative explanation. These discoveries illustrate how high-resolution wake structure diagnostics, in concert with simulations, advance plasma wakefield physics.

C. “Snapshots” of wake structures

Multi-shot techniques diagnose wakefield structure in microscopic detail, but require lengthy data acquisition, and thus cannot provide rapid feedback. Moreover, the data is subject to shot-to-shot fluctuations, especially when wakes are excited nonlinearly. These considerations motivated development of diagnostics that recover plasma wake structure with equivalent detail in a *single shot*. Single-shot diagnostics developed most rapidly with optical, rather than electron, probes because of the relative ease with which optical pulses can be stretched, compressed, expanded and imaged and with which their internal phase and amplitude structure can be measured. Nevertheless, single-shot, high-resolution electron radiography of internal fields of plasma-based electron accelerators was recently demonstrated (see Sec. IV.C.4).

The development of *optical* single-shot plasma wake diagnostics drew upon three established optical technologies, which have no counterpart in particle beam technology. The first of these was holography. Holographic wake diagnostics drew from conventional holography the concepts of a coherent “object” (or probe) pulse that illuminates the *entire* object of interest simultaneously, and of a mutually coherent “reference” pulse with which the “object” pulse interferes on a recording medium. New challenges for holographic wake diagnostics included adapting these concepts to a near light-speed object, and developing methods for “reading” the “hologram” quickly and accurately (Sec. IV.C.1). The second underlying technology was ultrafast optics. By the year 2000, chirped-pulse-amplified (CPA) lasers producing terawatt pulses of tens of fs duration were widely available, and techniques for stretching, manipulating and re-compressing such pulses while maintaining their coherence had matured (Backus *et al.*, 1998). Moreover, pulse retrieval algorithms such as frequency-resolved optical gating (Trebin *et al.*, 1997) and spectral shearing interferometry (Iaconis and Walmesley, 1998) for characterizing the internal amplitude and phase structure of individual laser pulses had been developed, and advanced to single-shot implementation (Dorner *et al.*, 1999; O’Shea *et al.*, 2001). Single-shot optical wake diagnostics developed naturally from these techniques. A third underlying technology was computerized

tomography (CT), developed as an x-ray-based internal medical diagnostic in the 1970s (Kak and Slaney, 1998). Tomographic wake diagnostic methods are just beginning to emerge (Li *et al.*, 2014b). They draw from established CT the concept of reconstructing multi-dimensional images of difficult-to-access objects from multiple projections. They also utilize elements of established reconstruction algorithms. New challenges include adapting these concepts to an evolving light-speed object, recovering its picosecond evolution, and achieving high spatial and temporal resolution simultaneously.

1. Frequency-domain holography

(Siders *et al.*, 1996a) first proposed extending FDI to a single-shot plasma wake diagnostic. One way of doing this is simply to time N probe pulses at different delays $\tau_{pr}^{(i)}$ ($i = 1, 2, \dots, N$) behind the pump (see Fig. 25a). A multi-armed Michelson interferometer, for example, has produced 16-pulse trains with high throughput (Siders *et al.*, 1998). Since each probe-reference delay $T^{(i)} = \tau_{ref} - \tau_{pr}^{(i)}$ corresponds to a different oscillation period of the resulting multi-period FD interferogram (Fig. 25a, inset), Fourier analysis (Takeda *et al.*, 1982) would then yield the time-domain phase shift $\Delta\phi(\tau_{pr}^{(i)})$ on each probe in one shot. More simply, one can replace this multiplexed probe pulse train with a single continuous long pulse (see Fig. 25b). (Siders *et al.*, 1996a) called the latter configuration “frequency-domain holography” (FDH), and envisioned creating the long probe pulse by inserting a flat-phase bandpass filter in the probe arm of a two-armed Michelson interferometer. This broadens the probe temporally, but maintains its phase coherence with the (still short) reference pulse. (LeBlanc *et al.*, 2000) realized this goal in the laboratory by inserting phase-matched frequency-doubling crystals of different thickness into each arm of the interferometer (see Fig. 25b, inset). The thicker crystal (2 mm LiIO₃) had a narrow phase-matching bandwidth that generated a temporally long (1 ps) probe pulse, while the thinner crystal (150 μ m KDP) generated a temporally short (70 fs) reference pulse. The unperturbed probe and reference pulses formed FD fringes only within the narrower bandwidth of the probe pulse. However, after interacting with the ultrafast pump-induced index transient, the probe acquired new frequency components that interfered with the broader reference spectrum. The latter bandwidth determined the temporal resolution of the phase reconstruction. (LeBlanc *et al.*, 2000) recovered laser-induced Kerr index transients in fused silica and ionization fronts in air over ~ 1 ps range with 70 fs time resolution, and 1D transverse spatial profiling, in a single shot.

(Chien *et al.*, 2000; Geindre *et al.*, 2001) implemented FDH using probe and reference pulses that were *both* broad-bandwidth and *both* temporally broadened simply

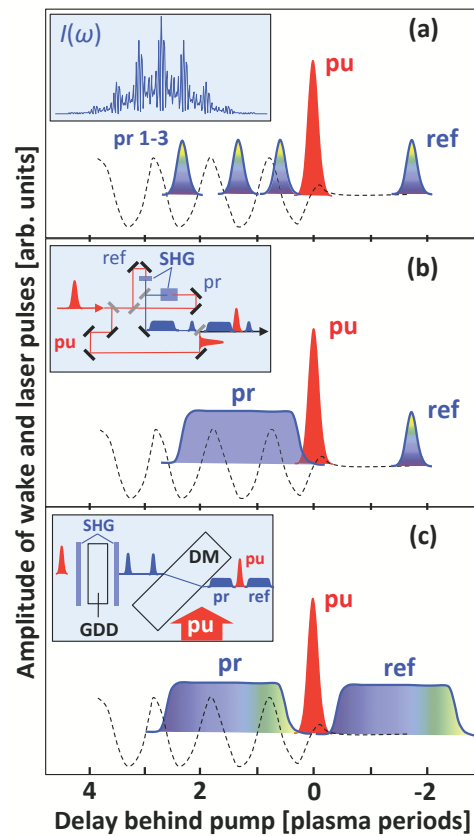


FIG. 25 Color online. Early development of frequency-domain holography (FDH) concept based on right-propagating pump (pu), probe (pr) and reference (ref) pulses, and wake (dashed curve). (a) Multiplexed FDI with several temporally short probe pulses (Siders *et al.*, 1996a). Inset: Spectral intensity $I(\omega)$ of 3 probes and 1 reference pulse at detector. (b) FDH with single temporally long, transform-limited probe and temporally short, transform-limited reference (Siders *et al.*, 1996a). Inset: laboratory implementation (LeBlanc *et al.*, 2000). (c) FDH with equivalent chirped, wide-bandwidth probe and reference pulses (Chien *et al.*, 2000; Geindre *et al.*, 2001; Kim *et al.*, 2002b). Inset: laboratory implementation (Matlis *et al.*, 2006): incident 800nm diagnostic pulse split from pump up-converts to 400 nm via second-harmonic generation (SHG) in thin crystal, creating probe; glass plate group-delays (GDs) probe by ~ 2 ps from transmitted fundamental, which up-converts in second thin SHG crystal, creating reference; both chirp to ~ 1 ps duration in thick dichroic mirror (DM), which recombines them collinearly with pump.

by linearly chirping them, without narrowing their spectra (see Fig. 25c). In a chirped pulse, frequency components are distributed in a monotonic time sequence $\omega(t)$ within the stretched pulse. (Chien *et al.*, 2000; Geindre *et al.*, 2001) introduced chirp by passing the diagnostic pulse through a transparent, linear dispersive material before a Michelson interferometer split it into probe and reference pulses. This simplified FDH by eliminating alignment-sensitive transmissive optics inside the

interferometer. These authors demonstrated single-shot recovery of the dynamics of laser-induced air ionization (Chien *et al.*, 2000) and plastic target breakdown (Geindre *et al.*, 2001), also with 1D transverse spatial profiling.

Chirped-pulse FDH had the additional advantage of lending itself to wide bandwidth supercontinuum probe and reference pulses (Kim *et al.*, 2002b), which provide high longitudinal time resolution, wide temporal range, and (when generated in a frequency band near the pump) smaller group-velocity walk-off from the pump than frequency-doubled pulses. This approach yielded high-resolution measurements of *e.g.* double ionization in He (Kim *et al.*, 2002a) and Kerr effect and plasma generation in various gases (Chen *et al.*, 2007; Wahlstrand *et al.*, 2011). However, nonlinear laser-wakefield excitation itself produces copious forward-directed chirped supercontinuum (Ralph *et al.*, 2009), which interferes with co-propagating diagnostic pulses close to the drive pulse frequency, complicating image recovery. To avoid this, (Matlis *et al.*, 2006) returned to frequency-doubled diagnostic pulses to obtain the first FDH “snapshots” of laser wakefields. The inset of Fig. 25c shows the compact probe-reference generator, based on a linear Fabry-Perot interferometer configuration, that (Matlis *et al.*, 2006) introduced. This configuration proved more robust against vibrations and alignment errors than Michelson interferometers, while avoiding phase noise from background pump-generated supercontinuum. Visible supercontinuum pulses may nevertheless prove useful in imaging plasma wakes driven by particle-beams or mid-to long-wavelength-infrared laser pulses, for which this background is absent or at much longer wavelengths.

Using chirped pulses offers the intuitively attractive possibility of mapping the evolving pump-induced index transient $\eta(t)$ directly onto the probe spectrum $\omega(t)$ (Chien *et al.*, 2000). In a simplified analysis, one divides the FD interferogram into N frequency bands $\Delta\omega^{(i)}(t^{(i)})$ ($i = 1, 2, \dots, N$), then measures the fringe shift within each band to find the corresponding instantaneous index $\eta(t^{(i)})$. However, (Geindre *et al.*, 2001; Kim *et al.*, 2002b) pointed out that the narrow bandwidth of each bin limits $\eta(t)$ recovery to slowly-varying index transient that satisfy $\partial\eta/\partial t|_{t^{(i)}} < \Delta\omega^{(i)}$. More rapidly varying index transients shift spectral content out of bin $\Delta\omega^{(i)}$ into neighboring bins, causing inaccurate recovery of $\eta(t)$. Research on THz pulse modulation of chirped optical pulses has resulted in various strategies for addressing the distorted frequency-time relationship that the imprinting process causes (Fletcher, 2002; Peng *et al.*, 2008; Yellampalle *et al.*, 2005).

To recover rapidly-varying $\eta(\Delta t)$ by FDH, limited only by the bandwidth $\Delta\omega$ of the entire reference pulse, (Geindre *et al.*, 2001; Kim *et al.*, 2002b; LeBlanc *et al.*, 2000) introduced a holistic FDH signal reconstruction procedure valid for either transform-limited (Fig. 25b) or chirped (Fig. 25c) probes. Figs. 26 and 27 illustrate the

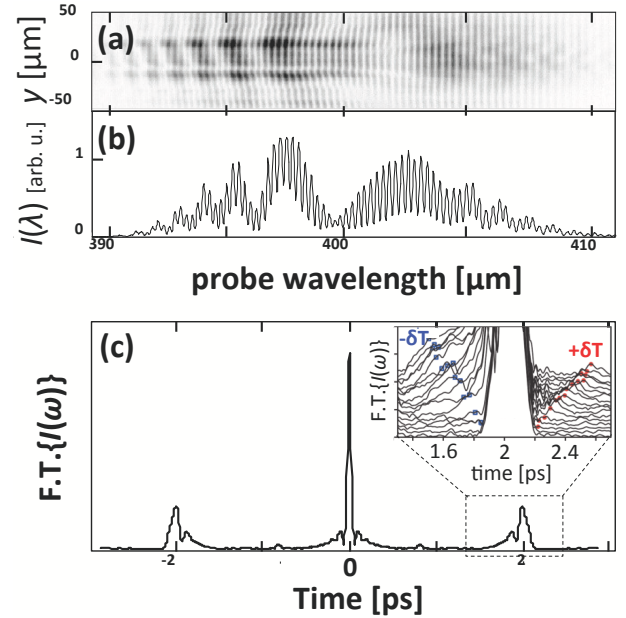


FIG. 26 Color online. FDH signal reconstruction procedure. (a) Raw FD hologram showing interference of chirped 400 nm probe and reference pulses at detection plane of imaging spectrometer, after co-propagating through He gas jet with 0.3 J, 30 fs, 800nm pump pulse focused to $w_0 = 50\mu\text{m}$, and imaging from jet exit to spectrometer slit through a 400nm bandpass filter. Variations along y -axis, parallel to spectrometer slit, reflect transverse spatial structure of pump-induced plasma. Adapted from (Matlis *et al.*, 2006). (b) Line-out of hologram at one y position. (c) Fourier transform of line-out in (b). Dashed rectangle: cross-correlation peak at $T = 2$ ps is isolated, then Fourier-transformed for further processing. Panels (b) and (c) adapted from (Dong *et al.*, 2010a): © Deutsche Physikalische Gesellschaft, reproduced by permission of IOP Publishing (CC-BY-NC-SA). Inset: detailed sub-structure of $T = 2$ ps peak for \bar{n}_e from 0.95 to $6 \times 10^{18} \text{ cm}^{-3}$ (bottom to top). Adapted from (Matlis *et al.*, 2016).

main steps, using data from (Matlis *et al.*, 2006) as an example. For the data shown, a 0.3 J, 30 fs (10 TW) Ti:S pump pulse focused to beam waist $w_0 \approx 50\mu\text{m}$ in a 2-mm-long He gas jet created plasma of average density $\bar{n}_e \sim 10^{18} \text{ cm}^{-3}$ and a wake of wavelength $\lambda_p \sim 25\mu\text{m}$ in the doubly-ionized region. Fig. 26a shows a raw FD hologram, acquired using the “standard” chirped pulse FDH configuration shown in Fig. 25c. Both ionization front (not shown in Fig. 25c) and wake oscillations contributed to the fringe distortions in Fig. 26a. Fig. 26b shows a line-out of the hologram $I(y_0, \omega)$ at $y = y_0$. Formally, $I(y_0, \omega)$ is given by Eq. (46), and for identical unperturbed probe and reference pulses, by Eq. (46c). However, Eq. (46d) does *not* apply, since the FD phase $\Delta\phi_{pr}(y, \omega)$ is no longer equivalent to, nor simply related to, the desired pump-induced TD phase shift $\Delta\phi(y, \Delta t)$ as in FDI.

To recover $\Delta\phi(y, \Delta t)$, (Geindre *et al.*, 2001; Kim *et al.*, 2002b; LeBlanc *et al.*, 2000) began by isolating the com-

plete *frequency-domain* probe electric field

$$E_{pr}(y, \omega) = |E_{pr}(y, \omega)| e^{i[\Delta\phi_{pr}(y, \omega) + \phi_{ch}(\omega)]} \quad (47)$$

from the FD hologram, using a computer-based fringe-pattern analysis method introduced by (Takeda *et al.*, 1982). Here $\phi_{ch}(\omega)$ is the FD phase due to the probe chirp. We now suppress the argument y for brevity. To isolate $E_{pr}(\omega)$, they first inverse-Fourier-transformed the recorded FD hologram $I(\omega)$, given by Eq. (46)b or Fig. 26b, at each y :

$$S(t) = \tilde{F}[I(\omega)] \quad (48)$$

This operation electronically “reads” the recorded hologram with a plane wave, analogous to physically reading a conventional film-recorded hologram with the reference wave (Siders *et al.*, 1996a). The resulting complex time-domain function $S(t)$, of which Fig. 26c shows the amplitude, has the form $S(t) = 2h(t) + h(t + T) + h(t - T)$ with peaks at $t = 0, -T$ and T . These peaks correspond, respectively, to \tilde{F} of the 3 terms in Eq. (46)b. The central ($t = 0$) peak is the intensity autocorrelation of the reference and probe pulses, but lacks phase information. Only the side (cross-correlation) peaks at $t = \pm T$ encode the desired phase of E_{pr} . (Siders *et al.*, 1996a) gives complete expressions for all 3 peaks. The side peak at $t = T$ has the general form

$$h(t - T) = \tilde{F}[E_{ref}^*(y, \omega) E_{pr}(y, \omega) e^{-i\omega T}]. \quad (49a)$$

For unperturbed linearly-chirped, Gaussian pulses $E_{pr}(\omega) = E_{ref}(\omega) = E_0 \exp -(1/2)(1 + i\sigma)[(\omega - \omega_0)/\Delta\omega]^2$, where σ represents the FD chirp, it has the specific form (Matlis *et al.*, 2016)

$$h(t - T) = \Delta\omega \left(E_0^2 / \sqrt{2} \right) e^{-i\omega_0(t-T)} e^{-\frac{1}{4}(t/\delta t)^2}, \quad (49b)$$

where $\delta t \equiv 1/\Delta\omega$ is the coherence time of the probe and reference pulses. When a temporal phase shift $\Delta\phi_{pr}(\Delta t)$ modulates the probe, $h(t - T)$ develops informative sub-structure, shown for $0.95 \times 10^{18} \text{ cm}^{-3} < \bar{n}_e < 6 \times 10^{18} \text{ cm}^{-3}$ in the magnified view of the base of the $t = T$ peak in the inset of Fig. 26c. The step-function-like ionization front, which in the FD blue-shifts frequency components that it overlaps, appears as a shoulder on the $t < T$ side of $h(t - T)$. This shoulder becomes more prominent at higher \bar{n}_e . A sinusoidal wake oscillation, which in the FD creates Stokes and anti-Stokes sidebands at $\pm\omega_p$, appears in the TD as sidebands at $T \pm \delta T$. Here δT , which is $\sigma\omega_p/\delta\omega^2$ for linearly-chirped probe and reference pulses (Matlis *et al.*, 2016), increases as $\sqrt{\bar{n}_e}$, and exceeds δt throughout the \bar{n}_e range shown. A nonlinear wake, which contains harmonics of ω_p , would create additional higher-order TD sidebands at $T \pm m\delta T$, where $m = 2, 3, \dots$ (not shown in the inset of Fig. 26c). For cases of interest, these ionization- and wake-induced *spectral*

shifts are smaller than $\Delta\omega$, and thus are not visible directly in the FD. Chirped pulse FDH, however, encodes them in the TD, and by Fourier-transforming $I(\omega)$, converts them to *temporal* shifts δT greater than the temporal width δt of the reconstructed $h(t - T)$ peak. (Matlis *et al.*, 2016) called this process temporally-encoded spectral shifting (TESS). TESS analysis enables subtle wake-induced phase modulations to be separated from the often much larger phase modulations that ionization fronts imprint, *e.g.* by analyzing the wake-induced sideband on the $t > T$ side of $h(t - T)$. This gives FDH a capability analogous to “differential” FDI mode (see Sec. IV.B.2). Recently (Cowley *et al.*, 2017) used TESS to characterize plasma wakes driven by optimized trains of laser pulses.

To complete the extraction of $E_{pr}(\omega)$, (Geindre *et al.*, 2001; Kim *et al.*, 2002b; LeBlanc *et al.*, 2000) multiplied $h(t - T)$ by a soft-edged apodizing window centered at $t = T$ to isolate this peak (indicated by dashed rectangle in Fig. 26c). The window must be wide enough to include all sub-structure that the interaction introduced. Fourier-transformation back to the FD yields

$$|E_{ref}(\omega)| |E_{pr}(y, \omega)| e^{i\Delta\phi_{pr}(y, \omega)} \quad (50)$$

for the $t = T$ peak. Finally, one divides Eq. (50) by the independently-measured reference pulse power spectrum $|E_{ref}(\omega)|$ and augmented it with the FD chirp phase $\phi_{ch}(\omega)$, measured by standard single-shot pulse characterization methods (Dorrer *et al.*, 1999; O’Shea *et al.*, 2001), to complete reconstruction of the field Eq. (47).

The final step in recovering $\Delta\phi(y, \Delta t)$ is inverse Fourier transformation of $E_{pr}(y, \omega)$ to get the complete *time-domain* probe electric field

$$\begin{aligned} E_{pr}(y, \Delta t) &= \tilde{F}[E_{pr}(y, \omega)] \\ &= |E_{pr}(y, \Delta t)| e^{i[\Delta\phi_{pr}(y, \Delta t) + \phi_{ch}(y, \Delta t)]}. \end{aligned} \quad (51)$$

After subtracting the independently characterized time-domain chirp $\phi_{ch}(y, \Delta t)$ from its phase, we recover $\Delta\phi(y, \Delta t)$ at one y . Repeating this analysis for each y yields the 2D phase map shown in Fig. 27a.

Fig. 27b compares this phase map with simulated plasma density perturbations $\delta n_e(y, \Delta t)$ near the center of the gas jet ($z = 1 \text{ mm}$) for the same conditions. The overall structures of $\delta n_e(y, \Delta t)$ and $\Delta\phi_{pr}(y, \Delta t)$ match closely: boundaries of He^{2+} and He^+ regions in Fig. 27b appear at y values similar to those of sharp $\Delta\phi_{pr}$ boundaries in Fig. 27a; plasma density oscillations in the He^{2+} region in Fig. 27b have the same wavelength and radial structure as corresponding $\Delta\phi_{pr}$ oscillations in Fig. 27a. (Matlis *et al.*, 2006) found similar correspondence for shots over a wide \bar{n}_e range, showing that the approximation of a collimated probe pulse, discussed in connection with FDI in Sec. IV.B.2, remained valid here. Nevertheless, (Matlis *et al.*, 2006) found the *amplitude* of phase oscillations in Fig. 27a was significantly *smaller* than expected from probing the density perturbations in Fig. 27b

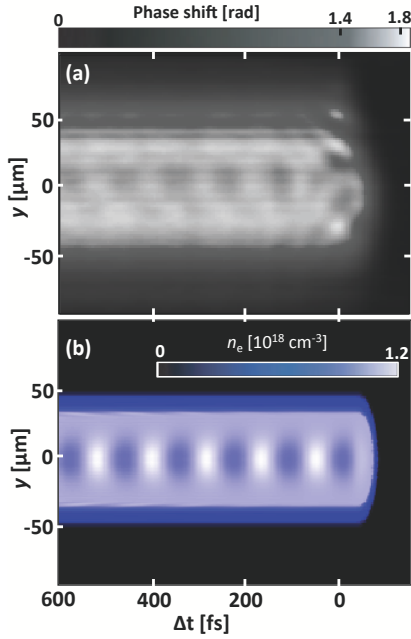


FIG. 27 Color online. (a) Composite “snapshot” of right-propagating wake formed by stacking temporal pump-induced phase structure $\Delta\phi_{pr}(y, \Delta t)$ extracted from cross-correlation peaks at each y . (b) Simulated wake density profile $n_e(y, \Delta t)$ near center of gas jet for conditions matching the experimental data. Adapted from (Matlis *et al.*, 2006).

over a *uniform* jet. Group velocity walk-off of 400nm probe from 800 nm pump did not explain the discrepancy. Instead it arose from longitudinal density nonuniformity of the gas jet, which caused the pump to generate, and probe to sample, wakes of different frequencies as they co-propagated through the 2 mm jet. Remarkably, despite this averaging, the recovered hologram Fig. 27b preserved the main features of the wake near the center of the jet. Longitudinally uniform gas targets are thus preferred to obtain accurate wake amplitudes from FDH.

(Dong *et al.*, 2010a; Matlis *et al.*, 2006) found that imaging of *nonlinear* wakes generated by 1 J, 30 fs (30 TW) pump pulses enabled independent *in-situ* calibration of absolute wake oscillation amplitude. FDH images of wakes excited under these conditions had curved wavefronts (Fig. 28a), a signature of strongly driven, nonlinear laser-plasma interaction (Andreev *et al.*, 1997b; Decker *et al.*, 1994). Wavefronts that were flat immediately behind the pump evolved into curved ‘horse-shoe’ profiles after several periods. Simultaneously, the *amplitude* of the phase-shift oscillations increased over the same interval. A particle-in-cell simulation of the wake (Fig. 28b) showed that plasma density oscillations $\delta n_e(y, \Delta t)/\bar{n}_e$ near the center of the gas jet also exhibited both of these features. Both are relativistic in origin. The wavefronts curve because as $|\delta n_e(r = 0, \Delta t)|$ approaches unity on axis ($r = 0$), electrons making up the wave oscillate relativistically ($\gamma > 1$), causing $\omega_p(r = 0)$ to decrease by

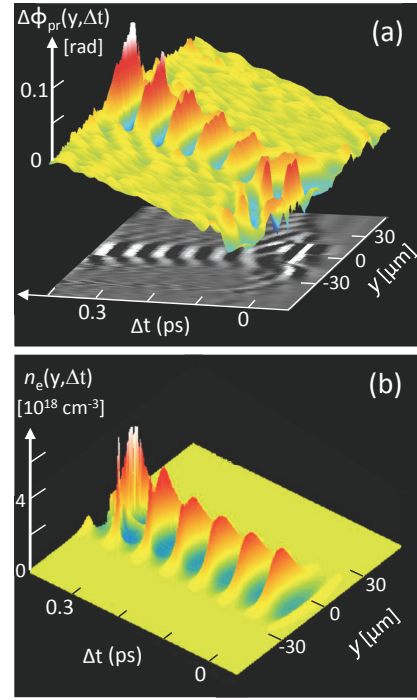


FIG. 28 Color online. Strongly-driven right-propagating wake with curved wavefronts. (a) FDH phase profile $\Delta\phi_{pr}(y, \Delta t)$ of wake (colored surface) that a 30 TW pump pulse generated in He^{2+} plasma with $\bar{n}_e = 2.2 \times 10^{18} \text{ cm}^{-3}$. The grey-scale image is a projection onto a plane. DC phase shift from surrounding plasma profile has been subtracted to highlight wake oscillations. (b) Simulated wake density profile $n_e(y, \Delta t)$ near the gas jet center, showing growth of wavefront curvature and amplitude with increasing Δt as in (a). Adapted from (Dong *et al.*, 2010a): © Deutsche Physikalische Gesellschaft, reproduced by permission of IOP Publishing (CC-BY-NC-SA).

$\sqrt{\gamma}$ relative to its off-axis value (Andreev *et al.*, 1997b; Decker *et al.*, 1994). Simulations showed that the reciprocal radius of curvature $\rho^{-1} = g\Delta t$ grows linearly with Δt , where growth rate g depends sensitively on $|\delta n_e(r = 0, \Delta t)/\bar{n}_e|$. Analysis of ρ^{-1} in the FDH image in Fig. 28a showed $|\delta n_e(r = 0, \Delta t)/\bar{n}_e|$ was ~ 0.5 immediately behind the pump, then grew steadily over 6 cycles. (Dong *et al.*, 2010a) explained this growth by analogy with amplitude growth observed in simulations of wakes generated in plasma channels with parabolic radial density profiles (Andreev *et al.*, 1997a; Shvets and Li, 1999). Here the radial relativistic $\gamma(r)\omega_p$ profile played the role of the channel density profile. With increasing Δt , trajectories of radially neighboring electron fluid elements, oscillating at slightly different frequencies, approach. In a process akin to optical pulse compression, interaction amongst fluid elements spanning the $\gamma(r)\omega_p$ bandwidth steepen and narrow the plasma wavefronts, causing the observed amplitude growth. As trajectories cross, the waves can eventually break, although the image and simulation in Fig. 28 stop before this happens.

Correlated growth of wave curvature and amplitude, effects never previously observed in the laboratory, are thus precursors of wave breaking and electron injection. The example illustrates the new wakefield physics that is accessible from dialog between *in-situ* plasma structure diagnostics and simulations.

2. Longitudinal optical shadowgraphy

The images in Figs. 27a and 28a were reconstructed entirely from accumulated *phase* shift $\Delta\phi_{pr}(r, \Delta t, z_{exit})$ on the wake-modulated probe pulse at the exit plane of the accelerator. Corresponding changes in the probe *amplitude* $|E_{pr}(r, \Delta t, z_{exit})|$ were negligible under these conditions. As $\bar{n}_e L$ increases, plasma structures with high index contrast not only re-shape the drive pulse (Decker *et al.*, 1996), but refract a co-propagating FDH probe as well. As an example, the top row of Fig. 29 shows a PIC simulation using the code WAKE (Mora and Antonsen, 1997) of guiding and compression of an initially 30 fs, 30 TW drive pulse (outlined in red) as it generates nonlinear wake profile $n_e(r, \Delta t, z)$ (grey scale) upon propagating from $z = 0.1$ mm (left) to its depletion distance $z = L_d = 1.8$ mm (right) in plasma of average density $\bar{n}_e = 8 \times 10^{18}$ cm⁻³. The second row of Fig. 29 shows corresponding changes in the amplitude envelope $|E_{pr}(r, \Delta t, z)|$ of a co-propagating 400 nm FDH probe pulse. By $z = 0.5$ mm, the pump compresses to 20 fs (top middle) as it blows out electrons from the first wake bucket. This high-index ($\eta = 1$) plasma bubble also focuses *probe* light inside it (bottom middle), and, by $z = 1.8$ mm, compresses it near the front of the bubble to dimensions $\lambda_p^3 \sim (10\mu\text{m})^3$. Formation of such 3D-confined light packets correlates closely with, and non-invasively diagnoses, bubble formation.

(Dong *et al.*, 2010b) observed bubble-formed light packets, which they called “optical bullets”, in the laboratory by recovering the *amplitude* profile $|E_{pr}(r, \zeta, z_{exit})|$ of an FDH probe pulse co-propagating with a laser-generated bubble. Fig. 30 shows sample results using a ~ 2 -mm-thick He gas jet, and laser parameters as in the simulations above. Fig. 30a shows a reference reconstruction of the unaltered incident probe profile, acquired with the gas jet turned off. For Fig. 30b, the pump created plasma of density $\bar{n}_e = 1.2 \times 10^{19}$ cm⁻³, and an optical bullet (highlighted by vertical arrow), signifying bubble formation, appeared near the probe leading edge. Yet no electrons were produced in this case, showing that bubbles can form below the threshold for spontaneous electron injection. With further increase of density ($\bar{n}_e = 3.2 \times 10^{19}$ cm⁻³), a smaller, brighter optical bullet formed (Fig. 30c-1) and nearly mono-energetic electrons were produced (Fig. 30c-2). Supporting simulations confirmed the observed bubble formation and injection thresholds (Dong *et al.*, 2010a,b).

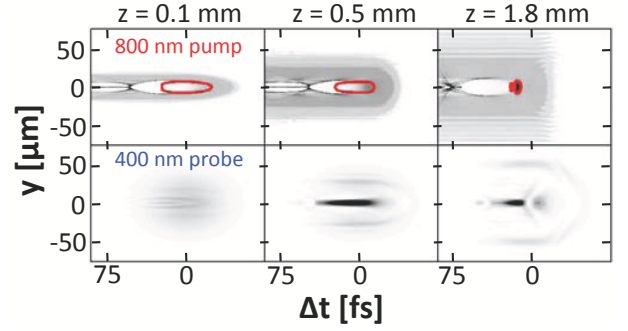


FIG. 29 Color online. WAKE simulations for $\bar{n}_e = 8 \times 10^{18}$ cm⁻³ showing formation of plasma wake (top row), with pump e^{-2} isointensity contours outlined by solid red curves, and refraction of 400 nm FDH probe to form optical bullet inside the bubble (bottom row). Pump and probe pulses propagate from gas jet entrance (left column) to $z = 0.5$ mm (middle column) to the pump depletion and bullet formation length z_{exit} (right column) near jet exit. Grey scale indicates electron density (top) or probe intensity (bottom). Adapted from (Dong *et al.*, 2010a).

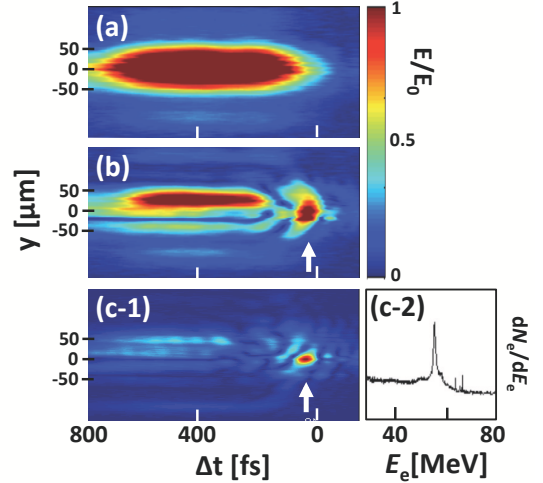


FIG. 30 Color online. Longitudinal shadowgraphy of strongly nonlinear LWFA. Probe amplitude profile $|E_{pr}(r, \Delta t, z_{exit})|$ is reconstructed using FDH methods (a) with no gas jet (undistorted profile), and after co-propagating left to right with wake in doubly-ionized He plasma of density $\bar{n}_e [10^{19}$ cm⁻³] = 1.2 (b) or 3.2 (c-2), showing optical bullets (highlighted with vertical arrows) trapped inside “bubble”. (c-2): electron energy spectrum. Adapted from (Dong *et al.*, 2010a).

The FDH analysis procedure also outputs probe phase profiles $\Delta\phi_{pr}(r, \zeta, z_{exit})$ in the bullet formation regime. However, they are no longer as simply related to plasma structure as in the quasi-linear regime of (Matlis *et al.*, 2006). This is in part because $\Delta\phi_{pr}$ often exceeds 2π , creating phase jumps that are difficult to unwrap (Ghiglia and Romero, 1994), and in part because refraction distorts the radial distribution of $\Delta\phi_{pr}(r, \zeta, z_{exit})$. $|E_{pr}(r, \zeta, z_{exit})|$ profiles alone lend themselves to clear physical interpretation in highly refractive plasmas.

Since they resemble shadowgraphs projected on a virtual screen at z_{exit} , FDH can be called “FD shadowgraphy” (FDS) in this regime.

3. Transverse optical probing

In discussing scattering of long ($\tau_{pr} > \omega_p^{-1}$) probe pulses from plasma waves (Sec. IV.A), we noted that co-propagating and transverse probes yielded complementary diagnostic information. The same is true of ultra-short ($\tau_{pr} < \omega_p^{-1}$) probe pulses. Co-propagating CTS (Sec. IV.A), FDI (Sec. IV.B.2), FDH (Sec. IV.C.1), and FDS (Sec. IV.C.2) probes integrate longitudinally over the wake’s *evolution* as it propagates. Yet such evolution is an essential part of nonlinear wakefield acceleration. Its diagnosis requires a probe with a velocity component *transverse* to \vec{k}_p . Wake-induced alteration of an *ultra-short* transverse probe pulse can yield a snapshot related to the wake’s internal plasma density (Sävert *et al.*, 2015) or magnetic field (Kaluza *et al.*, 2010) profile, or both (Buck *et al.*, 2011), with sub- λ_p resolution at time Δt . When shot-to-shot-fluctuations are small, a Δt -sequence of such images from successive shots forms a *movie* of the evolving wake (see Sec. IV.D). Figure 31 shows a transversely probed plasma accelerator schematically.

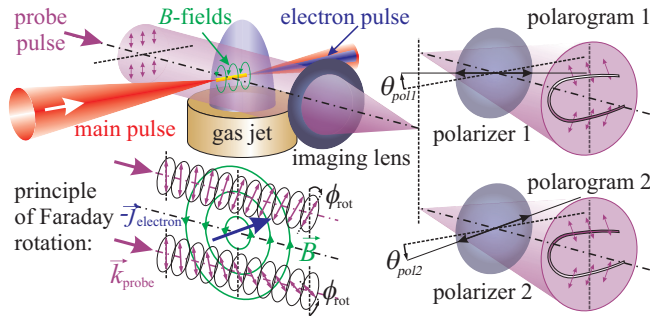


FIG. 31 Color online. Schematic experimental setup for transverse optical probing of wakefield accelerator. A main laser pulse or particle bunch excites a gas jet, driving a plasma wake that captures and accelerates electrons. A transverse probe pulse backlights the interaction region. High-resolution optics (here represented by a simple lens) image probe light from the interaction region to CCD cameras. In the example shown, two CCDs, each equipped with a polarizer, locally detect B -field induced rotation of the probe pulse’s polarization. Lower left inset: principle of polarization rotation induced by the Faraday effect. From (Kaluza *et al.*, 2010).

a. Magnetic field measurements. Inside plasma electron accelerators, the current density $\vec{j}(\vec{r}, t)$ of accelerating electrons and the displacement current density $\epsilon_0 \partial \vec{E}(\vec{r}, t) / \partial t$ of time-varying plasma wave electric fields

produce azimuthal magnetic fields

$$\nabla \times \vec{B}(\vec{r}, t) = \mu_0 \left(\vec{j}(\vec{r}, t) + \epsilon_0 \frac{\partial \vec{E}(\vec{r}, t)}{\partial t} \right) \quad (52)$$

that reach kilo-Tesla strength in plasma surrounding a bubble. A transverse linearly-polarized probe impinging on the wake thus “sees” \vec{B} components that are both parallel and perpendicular to \vec{k}_{pr} (see Fig. 31, lower left inset) that alter its polarization by the Faraday or Cotton-Mouton effects, respectively. The Faraday effect ($\vec{k}_{pr} \parallel \vec{B}(\vec{r}, t)$) locally rotates probe polarization, which remains linear. The Cotton-Mouton effect ($\vec{k}_{pr} \perp \vec{B}(\vec{r}, t)$) locally induces polarization ellipticity. However, a transverse probe experiences equivalent components $\vec{B} \perp \vec{k}_{pr}$ of opposite sign on the entrance and exit sides of the azimuthal field profile. Thus, the Cotton-Mouton effect approximately cancels out. In contrast, probe rays propagating above or below the central axis of the plasma wave experience components $\vec{B} \parallel \pm \vec{k}_{pr}$ that retain their direction along each ray’s entire path. Consequently, Faraday polarization rotation accumulates up to angle

$$\phi_{rot} = \frac{e}{2m_e c} \int_{\text{plasma}} \frac{n_e(\vec{r})}{\langle \gamma \rangle \cdot n_{cr}} \vec{B}(\vec{r}) \cdot d\vec{s}, \quad (53)$$

where the integration is along the path of each probe ray through the magnetized plasma, n_{cr} is the critical density at λ_{pr} (see Eq. (5)), and $\langle \gamma \rangle$ is the time-averaged Lorentz factor of streaming magnetized background plasma electrons (*not* of the accelerated electron bunch) that induce Faraday rotation. (Buck *et al.*, 2011; Kaluza *et al.*, 2010) observed typical Faraday rotations $\phi \sim 1^\circ$.

The polarization of probe rays propagating above or below the plasma wave’s axis rotates in opposite directions, since $\vec{B}(\vec{r}) \cdot d\vec{s}$ changes sign. A linear polarizer converts these local Faraday rotations into intensity modulations that a CCD camera detects. To distinguish subtle Faraday modulations from background probe intensity variations, (Buck *et al.*, 2011; Kaluza *et al.*, 2010) employed differential detection with *two* CCD cameras imaging the same region of plasma, as shown in Fig. 31. They detuned polarizers in front of each CCD in opposite directions from the blocking angle for the initial probe polarization. Consequently, when they divided the two raw images Figs. 32a,b, intensity variations unrelated to polarization rotation canceled out, whereas those induced by Faraday rotation doubled. Magnetized plasma regions then stood out clearly, as shown in Fig. 32c,d,e.

The transverse size ($\sim 55 \times 35 \mu\text{m}^2$) of the Faraday-rotated region in Fig. 32c (see dotted ellipse) was determined mostly by imperfect imaging and by ~ 100 fs probe pulse duration (Kaluza *et al.*, 2010). With improved imaging resolution ($\sim 1 \mu\text{m}$) and a shorter (8.5 fs) probe, the imaged signal shrank (see Fig. 32f) to a size limited by the transverse diameter of the plasma wave and the duration of the accelerating electron bunch, rather than the

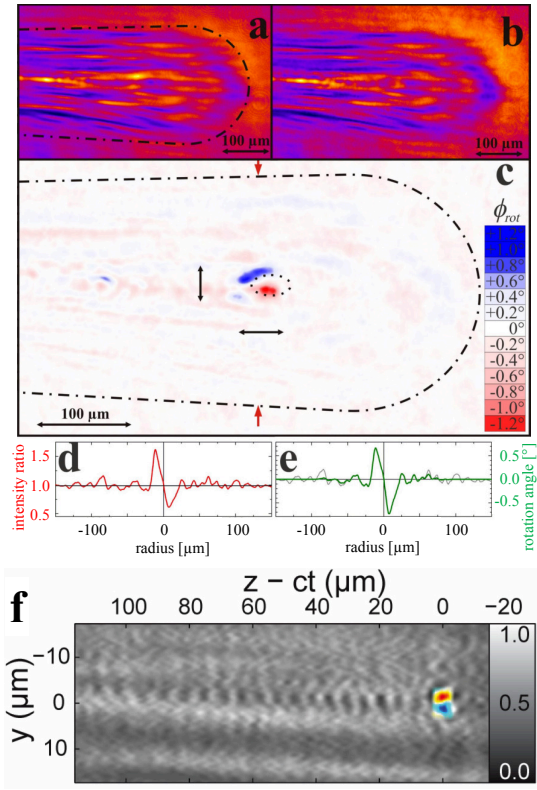


FIG. 32 Color online. Faraday rotation measurements of quasi-linear LWFA. (a, b) Two CCD camera images of the same interaction region in $\bar{n}_e = 4 \times 10^{19} \text{ cm}^{-3}$ plasma taken with 100 fs transverse probe light through polarization analyzers detuned in opposite directions from the blocking orientation. (c) Ratio of images (a)/(b), to highlight intensity variations caused by \pm Faraday rotation (blue, upper / red, lower). (d) Lineout of intensity ratio along vertical line connecting single red arrows at top and bottom of (c); (e) deduced rotation angle. Panels a) thru e) from (Kaluza *et al.*, 2010). f) Similar result in $\bar{n}_e = 3.2 \times 10^{19} \text{ cm}^{-3}$ plasma using 8.5 fs transverse probe and higher resolution imaging, showing Faraday rotation signal (color at $z - ct = y = 0$) induced by magnetic fields from laser-accelerated electron bunch of $5.8_{-2.1}^{+1.9}$ fs duration, superposed on periodic structure (grey scale) observed in single detector, from probe refraction by plasma wave. Panel f) adapted from (Buck *et al.*, 2011).

measurement system. Analysis of the horizontal extent of this improved Faraday signal yielded electron bunch duration $\tau_e = 5.8_{-2.1}^{+1.9}$ fs (see Sec. III.D). As Δt changed, this signal visualized formation and acceleration of the electron bunch (Buck *et al.*, 2011).

b. Transverse shadowgraphy of plasma wakes. Shadowgraphic images of the laser-driven plasma that (Kaluza *et al.*, 2010) recorded on each *individual* detector using $\tau_{pr} \approx 100$ fs probe pulses (see Fig. 32a,b), despite clear intensity variations, showed no evidence of a wake structure oscillating with the period $\lambda_p \approx 5 \mu\text{m}$ expected in $\bar{n}_e = 4 \times 10^{19} \text{ cm}^{-3}$ plasma. This is because $c\tau_{pr}/\lambda_p \approx 6$

cycles of the light-speed wake passed while the probe illuminated it transversely, washing out any signature of individual cycles in the shadowgraphic image. (Buck *et al.*, 2011) found that only by using probe pulses compressed to $c\tau_{pr} \lesssim 0.5\lambda_p$ did a periodic wake appear in the shadowgraph, as shown in Fig. 32f for $c\tau_{pr} \approx 0.43\lambda_p$ ($\tau_{pr} = 8.5$ fs, $\lambda_p \approx 6 \mu\text{m}$, $\bar{n}_e = 3.2 \times 10^{19} \text{ cm}^{-3}$). The period scaled with $\bar{n}_e^{-1/2}$, confirming that it originated from plasma waves. Superposition of Faraday rotation and shadowgraphic images derived from a common detection system (Fig. 32f) then localized the magnetized region surrounding the electron bunch with respect to the wake.

(Buck *et al.*, 2011) split 8.5 fs probe pulses from ~ 65 mJ (< 10 TW) pump pulses that were also compressed to 8.5 fs. Such short drive pulses had only enough energy to generate mildly nonlinear wakes and tens of MeV electrons. Later (Schwab *et al.*, 2013) spectrally broadened split-off probes in a gas-filled hollow core fiber before compressing them to the required few-cycle duration, thereby decoupling probe from drive pulse duration. This enabled transverse probing of strongly nonlinear wakes driven by more powerful (> 30 TW), albeit longer (~ 30 fs), pulses. Moreover, they generated diagnostic pulses as short as $\tau_{pr} = 5.9 \pm 0.4$ fs. A wider range of wakes could thereby be transversely imaged.

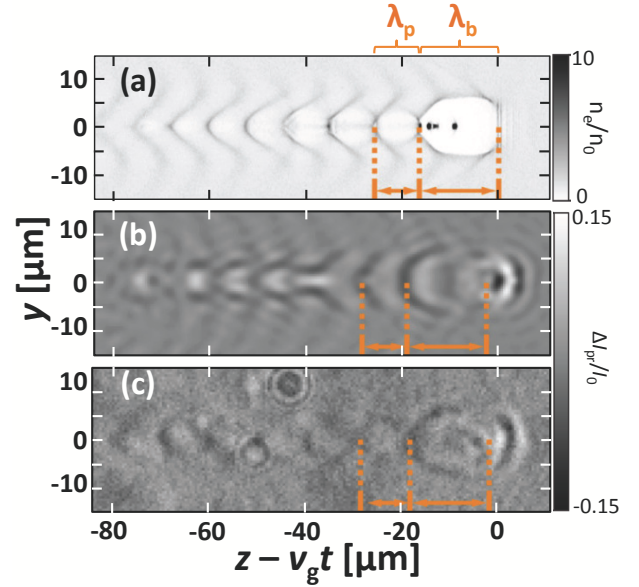


FIG. 33 Color online. Simulated and measured shadowgraphs of strongly nonlinear wake. (a) Simulated electron density relative to ambient $\bar{n}_e \equiv n_0 = 1.7 \times 10^{19} \text{ cm}^{-3}$, driven by 36 fs, 810 nm pulse focused to intensity $2.5 \times 10^{18} \text{ W/cm}^2$, $18.8 \mu\text{m}$ spot (FWHM) after propagating $v_g t \approx 1.2$ mm. (b) Simulated shadowgraph for this distribution, and (c) corresponding experimental shadowgraph using $\lambda_{pr} = 0.75 \mu\text{m}$. Probe intensity change ΔI_{pr} relative to incident probe intensity I_0 is plotted. Brown dotted lines indicate lengths of first (λ_b) and second (λ_p) plasma wave periods. Adapted from (Siminos *et al.*, 2016).

Figure 33c shows a shadowgraph of a right-propagating bubble-regime wake acquired with this versatile system (Sävert *et al.*, 2015). At the head of the wake, two dark, oppositely-curved, arcs define an ellipse with major (minor) axis 10 (7) μm . This feature originates from the first, directly-laser-driven period of the wake. Behind are several smaller (radius $\sim 5\mu\text{m}$), lower-contrast dark circles that originate from subsequent periods of the wake. While it is tempting to correlate these features directly with electron density, in reality dark regions form when probe rays refract in density *gradients*. In addition, the wake moves distance λ_p during transit of even a δ -function probe pulse across the wake, causing temporal blurring. Optical aberrations and the finite light collection angle also influence the image.

To relate light intensity distribution in the shadowgraph to electron density distribution in the wake, (Siminos *et al.*, 2016) carried out 3D PIC simulations using the code EPOCH (Arber *et al.*, 2015) that included a transverse probe pulse. Fig. 33a shows the simulated wake density distribution for conditions and propagation distance ($z = 1.2$ mm) corresponding to the shadowgraph in Fig. 33c. Fig. 33b shows the simulated shadowgraph, taking into account realistic imaging optics. The simulation showed that the probe refracted most strongly as it crossed the propagation axis, where *longitudinal* density gradients $\partial n_e / \partial z$ were strongest. This explained how sharp sub- λ_p features appeared in the shadowgraphs, even though the wake propagated $\sim \lambda_p$ during a probe transit. The length λ_b of the simulated, fully-evacuated leading bubble (Fig. 33a) is $\sim 20\%$ smaller than the major axis of the simulated (Fig. 33b) and measured (Fig. 33c) leading shadowgraph ellipse. This is the result of transverse deflection of probe light at the dense front and back walls of the leading bubble. On the other hand, the diameters of near-circular trailing shadows closely match the length λ_p of trailing buckets of the simulated wake (Fig. 33a). These trailing buckets are less fully evacuated, and have less dense walls, than the leading bucket, and thus deflect probe rays less. (Sävert *et al.*, 2015; Siminos *et al.*, 2016) attributed lengthening of the first bucket to a rapid increase of drive pulse intensity and of the associated relativistic mass of plasma electrons that immediately precedes, and prompts, self-injection of electrons into this bucket. Transverse shadowgraphy enabled direct visualization of this critical, and otherwise elusive, stage of wakefield physics.

4. Electron radiography

Transverse electron radiography complements transverse optical shadowgraphy by probing internal electromagnetic *fields* of a dynamic wake. *Relativistic* electron bunches probe wakes in the ray optics regime, limited by their energy bandwidth, transverse emittance and du-

ration rather than by refraction or diffraction. Hence they are subject to different resolution limits than optical probes. Moreover, as with *longitudinal* electron witness bunches (see Sec. IV.B.1), electron probes are sensitive to lower density plasma structures than optical probes, an advantage for diagnosing GeV plasma accelerators. Electron probes are also insensitive to quasi-neutral plasma and gas *surrounding* a wake, which can imprint unwanted background phase shift on a transverse optical probe.

(Williams, 1995; Williams *et al.*, 1990a,b) simulated interaction of *long* ($\tau > \omega_p^{-1}$), transverse electron probes with wakes in $10^{16} \text{ cm}^{-3} \lesssim \bar{n}_e \lesssim 10^{17} \text{ cm}^{-3}$ plasma. As for long optical probes (see Sec. IV.A), the simulations showed that scatter of low-emittance bunches could characterize global wake structure, but not sub- λ_p structure. (Fainberg *et al.*, 1998, 1996) proposed to resolve sub- λ_p structure of wakes in $\bar{n}_e \sim 10^{11} \text{ cm}^{-3}$ plasma via picosecond transverse electron radiography. At such low \bar{n}_e , however, accelerating fields would be smaller than in conventional RF accelerators. Electron radiography of sub- λ_p structure of wakes in $\bar{n}_e \sim 10^{17} \text{ cm}^{-3}$ plasma requires bunches of few femtosecond duration.

LWFAs themselves provide bunches of this duration (see Sec. III.D), and of very small ε_n (see Sec. III.C). (Schumaker *et al.*, 2013) exploited these properties to probe evolving magnetic fields in a laser-excited solid target with sub-picosecond time- and micrometer space-resolution. (Zhang *et al.*, 2017, 2016b) used ultrashort, low- ε_n , 60-80 MeV electron bunches from one LWFA to probe transversely the internal electromagnetic fields of a second LWFA ($\lambda_p \approx 65\mu\text{m}$) driven by a split-off portion of the same laser pulse (see Fig. 34a). The diverging probe, after expanding to $\sim 800\mu\text{m}$ diameter, irradiated a multi- λ_p section of the subject wake, which deflected probe electrons transversely. A scintillating screen at distance L_{scr} from the interaction recorded the 2D profile $I(x, y)$ of the transmitted electron bunch (see Fig. 34a). The wide field of view enabled observation of variations in wake structure along its length. For example, a radiograph of a wake within a density ramp $n_e(z)$ (Fig. 34b,c) revealed changing λ_p along the ramp.

As with transverse optical shadowgraphs (see Sec. IV.C.3), the electron radiograph $I(x, y)$, though not a simple projection, is closely related to the wakefield that produced it. For best wake reconstruction, L_{scr} should be small enough to avoid electron trajectory crossing, which loses information. For wakefield amplitude given by Eq.(4a), this condition leads to $L_{scr} \lesssim M\gamma_{pr}\lambda_p/10$, where M is a geometric magnification factor such that $M = 1 (> 1)$ for a collimated (diverging) probe, and $\gamma_{pr} = (1 - \beta_{pr}^2)^{-1/2}$ is the probe Lorentz factor (β_{pr} = normalized probe velocity). Optimal L_{scr} can range from a few to hundreds of millimeters. In the limit of an extremely short ($\tau_{pr} \ll \omega_p^{-1}$) bunch probing a quasi-static linear wake that perturbs

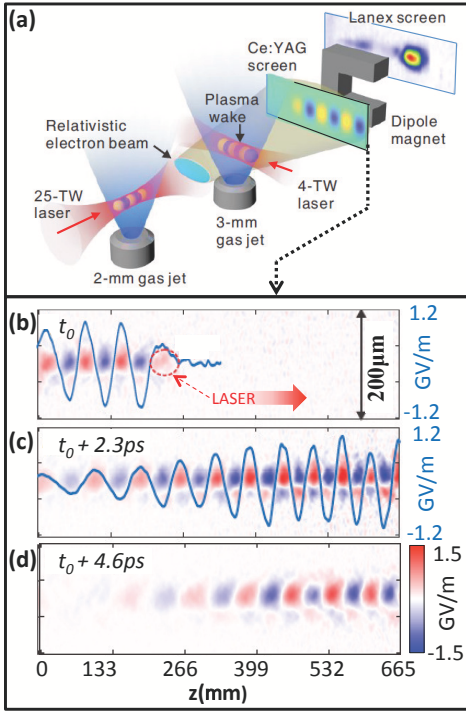


FIG. 34 Color online. Transverse electron radiography of laser wakefield. (a) Schematic experimental setup. The electron probe bunch (4 fs FWHM, 2-10 pC, 7 mrad FWHM divergence) from one plasma accelerator (2mm gas jet, $\bar{n}_e = 8 \times 10^{18} \text{ cm}^{-3}$, 95% He, 5% N₂) driven by a 25 TW, 40 fs FWHM Ti:S laser pulse, propagates transversely through the “subject” plasma accelerator (3mm gas jet, with synchronized 4 TW, 100 fs FWHM Ti:S drive pulse) located 11 cm away, then exposes a Ce:YAG scintillator further downstream. Magnetic spectrometer can measure probe bunch energy with scintillator removed. From (Zhang *et al.*, 2017). Below: scintillator images at probe delays (b) t_0 , (c) $t_0 + 2.3 \text{ ps}$, and (d) $t_0 + 4.6 \text{ ps}$ of wake generated in tapered density up-ramp ($\bar{n}_e \approx 2.5 \times 10^{17} \text{ cm}^{-3}$ at $z = 0$ to $3.5 \times 10^{17} \text{ cm}^{-3}$ at $z = 665 \mu\text{m}$), yielding decreasing plasma period evident in panels (b), (c). Panels b) thru d) from (Zhang *et al.*, 2018).

incident electron momentum p_{pr} only slightly, the effects of the radial $[E_r(r, z)]$ and longitudinal $[E_z(r, z)]$ wake electric fields on the probe decouple via the Panofsky-Wenzel theorem (Panofsky, 1956). $E_{r,z}(r, z)$ can then be recovered exactly by solving two Abel transforms

$$\frac{\partial I}{\partial z} = \kappa K_m \nabla^2 \int_{-s}^s E'_z(r, z) dx \quad (54a)$$

$$\frac{\partial I}{\partial y} = \kappa K_m \nabla^2 \int_{-s}^s E'_r(r, z) dx, \quad (54b)$$

where $\kappa = eL_m/\beta_{pr}cp_{pr}$, $K_m = \exp[-(k_p\sigma_E)^2/2]$ is an averaging factor caused by wake motion that depends on wake width σ_E , and $E'_{r,z}$ denote static fields with the same form as $E_{r,z}$. Reconstruction becomes less accurate, but still possible, for strongly nonlinear wakes. The wake’s magnetic field then contributes significantly

to electron deflection. Unlike an optical probe, the electron probe senses the electric (as well as magnetic) field of the accelerating electron bunch inside the wake. This is because the bunch’s electric field, unlike its refractive index, is not suppressed by a factor γ_e^{-1} , which makes a highly relativistic bunch practically invisible to an optical probe, except via Faraday rotation (see Sec. IV.C.3). Simultaneous sensitivity to the electric and magnetic fields of highly relativistic accelerating bunches and of tenuous plasma structures will make transverse electron radiography an attractive choice for characterizing multi-GeV laser- and beam-driven plasma accelerators.

(Clayton *et al.*, 2016), working at SLAC’s FACET (Hogan *et al.*, 2010), mapped longitudinal variation of fields within a strongly blown out PWFA in one shot, using electrons in the trailing portion of the drive bunch itself ($\sim 20 \text{ GeV}$, $\sigma_z \sim 25 \mu\text{m}$) as witnesses. The energy spectrum of these electrons, imaged from the PWFA exit plane, exhibited a series of energy peaks and transverse bunch size modulations originating from their transverse oscillations in the bubble’s radial E_r fields as they accelerated in its longitudinal E_z fields. Analysis of this structure enabled reconstruction of E_r along the bubble’s length, and showed that it was longitudinally uniform to within $\pm 3\%$, as expected for a nearly fully blown out bubble. From the Panofsky-Wenzel theorem, the authors inferred comparable radial uniformity of E_z , a key requirement for emittance preservation. Such field maps can help to optimize placement and shape of separate, shorter, higher charge witness bunches.

D. “Movies” of wake evolution

1. Multi-shot transverse probes

Transverse optical (Sec. IV.C.3) or electron (Sec. IV.C.4) probing records wake shadowgraphs or radiographs at fixed delay Δt between drive and probe pulses. If shot-to-shot variations can be neglected, a sequence of projections recorded over multiple shots with varying Δt yields a “movie” of the wake’s evolution as it propagates through the plasma.

Fig. 35 shows a Δt -sequence of six optical shadowgraphs of a strongly nonlinear wake driven by 35-fs, 750 mJ pulses in $\bar{n}_e = 1.65 \times 10^{19} \text{ cm}^{-3}$ plasma (Sävert *et al.*, 2015). They illustrate several stages of wake evolution. Early in the laser-plasma interaction [Fig. 35 (a)], successive dark regions in the shadowgraph (positions highlighted by white vertical lines beneath) were spaced nearly equally, indicating a linear plasma wave. Subsequently, contrast between dark and light regions increased [Fig. 35(b)], signifying increased wave amplitude. In Fig. 35(c), the first plasma period lengthened, signaling onset of strongly nonlinear laser-plasma interaction (see Sec. IV.C.3.b). Simultaneously, $\sim 65 \mu\text{m}$ ahead of the

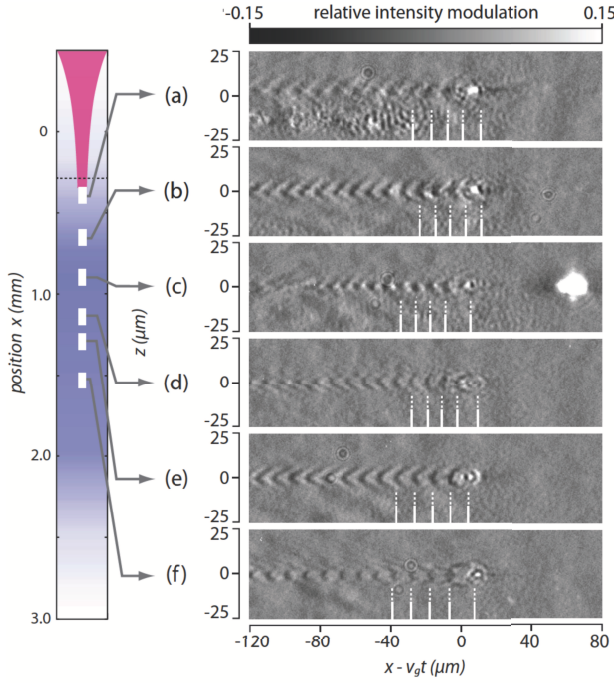


FIG. 35 Color online. Multi-shot shadowgraphic “movie” of strongly nonlinear wake propagating through gas jet. Left: ionized gas density profile (deepest purple shading: $\bar{n}_e = 1.65 \times 10^{19} \text{ cm}^{-3}$; white: $\bar{n}_e = 0$), intensity profile of focusing, downward-propagating laser (red funnel-shaped region; tightest focus at horizontal dashed line). (a)-(f): experimental shadowgraphs (right) at six positions within jet indicated by white rectangles (left), recorded with probes of wavelength $\lambda_{pr} \approx 0.75 \mu\text{m}$ and transform-limited duration 4.4 fs. White vertical lines (right): axial positions of plasma wave’s peaks as deduced from simulated shadowgraphs (see Sec. IV.C.3). From (Sävert *et al.*, 2015).

wake, bright plasma emission, spectrally much broader (600-1000 nm) than the drive pulse, was observed, consistent with “wave breaking” radiation (see Sec. IV.A), a signature of onset of self-injection (Thomas *et al.*, 2007). Continuing increase in shadow contrast at the beginning of the wave train [Figs. 35(d)-(f)] signifies increasing density gradient at the front of the bubble as the wave becomes highly nonlinear. In Fig. 35(f), the direction of curvature of the trailing shadowgraph wave periods even reverses. These features are closely linked to transverse wave breaking (Bulanov *et al.*, 1997a).

Two extensions of the results in Fig. 35 offer rich possibilities for future diagnostic development. First, the shadowgraphic movie of the evolving plasma structure can be coordinated with a Faraday rotation movie of the evolving electron bunch, as (Buck *et al.*, 2011) already did for single frames [see Fig. 32(f)]. The magnetic signature of injected electrons should appear with wave-breaking radiation as the primary bubble lengthens [Fig. 35(c)], and evolve in subsequent frames. Second, one could acquire the movie in one shot by multiplexing

the probe pulse. The possibilities parallel those considered in developing single-shot FDH from multi-shot FDI (see Fig. 25). One is to split the probe into N replicas, each backlighting a different section of the interaction region, and projecting its shadowgraph onto a separate detector. Another possibility (*cf.* FDH) is to chirp the probe pulse. This relieves the requirement of maintaining few-cycle pulse duration, and maps probe arrival time at the wake onto probe frequency (Siminos *et al.*, 2016). One could then distribute frequency bands $\Delta\omega_i$ ($i = 1, 2, \dots, N$) of the wake-diffracted probe to separate detectors, each recording a color-coded 2D shadowgraph of a different stage of wake evolution. However, as discussed in connection with a similar suggestion for chirped longitudinal probes (see Sec. IV.C.1), the wake diffracts the probe over time scale $t \ll \Delta\omega_i^{-1}$, imprinting new frequency components on each band that cause them to contaminate neighboring bands. Instead a holistic algorithm, analogous to FDH, is needed to deconvolve a time sequence of 2D images from the shadowgram of a chirped pulse. (Nakagawa *et al.*, 2014) recently demonstrated an all-optical “motion picture femto-photography” method that recovered images of propagating lattice vibration waves or expanding plasmas with few- μm spatial resolution and frame interval ~ 200 fs. Extension of such methods to transverse wake shadowgraphy is a promising direction for future research.

2. Single-shot frequency-domain streak camera

(Li *et al.*, 2014b, 2010) introduced an alternative way to record single-shot “movies” using temporally broad, chirped probe pulses propagating *obliquely* to the pump pulse, as shown in Fig. 36a,b. This approach generalized FDH, and was insensitive to slight temporal broadening that occurred in manipulating the probe pulses.

In Fig. 36a,b a chirped probe pulse crosses the path of a pump-driven object (“wake”) at angle α inside a medium (“jet”) of thickness L . In the probe frame, the evolving object sweeps across the probe pulse profile, imprinting a phase shift “streak” of length vector

$$\vec{L}_{streak} = L[(\cos \alpha - v_{pr}/v_{ob})\hat{z}_{pr} + \sin \alpha \hat{y}_{pr}], \quad (55)$$

that makes projection angle

$$\phi = \tan^{-1} \frac{(v_{pr}v_{ob}/c) \sin \alpha}{v_{ob} - v_{pr} \cos \alpha} \quad (56)$$

with the object’s propagation direction \hat{z}_{ob} . Here v_{ob} and v_{pr} denote lab frame group velocities of object and probe, respectively, in the medium. The streak is recovered by interfering the probe spectrally with a temporally advanced, equivalently chirped reference pulse (not shown in Fig. 36a,b), as in FDH (see Sec. IV.C.1). Figure 36c-e shows streaks of the nonlinear index of a pump transiting

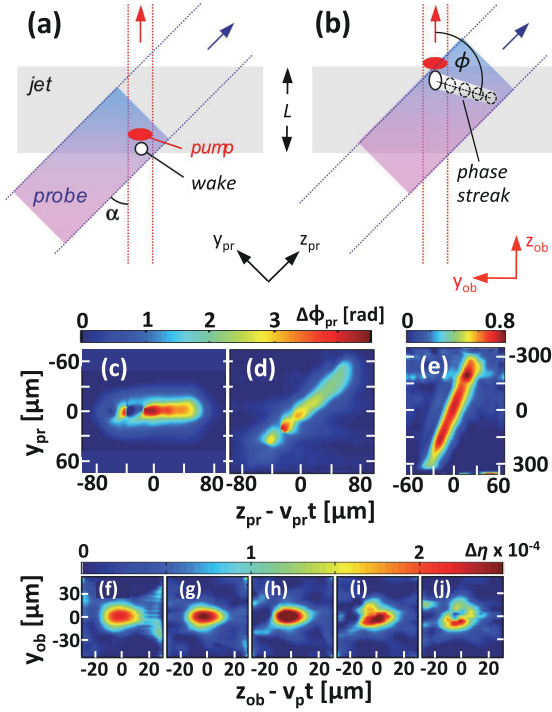


FIG. 36 Color online. Imprint of phase-shift streak on chirped probe pulse propagating obliquely to evolving laser-driven wake. Beginning (a) and end (b) of imprint, showing lab (α) and projection (ϕ) angles. Middle: 3 phase streaks from pump pulse transit through glass Kerr medium, recorded simultaneously for α (ϕ) = 0.1° (1°) (c); 1.4° (27°) (d); 9.7° (68°) (e). Pump entrance into medium corresponds to right-most end of each streak. Bottom: 5-frame “movie” of pump-induced index change profile $\Delta\eta$ at normalized propagation distances $z_{ob}/L = 0.17$ (f), 0.33 (g), 0.49 (h), 0.65 (i), 0.81 (j) into Kerr medium, reconstructed tomographically from 5 streaks. Adapted from (Li *et al.*, 2014b).

a glass Kerr medium, recorded simultaneously on probe pulses propagating at 3 different angles. A series of line-outs perpendicular to each streak axis \hat{L}_{streak} constitutes a time sequence of the wake’s projections at angle ϕ .

The streak resolves N stages of the object’s evolution, where N is the number of separated objects that can be lined up sequentially along \hat{L}_{streak} (*e.g.* $N = 5$ for the situation in Fig. 36b). Phase streaks with $\phi = 0$ (Fig. 36c), obtained with co-propagating pump and probe with $v_{pr} \neq v_{ob}$, reveal evolution of the object’s *transverse* profile, as it drifts longitudinally along the probe profile. This drift, a disadvantage in FDH because it blurs the recovered image, here provides valuable dynamic information. Streaks at $\phi = \pi/2$ (approximated by Fig. 36e) record evolution of the object’s *longitudinal* profile as it drifts sideways across the probe profile. Streaks at intermediate ϕ (Fig. 36d) record evolution of a diagonal profile. (Li *et al.*, 2010) called this type of measurement a “frequency-domain streak camera” (FDSC).

By probing an evolving object simultaneously at *sev-*

eral discrete angles, (Li *et al.*, 2014b) reconstructed a time sequence of its entire 2D profile using tomographic algorithms. For example, Fig. 36f-j shows a 5-frame “movie” of the nonlinear index profile of a 10 μJ , 30 fs laser pulse propagating through glass, reconstructed in one shot using five probes interfering with one reference pulse. Frames f-i show positive nonlinear index shift intensifying as the pump self-focuses, while in frame j a compensating negative shift appears in the center of the profile as a multi-photon-excited plasma appears. (Li *et al.*, 2014b) called this extension of FDSC “frequency-domain tomography” (FDT). (Matlis *et al.*, 2012) demonstrated a complementary *spectrally*-multiplexed tomography (SMT), that probed an object at a *continuous* range of angles by angularly dispersing the frequency components of an ultrafast probe pulse. After measuring the object-induced phase shift of each component by FDI, they reconstructed the position and cross-sectional structure of two quasi-stationary elliptical plasma filaments in one shot. Now that FDT and SMT have been demonstrated in such test experiments, their application to visualizing plasma wakes and plasma channels is a promising future direction.

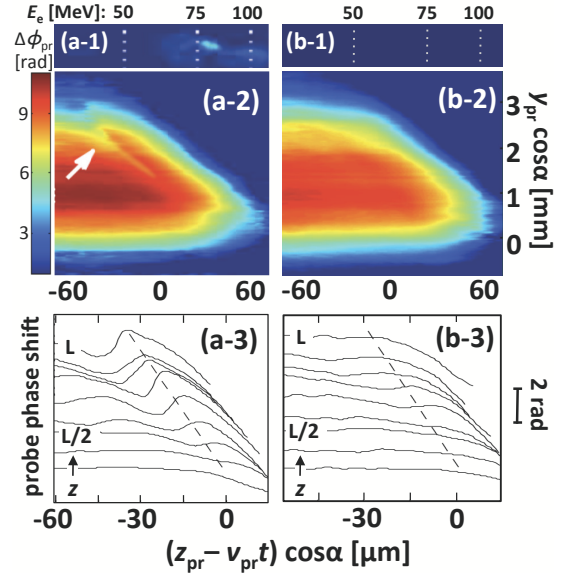


FIG. 37 Color online. FDSC study of nonlinear LWFA dynamics, showing data from shot (a) (left column) and (b) (right) at $\bar{n}_e = 2 \times 10^{19} \text{ cm}^{-2}$. Top row: electron spectra, showing quasi-monoenergetic 80 MeV electrons (a-1), and no electrons (b-1). Middle, bottom rows: reconstructed probe phase shift $\Delta\phi_{pr}$. Pump drifts from lower right to upper left as it transits jet, imprinting nearly uniform background plasma-induced phase-shift $\Delta\phi_p$ (yellow-orange area) as it ionizes gas. But only (a-2) shows narrow phase-shift dip $\Delta\phi_b$ (yellow streak, highlighted by white arrow in (a-2) and line-outs in (a-3)) imprinted by evolving bubble. Dashed lines in (a-3) and (b-3) show drift trajectory of center of pump pulse. Adapted from (Li *et al.*, 2014a).

Meanwhile, (Li *et al.*, 2014a) used *single*-probe FDSC

to characterize formation, propagation, and lengthening of a laser-generated plasma bubble as it accelerated electrons quasi-monoenergetically to ~ 100 MeV. Fig. 37 summarizes results for 2 contrasting shots, one (left column) that produced a high-quality electron bunch (a-1), the other (right) no relativistic electrons (b-1). During both shots, a loosely-focused chirped probe pulse of bandwidth $\Delta\lambda_{pr} \approx 10$ nm crossed the path of a tightly-focused drive pulse in a He gas jet of length $L \approx 3$ mm at angle $\alpha = 8.6^\circ$. At this α , plasma structures drifted across the probe profile at $\phi \approx 90^\circ$. For both shots, the quasi-static, pump-ionized plasma column imprinted a wide uniform background phase shift $\Delta\phi_p \sim 10$ mrad (orange areas in Fig. 37, middle row). Uniquely on shot (a), a dynamic bubble of diameter $\lambda_p\sqrt{a_0}/\pi \sim 10\mu\text{m}$ (Lu *et al.*, 2007) in the pump's immediate wake generated a narrow phase-shift streak $\Delta\phi_b \sim -2$ mrad of opposite sign, due to the absence of free electrons inside the bubble and the dearth of electrons in the bubble's side (relative to its front and rear end) walls. Thus, after the pump blew out a fully-formed bubble, which occurred at $z \approx 2L/3$ for the case shown in Fig. 37a, $\Delta\phi_b$ carved a narrow dip (yellow streak in Fig. 37a-2, highlighted by arrow, lineouts in a-3) into the broader $\Delta\phi_p$ profile, exhibiting a time sequence of *longitudinal* projections of the plasma bubble. On shot (b), no $\Delta\phi_b$ phase dip was observed, *i.e.* no bubble formed, consistent with no relativistic electrons.

(Li *et al.*, 2014a) observed variations in the length, depth and shape of the $\Delta\phi_b$ streak, and in corresponding electron spectra, as \bar{n}_e (and thus P/P_{cr}) changed. For example, at 15% *lower* \bar{n}_e than in Fig. 37a, the bubble formed fully only near the end of the jet ($z \approx 5L/6 \approx 2.5$ mm) due to weaker self-focusing, leaving acceleration length ($L/6 \approx 0.5$ mm) shorter than the dephasing length L_d . Consequently acceleration was incomplete, and broad low-energy electron spectra were observed. Conversely, at 10% *higher* \bar{n}_e than in Fig. 37a, the bubble formed at $z < L/2$, leaving acceleration length $> 4L_d$. This also yielded a broad electron energy spectrum and poor beam quality, due to strong dephasing. Stable, nearly mono-energetic electron beams were observed only in a narrow range $\bar{n}_e = 2.0 \pm 0.1 \times 10^{19} \text{ cm}^{-3}$, for which FDSC showed acceleration length $\sim 1.5L_d$, assuming injection coincided with full bubble formation. Simulations confirmed this optimal acceleration length, somewhat greater than L_d . Evidently moderate dephasing helps to compress the electron spectrum by decelerating the fastest electrons just enough for the slowest electrons to catch up (Yi *et al.*, 2010). Among other LWFA physics, (Li *et al.*, 2014a) also observed that bubbles lengthened as they finished accelerating electrons, a signature of beam loading, and that bubbles were only partially evacuated at the injection threshold.

Simulations show that FDSC can access additional LWFA physics by using wider bandwidth probe and reference pulses. As an example, Fig. 38a shows the 3D

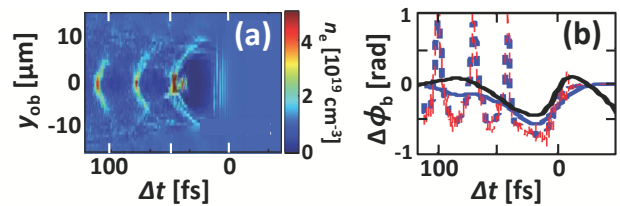


FIG. 38 Color online. Simulated FDSC experiment. (a) VLPL simulation of wake n_e profile at $z = 2L/3 = 2$ mm, for conditions of data in Fig. 37a. (b) Line-out of bubble phase shift $\Delta\phi_b$ for ideal FDSC probe (red dashed curve), and probes of 100 (thick blue dashed) and 10 nm (blue solid curve) bandwidth, compared with measured $\Delta\phi_b$ (black solid curve). Adapted from (Li *et al.*, 2014a).

wake electron density profile at $z = 2L/3 = 2$ mm for conditions corresponding to data in Fig. 37a, simulated using the PIC code Virtual Laser Plasma Lab (VLPL) (Pukhov, 1999). The primary accelerating cavity, with injected electrons at its rear, and two trailing cavities separated by electron-density sheaths of $\sim 1\mu\text{m}$ thickness, are visible. Fig. 38b shows a $z = 2L/3$ lineout of the $\Delta\phi_b$ streak of a simulated FDSC experiment, using a 400 nm probe of unlimited bandwidth (dashed red curve) and with finite bandwidths $\Delta\lambda_{pr} = 100$ nm (dashed blue) and 10 nm (solid blue). The last curve agrees well with the measured FDSC line-out (black curve) from Fig. 37a. However, both average over sharp electron density spikes separating the three cavities. Direct observation of these sheaths is an important future diagnostic goal, since subtle sheath thickness variations govern electron injection (Yi *et al.*, 2010). On the other hand, a simulated $\Delta\lambda_{pr} = 100$ nm probe resolves these spikes well (dashed blue curve). Visible supercontinuum probe-reference pulses (Kim *et al.*, 2002a) provide the necessary bandwidth, and should resolve μm -size structures in plasma accelerators that do not themselves produce strong background supercontinuum α (Ralph *et al.*, 2009) at the probe angle and wavelength range. Otherwise, ultraviolet supercontinuum probe-reference pulses and/or large α will be necessary for high-resolution FDSC.

3. Single-shot imaging of meter-long wakes

FDSC studies described in the previous sub-section relied on the assumption that a phase modulation $\Delta\phi_{pr}(z_0)$ of width w_{ob} that an object imprinted locally on a probe pulse at position $0 < z_0 < L$ within a medium preserved its shape until it reached the medium's exit plane ($z = L$). An imaging system then relayed it to a detector. If, however, the distance $\Delta z \equiv L - z_0$ had exceeded diffraction length $\Delta z_{diff} \approx \pi w_{ob}^2/\lambda_{pr}$, then the imprinted phase modulation would have diffracted before reaching the exit. Thus *e.g.* a $\lambda_{pr} = 0.4\mu\text{m}$ probe can faithfully record the evolving shape of a plasma bubble of radius

$w_{ob} = 10\mu\text{m}$ (see Fig. 38a) over propagation distance $\Delta z \sim 1\text{ mm}$, a limit that the experiment depicted in Fig. 37 barely satisfied, since the bubble formed $\sim 1\text{mm}$ from the jet exit. This places an additional limit on resolving *e.g.* bubble sheath structures, over and above the limit set by probe bandwidth.

The depth of field Δz_{dof} of the imaging system that relays the wake-modulated probe(s) from $z = L$ to the detector must similarly be matched to Δz_{diff} of the smallest sub-structure one wishes to resolve, otherwise portions of the imprinted streak will be out of focus at the detector. FDSC of plasma accelerators of length $\Delta z > \Delta z_{diff}$ encounters depth-of-field limits. Examples include multi-GeV LPAs of multi-cm acceleration length (Leemans *et al.*, 2014; Wang *et al.*, 2013), meter-scale e-beam-driven PWFAs (Blumenfeld *et al.*, 2007), and proton-driven PWFAs hundreds of meters long (Caldwell *et al.*, 2009; Geschwendtner *et al.*, 2016).

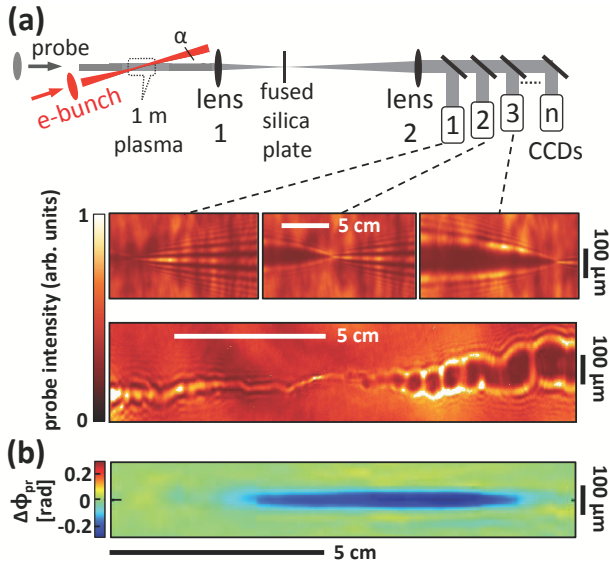


FIG. 39 Color online. Visualization of multi-cm plasma accelerator structures. (a) Top: schematic MOPI setup. Adapted from (Li *et al.*, 2013b). Middle, triple panel: intensity modulation of 100 fs probe that propagated at angle 4° , delay $\Delta t \approx 100\text{ ps}$ behind a 20 GeV, 2 nC, 100 fs electron bunch in hydrogen plasma of density $\bar{n}_e = 3 \times 10^{17}\text{ cm}^{-3}$, imaged from 3 object planes to each of 3 CCD cameras. Lower panel: image of unstable portion of electron trajectory captured by CCD1. (b) Plot of continuous phase shift $\Delta\phi_{pr}(y, z)$ induced by $\bar{n}_e \approx 10^{16}\text{ cm}^{-3}$ plasma over 10 cm path on 100 fs probe pulse that propagated at angle 1° , $\Delta t = 1.7\text{ ps}$ behind a 3 mJ laser pulse in air, reconstructed from 4 CCD images using Gerchberg-Saxton algorithm. Panel b) adapted from (Li *et al.*, 2013b).

Multiplexed transverse optical shadowgraphy (Sec. IV.B.2.3) or electron radiography (Sec. IV.B.4) provides one potential solution to single shot imaging of plasma structures without depth-of-field limits, but will require maintaining few-fs duration of multiple replicas

of the incoming probe. Alternatively, (Li *et al.*, 2013b) introduced multi-object-plane imaging (MOPI) of a small- α probe, illustrated in Fig. 39. MOPI multiplexes detection of a single probe after, rather than before, it interacts with the plasma structure. Fig. 39a (top) schematically depicts the setup. A collimated probe pulse (gray) crossed the path of a synchronized wake driver (red) at angle α , with beam waist w_0 , illuminating wake structures over propagation distance $z \sim w_0/\alpha$. In contrast to FDSC, (Li *et al.*, 2013b) used a probe pulse compressed to $\sim 100\text{ fs}$. Thus it characterized only a $\sim 100\text{ fs}$ longitudinal slice of the pump-generated structure. The illuminated slice swept transversely across the compressed probe profile, mapping its index profile at propagation distance z onto transverse position x on the probe profile via the relation $x = z\alpha$. Tilting the probe intensity front by angle $\alpha/2$ with a prism prevented the phase streak from walking off of the compressed probe profile, extending the propagation distance that could be probed. After the interaction, copies of the phase-modulated probe created by beam splitters were imaged through a $4f$ system from MOPs along the pump path to corresponding image planes. Phase-contrast imaging (PCI), which (Li *et al.*, 2013b) implemented by placing a thin Kerr medium at the Fourier plane of the $4f$ system (see Fig. 39a), converted phase modulations to easily detectable amplitude modulations. CCD cameras recorded “bow-tie”-shaped images (Fig. 39a, triple panel), in which “knots” corresponded to object planes, wider wings to nearby out-of-focus regions.

Transverse line-outs of the “knots” of recorded bow-tie intensity patterns straightforwardly yield phase shifts $\Delta\phi_{pr}(x_{ob}, z_i)$ that the plasma structure induced on the probe at selected object planes z_i . (Li *et al.*, 2013b) reconstructed phase shifts at intervening values of z by iteratively fitting the complete diffraction patterns of overlapping bow-ties using a Gerchberg-Saxton algorithm (Fienup, 1982). Fig. 39b shows an example of a continuous phase-shift streak $\Delta\phi_{pr}(x_{ob}, z)$ over a 10-cm propagation path, thus reconstructed from four MOPI bow-tie images of a probe that propagated at $\Delta t = 1.7\text{ ps}$ behind a pump pulse propagating in air. The main feature in this reconstructed phase profile originates from plasma of density $\bar{n}_e \approx 10^{16}\text{ cm}^{-3}$, demonstrating high sensitivity of MOPI + PCI to tenuous plasma structures.

(Zgadza *et al.*, 2016) have begun to use MOPI to image plasma wake structures driven by 20 GeV, 2 nC electron bunches over meter-scale propagation distances at SLAC’s FACET. The bottom panel in Fig. 39a shows a “bow-tie” image of a 15-cm segment of the unstable propagation path of a 20 GeV e-bunch through laser-ionized hydrogen plasma, observed at $\Delta t = 100\text{ ps}$ after passage of the bunch. At this late delay, the original electron wake had transferred most of its energy into an “ion wake” (Lotov *et al.*, 2014; Sahai *et al.*, 2016; Vieira *et al.*, 2012), that nevertheless preserved some features of the

electron wake's propagation history. For example, transverse oscillations with period of several cm evident in this image originated from the e-bunch's interaction with transverse density gradients in the laser-ionized plasma column (Adli *et al.*, 2016). Similarly, *longitudinal* oscillations of sub-cm period are a remnant of mismatched e-beam propagation with alternating focusing and defocusing. These MOPI studies are beginning to elucidate the largely unexplored relationship between short-lived electron and long-lived ion wakes, which in turn governs the repetition rate of PWFAs and LWFA.

Diagnosis of meter-scale plasma accelerator structures via MOPI is at an early stage. Many opportunities remain for future research. Here we emphasize two. First, MOPI-PCI should be used to probe *electron* wakes directly at delays $0 < \Delta t < 1$ ps behind e-bunch or laser pulse drivers. Second, advanced MOPI methods that visualize an extended Δt range, rather than only a single Δt slice, of a meter-scale plasma accelerator in a single shot, should be developed, analogous to the extension of FDI (Sec. IV.B.2) to FDH (Sec. IV.C.1). Straightforward multiplexing using multiple MOPI probes at different Δt (analogous to Fig. 25a) would be a first step. The possibility of combining MOPI with stretched-probe techniques (FDSC, FDT) should also be explored.

E. Scaling of wake probes with plasma density

Most single-shot optical wake diagnostics reviewed here were demonstrated on MeV plasma accelerators at $\bar{n}_e \sim 10^{19} \text{ cm}^{-3}$. However, future plasma accelerator research will focus on multi-GeV accelerators at $10^{17} \text{ cm}^{-3} < \bar{n}_e < 10^{18} \text{ cm}^{-3}$. Here we consider how these diagnostic methods scale as \bar{n}_e decreases.

For transverse optical probes, signal strength is proportional to plasma structure width L_\perp , which scales as $\lambda_p \sim \bar{n}_e^{-1/2}$. For shadowgraphs, plasma structure visibility is proportional to local probe deflection angle

$$\Delta\theta_{\text{def}} = \int_0^{L_\perp} \frac{d\eta}{dz} ds_\perp \approx \frac{d\eta}{dz} L_\perp \propto \frac{\bar{n}_e}{n_{cr}}, \quad (57)$$

where $d\eta/dz$ is the local gradient of refractive index $\eta = (1 - n_e/n_{cr})^{1/2} \approx 1 - n_e/2n_{cr}$ along the wake propagation axis z , approximated as a constant over L_\perp in the penultimate expression of Eq. (57). For local index change $\Delta\eta = \Delta n_e/2n_{cr}$ over distance Δz , $\Delta n_e \propto \bar{n}_e$ and $\Delta z \propto \lambda_p \sim \bar{n}_e^{-1/2}$ as \bar{n}_e changes. Taking $d\eta/dz \propto \Delta\eta/\Delta z$, and scaling L_\perp as noted above, we obtain the density scaling in the final expression of Eq. (57): equivalent shadowgraph contrast corresponds to constant \bar{n}_e/n_{cr} . Since $n_{cr} \propto \lambda_{pr}^{-2}$, equivalent contrast is maintained by scaling $\lambda_{pr} \sim \bar{n}_e^{-1/2}$ as \bar{n}_e changes. Fig. 40 presents simulated shadowgraphs of wakes in plasma of density $\bar{n}_e =$ (a) $1.7 \times 10^{19} \text{ cm}^{-3}$ and (b) $0.48 \times 10^{19} \text{ cm}^{-3}$

that confirm (57). Probe wavelength $\lambda_{pr} = 0.75 \mu\text{m}$ yields a high-contrast shadowgraph (c) at the higher \bar{n}_e , but low contrast at the lower \bar{n}_e (d). Shifting to $\lambda_{pr} = 1.4 \mu\text{m}$ recovers high contrast at the lower \bar{n}_e (e).

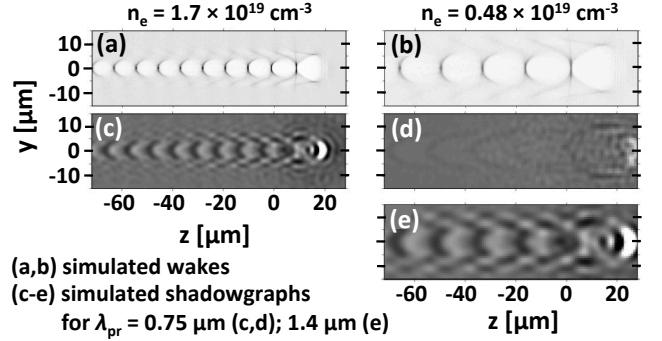


FIG. 40 3D PIC simulations showing scaling of transverse optical shadowgraphy with plasma density \bar{n}_e . Top row: electron density profiles of plasma wakes driven by $\lambda_{pu} = 0.8 \mu\text{m}$, $\sim 0.7 \text{ J}$, 30 fs pulses in $\bar{n}_e =$ (a) 1.7 ($\lambda_p = 9 \mu\text{m}$) and (b) $0.48 \times 10^{19} \text{ cm}^{-3}$ ($\lambda_p = 17 \mu\text{m}$) plasma. Second and third rows: simulated transverse shadowgraphs using $\lambda_{pr} = 0.75 \mu\text{m}$ [panels (c), (d)], and $1.4 \mu\text{m}$ [panel (e)]. Courtesy E. Siminos.

The condition (57) implies constant λ_{pr}/λ_p . Thus spatial imaging resolution *relative* to feature size remains constant, even though *absolute* resolution scales with λ_{pr} . Comparison of panels (c) and (e) of Fig. 40 confirms that constant \bar{n}_e/n_{cr} preserves feature resolution.

Similar arguments applied to Eq. (53) show that the sensitivity of Faraday rotation also depends on \bar{n}_e/n_{cr} , although the strength of \vec{B} remains an independent scaling parameter. For an interferometric probe propagating at angle α with respect to the wake (*e.g.* FDSC, MOPI), signal strength is given by local probe phase shift

$$\Delta\phi_{pr} = \frac{2\pi}{\lambda_{pr}} \int_0^{L_\perp/\sin\alpha} [\eta(s) - 1] ds \approx \frac{\pi}{\sin\alpha} \frac{L_\perp}{\lambda_{pr}} \frac{\bar{n}_e}{n_{cr}} \quad (58)$$

integrated over the probe's oblique path across the wake, along which the last expression in (58) assumes constant $n_e \propto \bar{n}_e$. The factor L_\perp/λ_{pr} now appears in addition to \bar{n}_e/n_{cr} . However, constant \bar{n}_e/n_{cr} implies constant L_\perp/λ_{pr} , and thus constant $\Delta\phi_{pr}$. The above remarks about resolution carry over without change. Thus \bar{n}_e/n_{cr} is a universal scaling factor for transverse optical probes.

For longitudinal optical interferometric probes (*e.g.* FDI, FDH), the phase shift is

$$\Delta\phi_{pr} = \frac{2\pi}{\lambda_{pr}} \int_0^{L_\parallel} [\eta(s) - 1] ds \approx \pi \frac{L_\parallel}{\lambda_{pr}} \frac{n_e}{n_{cr}}, \quad (59)$$

where again the last expression assumes constant $n_e \propto \bar{n}_e$ along the probed length L_\parallel . Here the limiting value of L_\parallel determines \bar{n}_e scaling. Several possibilities can arise. If the gas cell (or pump Rayleigh) length L limits the interaction and remains constant as \bar{n}_e changes, then

Eq. (59) yields $\Delta\phi_{pr} \propto \bar{n}_e$ for fixed λ_{pr} , $\Delta\phi_{pr} \propto \bar{n}_e^{1/2}$ for fixed \bar{n}_e/n_{cr} , or $\Delta\phi_{pr}$ constant for $\lambda_{pr} \propto \bar{n}_e^{-1}$. If L can be adjusted as \bar{n}_e changes, then often longitudinal drift of probe-driver delay due to group-velocity mismatch $\Delta v_g = v_g^{(pr)} - v_g^{(dr)}$, which must be limited to a small fraction $f \ll 1$ of λ_p to avoid washing out longitudinal wake structure, determines $L_{||}$. This limit is common for LWFA, where λ_{pr} must differ significantly from λ_{pu} so that it can be spectrally filtered from forward-scattered pump light, but would also arise for PWFA, where the velocity ($\approx c$) of a relativistic particle bunch driver would always exceed $v_g^{(pr)}$. In this case the allowable probe-driver drift occurs after propagation time $f\lambda_p/\Delta v_g$, yielding $L_{||} = cf\lambda_p/\Delta v_g$. For LWFA in which λ_{pr} and λ_{pu} remain fixed as \bar{n}_e changes, $\Delta v_g \propto \bar{n}_e$ and $L_{||} \propto \bar{n}_e^{-3/2}$, equivalent to the \bar{n}_e scaling of electron dephasing length L_d (see Eq. (6)). Then $\Delta\phi_{pr} \propto \bar{n}_e^{-1/2}$ — *i.e.* signal strength *increases* with decreasing density. (Dias *et al.*, 1998; Kasim *et al.*, 2015) discuss other cases that can arise if λ_{pr} and/or λ_{dr} scale systematically with \bar{n}_e , or when L_d or L_{pd} (Eq. (7)) determine $L_{||}$.

V. CONCLUSION

Approximately 10% of the budget of any accelerator is devoted to diagnostics. No accelerator can operate without them. The advent of plasma accelerators with cavities of dimensions $10\mu\text{m} \lesssim \lambda_p \lesssim 100\mu\text{m}$ that accelerate lepton bunches of dimensions $\sigma \ll \lambda_p$ has posed unprecedented diagnostic challenges. Not only are these cavities and bunches much smaller than their conventional counterparts, but they evolve rapidly during acceleration. Moreover, plasma cavities are transient and light-speed, and thus extraordinarily difficult to visualize accurately in the laboratory. Theory and simulations have provided essential, yet incomplete, guidance in understanding plasma accelerators. Predictions of bunch size varied widely before accurate measurements were carried out, while the dynamics of *e.g.* 3D wave-breaking, electron self-injection, and highly nonlinear wake evolution remained incompletely solved theoretical problems. Innovative laboratory diagnostics have filled many gaps in our understanding, and helped transform plasma electron acceleration from a fringe empirical activity to a quantitative science at the center of international planning for next-generation light sources and colliders.

The coming transition from prototype acceleration experiments to operating accelerators will place new demands on stability, energy spread and emittance of electron bunches, and thus on diagnostics. Early designs of plasma-accelerator-based light sources (Maier *et al.*, 2012) and colliders (Adli *et al.*, 2013; Leemans and Esarey, 2009) have already made clear that control of emittance growth and charge loss when transporting

bunches from LWFA to undulator, or between collider stages, will be major challenges. Development of versatile, accurate, noninvasive bunch diagnostics in transport regions will be as important in future research as intrastage diagnostics in past research. For colliders, diagnostics will have to be replicated over hundreds of stages. This will favor those that are simple, reliable and low-cost while still achieving high spatial and temporal resolution. Moreover, integration of these diagnostics into machine learning systems and genetic algorithms (He *et al.*, 2015; Wu *et al.*, 2017) for feedback control and optimization of accelerator performance will become a focus of research.

The greatest bunch diagnostic challenges that plasma accelerators posed were measurements of ultrasmall transverse emittance ($\varepsilon_n < 1$ mm mrad) and ultrashort duration ($\tau_b \sim$ few fs) of electron bunches that strongly nonlinear LWFA could uniquely produce (Secs. II.C.2, II.C.3). Ultrasmall bunch dimensions were a source of numerical instabilities in simulations (Lehe *et al.*, 2013), requiring small grids and time-steps as well as algorithmic advances for realistic results. Laboratory diagnostics therefore became the primary source of accurate information. Early efforts to measure ε_n of nonlinear LWFA bunches adapted the conventional pepper-pot method. However, it sampled phase space too sparsely, was limited in electron energy range, and was invasive (Sec. III.C.1.a). Similarly, early efforts to measure τ_b adapted EO methods in wide use for measuring compressed ps-duration bunches from conventional accelerators. However, strong THz dispersion of EO crystals limited even the most innovative measurements to > 10 fs RMS resolution when applied to nonlinear LWFA bunches (Sec. III.D.1). Thus these conventional beam diagnostics, pushed to their limits, managed only to set upper bounds on ε_n and τ_b .

The most important breakthroughs in beam diagnostics that plasma accelerators spurred in the past decade were noninvasive methods for resolving ε_n and τ_b in one shot. Betatron x-ray spectroscopy first found evidence of bunch radii $\sigma_r \sim 0.1\mu\text{m}$ inside the LWFA. Full trace-space analysis methods reconstructed complete ε_n , including the correlation term, in one shot without invoking a downstream divergence measurement, and found values up to an order of magnitude smaller than pepper-pot methods had resolved (Sec. III.C.2). New spectrally-resolved approaches to traditional quadrupole focus-scan methods avoided chromatic distortions, enabled single-shot measurements, and resolved ε_n values *outside* the accelerator as small as those that betatron spectroscopy measured inside (Sec. III.C.1.b).

Meanwhile, new methods for resolving few-fs τ_b emerged. MO measurements of Lorentz-contracted *magnetic* fields of relativistic bunches in plasma resolved τ_b down to ~ 5 fs (Buck *et al.*, 2011), free of phonon-dispersion limits of EO crystals. Combined with transverse optical shadowgraphy (Sec. IV.C.3.b), MO meth-

ods localize the accelerating bunch within an LWFA, but require probe pulses $\lesssim \tau_b$ in duration (Secs III.D.1.c and IV.C.3.a). The use of co-propagating infrared light pulses as transverse deflectors (TDs) of period $\lambda \sim 1\mu\text{m}$ has, in combination with a magnetic spectrometer, yielded single-shot measurements of internal energy-time structure of few-fs chirped LWFA bunches (Zhang *et al.*, 2016a). Though technically challenging, such micro-TD experiments directly measure slice emittance and slice energy spread, key parameters for LWFA-driven FELs and colliders (Sec. III.D.1). Finally, researchers transformed transition radiation (TR), a beam diagnostic of long standing for conventional accelerators, into an effective diagnostic of few-fs LWFA bunches by developing multi-octave, high-dynamic-range, single-shot spectrometers (Heigoldt *et al.*, 2015; Lundh *et al.*, 2011), and new algorithms for recovering bunch temporal profiles from TR spectral intensity measurements (Bakkali Taheri *et al.*, 2016). TR spectroscopy complements time-domain MO and TD methods by characterizing τ_b *outside* the accelerator without probe pulses (Sec. III.D.2).

The biggest future challenge facing plasma accelerator beam diagnostics is to develop single-shot methods for recovering sub- μm transverse, as well as few-fs longitudinal, beam profiles simultaneously and with high resolution throughout beam transport lines, and over multiple accelerator stages. This challenge will increase as electron energies reach multi-GeV. CTR methods show the greatest promise for this task because of their demonstrated ability to profile bunches both longitudinally and transversely with high resolution outside the accelerator, and because of the relatively low cost of the components. Combinations of CDR and Smith-Purcell methods with multi-octave spectroscopy appear promising for bringing about the required marriage of spatial and temporal diagnostics. In addition, all diagnostics must ultimately be applied to plasma-accelerated positron bunches.

The challenges that plasma accelerators posed for plasma structure diagnosis differed from those for beam diagnostics. Theory predicted the λ_p dimension of wake structural units with certainty from the beginning, and analytic 2D theories of the formation and internal morphology of linear and mildly nonlinear wakes were available early in the development of plasma electron accelerators (Chen, 1985; Esarey *et al.*, 1989; Gorbunov and Kirsanov, 1987). The main structural features of wakes that 3D simulations predicted even in the strongly nonlinear broken-wave regime (Pukhov and Meyer-ter-Vehn, 2002) were never in serious doubt, and most were large enough to be optically resolvable. The challenge lay rather in 4D visualization — *i.e.* 3D structure plus time evolution — a photography problem that Eadwaerd Muybridge solved for galloping horses in the 19th century (Clegg, 2007), but which remained unsolved for light-speed objects in the 21st century (Li *et al.*, 2014b; Pleasants, 2014). Divergent spatial-temporal scales — *i.e.* internal

wake structural dynamics measured in μm and fs, propagation in m and ns — together with low optical contrast and demand for single-shot visualization heightened the methodological challenge. The physics challenges were to observe difficult-to-simulate nonlinear features such as bubble formation and evolution, wavefront curvature, wave-breaking, self-injection and beam-loading dynamics. A practical challenge was to monitor shot-to-shot variations in wake structure and dynamics arising from non-ideal drivers or targets, which are often not fully included in idealized simulations.

Early wake diagnostic experiments drew upon established methods from other fields. Collective light scatter, a long-established diagnostic of holistic properties (ω_p , \vec{k}_p , $\delta n_e/\bar{n}_e$) of electron plasma waves (Froula *et al.*, 2011), helped early researchers discover laser wakefield growth and decay processes that remain important today, but did not resolve sub- λ_p wake structure (Sec. IV.A). Likewise pump-probe experiments using fully compressed, co-propagating optical or electron pulses, a staple of ultrafast science, first resolved sub- λ_p structure of plasma wakes, and observed variations in the length λ_p and amplitude $\delta n_e/\bar{n}_e$ of individual periods within a long wake, but required multiple shots and long, painstaking data acquisition (Sec. IV.B).

The singular *new* advances in wake diagnostics that plasma accelerators spurred were *single-shot* methods that resolved detailed sub- λ_p structure of plasma wakes. Frequency-domain holography (FDH), which recovers temporal phase $\phi_{pr}(t)$ of long, but spectrally broad, co-propagating probe pulses, captured “snapshots” of relativistic curvature (Matlis *et al.*, 2006) and amplitude spiking (Dong *et al.*, 2010a) of plasma wavefronts within mildly nonlinear wakes, and the variation of these effects from period to period (Sec. IV.C.1). Two generalizations of FDH expanded its diagnostic functionality: frequency-domain shadowgraphy (FDS), which recovers the probe’s temporal amplitude $|E_{pr}(t)|$, captured snapshots of strongly nonlinear plasma wakes (Dong *et al.*, 2010b) (Sec. IV.C.2); and frequency-domain streak camera (FDSC), in which the probe propagates obliquely, captured “movies” of projections of a laser-driven bubble forming, deepening and expanding as it propagated (Li *et al.*, 2014a) (Sec. IV.D.2). Synchronized *transversely*-propagating optical probes of few-fs duration projected shadowgraphs related to the wake’s instantaneous density profile (Buck *et al.*, 2011) onto a camera (Sec. IV.C.3.b). A change of pump-probe delay over successive shots revealed structural changes during propagation, and correlated these changes with injection of electrons (Sävert *et al.*, 2015), rendered visible by Faraday rotation (Kaluza *et al.*, 2010) (Sec. IV.D). *Electron* probes profiled the wake’s instantaneous electric field profile (Clayton *et al.*, 2016; Zhang *et al.*, 2017, 2016b), and proved sensitive at densities down to $\bar{n}_e \lesssim 10^{17} \text{ cm}^{-3}$ (Sec. IV.C.4). Computer simulations benchmarked im-

ages obtained with this diverse and unprecedented suite of single-shot probes in detail, opening a rich new line of communication between experimental and theoretical plasma accelerator science.

Future challenges for plasma wake diagnostics lie in three main directions. One is full realization of the potential for single-shot 4D visualization — *i.e.* experimental output of a propagation (z) sequence of instantaneous wakefield density $n_e(x, y, z - v_g t, z)$ or field $E_e(x, y, z - v_g t, z)$ profiles. Such outputs are similar to snapshots from PIC simulations, and thus might be called “PIC-tures”. Frequency-Domain Tomography (FDT) (Li *et al.*, 2014b) and Spectrally-Multiplexed Tomography (SMT) (Matlis *et al.*, 2012) are promising approaches that have been demonstrated on test index objects, but must be extended to plasma wakes using wide-bandwidth probes (Sec. IV.D.2). Another promising path is multiplexing of transverse optical probes, enabling capture of a z -sequence of transverse shadowgraphs and Faraday-rotation images in one shot. This approach uniquely observes the wake’s shadow, the accelerated electron bunch, and wave-breaking radiation with a common apparatus, enabling correlation of diverse features of the plasma acceleration process (Secs. IV.C.3).

A second future direction is incorporating advanced diagnostics and their results directly into simulations. This is essential not only for data analysis, but for making testable predictions. One frontier is “synthetic diagnostics”: simulating interactions of diagnostic probes with, or radiation from, the accelerator, not by post-processing a sub-set of previously simulated results, but *during* a simulation, when all physics quantities are accessible in memory. Another frontier is computational solution of inverse problems. Already well advanced in photon science, astronomy or geophysics, this approach uses diagnostic data from diverse sources to reconstruct quantities of interest — *e.g.* reconstructing electron bunch profiles using several diagnostics, even though part of the information (*e.g.* spectral phase) is not directly measurable (see Sec. III.D). This approach is especially powerful when analyzing diagnostics that are related by known physics, such as laser or electron beam profiles separated by propagation through vacuum.

A third future direction is expanding the application of single-shot wake diagnostics to a wider range of drivers, densities and contexts. Even though beam-driven PWFAs were among the first to be diagnosed with sub- λ_p precision (Sec. IV.B.1), researchers are now only beginning to apply modern single-shot optical wake diagnostics to strongly nonlinear PWFAs (Zgadzaaj *et al.*, 2016). This application brings the added methodological challenges of imaging sub-mm-wide wakes over multi-meter-long acceleration paths, synchronizing optical and electron probes with e-beam drivers, and probing wakes at lower density plasma ($\bar{n}_e < 10^{17} \text{ cm}^{-3}$) than in many past experiments. (Sec. IV.D.3). New physics challenges include visualiza-

tion of differences among electron-, positron- and proton-driven wakes, characterization of beam-plasma instabilities, and probing of ion wakes on a ns time scale after excitation. Pulses from emerging TW-peak-power CO₂ lasers (Polyanskiy *et al.*, 2015), because of the large ponderomotive force Eq. (1) they exert on a plasma for given pulse energy, duration and spot size, will similarly be able to drive bubble-regime wakes of hundreds of microns diameter in $\bar{n}_e < 10^{17} \text{ cm}^{-3}$ plasma. Such bubbles “writ large” offer the possibility not only of precisely injecting synchronized, low $\Delta E_e/E_e$, low- ε_n bunches from conventional linacs into plasma accelerators, but of probing their internal structures and evolution with higher resolution than in past experiments. Such challenges will continue to spur creativity and innovation in diagnostics for plasma electron accelerators for years to come.

Acknowledgments

M. C. D. acknowledges support from the Alexander von Humboldt Foundation during preparation of this manuscript, as well as support from the U. S. Department of Energy (grants DE-SC0011617, DE-SC0014043, DE-SC0014043), National Science Foundation (PHY-1734319), Air Force Office of Scientific Research (grants FA9550-16-1-0013, FA9550-14-1-0045), and the Robert Welch Foundation (grant F-1038).

REFERENCES

- Abuazoum, S., S. M. Wiggins, B. Ersfeld, K. Hart, G. Vieux, X. Yang, G. H. Welsh, R. C. Issac, M. P. Reijnders, D. R. Jones, and D. A. Jaroszynski (2012), *Appl. Phys. Lett.* **100**, 014106.
- Adli, E., J.-P. Delahaye, S. J. Gessner, M. J. Hogan, T. Raubenheimer, W. An, C. Joshi, and W. Mori (2013), arXiv:1308.1145.
- Adli, E., C. Lindstrøm, J. Allen, C. Clarke, J. Frederico, S. Gessner, S. Green, M. Hogan, M. Litos, G. White, *et al.* (2016), *Nucl. Instrum. Methods Phys. Res. A* **829**, 94.
- Albert, F., B. B. Pollock, J. L. Shaw, K. A. Marsh, J. E. Ralph, Y. H. Chen, D. Alessi, A. Pak, C. E. Clayton, S. H. Glenzer, and C. Joshi (2013), *Phys. Rev. Lett.* **111** (23), 1.
- Albert, F., R. Shah, K. T. Phuoc, R. Fitour, F. Burgy, J. P. Rousseau, A. Tafzi, D. Douillet, T. Lefrou, and A. Rousse (2008), *Phys. Rev. E* **77** (5), 1.
- Amemiya, Y., and J. Miyahara (1988), *Nature* **336** (6194), 89.
- Amiranoff, F., S. Baton, D. Bernard, B. Cros, D. Descamps, F. Dorchie, F. Jacquet, V. Malka, J. Marques, G. Matthieussent, *et al.* (1998), *Phys. Rev. Lett.* **81** (5), 995.
- Amiranoff, F., D. Bernard, B. Cros, F. Jacquet, G. Matthieussent, P. Miné, P. Mora, J. Morillo, F. Moulin, A. E. Specka, and C. Stenz (1995), *Phys. Rev. Lett.* **74**, 5220.
- Anania, M. P., E. Brunetti, S. M. Wiggins, D. W. Grant, G. H. Welsh, R. C. Issac, S. Cipiccia, R. P. Shanks, G. G. Manahan, C. Aniculaesei, S. B. van der Geer, M. J. de Loos, M. W. Poole, B. J. A. Shepherd, J. A. Clarke, W. A. Gillespie, A. M. MacLeod, and D. A. Jaroszynski (2014), *Appl. Phys. Lett.* **104**, 264102.
- Andreev, N. (1992), *JETP Lett* **55** (10), 571.
- Andreev, N., L. Gorbunov, V. Kirsanov, K. Nakajima, and A. Ogata (1997a), *Phys. Plasmas* **4** (4), 1145.
- Andreev, N., L. Gorbunov, and R. Ramazashvili (1997b), *Plasma Phys. Rpts.* **23** (4), 277.
- Andreev, N., V. Kirsanov, and L. Gorbunov (1995), *Phys. Plasmas* **2** (6), 2573.
- Andreev, N., S. Kuznetsov, A. Pogosova, L. Steinhauer, and W. Kimura (2003), *Phys. Rev. ST-Accel. Beams* **6** (4), 041301.
- Andrews, H., F. Bakkali Taheri, J. Barros, R. Bartolini, L. Cassinari, C. Clarke, S. Le Corre, N. Delerue, G. Doucas, N. Fuster-Martinez, I. Konoplev, M. Labat, C. Perry, A. Reichold, S. Stevenson, and M. Vieille Grosjean (2014a), *Nucl. Instrum. Methods Phys. Res. A* **740**, 212.
- Andrews, H. L., F. Bakkali Taheri, J. Barros, R. Bartolini, V. Bharadwaj, C. Clarke, N. Delerue, G. Doucas, N. Fuster-Martinez, M. Vieille-Grosjean, I. V. Konoplev, M. Labat, S. Le Corre, C. Perry, A. Reichold, and S. Stevenson (2014b), *Phys. Rev. ST - Accel. Beams* **17** (5), 1.
- Antici, P., A. Bacci, C. Benedetti, E. Chiadroni, M. Ferrario, A. R. Rossi, L. Lancia, M. Migliorati, A. Mostacci, L. Palumbo, and L. Serafini (2012), *J. Appl. Phys.* **112** (4), 044902.
- Antonsen, Jr, T., and P. Mora (1992), *Phys. Rev. Lett.* **69** (15), 2204.
- Arber, T., K. Bennett, C. Brady, A. Lawrence-Douglas, M. Ramsay, N. Sircombe, P. Gillies, R. Evans, H. Schmitz, A. Bell, *et al.* (2015), *Plasma Phys. Controlled Fusion* **57** (11), 113001.
- Artru, X., M. Castellano, L. Catani, R. Chehab, D. Giove, K. Honkavaara, P. Patteri, M. Taurigna-Quere, A. Variola, and L. Wartski (1998a), *Nucl. Instrum. Methods Phys. Res. A* **410** (2), 148.
- Artru, X., R. Chehab, K. Honkavaara, and A. Variola (1998b), *Nucl. Instrum. Methods Phys. Res. B* **145** (1), 160.
- Artru, X., G. B. Yodh, and G. Mennessier (1975), *Phys. Rev. D* **12** (5), 1289.
- Arutyunyan, F., A. K. Mkhitarian, R. Oganessian, B. Rostomyan, and M. Sarinyan (1979), *Sov. Phys.-JETP* **50** (5).
- Attwood, D. T., P. Naulleau, K. A. Goldberg, E. Tejnil, C. Chang, R. Beguiristain, P. Batson, J. Bokor, E. M. Gulikson, M. Koike, H. Medeck, and J. H. Underwood (1999), *IEEE J. Quantum Electron.* **35** (5), 709.
- Augst, S., D. D. Meyerhofer, D. Strickland, and S. L. Chin (1991), *J. Opt. Soc. Am. B* **8**, 858.
- Backus, S., C. G. Durfee III, M. M. Murnane, and H. C. Kapteyn (1998), *Rev. Sci. Instrum.* **69** (3), 1207.
- Baghiyan, R. A. (2001), *Physical Review E* **64** (2), 026610.
- Baghiyan, R. A. (2004), *Physical Review E* **69** (2), 026609.
- Bajlekov, S., M. Heigoldt, A. Popp, J. Wenz, K. Khrennikov, S. Karsch, and S. Hooker (2013), *Phys. Rev. ST-Accel. Beams* **16** (4), 040701.
- Bakkali Taheri, F., I. Konoplev, G. Doucas, P. Baddoo, R. Bartolini, J. Cowley, and S. Hooker (2016), *Physical Review Accelerators and Beams* **19**, 032801.
- Barber, S. K., J. van Tilborg, C. B. Schroeder, R. Lehe, H.-E. Tsai, K. K. Swanson, S. Steinke, K. Nakamura, C. G. R. Geddes, C. Benedetti, E. Esarey, and W. P. Leemans (2017), *Phys. Rev. Lett.* **119**, 104801.
- Bardsley, J. N., B. M. Penetrante, and M. H. Mittleman (1989), *Physical Review A* **40** (7), 3823.
- Barov, N., J. B. Rosenzweig, M. E. Conde, W. Gai, and J. G. Power (2000), *Phys. Rev. ST Accel. Beams* **3**, 011301.
- Bartolini, R., C. Clarke, N. Delerue, G. Doucas, and A. Reichold (2012), *J. Instrumentation* **7** (01), P01009.
- Becker, S., M. Bussmann, S. Raith, M. Fuchs, R. Weingartner, P. Kunz, W. Lauth, U. Schramm, M. El Ghazaly, F. Grüner, H. Backe, and D. Habs (2009), *Phys. Rev. ST Accel. Beams* **12**, 102801.
- Behnke, T. (2015), *The International Linear Collider Technical Design Report*, Tech. Rep. (U. S. Department of Energy).
- Behrens, C., F. J. Decker, Y. Ding, V. A. Dolgashev, J. Frisch, Z. Huang, P. Krejcik, H. Loos, A. Lutman, T. J. Maxwell, J. Turner, J. Wang, M. H. Wang, J. Welch, and J. Wu (2014), *Nat. Commun.* **5**, 3762.
- Behrens, C., C. Gerth, G. Kube, B. Schmidt, S. Wesch, and M. Yan (2012), *Physical Review Special Topics - Accelerators and Beams* **15** (6), 1.
- Berden, G., W. A. Gillespie, S. P. Jamison, E.-A. Knabbe, A. M. MacLeod, A. van der Meer, P. J. Phillips, H. Schlarb, B. Schmidt, P. Schmüser, *et al.* (2007), *Physical review letters* **99** (16), 164801.
- Berden, G., S. Jamison, A. MacLeod, W. Gillespie, B. Redlich, and A. van Der Meer (2004), *Phys. Rev. Lett.* **93** (11), 114802.
- Berezhiani, V., and I. Murusidze (1990), *Phys. Lett. A* **148** (6-7), 338.
- Bergoz, J., *et al.* (1991), *Nucl. Phys. A* **525**, 595.
- Bernard, D., F. Amiranoff, W. P. Leemans, E. Esarey, and

- C. Joshi (1999), Nucl. Instrum. Methods Phys. Res. A **432** (2), 227.
- Bettoni, S., P. Craievich, A. Lutman, and M. Pedrozzi (2016), Phys. Rev. Accel. Beams **19** (2), 021304.
- Blackmore, V., G. Doucas, C. Perry, B. Ottewell, M. F. Kimmitt, M. Woods, S. Molloy, and R. Arnold (2009), Phys. Rev. ST Accel. Beams **12**, 032803.
- Blue, B. E., C. E. Clayton, C. L. O'Connell, F.-J. Decker, M. J. Hogan, C. Huang, R. Iverson, C. Joshi, T. Katsouleas, W. Lu, K. A. Marsh, W. B. Mori, P. Muggli, R. H. Siemann, and D. Walz (2003), Phys. Rev. Lett. **90**, 214801.
- Blumenfeld, I., C. E. Clayton, F.-J. Decker, M. J. Hogan, C. Huang, R. Ischebeck, R. Iverson, C. Joshi, T. Katsouleas, N. Kirby, W. Lu, K. A. Marsh, W. B. Mori, P. Muggli, E. Oz, R. H. Siemann, D. Walz, and M. Zhou (2007), Nature (London) **445**, 741.
- Bolotovskii, B. M., and A. V. Serov (2009), Physics-Uspekhi **52** (5), 487.
- Bolotovskii, B. M., and G. V. Voskresenski (1966), Soviet Physics Uspekhi **9** (1), 73.
- Born, M., and E. Wolf (1980), *Principles of Optics* (Pergamon Press, Oxford).
- Bourgeois, N., M. Heigoldt, W. Rittershofer, A. Popp, K. Khrennikov, S. Bajlekov, S. Karsh, and S. Hooker (2012), in *AIP Conf. Proc.*, Vol. 1507 (AIP) pp. 258–261.
- Bret, A., L. Gremillet, and M. E. Dieckmann (2010), Phys. Plasmas **17** (12), 120501.
- Brown, G. L. (1975), *A First- and Second-order Matrix Theory for the Design of Beam Transport Systems and Charged Particle Spectrometers*, Tech. Rep. (SLAC).
- Brown, L. S., and T. W. B. Kibble (1964), Phys. Rev. **133** (3A), 10.1103/PhysRev.133.A705.
- Brown, W. J., and F. V. Hartemann (2004), Phys. Rev. ST Accel. Beams **7**, 060703.
- Brownell, J., J. Walsh, and G. Doucas (1998), Phys. Rev. E **57** (1), 1075.
- Brunetti, E., R. P. Shanks, G. G. Manahan, M. R. Islam, B. Ersfeld, M. P. Anania, S. Cipiccia, R. C. Issac, G. Raj, G. Vieux, G. H. Welsh, S. M. Wiggins, and D. A. Jaroszynski (2010), Phys. Rev. Lett. **105**, 215007.
- Buck, A., M. Nicolai, K. Schmid, C. M. S. Sears, A. Saevert, J. M. Mikhailova, F. Krausz, M. C. Kaluza, and L. Veisz (2011), Nature Phys. **7**, 543.
- Buck, A., J. Wenz, J. Xu, K. Khrennikov, K. Schmid, M. Heigoldt, J. M. Mikhailova, M. Geissler, B. Shen, F. Krausz, *et al.* (2013), Phys. Rev. Lett. **110** (18), 185006.
- Buck, A., K. Zeil, A. Popp, K. Schmid, A. Jochmann, S. D. Kraft, B. Hidding, T. Kudyakov, C. M. S. Sears, L. Veisz, S. Karsch, J. Pawelke, R. Sauerbrey, T. Cowan, F. Krausz, and U. Schramm (2010), Rev. Sci. Instrum. **81**, 033301.
- Bulanov, S., V. Kirsanov, and A. Sakharov (1989), JETP Lett **50** (0), 4.
- Bulanov, S., N. Naumova, F. Pegoraro, and J. Sakai (1998), Phys. Rev. E **58** (5), R5257.
- Bulanov, S., F. Pegoraro, and A. Pukhov (1995), Phys. Rev. Lett. **74** (5), 710.
- Bulanov, S. V., V. I. Irsanov, F. Pegoraro, and A. S. Sakharov (1993), Laser Phys. **3**, 1078.
- Bulanov, S. V., F. Pegoraro, A. M. Pukhov, and A. S. Sakharov (1997a), Phys. Rev. Lett. **78**, 4205.
- Bulanov, S. V., V. A. Vshivkov, G. I. Dudnikova, N. M. Naumova, F. Pegoraro, and I. V. Pogorelksy (1997b), Plasma Phys. Rep. **23**, 259.
- Caldwell, A., E. Adli, L. Amorim, R. Apsimon, T. Argyropoulos, R. Assmann, A.-M. Bachmann, F. Batsch, J. Bauche, V. B. Olsen, M. Bernardini, R. Bingham, B. Biskup, T. Bohl, C. Bracco, P. Burrows, G. Burt, B. Buttenschon, A. Butterworth, M. Cascella, S. Chattopadhyay, E. Chevallay, S. Cipiccia, H. Damerau, L. Deacon, P. Dirksen, S. Doebert, U. Dorda, E. Elsen, J. Farmer, S. Fartoukh, V. Fedosseev, E. Feldbaumer, R. Fiorito, R. Fonseca, F. Friebe, G. Geschonke, B. Goddard, A. Gorn, O. Grulke, E. Gschwendtner, J. Hansen, C. Hessler, S. Hillenbrand, W. Hofle, J. Holloway, C. Huang, M. Hther, D. Jaroszynski, L. Jensen, S. Jolly, A. Joulaei, M. Kasim, F. Keeble, R. Kersevan, N. Kumar, Y. Li, S. Liu, N. Lopes, K. Lotov, W. Lu, J. Machacek, S. Mandry, I. Martin, R. Martorelli, M. Martyanov, S. Mazzoni, M. Meddahi, L. Meringa, O. Mete, V. Minakov, J. Mitchell, J. Moody, A.-S. Miller, Z. Najmudin, T. Noakes, P. Norreys, J. Osterhoff, E. z, A. Pardons, K. Pepitone, A. Petrenko, G. Plyushchev, J. Pozimski, A. Pukhov, O. Reimann, K. Rieger, S. Roesler, H. Ruhl, T. Rusnak, F. Salveter, N. Savard, J. Schmidt, H. von der Schmitt, A. Seryi, E. Shaposhnikova, Z. Sheng, P. Sherwood, L. Silva, F. Simon, L. Soby, A. Sosedkin, R. Spitsyn, T. Tajima, R. Tarkeshian, H. Timko, R. Trines, T. Tckmantel, P. Tuv, M. Turner, F. Velotti, V. Verzilov, J. Vieira, H. Vincke, Y. Wei, C. Welsch, M. Wing, G. Xia, V. Yakimenko, H. Zhang, and F. Zimmermann (2016), Nucl. Instrum. Methods Phys. Res. A **829**, 3, 2nd European Advanced Accelerator Concepts Workshop - {EAAC} 2015.
- Caldwell, A., and K. Lotov (2011), Phys. Plasmas **18** (10), 103101.
- Caldwell, A., K. Lotov, A. Pukhov, and F. Simon (2009), Nature Phys. **5**, 363.
- Carron, N. (2000), Prog. Electromagnetics Res. **28**, 147.
- Casalbuoni, S., H. Schlarb, B. Schmidt, P. Schmüser, B. Steffen, and A. Winter (2008), Phys. Rev. ST Accel. Beams **11**, 072802.
- Casalbuoni, S., H. Schlarb, B. Schmidt, B. Steffen, P. Schmuser, and A. Winter (2005a), *TESLA Report: Numerical Studies on the Electro-Optic Sampling of Relativistic Electron Bunches*, Tech. Rep. 2005-01 (DESY Hamburg).
- Casalbuoni, S., B. Schmidt, and P. Schmser (2005b), *TESLA REPORT: Far-Infrared Transition and Diffraction Radiation*, Tech. Rep. 2005-15 (DESY Hamburg).
- Castellano, M., V. Verzilov, L. Catani, a. Cianchi, G. Orlandi, and M. Geitz (2001), Phys. Rev. E **63** (5), 056501.
- Castellano, M., and V. A. Verzilov (1998), Phys. Rev. ST Accel. Beams **1**, 062801.
- Catrasvas, P., W. P. Leemans, J. S. Wurtele, M. S. Zolotarev, M. Babzien, I. Ben-Zvi, Z. Segalov, X.-J. Wang, and V. Yakimenko (1999), Phys. Rev. Lett. **82**, 5261.
- Cha, H. J., I. W. Choi, H. T. Kim, I. J. Kim, K. H. Nam, T. M. Jeong, and J. Lee (2012), Rev. Sci. Instrum. **83**, 063301.
- Chen, P. (1985), Part. Accel. **20**, 171.
- Chen, P., J. M. Dawson, R. W. Huff, and T. Katsouleas (1985), Phys. Rev. Lett. **54**, 693.
- Chen, P., J. J. Su, J. M. Dawson, K. L. F. Bane, and P. B. Wilson (1986), Phys. Rev. Lett. **56**, 1252.
- Chen, Y.-H., S. Varma, I. Alexeev, and H. M. Milchberg (2007), Opt. Express **15** (12), 7458.
- Chien, C. Y., B. L. Fontaine, A. Despararois, Z. Jiang, T. W. Johnston, J. C. Kieffer, H. Pépin, F. Vidal, and H. P. Mercure (2000), Opt. Lett. **25**, 578.

- Chiou, T., and T. Katsouleas (1998), Phys. Rev. Lett. **81** (16), 3411.
- Chouffani, K., F. Harmon, D. Wells, J. Jones, and G. Lancaster (2006), Phys. Rev. ST Accel. Beams **9** (5).
- Cianchi, A., M. Anania, M. Bellaveglia, M. Castellano, E. Chiadroni, M. Ferrario, G. Gatti, B. Marchetti, A. Mostacci, R. Pompili, C. Ronsivalle, A. Rossi, and L. Serafini (2013), Nucl. Instrum. Meth. Phys. Res. A **720**, 153.
- Cipiccia, S., M. R. Islam, B. Ersfeld, R. P. Shanks, E. Brunetti, G. Vieux, X. Yang, R. C. Issac, S. M. Wiggins, G. H. Welsh, M.-P. Anania, D. Maneuski, R. Montgomery, G. Smith, M. Hoek, D. J. Hamilton, N. R. C. Lemos, D. Symes, P. P. Rajeev, V. O. Shea, J. M. Dias, and D. A. Jaroszynski (2011), Nature Phys. **7** (11), 867.
- Clarke, J. A. (2004), *The Science and Technology of Undulators and Wigglers (Oxford Series on Synchrotron Radiation)* (Oxford University Press, USA).
- Clayton, C. (2009), “An Experimentalist’s Perspective on Plasma Accelerators,” in *Laser-Plasma Interactions*, edited by D. A. Jaroszynski, R. Bingham, and R. A. Cairns, Chap. 2 (CRC Press - Taylor and Francis, Boca Raton) pp. 19–78.
- Clayton, C., M. Everett, A. Lal, D. Gordon, K. Marsh, and C. Joshi (1994), Phys. Plasmas **1** (5), 1753.
- Clayton, C., C. Joshi, C. Darrow, and D. Umstadter (1985), Phys. Rev. Lett. **54** (21), 2343.
- Clayton, C., J. Ralph, F. Albert, R. Fonseca, S. Glenzer, C. Joshi, W. Lu, K. Marsh, S. Martins, W. Mori, *et al.* (2010), Phys. Rev. Lett. **105** (10), 105003.
- Clayton, C. E., E. Adli, J. Allen, W. An, C. I. Clarke, S. Corde, J. Frederico, S. Gessner, S. Z. Green, M. J. Hogan, C. Joshi, M. Litos, W. Lu, K. A. Marsh, W. B. Mori, N. Vafaei-Najafabadi, X. Xu, and V. Yakimenko (2016), Nature Commun. **7** (12483).
- Clayton, C. E., K. A. Marsh, A. Dyson, M. Everett, A. Lal, W. P. Leemans, R. Williams, and C. Joshi (1992), Phys. Rev. Lett. **70**, 37.
- Clayton, C. E., K. A. Marsh, A. Dyson, M. Everett, A. Lal, W. P. Leemans, R. Williams, and C. Joshi (1993), Phys. Rev. Lett. **70**, 37.
- Clegg, B. (2007), *The Man Who Stopped Time: The Illuminating Story of Eadweard Muybridge – Pioneer Photographer, Father of the Motion Picture, Murderer* (Joseph Henry Press).
- Corde, S., E. Adli, J. M. Allen, W. An, C. I. Clarke, C. E. Clayton, J. P. Delahaye, J. Frederico, S. Gessner, S. Z. Green, M. J. Hogan, C. Joshi, N. Lipkowitz, M. Litos, W. Lu, K. A. Marsh, W. B. Mori, M. Schmeltz, N. Vafaei-Najafabadi, V. Yakimenko, and G. Yocky (2015), Nature (London) **524**, 442.
- Corde, S., K. Ta Phuoc, G. Lambert, R. Fitour, V. Malka, A. Rousse, A. Beck, and E. Lefebvre (2013), Rev. Mod. Phys. **85** (1), 1.
- Couperus, J., R. Pausch, A. Köhler, O. Zarini, J. Krämer, M. Garten, A. Huebl, R. Gebhardt, U. Helbig, S. Bock, A. Debus, M. Bussmann, U. Schramm, and A. Irman (2017), Nature Commun. , in press.
- Coverdale, C., C. Darrow, C. Decker, W. Mori, K. Tzeng, K. Marsh, C. Clayton, and C. Joshi (1995), Phys. Rev. Lett. **74** (23), 4659.
- Cowley, J., C. Thornton, C. Arran, R. J. Shalloo, L. Corner, G. Cheung, C. D. Gregory, S. P. D. Mangles, N. H. Matlis, D. R. Symes, R. Walczak, and S. M. Hooker (2017), Phys. Rev. Lett. **119**, 044802.
- Curcio, A., M. Anania, F. Bisesto, E. Chiadroni, A. Cianchi, M. Ferrario, F. Filippi, D. Giulietti, A. Marocchino, M. Petrarca, V. Shpakov, and A. Zigler (2017), Phys. Rev. Accel. Beams **20** (1), 012801.
- Curcio, A., D. Giulietti, G. Dattoli, and M. Ferrario (2015), J. Plasma Phys. **81** (5).
- Dawson, J. M. (1959), Phys. Rev. **113**, 383.
- Debus, A., S. Bock, M. Bussmann, T. E. Cowan, A. Jochmann, T. Kluge, S. D. Kraft, R. Sauerbrey, K. Zeil, and U. Schramm (2009), in *Proc. SPIE*, edited by D. A. Jaroszynski and A. Rousse, p. 735908.
- Debus, A., M. Bussmann, U. Schramm, R. Sauerbrey, C. Murphy, Z. Major, R. Hörlein, L. Veisz, K. Schmid, J. Schreiber, *et al.* (2010a), Phys. Rev. Lett. **104** (8), 084802.
- Debus, A., M. Bussmann, M. Siebold, A. Jochmann, U. Schramm, T. Cowan, and R. Sauerbrey (2010b), Appl. Phys. B **100** (1), 61.
- Decker, C., and W. Mori (1994), Phys. Rev. Lett. **72** (4), 490.
- Decker, C., W. Mori, and T. Katsouleas (1994), Phys. Rev. E **50** (5), R3338.
- Decker, C. D., W. B. Mori, K.-C. Tzeng, and T. Katsouleas (1996), Phys. Plasmas **3**, 2047.
- Delerue, N. (2011), Nucl. Instrum. Methods Phys. Res. A **644**, 1.
- Deng, S., C. D. Barnes, C. E. Clayton, C. O’Connell, F. J. Decker, O. Erdem, R. A. Fonseca, C. Huang, M. J. Hogan, R. Iverson, D. K. Johnson, C. Joshi, T. Katsouleas, P. Krejcik, W. Lu, K. A. Marsh, W. B. Mori, P. Muggli, and F. Tsung (2003), Phys. Rev. E **68**, 047401.
- Deng, S., C. D. Barnes, C. E. Clayton, C. O’Connell, F. J. Decker, R. A. Fonseca, C. Huang, M. J. Hogan, R. Iverson, D. K. Johnson, C. Joshi, T. Katsouleas, P. Krejcik, W. Lu, W. B. Mori, P. Muggli, E. Oz, F. Tsung, D. Walz, and M. Zhou (2006), Phys. Rev. Lett. **96**, 045001.
- Dewa, H., H. Ahn, H. Harano, M. Kando, K. Kinoshita, S. Kondoh, H. Kotaki, K. Nakajima, H. Nakanishi, A. Ogata, *et al.* (1998), Nucl. Instrum. Methods Phys. Res. A **410** (3), 357.
- Dias, J. M., L. O. e Silva, and J. T. Mendonca (1998), Phys. Rev. ST Accel. Beams **1**, 031301.
- Ding, Y., C. Behrens, P. Emma, J. Frisch, Z. Huang, H. Loos, P. Krejcik, and M. H. Wang (2011), Phys. Rev. ST Accel. Beams **14** (12), 1.
- Dodd, E. S., R. G. Hemker, C.-K. Huang, S. Wang, C. Ren, W. B. Mori, S. Lee, and T. Katsouleas (2002), Phys. Rev. Lett. **88**, 125001.
- Dohlus, M., T. Limberg, and P. Emma (2005), ICF Beam Dynamics Newsletter **38**, 15.
- Dolgashev, V. A., G. Bowden, Y. Ding, P. Emma, P. Krejcik, J. Lewandowski, C. Limborg, M. Litos, J. Wang, and D. Xiang (2014), Phys. Rev. ST Accel. Beams **17**, 102801.
- Dolgoshein, B. (1993), Nucl. Instrum. Meth. Phys. Res. A **326** (3), 434.
- Dong, P., S. A. Reed, S. A. Yi, S. Kalmykov, Z. Y. Li, G. Shvets, N. H. Matlis, C. McGuffey, S. S. Bulanov, V. Chvykov, G. Kalintchenko, K. Krushelnick, A. Maksimchuk, T. Matsuoka, A. G. R. Thomas, V. Yanovsky, and M. C. Downer (2010a), New J. Phys. **12**, 045016.
- Dong, P., S. A. Reed, S. A. Yi, S. Kalmykov, G. Shvets, M. C. Downer, N. H. Matlis, W. P. Leemans, C. McGuffey, S. S. Bulanov, V. Chvykov, G. Kalintchenko, K. Krushel-

- nick, A. Maksichuk, T. Matsuoka, A. G. R. Thomas, and V. Yanovsky (2010b), *Phys. Rev. Lett.* **104**, 134801.
- Dornmair, I., K. Floettmann, and A. R. Maier (2015), *Phys. Rev. ST Accel. Beams* **18**, 041302.
- Dornmair, I., C. B. Schroeder, K. Floettmann, B. Marchetti, and A. R. Maier (2016), *Phys. Rev. Accel. Beams* **19** (6), 062801.
- Dorrer, C., B. de Beauvoir, C. L. Blanc, S. Ranc, J.-P. Rousseau, P. Rousseau, J.-P. Chambaret, and F. Salin (1999), *Opt. Lett.* **24** (22), 1644.
- Durfee III, C., J. Lynch, and H. Milchberg (1995), *Phys. Rev. E* **51** (3), 2368.
- Eichner, T., F. Grüner, S. Becker, M. Fuchs, D. Habs, R. Weingartner, U. Schramm, H. Backe, P. Kunz, and W. Lauth (2007), *Phys. Rev. ST Accel. Beams* **10**, 082401.
- Esarey, E., R. Hubbard, W. Leemans, A. Ting, and P. Sprangle (1997), *Phys. Rev. Lett.* **79** (14), 2682.
- Esarey, E., J. Krall, and P. Sprangle (1994), *Phys. Rev. Lett.* **72** (18), 2887.
- Esarey, E., S. K. Ride, and P. Sprangle (1993), *Phys. Rev. E* **48** (4), 3003.
- Esarey, E., C. B. Schroeder, and W. P. Leemans (2009), *Rev. Mod. Phys.* **81**, 1229.
- Esarey, E., B. A. Shadwick, P. Catravas, and W. P. Leemans (2002), *Phys. Rev. E* **65** (5), 1.
- Esarey, E., A. Ting, and P. Sprangle (1990), *Phys. Rev. A* **42**, 3526.
- Esarey, E., A. Ting, P. Sprangle, and G. Joyce (1989), *Comments Plasma Phys. Control. Fusion* **12** (4), 191.
- Everett, M., A. Lal, C. Clayton, W. Mori, T. Johnston, and C. Joshi (1995), *Phys. Rev. Lett.* **74** (12), 2236.
- Fainberg, Y., N. Ayzatsky, V. Balakirev, A. Berezin, A. Dovbnya, V. Karas, V. Kiselev, V. Kushnir, A. Linnik, V. Mitrochenko, V. Stepin, I. Onishchenko, A. Tolstoluzhsky, and V. Uskov (1998), in *Proc. 1997 Particle Accelerator Conf., Vols. 1-3*, edited by M. Comyn, M. Craddock, M. Reiser, and J. Thomson, pp. 651–653.
- Fainberg, Y., V. Balakirev, A. Berezin, V. Karas, V. Kiselev, I. Onishchenko, and A. Tolstoluzhsky (1996), in *Proc. 17th Int. Symp. Discharges and Electrical Insulation in Vacuum, Vols. I,II* (IEEE) pp. 640–643.
- Farmer, J., R. Martorelli, and A. Pukhov (2015), *Phys. Plasmas* **22** (12), 123113.
- Faure, J. (2017), *CERN Yellow Reports* **1**, 143.
- Faure, J., Y. Glinec, A. Pukhov, S. Kiselev, S. Gordienko, E. Lefebvre, J.-P. Rousseau, F. Burgy, and V. Malka (2004), *Nature* **431** (7008), 541.
- Faure, J., C. Rechatin, A. Norlin, A. Lifschitz, Y. Glinec, and V. Malka (2006), *Nature* **444** (7120), 737.
- Fienup, J. R. (1982), *Appl. Opt.* **21** (15), 2758.
- Filip, C., R. Narang, S. Y. Tochitsky, C. Clayton, P. Musumeci, R. Yoder, K. Marsh, J. Rosenzweig, C. Pellegrini, and C. Joshi (2004), *Phys. Rev. E* **69** (2), 026404.
- Filip, C. V., S. Y. Tochitsky, R. Narang, C. E. Clayton, K. A. Marsh, and C. J. Joshi (2003), *Rev. Sci. Instrum.* **74** (7), 3576.
- Fiorito, R. (2001), *Nucl. Instrum. Meth. Phys. Res. B* **173** (1-2), 67.
- Fiorito, R. B., and D. W. Rule (1994), *AIP Conf. Proc.* **319** (1994), 21.
- Fiorito, R. B., A. G. Shkvarunets, T. Watanabe, V. Yakimenko, and D. Snyder (2006), *Phys. Rev. ST - Accel. Beams* **9** (5), 1.
- Fletcher, J. (2002), *Opt. Express* **10** (24), 1425.
- Floettmann, K. (2014), *Phys. Rev. ST Accel. Beams* **17**, 054402.
- Frank, I. (1966), *Sov. Phys. Uspekhi* **8** (5), 729.
- Fritzler, S., E. Lefebvre, V. Malka, F. Burgy, A. E. Dargor, K. Krushelnick, S. P. D. Mangles, Z. Najmudin, J.-P. Rousseau, and B. Walton (2004), *Phys. Rev. Lett.* **92**, 165006.
- Froula, D., C. Clayton, T. Döppner, K. Marsh, C. Barty, L. Divol, R. Fonseca, S. Glenzer, C. Joshi, W. Lu, *et al.* (2009), *Phys. Rev. Lett.* **103** (21), 215006.
- Froula, D. H., S. H. Glenzer, N. C. Luhmann, Jr., and J. Sheffield (2011), *Plasma Scattering of Electromagnetic Radiation, 2nd ed.* (Academic Press).
- Fubiani, G., E. Esarey, C. Schroeder, and W. Leemans (2004), *Phys. Rev. E* **70** (1), 016402.
- Fubiani, G., E. Esarey, C. Schroeder, and W. Leemans (2006), *Phys. Rev. E* **73** (2), 026402.
- Fuchs, M., R. Weingartner, A. Popp, Z. Major, S. Becker, J. Osterhoff, I. Cortrie, B. Zeitler, R. Hörlein, G. D. Tsakiris, U. Schramm, T. P. Rowlands-Rees, S. M. Hooker, D. Habs, F. Krausz, S. Karsch, and F. Grüner (2009), *Nature Phys.* **5** (11), 826.
- Gahn, C., G. Pretzler, A. Saemann, G. D. Tsakiris, K. J. Witte, D. Gassmann, T. Schtz, U. Schramm, P. Thirolf, and D. Habs (1998), *Appl. Phys. Lett.* **73**, 3662.
- Gahn, C., G. Tsakiris, K. Witte, P. Thirolf, and D. Habs (2000), *Rev. Sci. Instrum.* **71** (4), 1642.
- Galimberti, M., A. Giulietti, D. Giulietti, and L. A. Gizzi (2005), *Rev. Sci. Instrum.* **76**, 053303.
- Gallacher, J. G., M. P. Anania, E. Brunetti, F. Budde, A. Debus, B. Ersfeld, K. Haupt, M. R. Islam, O. Jäckel, S. Pfotenhauer, A. J. W. Reitsma, E. Rohwer, H.-P. Schlenvoigt, H. Schwoerer, R. P. Shanks, S. M. Wiggins, and D. A. Jaroszynski (2009), *Phys. Plasmas* **16**, 093102.
- Gallot, G., J. Zhang, R. W. McGowan, T. Jeon, and D. Grischkowsky (1999), *Appl. Phys. Lett.* **74**, 3450.
- Geddes, C., K. Nakamura, G. Plateau, C. Toth, E. Cormier-Michel, E. Esarey, C. Schroeder, J. Cary, and W. Leemans (2008), *Phys. Rev. Lett.* **100** (21), 215004.
- Geddes, C., C. Toth, J. Van Tilborg, E. Esarey, C. Schroeder, D. Bruhwiler, C. Nieter, J. Cary, and W. Leemans (2004), *Nature* **431** (7008), 538.
- Geindre, J. P., P. Audebert, S. Rebibo, and J. C. Gauthier (2001), *Opt. Lett.* **26**, 1612.
- Geindre, J. P., P. Audebert, A. Rousse, F. Fallières, J. C. Gauthier, A. Mysyrowicz, A. D. Santos, G. Hamoniaux, and A. Antonetti (1994), *Opt. Lett.* **19**, 1997.
- Geschwendtner, E., E. Adli, L. Amorim, R. Apsimon, R. Assmann, A.-M. Bachmann, F. Batsch, J. Bauche, and V. K. B. Olsen (2016), *Nucl. Instrum. Meth. Phys. Res. A* **829**, 76.
- Gessner, S., E. Adli, J. M. Allen, W. An, C. I. Clarke, C. E. Clayton, S. Corde, J. Delahaye, J. Frederico, S. Z. Green, *et al.* (2016), *Nat. Comms.* **7**.
- Ghiglia, D. C., and L. A. Romero (1994), *J. Opt. Soc. Am. A* **11** (1), 107.
- Ginzburg, V. (1979), 16th Int. Cosmic Ray Conf. **14**, 42.
- Ginzburg, V., and I. Frank (1946), *Sov. Phys. JETP* **16** (15).
- Giulietti, D., M. Galimberti, A. Giulietti, L. Gizzi, R. Nuccio, P. Tomassini, M. Borghesi, V. Malka, S. Fritzler, M. Pittman, *et al.* (2002), *Phys. Plasmas* **9** (9), 3655.
- Glinec, Y., J. Faure, A. Guemnie-Tafo, V. Malka, H. Monard, J. P. Larbre, V. D. Waele, J. L. Marignier, and M. Mostafavi (2006), *Rev. Sci. Instrum.* **77**, 103301.

- Glinec, Y., J. Faure, A. Norlin, A. Pukhov, and V. Malka (2007), Phys. Rev. Lett. **98**, 194801.
- Golovin, G., S. Banerjee, C. Liu, S. Chen, J. Zhang, B. Zhao, P. Zhang, M. Veale, M. Wilson, P. Seller, and D. Umstadter (2016), Sci. Rpts. **6** (1), 24622.
- Gonsalves, A., K. Nakamura, C. Lin, D. Panassenko, S. Shiraishi, T. Sokollik, C. Benedetti, C. Schroeder, C. Geddes, J. Van Tilborg, *et al.* (2011), Nature Phys. **7** (11), 862.
- Gorbunov, L., and V. Kirsanov (1987), Sov. Phys. JETP **66** (290-294), 40.
- Gordon, D., B. Hafizi, D. Kaganovich, and A. Ting (2008), Phys. Rev. Lett. **101** (4), 045004.
- Gordon, D., K. Tzeng, C. Clayton, A. Dangor, V. Malka, K. Marsh, A. Modena, W. Mori, P. Muggli, Z. Najmudin, *et al.* (1998), Phys. Rev. Lett. **80** (10), 2133.
- Green, S. Z., E. Adli, C. I. Clarke, S. Corde, S. A. Edstrom, A. S. Fisher, J. Frederico, J. C. Frisch, S. Gessner, S. Gilevich, P. Hering, M. J. Hogan, R. K. Jobe, M. Litos, J. E. May, D. R. Walz, V. Yakimenko, C. E. Clayton, C. Joshi, K. A. Marsh, N. Vafaei-Najafabadi, and P. Muggli (2014), Plasma Phys. Control. Fusion **56** (8), 084011.
- Green, S. Z., M. J. Hogan, N. Lipkowitz, B. O'Shea, G. White, V. Yakimenko, and G. Yocky (2017), in *Proc. Int. Beam Instrum. Conf. (IBIC'17), Grand Rapids, Michigan*, SLAC-PUB-17134.
- Gruener, F., S. Becker, U. Schramm, T. Eichner, M. Fuchs, R. Weingartner, D. Habs, J. Meyer-ter Vehn, M. Geissler, M. Ferrario, L. Serafini, B. van der Geer, H. Backe, W. Lauth, and S. Reiche (2007), Appl. Phys. B **86**, 431.
- Guillaume, E., A. Döpp, C. Thauray, K. T. Phuoc, A. Lifschitz, G. Grittani, J.-P. Goddet, A. Tafzi, S.-W. Chou, L. Veisz, *et al.* (2015), Phys. Rev. Lett. **115** (15), 155002.
- Günther, M. M., K. Sonnabend, E. Brambrink, K. Vogt, V. Bagnoud, K. Harres, and M. Roth (2011), Phys. Plasmas **18**, 083102.
- Hamster, H., A. Sullivan, S. Gordon, and R. W. Falcone (1994), Phys. Rev. E **49**, 671.
- Hamster, H., A. Sullivan, S. Gordon, W. White, and R. W. Falcone (1993), Phys. Rev. Lett. **71**, 2725.
- Harris, D. J. (2016), Proc. Natl. Acad. Sci. U. S. A. **113**, 1107.
- Hartemann, F., W. Brown, D. Gibson, S. Anderson, A. Tremaine, P. Springer, A. Wootton, E. Hartouni, and C. Barty (2005), Phys. Rev. ST Accel. Beams **8** (10), 100702.
- Hartemann, F., D. Gibson, W. Brown, A. Rousse, K. T. Phuoc, V. Malka, J. Faure, and A. Pukhov (2007), Phys. Rev. Special Topics-Accel. Beams **10** (1), 011301.
- He, Z.-H., B. Hou, V. Le Bailly, J. Nees, K. Krushelnick, and A. Thomas (2015), Nat. Commun. **6**, 7156.
- Heigoldt, M., A. Popp, K. Khrennikov, J. Wenz, S. W. Chou, S. Karsch, S. I. Bajlekov, S. M. Hooker, and B. Schmidt (2015), Phys. Rev. ST - Accel. Beams **18** (12), 1.
- Helle, M., D. Kaganovich, D. Gordon, and A. Ting (2010), Phys. Rev. Lett. **105** (10), 105001.
- HEPAP, (2015), *Accelerating Discovery: A Strategic Plan for Accelerator Research and Development in the U. S.*, Tech. Rep. (Accelerator Research and Development Subpanel of the High-Energy Physics Advisory Panel).
- Hidding, B., G. Pretzler, M. Clever, F. Brandl, F. Zamponi, A. Lbcke, T. Kämpfer, I. Uschmann, E. Förster, U. Schramm, R. Sauerbrey, E. Kroupp, L. Veisz, K. Schmid, S. Benavides, and S. Karsch (2007), Review of Scientific Instruments **78**, 083301.
- Hidding, B., G. Pretzler, J. Rosenzweig, T. Königstein, D. Schiller, and D. Bruhwiler (2012), Phys. Rev. Lett. **108** (3), 035001.
- Hogan, M. J., C. E. Clayton, C. Huang, P. Muggli, S. Wang, B. E. Blue, D. Walz, K. A. Marsh, C. L. O'Connell, S. Lee, R. Iverson, F.-J. Decker, P. Raimondi, W. B. Mori, T. C. Katsouleas, C. Joshi, and R. H. Siemann (2003), Phys. Rev. Lett. **90**, 205002.
- Hogan, M. J., T. O. Raubenheimer, A. Seryi, P. Muggli, T. Katsouleas, C. Huang, W. Lu, W. An, K. A. Marsh, W. B. Mori, C. E. Clayton, and C. Joshi (2010), New J. Physics **12**, 055030.
- Hooker, S. M. (2013), Nat. Photonics **7** (10), 775.
- Hooker, S. M., R. Bartolini, S. P. D. Mangles, A. Tünnermann, L. Corner, J. Limpert, A. Seryi, and R. Walczak (2014), J. Phys. B **47** (23), 234003.
- Horst, F., G. Fehrenbacher, T. Radon, E. Kozlova, O. Rosmej, D. Czarnecki, O. Schrenk, J. Breckow, and K. Zink (2015), Nucl. Instrum. Methods Phys. Res. A **782**, 69.
- Huang, C., W. Lu, M. Zhou, C. E. Clayton, C. Joshi, W. B. Mori, P. Muggli, S. Deng, E. Oz, T. Katsouleas, M. J. Hogan, I. Blumenfeld, F. J. Decker, R. Ischebeck, R. H. Iverson, N. A. Kirby, and D. Walz (2007), Phys. Rev. Lett. **99**, 255001.
- Huang, Z., Y. Ding, and C. B. Schroeder (2012), Phys. Rev. Lett. **109**, 204801.
- Huang, Z., and K.-J. Kim (2007), Phys. Rev. ST-Accel. Beams **10** (3), 034801.
- Iaconis, C., and I. A. Walmsley (1998), Opt. Lett. **23** (10), 792.
- Iwabuchi, Y., N. Mori, K. Takahashi, T. Matsuda, and S. Shionoya (1994), Jpn. J. Appl. Phys. **33** (1R), 178.
- Jackson, J. D. (1999), *Classical Electrodynamics, 3rd ed.* (John Wiley & Sons Inc, New York, NY).
- Jamison, S. P., J. Shen, A. M. MacLeod, W. A. Gillespie, and D. A. Jaroszynski (2003), Opt. Lett. **28**, 1710.
- Jochmann, A., A. Irman, M. Bussmann, J. P. Couperus, T. E. Cowan, A. D. Debus, M. Kuntzsch, K. W. D. Ledingham, U. Lehnert, R. Sauerbrey, H. P. Schlenvoigt, D. Seipt, T. Stöhlker, D. B. Thorn, S. Trotsenko, A. Wagner, and U. Schramm (2013), Phys. Rev. Lett. **111** (11), 114803.
- Kaganovich, D., P. Sasorov, C. Cohen, and A. Zigler (1999), Appl. Phys. Lett. **75**, 772.
- Kak, A. C., and M. Slaney (1998), *Principles of Computerized Tomographic Imaging* (IEEE Press).
- Kallos, E., T. Katsouleas, W. D. Kimura, K. Kusche, P. Muggli, I. Pavlishan, I. Pogorelsky, D. Stolyarov, and V. Yakimenko (2008), Phys. Rev. Lett. **100**, 074802.
- Kalmykov, S., S. A. Yi, and G. Shvets (2009), Phys. Rev. Lett. **103**, 135004.
- Kalmykov, S. Y., A. Beck, X. Davoine, E. Lefebvre, and B. A. Shadwick (2012), New J. Physics **14** (3), 033025.
- Kaluza, M. C., H.-P. Schlenvoigt, S. P. D. Mangles, A. G. R. Thomas, A. E. Dangor, H. Schwoerer, W. B. Mori, Z. Najmudin, and K. M. Krushelnick (2010), Phys. Rev. Lett. **105**, 115002.
- Karataev, P., A. Aryshev, S. Boogert, D. Howell, N. Terunuma, and J. Urakawa (2011), Phys. Rev. Lett. **107** (17), 174801.
- Karlovets, D. V., and A. P. Potylitsyn (2006), Phys. Rev. ST-Accel. Beams **9** (8), 080701.
- Karlovets, D. V., and a. P. Potylitsyn (2008), J. Exp. Theor. Phys. **107** (5), 755.
- Kasim, M. F., J. Holloway, L. Ceurvorst, M. C. Levy, N. Ratan, J. Sadler, R. Bingham, P. N. Burrows, R. Trines,

- M. Wing, and P. Norreys (2015), *Phys. Rev. ST Accel. Beams* **18**, 081302.
- Katsouleas, T. (1986), *Phys. Rev. A* **33**, 2056.
- Kesar, A. S. (2010), *Phys. Rev. ST Accel. Beams* **13** (2), 022804.
- Khrennikov, K., J. Wenz, A. Buck, J. Xu, M. Heigoldt, L. Veisz, and S. Karsch (2015a), *Phys. Rev. Lett.* **114** (19), 195003.
- Khrennikov, K., J. Wenz, A. Buck, J. Xu, M. Heigoldt, L. Veisz, and S. Karsch (2015b), *Phys. Rev. Lett.* **114**, 195003.
- Kim, H. T., K. Y. Pae, H. J. Cha, I. J. Kim, T. J. Yu, J. H. Sung, S. K. Lee, T. M. Jeong, and J. Lee (2013a), *Phys. Rev. Lett.* **111**, 165002.
- Kim, K. Y., I. Alexeev, and H. M. Milchberg (2002a), *Opt. Express* **10** (26), 1563.
- Kim, K. Y., I. Alexeev, and H. M. Milchberg (2002b), *Appl. Rev. Lett.* **81**, 4124.
- Kim, M. S., D. G. Jan, T. H. Lee, I. H. Nam, I. W. Lee, and H. Suk (2013b), *Appl. Phys. Lett.* **102**, 204103.
- Kimura, W., H. Milchberg, P. Muggli, X. Li, and W. Mori (2011), *Phys. Rev. ST-Accel. Beams* **14** (4), 041301.
- Kimura, W. D. (2006), in *AIP Conf. Proc.*, Vol. 877, pp. 527–533.
- Kitagawa, Y., T. Matsumoto, T. Minamihata, K. Sawai, K. Matsuo, K. Mima, K. Nishihara, H. Azechi, K. Tanaka, H. Takabe, *et al.* (1992), *Phys. Rev. Lett.* **68** (1), 48.
- Kitagawa, Y., Y. Sentoku, S. Akamatsu, W. Sakamoto, R. Kodama, K. A. Tanaka, K. Azumi, T. Norimatsu, T. Matsuoka, H. Fujita, *et al.* (2004), *Phys. Rev. Lett.* **92** (20), 205002.
- Kneip, S., C. McGuffey, J. L. Martins, M. S. Bloom, V. Chvykov, F. Dollar, R. Fonseca, S. Jolly, G. Kalintchenko, K. Krushelnick, A. Maksimchuk, S. P. D. Mangles, Z. Najmudin, C. A. J. Palmer, K. T. Phuoc, W. Schumaker, L. O. Silva, J. Vieira, V. Yanovsky, and A. G. R. Thomas (2012), *Phys. Rev. ST - Accel. Beams* **15** (2), 021302.
- Kneip, S., C. McGuffey, J. L. Martins, S. F. Martins, C. Bellei, V. Chvykov, F. Dollar, R. Fonseca, C. Huntington, G. Kalintchenko, A. Maksimchuk, S. P. D. Mangles, T. Matsuoka, S. R. Nagel, C. A. J. Palmer, J. Schreiber, K. T. Phuoc, A. G. R. Thomas, V. Yanovsky, L. O. Silva, K. Krushelnick, and Z. Najmudin (2010), *Nature Phys.* **6** (12), 980.
- Kneip, S., S. Nagel, C. Bellei, N. Bourgeois, A. Dangor, A. Gopal, R. Heathcote, S. Mangles, J. Marques, A. Maksimchuk, *et al.* (2008), *Phys. Rev. Lett.* **100** (10), 105006.
- Kneip, S., S. Nagel, S. Martins, S. Mangles, C. Bellei, O. Chekhlov, R. Clarke, N. Delerue, E. Divall, G. Doucas, *et al.* (2009), *Phys. Rev. Lett.* **103** (3), 035002.
- Köhler, A., J. Couperus, O. Zarini, A. Jochmann, A. Irman, and U. Schramm (2016), *Nucl. Instrum. Meth. Physics Res. A* **829**, 265.
- Korbly, S., A. Kesar, R. Temkin, and J. Brownell (2006), *Phys. Rev. ST Accel. Beams* **9** (2), 022802.
- Kostyukov, I., S. Kiselev, and A. Pukhov (2003), *Phys. Plasmas* **10** (12), 4818.
- Kostyukov, I., A. Pukhov, and S. Kiselev (2004), *Phys. Plasmas* **11**, 5256.
- Krall, J., and G. Joyce (1995), *Phys. Plasmas* **2** (4), 1326.
- Krämer, J., A. Jochmann, M. Budde, M. Bussmann, J. Couperus, T. Cowan, A. Debus, A. Köhler, M. Kuntzsch, A. L. García, *et al.* (2018), *Sci. Rpts.* **8** (1), 1398.
- Kruer, W. L. (1988), *The Physics of Laser-Plasma Interactions* (Addison-Wesley, Redwood City).
- Kurz, T., J. Couperus, A. Irman, S. Karsch, and U. Schramm (2018), unpublished.
- Lal, A., D. Gordon, K. Wharton, C. Clayton, K. Marsh, W. Mori, C. Joshi, M. Everett, and T. Johnston (1997), *Phys. Plasmas* **4** (5), 1434.
- Lambert, G., S. Corde, K. T. Phuoc, V. Malka, A. B. Ismail, E. Benveniste, A. Specka, M. Labat, A. Loulergue, R. Bachelard, *et al.* (2012), in *Proceed. FEL conf., Nara, Japan*, p. 2.
- Laziev, E. M., E. V. Tsakanov, and S. Vahanyan (1988), in *Proc. Eur. Particle Accelerator Conference*, p. 523.
- Le Blanc, S. P., M. C. Downer, R. Wagner, S.-Y. Chen, A. Maksimchuk, G. Mourou, and D. Umstadter (1996), *Phys. Rev. Lett.* **77**, 5381.
- LeBlanc, S. P., E. W. Gaul, N. H. Matlis, A. Rundquist, and M. C. Downer (2000), *Opt. Lett.* **25**, 764.
- Lee, S., T. Katsouleas, R. G. Hemker, E. S. Dodd, and W. B. Mori (2001), *Phys. Rev. E* **64**, 045501.
- Lee, S., T. Katsouleas, P. Muggli, W. B. Mori, C. Joshi, R. Hemker, E. S. Dodd, C. E. Clayton, K. A. Marsh, B. Blue, S. Wang, R. Assmann, F. J. Decker, M. Hogan, R. Iverson, and D. Walz (2002), *Phys. Rev. ST Accel. Beams* **5**, 011001.
- Lee, S.-Y. (2004), *Accelerator physics* (World Scientific Publishing Co Inc).
- Leemans, W., C. Geddes, J. Faure, C. Tóth, J. Van Tilborg, C. Schroeder, E. Esarey, G. Fubiani, D. Auerbach, B. Marcellis, *et al.* (2003), *Phys. Rev. Lett.* **91** (7), 074802.
- Leemans, W., B. Nagler, A. Gonsalves, C. Tóth, K. Nakamura, C. Geddes, E. Esarey, C. Schroeder, and S. Hooker (2006), *Nature Phys.* **2** (10), 696.
- Leemans, W., D. Rodgers, P. Catravas, C. Geddes, G. Fubiani, E. Esarey, B. Shadwick, R. Donahue, and A. Smith (2001), *Phys. Plasmas* **8** (5), 2510.
- Leemans, W. P., and E. Esarey (2009), *Physics Today* **62**, 44.
- Leemans, W. P., A. J. Gonsalves, H. Mao, K. Nakamura, C. Benedetti, C. B. Schroeder, C. Tth, J. Daniels, D. E. Mittelberger, S. S. Bulanov, J.-L. Vay, C. G. R. Geddes, and E. Esarey (2014), *Phys. Rev. Lett.* **13**, 245002.
- Leemans, W. P., R. W. Schoenlein, P. Volfbeyn, A. H. Chin, T. E. Glover, P. Balling, M. Zolotarev, K. J. Kim, S. Chattopadhyay, and C. V. Shank (1996), *Phys. Rev. Lett.* **77**, 4182.
- Lehe, R., A. Lifschitz, C. Thauray, V. Malka, and X. Davoine (2013), *Phys. Rev. ST - Accel. Beams* **16** (2), 1.
- Lejeune, C., and J. Aubert (1980), *Appl. Charged Part. Opt. Supp.* **13A**.
- Li, F., Z.-M. Sheng, Y. Liu, J. Meyer-ter Vehn, W. Mori, W. Lu, and J. Zhang (2013a), *Phys. Rev. Lett.* **110** (13), 135002.
- Li, F., C. Zhang, Y. Wan, Y. Wu, X. Xu, J. Hua, C. Pai, W. Lu, Y. Gu, W. Mori, *et al.* (2016), *Plasma Phys. Control. Fusion* **58** (3), 034004.
- Li, S. Z., and M. J. Hogan (2011), in *Proc. Part. Accel. Conf. (PAC'11), New York*, SLAC-PUB-14412 (IEEE).
- Li, Y., D. Li, K. Huang, M. Tao, M. Li, J. Zhao, Y. Ma, X. Guo, J. Wang, M. Chen, *et al.* (2017), *Phys. Plasmas* **24** (2), 023108.
- Li, Z., C.-H. Pai, Y. Y. Chang, R. Zgadzaj, X. Wang, and M. C. Downer (2013b), *Opt. Lett.* **38**, 5157.
- Li, Z., H.-E. Tsai, X. Zhang, C.-H. Pai, Y.-Y. Chang,

- R. Zgadzaj, X. Wang, V. Khudik, G. Shvets, and M. C. Downer (2014a), Phys. Rev. Lett. **113**, 085001.
- Li, Z., R. Zgadzaj, X. Wang, Y.-Y. Chang, and M. C. Downer (2014b), Nat. Commun. **5**, 3085.
- Li, Z., R. Zgadzaj, X. Zhang, S. Reed, P. Dong, and M. C. Downer (2010), Opt. Lett. **35**, 4087.
- Lin, C., J. van Tilborg, K. Nakamura, A. J. Gonsalves, N. H. Matlis, T. Sokollik, S. Shiraishi, J. Osterhoff, C. Benedetti, C. B. Schroeder, C. Tóth, E. Esarey, and W. P. Leemans (2012), Phys. Rev. Lett. **108**, 094801.
- Litos, M., E. Adli, W. An, C. I. Clarke, C. E. Clayton, S. Corde, J. P. Delahaye, R. J. England, A. S. Fisher, J. Frederico, S. Gessner, S. Z. Green, M. J. Hogan, C. Joshi, W. Lu, K. A. Marsh, W. B. Mori, P. Muggli, N. Vafaie-Najafabadi, D. Walz, G. White, Z. Wu, V. Yakimenko, and G. Yocky (2014), Nature (London) **515** (7525), 92.
- Litos, M., and S. Corde (2012), in *AIP Conf. Proc.*, Vol. 1507 (AIP) pp. 705–710.
- Liu, J., C. Xia, W. Wang, H. Lu, C. Wang, A. Deng, W. Li, H. Zhang, X. Liang, Y. Leng, *et al.* (2011), Phys. Rev. Lett. **107** (3), 035001.
- Lotov, K. (2010), Phys. Rev. ST Accel. Beams **13** (4), 041301.
- Lotov, K. (2013), Phys. Plasmas **20** (8), 083119.
- Lotov, K. V., A. P. Sosedkin, and A. V. Petrenko (2014), Phys. Rev. Lett. **112**, 194801.
- Lu, W., C. Huang, M. Zhou, W. Mori, and T. Katsouleas (2005), Physics of Plasmas **12** (6), 063101.
- Lu, W., C. Huang, M. Zhou, W. B. Mori, and T. Katsouleas (2006), Phys. Rev. Lett. **96**, 165002.
- Lu, W., M. Tzoufras, C. Joshi, F. S. Tsung, W. B. Mori, J. Vieira, R. A. Fonseca, and L. O. Silva (2007), Phys. Rev. Special Topics - Accel. Beams **10**, 061301.
- Lundh, O., J. Lim, C. Rechatin, L. Ammoura, a. Ben-Ismaïl, X. Davoine, G. Gallot, J.-P. Goddet, E. Lefebvre, V. Malka, and J. Faure (2011), Nature Phys. **7** (3), 219.
- Lundh, O., C. Rechatin, J. Lim, V. Malka, and J. Faure (2013), Physical review letters **110** (6), 065005.
- Maeda, R., T. Katsouleas, P. Muggli, C. Joshi, W. B. Mori, and W. Quillinan (2004), Phys. Rev. ST Accel. Beams **7**, 111301.
- Maier, A. R., A. Meseck, S. Reiche, C. B. Schroeder, T. Seggebrock, and F. Grüner (2012), Phys. Rev. X **2**, 031019.
- Malka, V. (2012), Phys. Plasmas **19** (5), 055501.
- Malka, V., J. Faure, Y. A. Gauduel, E. Lefebvre, A. Rousse, and K. T. Phuoc (2008), Nat. Phys. **4** (6), 447.
- Manahan, G. G., E. Brunetti, C. Aniculaesei, M. P. Anania, S. Cipiccia, M. R. Islam, D. W. Grant, A. Subiel, R. P. Shanks, R. C. Issac, G. H. Welsh, S. M. Wiggins, and D. A. Jaroszynski (2014), New J. Phys. **16** (10), 103006.
- Mangles, S. P., C. Murphy, Z. Najmudin, A. G. R. Thomas, J. Collier, A. E. Dangor, E. Divall, P. Foster, J. Gallacher, C. Hooker, *et al.* (2004), Nature **431** (7008), 535.
- Mangles, S. P. D., A. G. R. Thomas, M. C. Kaluza, O. Lundh, F. Lindau, A. Persson, F. S. Tsung, Z. Najmudin, W. B. Mori, C.-G. Wahlström, and K. Krushelnick (2006), Phys. Rev. Lett. **96**, 215001.
- Marquès, J., F. Dorchies, F. Amiranoff, P. Audebert, J. Gauthier, J. Geindre, A. Antonetti, T. Antonsen Jr., P. Chessa, and P. Mora (1998), Phys. Plasmas **5** (4), 1162.
- Marquès, J. R., F. Dorchies, P. Audebert, J. P. Geindre, F. Amiranoff, J. C. Gauthier, G. Hammoniaux, A. Antonetti, P. Chessa, P. Mora, and J. T. M. Antonsen (1997), Phys. Rev. Lett. **78**, 3463.
- Marquès, J. R., J. P. Geindre, F. Amiranoff, P. Audebert, J. C. Gauthier, A. Antonetti, and G. Grillon (1996), Phys. Rev. Lett. **76**, 3566.
- Matlis, N., A. Axley, and W. Leemans (2012), Nat. Commun. **3**, 1111.
- Matlis, N. H., A. Maksimchuk, V. Yanovsky, W. P. Leemans, and M. C. Downer (2016), Opt. Lett. **41**, 5503.
- Matlis, N. H., S. Reed, S. S. Bulanov, V. Chvykov, G. Kalintchenko, T. Matsuoka, P. Rousseau, V. Yanovsky, A. Maksimchuk, S. Kalmykov, G. Shvets, and M. C. Downer (2006), Nature Physics **2**, 749.
- McGuffey, C., A. G. R. Thomas, W. Schumaker, T. Matsuoka, V. Chvykov, F. J. Dollar, G. Kalintchenko, V. Yanovsky, A. Maksimchuk, K. Krushelnick, V. Y. Bychenkov, I. V. Glazyrin, and A. V. Karpeev (2010), Phys. Rev. Lett. **104**, 025004.
- Minty, M. G., and F. Zimmermann (2013), *Measurement and control of charged particle beams* (Springer Science & Business Media).
- Mirzaie, M., S. Li, M. Zeng, N. A. M. Hafz, M. Chen, G. Y. Li, Q. J. Zhu, H. Liao, T. Sokollik, F. Liu, Y. Y. Ma, L. M. Chen, Z. M. Sheng, and J. Zhang (2015), Sci. Rpts. **5**, 14659.
- Miyahara, J., K. Takahashi, Y. Amemiya, N. Kamiya, and Y. Satow (1986), Nucl. Instrum. Meth. Phys. Res. A **246** (1-3), 572.
- Modena, A., Z. Najmudin, A. Dangor, C. Clayton, K. Marsh, C. Joshi, V. Malka, C. Darrow, C. Danson, D. Neely, *et al.* (1995), Nature (London) **377** (6550), 606.
- Mora, P., and T. M. Antonsen, Jr (1997), Phys. Plasmas **4** (1), 217.
- Mora, P., D. Pesme, A. Héron, G. Laval, and N. Silvestre (1988), Phys. Rev. Lett. **61** (14), 1611.
- Mostacci, A., A. Bacci, M. Boscolo, E. Chiadroni, A. Cianchi, D. Filippetto, M. Migliorati, P. Musumeci, C. Ronsivalle, and A. Rossi (2008), Rev. Sci. Instrum. **79** (1), 013303.
- Mostacci, A., M. Bellaveglia, E. Chiadroni, A. Cianchi, M. Ferrario, D. Filippetto, G. Gatti, and C. Ronsivalle (2012), Phys. Rev. ST Accel. Beams **15**, 082802.
- Muggli, P. (2016), arXiv:1705.10537v1, 1.
- Muggli, P., B. Allen, Y. Fang, V. Yakimenko, M. Fedurin, K. Kusche, M. Babzien, C. Swinson, and R. Malone (2011), in *Proc. Part. Accel. Conf.*, pp. 712–714.
- Muggli, P., and M. J. Hogan (2009), Comptes Rendus Physique **10** (2), 116.
- Muggli, P., K. A. Marsh, S. Wang, C. E. Clayton, S. Lee, T. C. Katsouleas, and C. Joshi (1999), IEEE Trans. Plasma Science **27**, 791.
- Muggli, P., V. Yakimenko, M. Babzien, E. Kallos, and K. P. Kusche (2008a), Phys. Rev. Lett. **101**, 054801.
- Muggli, P., V. Yakimenko, M. Babzien, E. Kallos, and K. P. Kusche (2008b), Phys. Rev. Lett. **101**, 055001.
- Murphy, C. D., R. Trines, J. Vieira, A. J. W. Reitsma, R. Bingham, J. L. Collier, E. J. Divall, P. S. Foster, C. J. Hooker, A. J. Langley, P. A. Norreys, R. A. Fonseca, F. Fiuza, L. O. Silva, J. T. Mendonca, W. B. Mori, J. G. Gallacher, R. Viskup, D. A. Jaroszynski, S. P. D. Mangles, A. G. R. Thomas, K. Krushelnick, and Z. Najmudin (2006), Phys. Plasmas. **13**, 055001.
- Nakagawa, K., A. Iwasaki, Y. Oishi, R. Horisaki, A. Tsukamoto, A. Nakamura, K. Hirokawa, H. Liao, T. Ushida, K. Goda, *et al.* (2014), Nature Photon. **8** (9), 695.
- Nakajima, K. (1989), Part. Accel. **32** (KEK-89-79), 209.
- Nakajima, K. (2008), Nat. Phys. **4**, 92.

- Nakajima, K., D. Fisher, T. Kawakubo, H. Nakanishi, A. Ogata, Y. Kato, Y. Kitagawa, R. Kodama, K. Mima, H. Shiraga, K. Suzuki, K. Yamakawa, T. Zhang, Y. Sakawa, T. Shoji, Y. Nishida, N. Yugami, M. Downer, and T. Tajima (1995), *Phys. Rev. Lett.* **74**, 4428.
- Nakamura, K., A. Gonsalves, C. Lin, A. Smith, D. Rodgers, R. Donahue, W. Byrne, and W. Leemans (2011), *Phys. Rev. ST Accel. Beams* **14**, 062801.
- Nakamura, K., D. E. Mittelberger, A. J. Gonsalves, J. Daniels, H.-S. Mao, F. Stulle, J. Bergoz, and W. P. Leemans (2016), *Plasma Phys. Control. Fusion* **58** (3), 034010.
- Nakamura, K., W. Wan, N. Ybarrolaza, D. Syversrud, J. Wallig, and W. P. Leemans (2008), *Rev. Sci. Instrum.* **79**, 053301.
- Németh, K., B. Shen, Y. Li, H. Shang, R. Crowell, K. Harkay, and J. Cary (2008), *Phys. Rev. Lett.* **100** (9), 1.
- Norreys, P. A. (2009), *Nat. Photonics* **3** (8), 423.
- O’Connell, C. L., C. D. Barnes, F.-J. Decker, M. J. Hogan, R. Iverson, P. Krejcik, R. Siemann, D. R. Walz, C. E. Clayton, C. Huang, D. K. Johnson, C. Joshi, W. Lu, K. A. Marsh, W. Mori, M. Zhou, S. Deng, T. Katsouleas, P. Muggli, and E. Oz (2006), *Phys. Rev. ST Accel. Beams* **9**, 101301.
- Ohkubo, T., A. Maekawa, R. Tsujii, T. Hosokai, K. Kinoshita, K. Kobayashi, M. Uesaka, A. Zhidkov, K. Nemoto, Y. Kondo, and Y. Shibata (2007), *Phys. Rev. Spec. Top. - Accel. and Beams* **10**, 031301.
- Onuki, H., and P. Elleaume (2002), *Undulators, Wigglers and Their Applications* (CRC Press).
- O’Shea, P., M. Kimmel, X. Gu, and R. Trebino (2001), *Optics Letters* **26** (12), 932.
- Osterhoff, J., A. Popp, Z. Major, B. Marx, T. P. Rowlands-Rees, M. Fuchs, M. Geissler, R. Hörlein, B. Hidding, S. Becker, E. A. Peralta, U. Schramm, F. Grüner, D. Habs, F. Krausz, S. M. Hooker, and S. Karsch (2008), *Phys. Rev. Lett.* **101**, 085002.
- Pafomov, V. E. (1971), “Radiation of a Charged Particle in the Presence of a Separating Boundary,” in *Nuclear Physics and Interaction of Particles with Matter*, edited by D. V. Skobel’tsyn (Springer US, Boston, MA) pp. 25–157.
- Pak, A., K. A. Marsh, S. F. Martins, W. Lu, W. B. Mori, and C. Joshi (2010), *Phys. Rev. Lett.* **104**, 025003.
- Panofsky, W. K. H. (1956), *Rev. Sci. Instrum.* **27**, 967.
- Pausch, R., H. Burau, M. Bussmann, J. Couperus, T. E. Cowan, A. Debus, A. Huebl, A. Irman, A. Köhler, U. Schramm, K. Steiniger, and R. Widera (2014a), in *Proc. IPAC2014*, pp. 761–764.
- Pausch, R., A. Debus, R. Widera, K. Steiniger, A. Huebl, H. Burau, M. Bussmann, and U. Schramm (2014b), *Nucl. Instrum. Methods Phys. Res. A* **740**, 250.
- Peng, X.-Y., O. Willi, M. Chen, and A. Pukhov (2008), *Opt. Express* **16** (16), 12342.
- Phuoc, K., S. Corde, R. Shah, F. Albert, R. Fitour, J.-P. Rousseau, F. Burgy, B. Mercier, and A. Rousse (2006), *Phys. Rev. Lett.* **97** (22), 1.
- Plateau, G. R., C. G. R. Geddes, D. B. Thorn, M. Chen, C. Benedetti, E. Esarey, A. J. Gonsalves, N. H. Matlis, K. Nakamura, C. B. Schroeder, S. Shiraishi, T. Sokollik, J. van Tilborg, C. Toth, S. Trotsenko, T. S. Kim, M. Battaglia, T. Stöhlker, and W. P. Leemans (2012), *Phys. Rev. Lett.* **109**, 064802.
- Platt, B., and R. Shack (2001), *J. Refractive Surgery* **17** (5), S573.
- Pleasant, S. (2014), *Nature Photon.* **8** (4), 271.
- Pogorelsky, I., and I. Ben-Zvi (2014), *Plasma Phys. Control. Fusion* **56** (8), 084017.
- Pollock, B., C. Clayton, J. Ralph, F. Albert, A. Davidson, L. Divol, C. Filip, S. Glenzer, K. Herpoldt, W. Lu, *et al.* (2011), *Phys. Rev. Lett.* **107** (4), 045001.
- Pollock, B., J. Ross, G. Tynan, L. Divol, S. Glenzer, V. Leurent, J. Palaastro, J. Ralph, D. Froula, C. Clayton, *et al.* (2009), *Two-screen method for determining electron beam energy and deflection from laser wakefield acceleration*, Tech. Rep. (Lawrence Livermore National Laboratory (LLNL), Livermore, CA).
- Polyanskiy, M. N., M. Babzien, and I. V. Pogorelsky (2015), *Optica* **2** (8), 675.
- Powers, N. D., I. Ghebregziabher, G. Golovin, C. Liu, S. Chen, S. Banerjee, J. Zhang, and D. P. Umstadter (2014), *Nature Photon.* **8**, 29.
- Protopapas, M., C. H. Keitel, and P. L. Knight (1997), *Rep. Prog. Physics* **60** (4), 389.
- Pukhov, A. (1999), *J. Plasma Phys.* **61** (3), 425.
- Pukhov, A., and J. Meyer-ter-Vehn (2002), *Appl. Phys. B* **74**, 355.
- Ralph, J. E., K. A. Marsh, A. E. Pak, W. Lu, C. E. Clayton, F. Fang, W. B. Mori, and C. Joshi (2009), *Phys. Rev. Lett.* **102**, 175003.
- Rechatin, C., J. Faure, A. Ben-Ismaïl, J. Lim, R. Fitour, A. Specka, H. Videau, A. Tafzi, F. Burgy, and V. Malka (2009), *Phys. Rev. Lett.* **102** (16), 164801.
- Reed, S., V. Chvykov, G. Kalintchenko, T. Matsuoka, V. Yanovsky, C. R. Vane, J. R. Beene, D. Stracener, D. R. Schultz, and A. Maksimchuk (2007), *J. Appl. Phys.* **102** (7), 073103.
- Rees, J., and L. Rivkin (1984), *Measuring emittances and sigma matrices*, Tech. Rep. (Stanford Linear Accelerator Center, CA (USA)).
- Reiche, S., and J. Rosenzweig (2001), *PACS2001. Proc. 2001 Part. Accel. Conf. (Cat. No.01CH37268)*, 7.
- Reiser, M. (2008), *Theory and design of charged particle beams* (Wiley-VCH).
- Reynaud, F., F. Salin, and A. Barthelemy (1989), *Opt. Lett.* **14**, 275.
- Ride, S. K., E. Esarey, and M. Baine (1995), *Phys. Rev. E* **52**, 5425.
- Rittershofer, W., C. B. Schroeder, E. Esarey, F. J. Grüner, and W. P. Leemans (2010), *Phys. Plasmas* **17**, 063104.
- Ritz, S. (2014), *Building for Discovery: Strategic Plan for U. S. Particle Physics in the Global Context*, Tech. Rep. (Particle Physics Project Prioritization Panel (P5)).
- Röhrs, M., C. Gerth, H. Schlarb, B. Schmidt, and P. Schmüser (2009), *Phys. Rev. ST Accel. Beams* **12**, 050704.
- Rosenbluth, M., and C. Liu (1972), *Phys. Rev. Lett.* **29** (11), 701.
- Rosenzweig, J., N. Barov, A. Murokh, E. Colby, and P. Colestock (1998), *Nucl. Instrum. Meth. Phys. Res. A* **410** (3), 532.
- Rosenzweig, J. B. (1987), *Phys. Rev. Lett.* **58**, 555.
- Rosenzweig, J. B., B. Breizman, T. Katsouleas, and J. J. Su (1991), *Phys. Rev. A* **44**, R6189.
- Rosenzweig, J. B., D. B. Cline, B. Cole, H. Figureroa, W. Gai, R. Konecny, J. Norem, P. Schoessow, and J. Simpson (1988), *Phys. Rev. Lett.* **61**, 98.
- Rosenzweig, J. B., P. Schoessow, B. Cole, W. Gai, R. Konecny, J. Norem, and J. Simpson (1989), *Phys. Rev. A* **39**, 1586.

- Rousse, A., K. Ta Phuoc, R. Shah, A. Pukhov, E. Lefebvre, V. Malka, S. Kiselev, F. Burgy, J. P. Rousseau, D. Umstadter, and D. Hulin (2004), *Phys. Rev. Lett.* **93** (13), 135005.
- Ruth, R. D., P. Morton, P. B. Wilson, and A. Chao (1984), *Part. Accel.* **17** (SLAC-PUB-3374), 171.
- Rykovanov, S., C. Geddes, J. Vay, C. Schroeder, E. Esarey, and W. Leemans (2014), *J. Phys. B* **47** (23), 234013.
- Sahai, A. A., T. C. Katsouleas, F. S. Tsung, and W. B. Mori (2016), arXiv preprint arXiv:1405.4302.
- Salin, F., P. Georges, G. Roger, and A. Brun (1987), *Appl. Opt.* **26** (21), 4528.
- Sannibale, F., G. V. Stupakov, M. S. Zolotarev, D. Filippetto, and L. Jägerhofer (2009), *Phys. Rev. ST Accel. Beams* **12**, 032801.
- Sarri, G., D. J. Corvan, W. Schumaker, J. M. Cole, A. Di Piazza, H. Ahmed, C. Harvey, C. H. Keitel, K. Krushelnick, S. P. D. Mangles, Z. Najmudin, D. Szymes, A. G. R. Thomas, M. Yeung, Z. Zhao, and M. Zepf (2014), *Phys. Rev. Lett.* **113** (22), 224801.
- Sävert, A., S. P. D. Mangles, M. Schnell, E. Siminos, J. M. Cole, M. Leier, M. Reuter, M. B. Schwab, M. Möller, K. Poder, O. Jäckel, G. G. Paulus, C. Spielmann, S. Skupin, Z. Najmudin, and M. C. Kaluza (2015), *Phys. Rev. Lett.* **115**, 055002.
- Savran, D., K. Lindenberg, J. Glorius, B. Loeher, S. Mueller, N. Pietralla, N. Schnorrenberger, V. Simon, K. Sonnabend, C. Waelzlein, M. Elvers, J. Endres, J. Hasper, and A. Zilges (2010), *Nucl. Instrum. Meth. Phys. Res. A* **613**, 232.
- Schlenvoigt, H. P., K. Haupt, A. Debus, F. Budde, O. Jaekel, S. Pfoth, H. Schwoerer, E. Rohwer, J. G. Gallacher, E. Brunetti, R. P. Shanks, S. M. Wiggins, and D. A. Jaroszynski (2008), *Nature Phys.* **4**, 130.
- Schmid, K., A. Buck, C. M. Sears, J. M. Mikhailova, R. Tautz, D. Herrmann, M. Geissler, F. Krausz, and L. Veisz (2010), *Phys. Rev. ST Accel. Beams* **13** (9), 091301.
- Schmidt, B. (2006), in *Proc. 28th Int. Free Electron Laser Conf., Berlin, Germany*, p. 761.
- Schnell, M., A. Sävert, B. Landgraf, M. Reuter, M. Nicolai, O. Jäckel, C. Peth, T. Thiele, O. Jansen, A. Pukhov, *et al.* (2012), *Phys. Rev. Lett.* **108** (7), 075001.
- Schnell, M., A. Sävert, I. Uschmann, M. Reuter, M. Nicolai, T. Kämpfer, B. Landgraf, O. Jäckel, O. Jansen, A. Pukhov, M. C. Kaluza, and C. Spielmann (2013), *Nature Commun.* **4** (May), 2421.
- Schramm, U., M. Bussmann, A. Irman, M. Siebold, K. Zeil, D. Albach, C. Bernert, S. Bock, F. Brack, J. Branco, *et al.* (2017), in *J. Physics: Conf. Ser.*, Vol. 874 (IOP Publishing) p. 012028.
- Schroeder, C., E. Esarey, J. Van Tilborg, and W. Leemans (2004), *Phys. Rev. E* **69** (1), 16501.
- Schroeder, C., P. Lee, J. Wurtele, E. Esarey, and W. Leemans (1999a), *Phys. Rev. E* **59** (5), 6037.
- Schroeder, C., D. Whittum, and J. Wurtele (1999b), *Phys. Rev. Lett.* **82** (6), 1177.
- Schumaker, W., N. Nakanii, C. McGuffey, C. Zulick, V. Chyvkov, F. Dollar, H. Habara, G. Kalintchenko, A. Maksimchuk, K. A. Tanaka, A. G. R. Thomas, V. Yanovsky, and K. Krushelnick (2013), *Phys. Rev. Lett.* **110** (1).
- Schwab, M. B., A. Sävert, O. Jäckel, J. Polz, M. Schnell, T. Rinck, L. Veisz, M. Möller, P. Hansinger, G. G. Paulus, and M. C. Kaluza (2013), *Appl. Phys. Lett.* **103**, 191118.
- Schwoerer, H., B. Liesfeld, H. Schlenvoigt, K. Amthor, and R. Sauerbrey (2006), *Phys. Rev. Lett.* **96** (1), 014802.
- Sears, C. M. S., A. Buck, K. Schmid, J. Mikhailova, F. Krausz, and L. Veisz (2010a), *Phys. Rev. ST Accel. Beams* **13**, 092803.
- Sears, C. M. S., S. B. Cuevas, U. Schramm, K. Schmid, A. Buck, D. Habs, F. Krausz, and L. Veisz (2010b), *Rev. Sci. Instrum.* **81**, 073304.
- Seggebrock, T., A. R. Maier, I. Dornmair, and F. Gruener (2013), *Phys. Rev. ST Accel. Beams* **16**, 070703.
- Serafini, L. (1996), *IEEE Trans. Plasma Sci.* **24** (2), 421.
- Shah, R. C., F. Albert, K. Ta Phuoc, F. Burgy, J. P. Rousseau, O. Shevchenko, D. Boschetto, A. Rousse, A. Pukhov, and S. Kiselev (2007), *Conf. Lasers and Electro-Optics, 2007*, 1.
- Shaw, B., J. van Tilborg, A. Gonsalves, K. Nakamura, T. Sokollik, S. Shiraishi, R. Mittal, E. Esarey, C. Schroeder, C. Toth, *et al.* (2012), in *AIP Conf. Proc.*, Vol. 1507 (AIP) pp. 310-314.
- Shaw, J., A. Bernstein, R. Zgadaj, A. Hannasch, M. LaBerge, Y. Chang, K. Weichman, J. Welch, W. Henderson, H.-E. Tsai, *et al.* (2017), arXiv preprint arXiv:1705.08637.
- Shiraishi, S., C. Benedetti, A. J. Gonsalves, K. Nakamura, B. H. Shaw, T. Sokollik, J. van Tilborg, C. G. R. Geddes, C. B. Schroeder, C. Tth, E. Esarey, and W. P. Leemans (2013), *Phys. Plasmas* **20** (6), 063103.
- Shkvarunets, A. G., and R. B. Fiorito (2008), *Phys. Rev. ST Accel. Beams* **11** (1), 1.
- Shvets, G., and X. Li (1999), *Phys. Plasmas* **6** (2), 591.
- Siders, C. W., S. P. LeBlanc, A. Babine, A. Stepanov, A. Sergeev, T. Tajima, and M. C. Downer (1996a), *IEEE Trans. Plasma Sci.* **24**, 301.
- Siders, C. W., S. P. LeBlanc, D. Fisher, T. Tajima, M. C. Downer, A. Babine, A. Stepanov, and A. Sergeev (1996b), *Phys. Rev. Lett.* **76**, 3570.
- Siders, C. W., J. L. Siders, A. J. Taylor, S.-G. Park, and A. M. Weiner (1998), *Appl. Opt.* **37** (22), 5302.
- Siminos, E., S. Skupin, A. Sävert, J. M. Cole, S. P. D. Mangles, and M. C. Kaluza (2016), *Plasma Phys. Control. Fusion* **58**, 065004.
- Slusher, R., and C. M. Surko (1980), *Phys. Fluids* **23** (3), 472.
- Smith, S. J., and E. Purcell (1953), *Phys. Rev.* **92** (4), 1069.
- Sprangle, P., E. Esarey, J. Krall, and G. Joyce (1992), *Phys. Rev. Lett.* **69** (15), 2200.
- Sprangle, P., E. Esarey, and A. Ting (1990a), *Phys. Rev. A* **41** (8), 4463.
- Sprangle, P., E. Esarey, and A. Ting (1990b), *Phys. Rev. Lett.* **64** (17), 2011.
- Sprangle, P., B. Hafizi, J. R. Peano, R. F. Hubbard, A. Ting, C. I. Moore, D. F. Gordon, A. Zigler, D. Kaganovich, and J. T. M. Antonsen (2001), *Phys. Rev. E* **63**, 056405.
- Sprangle, P., C.-M. Tang, and E. Esarey (1987), *IEEE Trans. Plasma Sci.* **15** (2), 145.
- Steffen, B., V. Arsov, G. Berden, W. A. Gillespie, S. Jamison, A. M. MacLeod, A. van der Meer, P. Phillips, H. Schlarb, B. Schmidt, *et al.* (2009), *Phys. Rev. ST Accel. Beams* **12** (3), 032802.
- Steinke, S., J. van Tilborg, C. Benedetti, C. G. R. Geddes, C. B. Schroeder, J. Daniels, K. K. Swanson, A. J. Gonsalves, K. Nakamura, N. H. Matlis, B. H. Shaw, E. Esarey, and W. P. Leemans (2016), *Nature (London)* **530**, 190.
- Suk, H., N. Barov, J. B. Rosenzweig, and E. Esarey (2001), *Phys. Rev. Lett.* **86** (6), 1011.

- Sun, F. G., Z. Jiang, and X.-C. Zhang (1998), *Appl. Phys. Lett.* **73** (16), 2233.
- Sütterlin, D., D. Erni, M. Dehler, H. Jäckel, H. Sigg, and V. Schlott (2007), *Nucl. Instrum. Meth. Phys. Res. B* **264** (2), 361.
- Swanson, K., H.-E. Tsai, S. Barber, R. Lehe, H.-S. Mao, S. Steinke, J. van Tilborg, K. Nakamura, C. Geddes, C. Schroeder, *et al.* (2017), *Phys. Rev. Accel. Beams* **20** (5), 051301.
- Ta Phuoc, K., S. Corde, C. Thaury, V. Malka, A. Tafzi, J. P. Goddet, R. C. Shah, S. Sebban, and A. Rousse (2012), *Nature Photon.* **6** (5), 308.
- Tajima, T., and J. M. Dawson (1979), *Phys. Rev. Lett.* **43**, 267.
- Takeda, M., H. Ina, and S. Kobayashi (1982), *J. Opt. Soc. Am.* **72** (1), 156.
- Tanaka, K. A., T. Yabuuchi, T. Sato, R. Kodama, Y. Kitagawa, T. Takahashi, T. Ikeda, Y. Honda, and S. Okuda (2005), *Rev. Sci. Instrum.* **76**, 013507.
- Tarantola, A. (2006), *Nature Phys.* **2** (8), 492.
- Ter-Mikaelian, M. L. (1972), *New York* (John Wiley & Sons Inc, New York, NY).
- Thaury, C., E. Guillaume, S. Corde, R. Lehe, M. Le Bouteiller, K. Ta Phuoc, X. Davoine, J. M. Rax, A. Rousse, and V. Malka (2013), *Phys. Rev. Lett.* **111** (13), 1, arXiv:arXiv:1306.0016v2.
- Thomas, A. G. R. (2010), *Phys. Plasmas* **17** (5).
- Thomas, A. G. R., S. P. D. Mangles, Z. Najmudin, M. C. Kaluza, C. D. Murphy, and K. Krushelnick (2007), *Phys. Rev. Lett.* **98**, 054802.
- Thomas, C., N. Delerue, and R. Bartolini (2013), *Nucl. Instrum. Meth. Phys. Res. A* **729**, 554.
- Ting, A., K. Krushelnick, C. Moore, H. Burris, E. Esarey, J. Krall, and P. Sprangle (1996), *Phys. Rev. Lett.* **77** (27), 5377.
- Tokunaga, E., A. Terasaki, and T. Kobayashi (1992), *Opt. Lett.* **17**, 1131.
- Trebino, R., K. W. DeLong, D. N. Fittinghoff, J. N. Sweetser, M. A. Krumbügel, B. A. Richman, and D. J. Kane (1997), *Rev. Sci. Instrum.* **68** (9), 3277.
- Trines, R. M. G. M., C. D. Murphy, K. L. Lancaster, O. Chekhlov, P. A. Norreys, R. Bingham, J. T. Mendonca, L. O. Silva, S. P. D. Mangles, C. Kamperidis, A. Thomas, K. Krushelnick, and Z. Najmudin (2009), *Plasma Phys. Control. Fusion* **51** (2), 024008.
- Tsai, H. E., X. Wang, J. M. Shaw, Z. Li, A. V. Arefiev, X. Zhang, R. Zgadzaj, W. Henderson, V. Khudik, G. Shvets, and M. C. Downer (2015), *Phys. Plasmas* **22** (2), 10.1063/1.4907655, arXiv:1411.2134.
- Tzeng, K., W. B. Mori, and C. Decker (1996), *Phys. Rev. Lett.* **76** (18), 3332.
- Tzoufras, M., W. Lu, F. S. Tsung, C. Huang, W. B. Mori, T. Katsouleas, J. Vieira, R. A. Fonseca, and L. O. Silva (2008), *Phys. Rev. Lett.* **101**, 145002.
- Umstadter, D., S.-Y. Chen, A. Maksimchuk, G. Mourou, and R. Wagner (1996), *Science* **273** (5274), 472.
- Umstadter, D., E. Esarey, and J. Kim (1994), *Phys. Rev. Lett.* **72** (8), 1224.
- Umstadter, D., J. Kim, E. Esarey, E. Dodd, and T. Neubert (1995), *Phys. Rev. E* **51** (4), 3484.
- Umstadter, D. P. (2015), *Contemp. Phys.* **56** (4), 417.
- Unser, K. (1989), in *Proc. Part. Accel. Conf.* (IEEE) pp. 71–73.
- van Tilborg, J., C. Schroeder, C. Filip, C. Tóth, C. Geddes, G. Fubiani, R. Huber, R. Kaindl, E. Esarey, and W. Leemans (2006), *Phys. Rev. Lett.* **96** (1), 5.
- van Tilborg, J., C. B. Schroeder, E. Esarey, and W. P. Leemans (2004), *Laser and Particle Beams* **22**, 415.
- van Tilborg, J., S. Steinke, C. G. R. Geddes, N. H. Matlis, B. H. Shaw, A. J. Gonsalves, J. V. Huijts, K. Nakamura, J. Daniels, C. B. Schroeder, C. Benedetti, E. Esarey, S. S. Bulanov, N. A. Bobrova, P. V. Satorov, and W. P. Leemans (2015), *Phys. Rev. Lett.* **115**, 184802.
- Vieira, J., R. Fonseca, W. Mori, and L. Silva (2012), *Phys. Rev. Lett.* **109** (14), 145005.
- Villeneuve, D., H. Baldis, J. Bernard, and R. Benesch (1991), *J. Opt. Soc. Am. B* **8** (4), 895.
- Wagner, R., S.-Y. Chen, A. Maksimchuk, and D. Umstadter (1997), *Phys. Rev. Lett.* **78** (16), 3125.
- Wahlstrand, J., Y.-H. Cheng, Y.-H. Chen, and H. Milchberg (2011), *Phys. Rev. Lett.* **107** (10), 103901.
- Wang, S., C. E. Clayton, B. E. Blue, E. S. Dodd, K. a. Marsh, W. B. Mori, C. Joshi, S. Lee, P. Muggli, T. Katsouleas, F. J. Decker, M. J. Hogan, R. H. Iverson, P. Raimondi, D. Walz, R. Siemann, and R. Assmann (2002), *Phys. Rev. Lett.* **88** (13), 135004.
- Wang, W., W. Li, J. Liu, Z. Zhang, R. Qi, C. Yu, J. Liu, M. Fang, Z. Qin, C. Wang, *et al.* (2016), *Phys. Rev. Lett.* **117** (12), 124801.
- Wang, X., R. Zgadzaj, N. Fazel, Z. Li, S. A. Yi, X. Zhang, W. Henderson, Y. Y. Chang, R. Korzekwa, H.-E. Tsai, C.-H. Pai, H. Quevedo, G. Dyer, E. Gaul, M. Martinez, A. C. Bernstein, T. Borger, M. Spinks, M. Donovan, V. Khudik, G. Shvets, T. Ditmire, and M. C. Downer (2013), *Nature Commun.* **4**, 1988.
- Wartski, L., S. Roland, J. Lasalle, M. Bolore, and G. Filippi (1975), *J. Appl. Phys.* **46** (8), 3644.
- Weiner, A. M. (2000), *Rev. Sci. Instrum.* **71**, 1929.
- Weingartner, R., M. Fuchs, A. Popp, S. Raith, S. Becker, S. Chou, M. Heigoldt, K. Khrennikov, J. Wenz, T. Seggebrock, B. Zeitler, Z. Major, J. Osterhoff, F. Krausz, S. Karsch, and F. Grüner (2011), *Phys. Rev. ST Accel. Beams* **14**, 052801.
- Weingartner, R., S. Raith, A. Popp, S. Chou, J. Wenz, K. Khrennikov, M. Heigoldt, A. R. Maier, N. Kajumba, M. Fuchs, B. Zeitler, F. Krausz, S. Karsch, and F. Grüner (2012), *Phys. Rev. ST Accel. Beams* **15**, 111302.
- Wickersheim, K., R. Alves, and R. Buchanan (1970), *IEEE Trans. Nucl. Sci.* **17** (1), 57.
- Wilke, I., A. M. MacLeod, W. A. Gillespie, G. Berden, G. M. H. Knippels, and A. F. G. van der Meer (2002), *Phys. Rev. Lett.* **88** (12), 124801.
- Wilks, S. C., J. M. Dawson, W. B. Mori, T. Katsouleas, and M. E. Jones (1989), *Phys. Rev. Lett.* **62**, 2600.
- Williams, R. L. (1995), *Rev. Sci. Instrum.* **66** (1), 468.
- Williams, R. L., C. E. Clayton, C. Joshi, and T. Katsouleas (1990a), *Rev. Sci. Instrum.* **61** (10), 3037.
- Williams, R. L., C. E. Clayton, C. Joshi, T. Katsouleas, and W. B. Mori (1990b), *Laser and Particle Beams* **8** (3), 427.
- Wittig, G., O. Karger, A. Knetsch, Y. Xi, A. Deng, J. Rosenzweig, D. Bruhwiler, J. Smith, G. Manahan, Z.-M. Sheng, *et al.* (2015), *Phys. Rev. ST-Accel. Beams* **18** (8), 081304.
- Wood, W. M., C. W. Siders, and M. C. Downer (1991), *Phys. Rev. Lett.* **67**, 3523.
- Wu, J., N. Hu, H. Setiawan, X. Huang, T. O. Raubenheimer, Y. Jiao, G. Yu, A. Mandlekar, S. Spampinati, K. Fang, *et al.* (2017), *Nucl. Instrum. Methods Phys. Res. A* **846**, 56.

- Xiang, D., E. Colby, M. Dunning, S. Gilevich, C. Hast, K. Jobe, D. McCormick, J. Nelson, T. O. Raubenheimer, K. Soong, G. Stupakov, Z. Szalata, D. Walz, S. Weathersby, and M. Woodley (2011), *Phys.Rev. ST Accel. Beams* **14** (11), 1.
- Xiang, D., and W.-h. Huang (2007), *Physical Review Special Topics - Accelerators and Beams* **10** (1), 012801.
- Xin, M., K. Safak, M. Y. Peng, A. Kalaydzhyan, P. T. Callahan, W. Wang, O. D. Muecke, and F. X. Kaertner (2017), *IEEE J. ST Quant. Electron.* **23** (3).
- Xu, X. L., J. F. Hua, Y. P. Wu, C. J. Zhang, F. Li, Y. Wan, C.-H. Pai, W. Lu, W. An, P. Yu, M. J. Hogan, C. Joshi, and W. B. Mori (2016), *Phys. Rev. Lett.* **116**, 124801.
- Yan, W., C. Fruhling, G. Golovin, D. Haden, J. Luo, P. Zhang, B. Zhao, J. Zhang, C. Liu, M. Chen, *et al.* (2017), *Nature Photon.*
- Yellampalle, B., K. Y. Kim, G. Rodriguez, J. H. Glowina, and A. J. Taylor (2005), *Appl. Phys. Lett.* **87** (21), 211109.
- Yi, S., V. Khudik, S. Y. Kalmykov, and G. Shvets (2010), *Plasma Phys. Control. Fusion* **53** (1), 014012.
- Zakharov, V. E. (1972), *Sov. Phys. JETP* **35** (5), 908.
- Zeil, K., S. D. Kraft, A. Jochmann, F. Kroll, W. Jahr, U. Schramm, L. Karsch, J. Pawelke, B. Hidding, and G. Pretzler (2010), *Rev. Sci. Instrum.* **81**, 013307.
- Zgadzaaj, R., Z. Li, M. Downer, S. Gessner, S. Corde, M. Litos, C. Clarke, M. Schmeltz, J. Allen, S. Green, *et al.* (2016), in *AIP Conf. Proc.*, Vol. 1777 (AIP Publishing) p. 070014.
- Zhang, C., J. Hua, Y. Wan, B. Guo, C.-H. Pai, Y. Wu, F. Li, H.-H. Chu, Y. Gu, W. Mori, *et al.* (2016a), *Phys. Rev. Accel. Beams* **19** (6), 062802.
- Zhang, C., J. Hua, Y. Wan, C.-H. Pai, B. Guo, J. Zhang, Y. Ma, F. Li, Y. Wu, F. Li, H.-H. Chu, Y. Gu, X. Xu, M. WB, J. C, W. J, and W. Lu (2017), *Phys. Rev. Lett.* **119**, 064801.
- Zhang, C., Y. Wan, B. Guo, J. Hua, C. Pai, F. Li, J. Zhang, Y. Ma, Y. Wu, X. Xu, *et al.* (2018), *Plasma Phys. Control. Fusion* **60** (4), 044013.
- Zhang, C. J., J. F. Hua, X. L. Xu, F. Li, C. H. Pai, Y. Wan, Y. P. Wu, Y. Q. Gu, W. B. Mori, C. Joshi, and W. Lu (2016b), *Sci. Rpts.* **6**, 29485.
- Zhang, M. (1996), "Fermilab-tm-1988,".